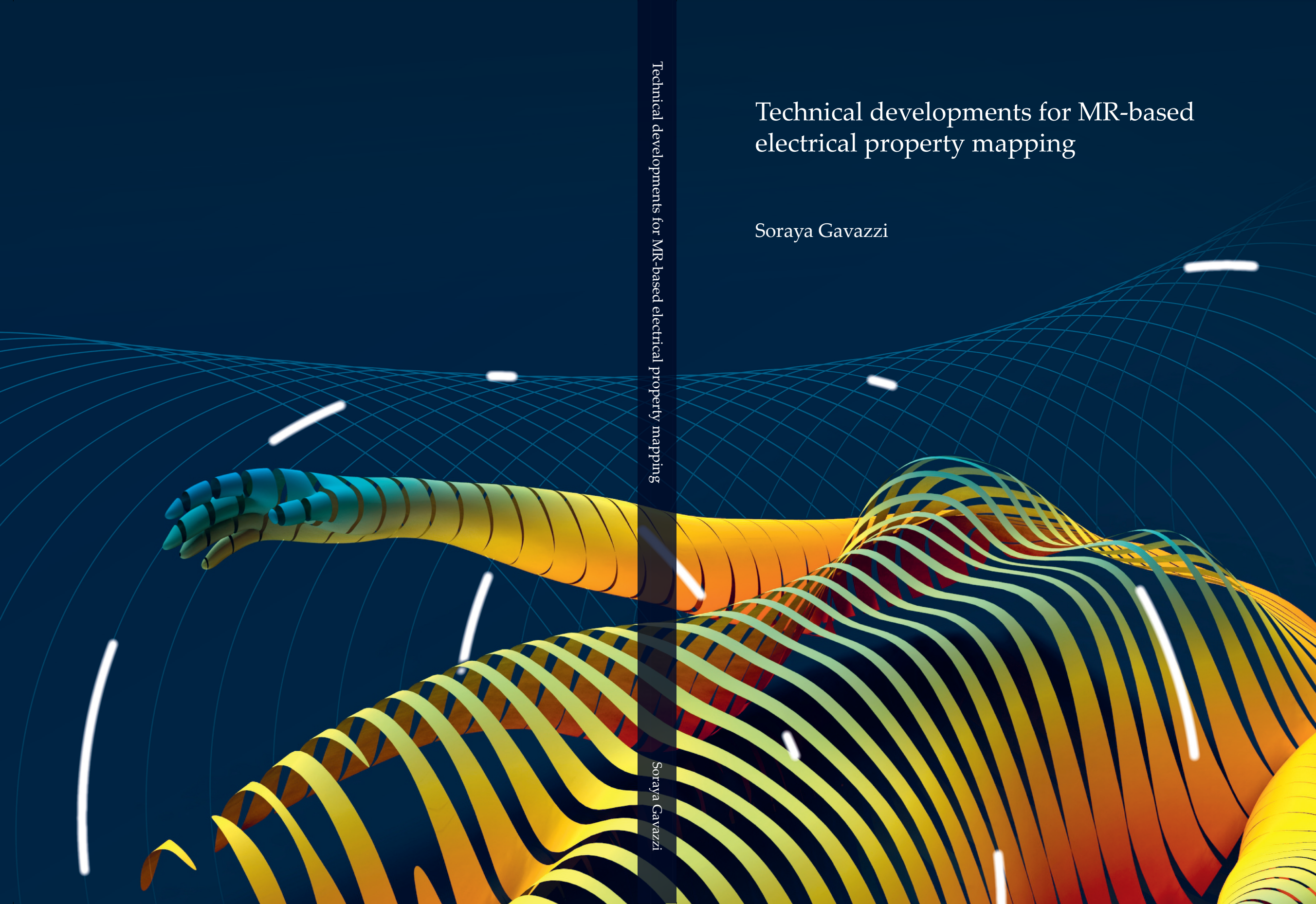


Technical developments for MR-based electrical property mapping

Soraya Gavazzi

Technical developments for MR-based electrical property mapping

Soraya Gavazzi



Technical developments for MR-based electrical property mapping

Soraya Gavazzi

Cover The cover is an artist's impression of the B_1^+ field in the human body. The B_1^+ is the magnetic field that we measure with MRI to map the electrical properties of body tissues.

Technical developments for MR-based electrical property mapping
PhD thesis, Utrecht University, The Netherlands

Manuscript

Layout: Soraya Gavazzi
Cover Design: Matteo Nebiolo
Typeset in: L^AT_EX 2_ε
Printed by: PrintSupport4U
ISBN: 978-94-92597-51-9

Copyright © 2020 Soraya Gavazzi

All rights reserved. The copyright of the chapters that have been published or accepted for publication has been transferred to the respective journals. No part of this thesis may be reproduced, distributed, or transmitted in any form or by any means without the prior written permission of the author or, when applicable, of the publishers of the scientific articles.

Financial support for publication of this thesis was kindly provided by ALBA Precision Hyperthermia.

Technical developments for MR-based electrical property mapping

Technische ontwikkelingen voor elektrische eigenschappen visualisatie met MRI

(met een samenvatting in het Nederlands)

Proefschrift

ter verkrijging van de graad van doctor aan de
Universiteit Utrecht
op gezag van de
rector magnificus, prof. dr. H.R.B.M. Kummeling,
ingevolge het besluit van het college voor promoties
in het openbaar te verdedigen op
vrijdag 25 september 2020 des middags te 2.30 uur

door

Soraya Gavazzi

geboren op 15 december 1990
te Aosta, Italië

Promotoren: Prof. dr. ir. J.J.W. Lagendijk
Prof. dr. ir. C.A.T. van den Berg

Copromotoren: Dr. ir. A.L.H.M.W. van Lier
Dr. J. Crezee

This work is part of the research project “MRI based hyperthermia treatment planning for improved hyperthermia delivery in cervical cancer patients” financially supported by the Dutch Cancer Society (KWF, grant UVA 2014-7197).

*La sconfitta è un'eleganza per l'ipocrisia
di chi si arrende in partenza.*

Subsonica

*It is not knowledge, but the act of learning,
not possession but the act of getting there,
which grants the greatest enjoyment.*

Carl Friedrich Gauss

Contents

Acronyms & Symbols	xi
1 General Introduction	1
1.1 Electrical properties of tissues	2
1.2 Measuring the electrical properties	3
1.3 Magnetic Resonance Imaging	4
1.3.1 The B_1^+ field	5
1.4 MR-based Electrical Properties Tomography	6
1.5 Deep Learning & Convolutional Neural Networks	7
1.6 MR sequences for EPT	8
1.6.1 $ B_1^+ $ mapping sequences	8
1.6.2 Transceive phase mapping sequences	9
1.7 Reconstruction methods for EPT	9
1.7.1 Direct EPT	10
1.7.1.1 Helmholtz-based EPT	10
1.7.1.2 Beyond Helmholtz-based EPT	10
1.7.2 Inverse EPT	11
1.7.3 Learning-based EPT	11
1.8 Validation of EPT methods	11
1.9 Pre-clinical & clinical EPT studies	12
1.10 Outline of this thesis	13
2 Transceive phase mapping using the PLANET method and its application for conductivity mapping in the brain	15
2.1 Introduction	16
2.2 Theory	17
2.2.1 The phase-cycled bSSFP signal	17
2.2.2 Estimation of the transceive phase ϕ^\pm with bSSFP and PLANET	17
2.2.2.1 bSSFP	17
2.2.2.2 PLANET	19
2.3 Methods	19
2.3.1 Simulations	19
2.3.2 Measurements	20
2.3.3 Post-processing	22
2.3.4 Accuracy	22

2.3.5	Precision	22
2.4	Results	23
2.4.1	Simulation results	23
2.4.1.1	Simulations I & II	23
2.4.1.2	Simulation III	25
2.4.1.3	Simulation IV	25
2.4.1.4	Simulation V	26
2.4.2	Measurement results	26
2.4.2.1	Phantom Experiments	26
2.4.2.2	In vivo brain experiments	29
2.5	Discussion	32
2.6	Conclusion	36
2.A	Appendix A: The bSSFP signal	36
2.B	Appendix B: Supplementary figures	37
3	Accuracy & precision of electrical permittivity mapping at 3T: the impact of three B_1^+ mapping techniques	41
3.1	Introduction	42
3.2	Methods	43
3.2.1	Phantom and in vivo	43
3.2.2	MR Experiments	45
3.2.3	MR Simulations	47
3.2.4	Permittivity reconstruction	47
3.2.5	Effect of transceive phase assumption	48
3.2.6	ROI delineation	48
3.2.7	Accuracy assessment	48
3.2.8	Precision assessment	48
3.3	Results	49
3.3.1	Simulation results	49
3.3.1.1	Accuracy	49
3.3.1.2	Effect of transceive phase assumption	50
3.3.2	Measurement results	52
3.3.2.1	Precision	53
3.4	Discussion	55
3.5	Conclusion	58
3.A	Appendix: Derivation of error propagation (precision) in the B_1^+ , $\zeta_{B_1^+}$	59
3.A.1	AFI	59
3.A.2	BLOCH-SIEGERT SHIFT (BS)	59
3.A.3	DREAM	60
4	Deep learning-based reconstruction of in vivo pelvis conductivity with a 3D patch-based CNN trained on simulated MR data	61
4.1	Introduction	62
4.2	Methods	63
4.2.1	Database construction	63
4.2.1.1	Human pelvic models	63
4.2.1.2	Construction of dielectric models	63

4.2.1.3	EM simulations	64
4.2.1.4	MR simulations	66
4.2.2	MR experiments	66
4.2.3	Conductivity mapping	66
4.2.3.1	DL-EPT	66
4.2.3.2	Helmholtz-based EPT (H-EPT)	70
4.3	Results	70
4.3.1	In silico results	70
4.3.2	In vivo results	75
4.4	Discussion	76
4.5	Conclusion	81
4.A	Appendix A: Determining tissue-specific EP uniform distributions	81
4.B	Appendix B: Supplementary figures	83
5	Advanced patient-specific hyperthermia treatment planning	85
5.1	Introduction	86
5.2	Hyperthermia Treatment Planning workflow	88
5.2.1	Imaging protocols	89
5.2.1.1	MR	89
5.2.1.2	CT	89
5.2.2	Preparation of the patient model for HTP	91
5.2.2.1	Tissue geometry	91
5.2.2.2	Electrical properties of tissues	91
5.2.2.3	Thermal properties of tissues	92
5.2.3	Hyperthermia Treatment Planning	92
5.2.3.1	Simulation of the electric field	92
5.2.3.2	Thermal modelling and temperature-based optimization	93
5.2.4	Biological modelling	93
5.2.4.1	Preparation	93
5.2.4.2	Equivalent radiation dose calculation	94
5.3	HTP workflow results	95
5.3.1	HTP preparation results	95
5.3.2	Hyperthermia treatment planning results	98
5.3.3	Biological modelling results	99
5.4	Discussion	99
5.5	Conclusion	105
6	General Discussion	107
6.1	B_1^+ acquisition & EPT	108
6.1.1	Error quantification in EPT	108
6.1.1.1	The added value of MR sequence simulations in EPT	108
6.1.2	The impact of B_1^+ acquisition on Helmholtz-based EPT	109
6.1.2.1	Accuracy	109
6.1.2.2	Precision	109
6.1.3	The impact of B_1^+ acquisition on DL-EPT	110
6.1.4	Future perspectives	110

6.1.4.1	Permittivity mapping	110
6.1.4.2	Accuracy in EPT	110
6.1.4.3	Faster acquisition	110
6.1.4.4	Simultaneous $ B_1^+ $ and ϕ^\pm acquisition	111
6.2	Deep Learning & EPT	111
6.2.1	DL-EPT	111
6.2.1.1	Reconstruction accuracy & precision	113
6.2.1.2	Generalization	113
6.2.1.3	Confidence	114
6.2.1.4	Experimental validation	115
6.2.1.5	DL-EPT conductivity as a biomarker?	115
6.2.2	New frontiers for deep learning in EPT	116
6.3	Hyperthermia treatment planning	116
6.3.1	Advanced hyperthermia treatment planning	116
6.3.2	The role of EPT in hyperthermia treatment planning	117
6.3.3	Future perspectives	118
6.3.3.1	Deep learning for hyperthermia treatment planning	118
6.3.3.2	Field of view in MR-based HTP	118
6.4	Conclusion	119
Bibliography		121
Summary		141
Samenvatting		145
Publications		149
Acknowledgments		151
About the author		155

Acronyms & Symbols

Acronyms

2D, 3D	Two, three dimensional
ADC	Apparent Diffusion Coefficient
AFI	Actual Flip angle Imaging
BS	Bloch-Siegert
bSSFP	balanced Steady State Free Precession
CLEAR	Constant LEvel of AppeaRance
CNN	Convolutional Neural Network
CSF	Cerebrospinal Fluid
CSI	Contrast Source Inversion
CT	Computed Tomography
DL	Deep Learning
DREAM	Dual Refocusing Echo Acquisition Mode
DVH	Dose Volume Histogram
EM	Electromagnetic
EP	Electrical Property
EPT	Electrical Properties Tomography
FA	Flip Angle
FDTD	Finite-Difference Time-Domain
FOV	Field Of View
GM	Gray Matter
GPU	Graphics Processing Unit
GTV	Gross Tumour Volume
H-EPT	Helmholtz-based Electrical Properties Tomography
HT	Hyperthermia
HTP	Hyperthermia Treatment Planning
LQ	Linear-Quadratic
MR	Magnetic Resonance
MRI	Magnetic Resonance Imaging
NMR	Nuclear Magnetic Resonance
QSM	Quantitative Susceptibility Mapping
RF	Radiofrequency

ROI	Region Of Interest
RT	Radiation Therapy (or radiotherapy)
SAR	Specific Absorption Rate
SE	Spin Echo
SNR	Signal-to-Noise Ratio
std	Standard deviation
TE	Echo Time
TR	Repetition Time
WM	White Matter

Symbols

B_0	Static magnetic field
B_1	Radiofrequency magnetic field
B_1^+	Complex transmit magnetic field
B_1^-	Complex receive magnetic field
$ B_1^+ $	Amplitude of B_1^+ field
E (or E-field)	Electric field
M	Magnetization
T_1	spin-lattice relaxation time
T_2	spin-spin relaxation time
γ	Gyromagnetic ratio
Δf_0	Off-resonance frequency
ϵ_0	Permittivity of free space
ϵ_r	Relative permittivity
μ_0	Magnetic permeability of free space
ρ	Tissue density
σ	Electrical conductivity
ζ	Standard deviation
$\zeta_{B_1^+}$	Standard deviation of $ B_1^+ $
ζ_{ϕ^\pm}	Standard deviation of transceive phase
ϕ^+	Phase of B_1^+ field
ϕ^-	Phase of B_1^- field
ϕ^\pm	Transceive phase (sum of ϕ^+ and ϕ^-)
ω	Larmor (angular) frequency
Ω	Rotation angle

General Introduction

This thesis revolves around the concept of measuring the electrical (or dielectric) properties of human tissues. The electrical properties regulate the electromagnetic field behaviour in the tissue. Characterizing the electrical properties of tissues is important to understand the effects of electromagnetic fields on our body and has provided important insights into tissue composition and physiology for over a century.

In the early 1920s, for example, Fricke deduced the presence and thickness of the cell membrane from electrical property measurements on red blood cells [1]. In the following decades, the structure of several molecules and cells, as well as their interactions, began to be understood from the interpretation of dielectric measurements [2–4]. At the same time, equivalent circuits and dispersion models were proposed to describe the electrical behaviour of tissues [2, 5].

Around the 1970s, there was a surge of interest in the study of electrical properties of tissues. In addition to the ever-present desire for understanding the underlying biophysical mechanisms, this increased interest was motivated by concerns on the potential health hazards arising from exposure to electromagnetic fields and by the worldwide research on radiofrequency (RF) hyperthermia as anti-cancer therapy. This spurred important developments in electromagnetic dosimetry and in dielectric measurement procedures [6]. Between the late 1970s and the 1990s [7], many dielectric characterization experiments were performed both on excised animal tissue specimens and *in vivo*, and the first reports on the electrical properties of cancerous tissues also appeared [8, 9]. A comprehensive database of the electrical properties of almost all biological tissues was published in 1996, mostly based on *ex vivo* dielectric measurements of human tissues [10]. This database is still used today for electromagnetic dosimetric simulations.

In the last twenty years, dielectric probe measurements on healthy and malignant tissues (e.g. [11–18]) and *in vivo* electrical property mapping have been pursued, spurred by the same driving motives and by emerging applications utilizing electromagnetic fields for diagnosis and therapy [19]. Research on *in vivo* electrical property mapping was particularly stimulated by the use of Magnetic Resonance Imaging (MRI) technology.

This thesis describes technical developments for *Electrical Properties Tomography*, a technique that allows mapping the in vivo electrical properties of tissues from the magnetic field produced within the human body during an MRI examination.

1.1 Electrical properties of tissues

Biological tissues behave like lossy dielectric materials (a mix between insulators and conductors) when exposed to external electromagnetic (EM) fields. Their response to the external EM field is determined by a complex interrelation of biophysical properties, such as water content, ion concentration, pH, tissue composition, cellular structure, permeability of cell membrane [2,20,21], and can be described by their *electrical properties*. The electrical properties (EPs) comprise the *relative permittivity* ϵ_r and the *conductivity* σ . The (relative) permittivity characterizes the tissue's ability to polarize; that is, to induce or rotate dipoles to counteract the external electric field. The conductivity describes the tissue's ability to transfer charges (ions) inside its volume. Because the above-mentioned biophysical properties vary per tissue, the EPs are tissue-specific (Figure 1.1).

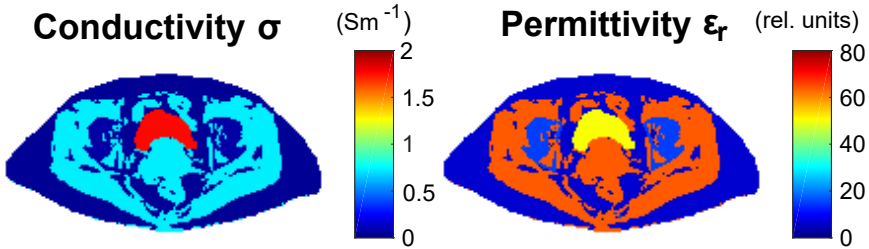


Figure 1.1. Conductivity and permittivity maps of the human pelvis at 128 MHz. Values of the electrical properties in each tissue were taken from [22].

The EPs of biological tissues vary with temperature [12,23], hydration [24] and age [25]. They also vary with frequency, because different polarization mechanisms and ionic conduction are stimulated or stopped according to the frequency of the applied EM field [3,20]. Examples of EP frequency-dependence are shown in Figure 1.2 for muscle, fat and blood. In Figure 1.2 it can be appreciated that both properties maintain stable values for certain frequency ranges, followed by a rapid increase/decrease, which is called "dispersion region". Tissues with heterogeneous composition and complex structure, for example muscle or fat, display three main dispersion regions, whereas blood, a viscous fluid with suspended cells, lacks one dispersion (α -dispersion) [3,20]:

- (i) α -dispersion (below ~ 10 kHz): dominated by ionic diffusion along cell membranes;
- (ii) β -dispersion (0.1 - 100 MHz): dominated by interface polarization of cell membranes;
- (iii) γ -dispersion (above 1 GHz): caused by orientation polarization, mostly of water molecules.

Figure 1.2 also shows that the EPs are only slightly frequency-dependent at MRI frequencies, which lie between β and γ dispersion regions. The frequency spectrum of tissue EPs can be described by mathematical models accounting for a single or multiple dispersions, such as Debye and Cole-Cole models [5].

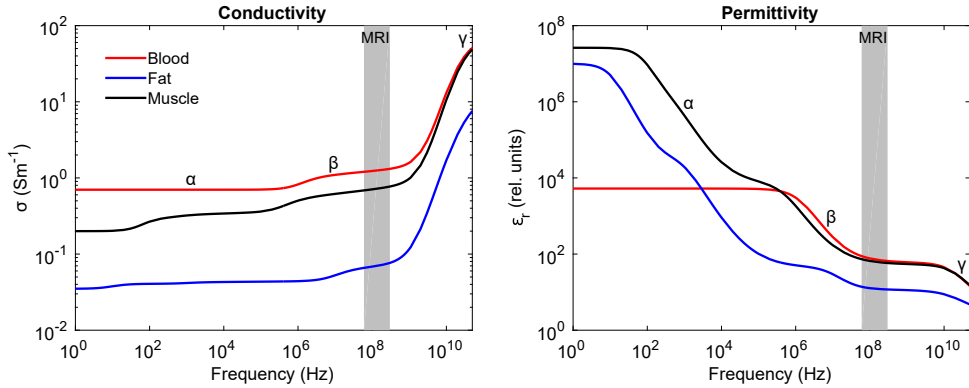


Figure 1.2. Frequency-dependence of conductivity and permittivity for three different biological media: blood, fat and muscle. The three dispersions regions are also indicated and are better visualized in the permittivity graph. Electrical properties were taken from [22]. The shaded area highlights the frequencies typically used in MRI (64 MHz - 300 MHz).

1.2 Measuring the electrical properties

Since the EPs are intrinsically related to biophysical processes, changes in tissue physiology affect the tissue EPs, which is why the EPs can potentially be used as biomarkers indicating the presence and/or state of a pathologic condition [26]. Furthermore, knowledge of tissue EPs is crucial for applications that utilize electromagnetic fields because the induced electric currents and the power absorbed inside the body are regulated by the electrical properties of tissues. Such applications include: specific absorption rate (SAR) assessment for RF safety (e.g. in MRI or telecommunications), RF hyperthermia for cancer treatment, medical EM imaging for diagnostic purposes, transcranial magnetic stimulation and transcranial direct current stimulation, both for treatment of neurological disorders. The tissue EPs need to be characterized at different frequencies depending on the application; this section focuses only on EPs at radiofrequencies between tens of MHz and tens of GHz, which span the working frequency range for MRI and hyperthermia.

A database of tissue EPs exist [22]. This database is predominantly based on dielectric probe measurements performed *ex vivo* on animal and human healthy tissues [7,10,11]. In general, there is a large variation in the reported EP values for the same tissue. This could be explained by the different species examined, but also by a number of confounders related to measurement conditions, including tissue handling procedures, temperature, time between excision and measurement [24,27,28], probe sensing volume [29], sample size. La Gioia et al. [30] have recently reviewed all the possible confounders contributing to the EP uncertainty from dielectric probe measurements.

An increasing body of literature has also focused on comparing the *ex vivo* EPs of healthy and pathologic tissues (e.g. cancer [8,9,13–17] and stroke [18]). Various studies unanimously reported that the EPs are higher in tumours than in normal tissues. This finding could be attributed to the fact that cancer cells have altered membrane composition and permeability, which results in potassium, magnesium, and calcium exiting the cell and sodium and water accumulating into the cell [31]. However, the discrepancy between malignant and healthy

tissue ϵ_p s can vary significantly. For example, the tumour/healthy dielectric contrast for breast can be as large as 10:1 if normal breast tissue is predominantly adipose [8,13], but it decreases to $\sim 10\%$ when normal breast tissue is glandular/fibroconnective [13]. Moreover, in the frequency range 0.5–20 GHz, the ϵ_p s of malignant tissue are 19% to 30%, $\sim 10\%$ and 8% to 20% higher than those of normal tissue in liver [14], colon [16] and thyroid gland [17], respectively.

In vivo dielectric probe measurements are mostly performed on sedated animals (e.g. [32]). Because of ethical and practical reasons, only a few studies reported in vivo human ϵ_p s from dielectric probe measurements, showing that in vivo values are higher than ex vivo ϵ_p s [14,28]. Microwave Imaging (MI) and MR-based Electrical Properties Tomography (MR-EPT) are alternative technologies for in vivo tissue ϵ_p detection at RF frequencies. More insight into the Microwave Imaging technique, its advantages, disadvantages and application can be found in references [33,34]. As previously mentioned, this thesis gravitates around MR-based Electrical Properties Tomography. Before we delve into the concept and implementation of this dielectric characterization method, a propaedeutic excursus on MRI and the B_1^+ field follows.

1.3 Magnetic Resonance Imaging

Magnetic Resonance Imaging (MRI) enables non-invasive imaging of anatomical structures and (patho)physiologic processes of the human body. MRI is based on the phenomenon of nuclear magnetic resonance (NMR) [35–38]. In this section, the principle of MR signal formation is briefly outlined; exhaustive descriptions of NMR theory, MR image formation and MRI techniques can be found in several books [39–41].

When a patient is placed within the bore of an MR system, where the static background (B_0) field is constantly present, the atomic nuclei (hydrogen protons) in the human body tend to align with the main magnetic field. As a result, a net magnetization (M) in the B_0 direction is established (Figure 1.3b). Furthermore, the B_0 field exerts a torque on the magnetic moments of these nuclei (or “spins”). Thus, the spins are deflected into a precessional motion (*Larmor precession*) around the B_0 , with Larmor (angular) frequency ω proportional to the static B_0 field strength and the proton gyromagnetic ratio γ (i.e., $\gamma_{\text{proton}} = 2\pi \cdot 42.58 \text{ MHz/T} = 2.7 \times 10^8 \text{ rad s}^{-1} \text{ T}^{-1}$):

$$\omega = \gamma B_0. \quad (1.1)$$

The Larmor frequency ($f = \omega/2\pi$) of hydrogen protons is in the radiofrequency range (64, 128 or 298 MHz) for commonly used magnetic field strengths (1.5, 3 or 7 tesla).

An RF electromagnetic pulse is used to generate the MR signal from the precessing spins. The RF pulse creates a magnetic field within the RF transmit coil which is orthogonal to B_0 and oscillates at (or near) the Larmor frequency. This transverse magnetic field, called B_1 , “excites” the spins such that the net magnetization is flipped away from its original alignment with B_0 by an angle called “flip angle” (FA). Because of the flipping, the net magnetization starts to precess around the B_0 direction at the Larmor frequency (Figure 1.3c), developing transverse components. After the B_1 field is turned off, the precessing net magnetization tends to realign with the static magnetic field through two relaxation mechanisms: the T_1 relaxation, responsible for the regrowth of the longitudinal magnetization component, and the T_2 relaxation, reflecting the decay of the transverse magnetization. The evolution of the precessing net magnetization and the relaxation effects are described by the so-called *Bloch equations* [42].

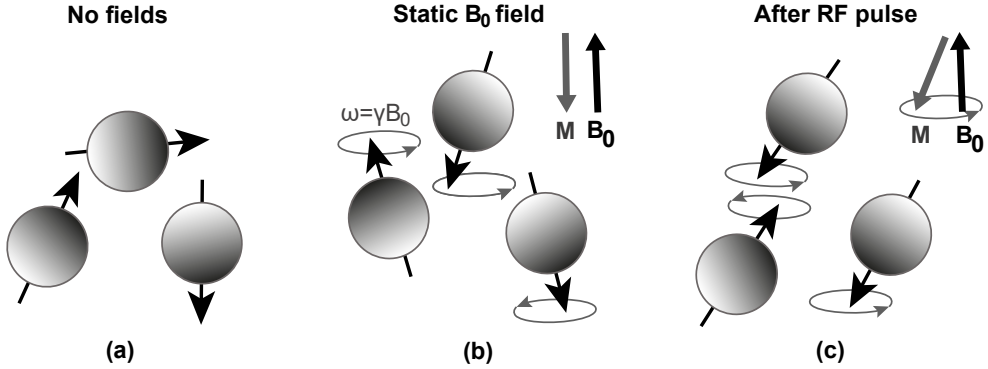


Figure 1.3. MRI in the classical representation. (a) The spins of hydrogen protons are randomly oriented when no magnetic field is present. (b) The spins align parallel or antiparallel with the static magnetic field B_0 and a net magnetization M is formed (typically in antiparallel alignment with B_0). Furthermore, they precess around the main magnetic field direction with Larmor frequency ω . (c) After being flipped by the RF pulse, the magnetization precesses around the B_0 and tends to realign with the main magnetic field, creating a measurable signal.

The induction signal caused by the precessing net magnetization can be detected with a receive coil, according to Faraday's law. This signal, however, is not spatially localized at this stage. Thus, magnetic gradient fields are produced with gradient coils either during or after the RF excitation to spatially encode the MR signal. In general, these magnetic gradient fields vary linearly along the x -, y - and z -directions and add up to the strength of the static magnetic field. Hence, the total magnetic field experienced by the nuclei and their Larmor frequency (tied by Equation 1.1) become spatially dependent. It is based upon this spatial encoding mechanism that an MR image is created.

The RF and gradient pulses can be orchestrated in a controlled fashion, i.e. with definite strengths, shapes, durations and spacing, to form an MR *pulse sequence*. Different design or parameter settings in the MR pulse sequence can change the contrast of the anatomical MR image (e.g. T_1 - or T_2 -weighting), suppress the signal of certain tissues (e.g. fat or fluids), and encode information on biophysical processes (e.g. diffusion, perfusion, oxygenation) and tissue properties (e.g. magnetic susceptibility, electrical properties). Furthermore, given the pulse sequence and the properties of tissues, a specific MR signal (and even the MR image) can be replicated with Bloch simulations, which are based on Bloch equations.

1.3.1 The B_1^+ field

As mentioned above, the B_1 field is a time-varying magnetic field rotating in the transverse plane at the Larmor frequency. Its projection onto the frame of reference rotating at the Larmor frequency in the same direction as the nuclear spins results in a stationary field, called the B_1^+ field (or transmit field) [43]:

$$B_1^+ = \frac{B_{1x} + iB_{1y}}{2} \quad (1.2)$$

with B_{1x} and B_{1y} denoting the x and y components of the B_1 field. The B_1^+ field is the effective excitation field experienced by the spins. With an analogous reasoning, the projection of B_{1x}

and B_{1y} components onto the frame rotating in the opposite direction of the spins results in the B_1^- field (or receive field). The B_1^- field does not lead to any excitation and is proportional to the signal sensitivity of the RF receive coil [43].

The spatial distribution of B_1^+ and B_1^- can be altered depending on the operating Larmor frequency, the driving scheme of the RF coil, the geometry of the imaged body site and its electrical properties [44–47]. In particular, the electric field associated with the transmit coil's RF magnetic field induces displacement currents and conduction currents within the dielectric body, where a total magnetic field with net elliptically-polarized B_1^+ and B_1^- components is established. For frequencies $f < 64$ MHz ($B_0 < 1.5$ T), the B_1^+ and B_1^- fields are only marginally distorted by these induced currents; for increasing B_0 field strengths, nevertheless, the spatial distribution of the B_1^+ and B_1^- progressively becomes more inhomogeneous since interference patterns appear due to wave effects caused by the reduced wavelength of the B_1 field, which becomes comparable to the dimensions of the imaged body [47–49].

In short, the electrical properties of tissues effectively shape the transmit B_1^+ field within the body. This is particularly important in MRI since the complex MR signal S is a function of the complex transmit and receive fields:

$$S(\mathbf{r}) \propto |B_1^-(\mathbf{r})| f(\alpha_{nom} |B_1^+(\mathbf{r})|) \times e^{i(\phi^+(\mathbf{r}) + \phi^-(\mathbf{r}))} \quad (1.3)$$

where f is a function depending on the MR sequence and can also include the signal contributions due to proton density, relaxation, off-resonance effects; α_{nom} represents the nominal flip angle setting of the sequence, and $|B_1^{+/-}|$ and $\phi^{+/-}$ are the magnitude and phase of the complex B_1^+ and B_1^- fields, respectively.

1.4 MR-based Electrical Properties Tomography

In the previous section, we have learnt that:

- (i) the tissue EPs distort the B_1^+ field in the human body;
- (ii) the B_1^+ field affects the effective flip angle and therefore the MR signal (Equation 1.3);
- (iii) the measurable MR signal can be manoeuvred with MR sequences to reveal certain processes or properties.

Hence, the electrical properties of tissues can be retrieved non-invasively from MR measurements of the B_1^+ field. This is the key concept of MR-based Electrical Properties Tomography (EPT). EPT is effectively a quantitative MR contrast that reveals the subject-specific electrical properties. For completeness, we mention that EPT methods based on MR measurements of the B_1^- field [50] or of the tissue water content [51–53] have also been reported. Although the name "EPT" was coined in 2009 [54], this underlying concept of mapping the EPs from MR signals reflecting the distorted RF magnetic field was first suggested in 1991 by Haacke et al. [55]. A decade later, Wen [56] used Maxwell's equations to map the EPs of a phantom from the RF magnetic field. The full Helmholtz equation derived by Wen has become the central equation for EPT [57, 58]:

$$-\nabla^2 \mathbf{B}_1(\mathbf{r}) = \omega^2 \mu_0 \tilde{\epsilon}(\mathbf{r}) \mathbf{B}_1(\mathbf{r}) + \frac{\nabla \tilde{\epsilon}(\mathbf{r})}{\tilde{\epsilon}(\mathbf{r})} \times [\nabla \times \mathbf{B}_1(\mathbf{r})] \quad (1.4)$$

where ω is the Larmor frequency, μ_0 is the magnetic permeability of free space and $\tilde{\epsilon}(\mathbf{r}) = \epsilon_0(\mathbf{r})\epsilon_r - i\sigma(\mathbf{r})/\omega$, with ϵ_0 the permittivity in vacuum. By neglecting the derivatives of the B_{1z} component, which is acceptable close to the iso-center for many coil types [54], Equation

1.4 can also be rewritten in terms of B_1^+ (or of B_1^-) [57,58]. Furthermore, Equation 1.4 can be simplified by assuming piece-wise constant and isotropic ϵ_r s (i.e. $\nabla\tilde{\epsilon}(\mathbf{r}) \approx 0$) [54,56,59], yielding the so-called "homogeneous Helmholtz equation":

$$-\nabla^2 B_1^+(\mathbf{r}) = \omega^2 \mu_0 \tilde{\epsilon}(\mathbf{r}) B_1^+(\mathbf{r}). \quad (1.5)$$

After replacing $B_1^+(\mathbf{r}) = |B_1^+(\mathbf{r})|e^{i\phi^+(\mathbf{r})}$ and $\tilde{\epsilon}(\mathbf{r}) = \epsilon_0 \epsilon_r(\mathbf{r}) - i\sigma(\mathbf{r})/\omega$ in Equation 1.5, the permittivity $\epsilon_r(\mathbf{r})$ and conductivity $\sigma(\mathbf{r})$ can be quantitatively retrieved as follows [56–59]:

$$\epsilon_r(\mathbf{r}) = -\frac{1}{\mu\epsilon_0\omega^2} \Re\left(\frac{\nabla^2 B_1^+(\mathbf{r})}{B_1^+(\mathbf{r})}\right) = -\frac{1}{\mu\epsilon_0\omega^2} \left[\frac{\nabla^2 |B_1^+(\mathbf{r})|}{|B_1^+(\mathbf{r})|} - (\nabla\phi^+(\mathbf{r}))^2 \right] \quad (1.6)$$

$$\sigma(\mathbf{r}) = \frac{1}{\mu\omega} \Im\left(\frac{\nabla^2 B_1^+(\mathbf{r})}{B_1^+(\mathbf{r})}\right) = \frac{1}{\mu\omega} \left[\nabla^2 \phi^+(\mathbf{r}) + 2 \frac{\nabla |B_1^+(\mathbf{r})| \cdot \nabla \phi^+(\mathbf{r})}{|B_1^+(\mathbf{r})|} \right]. \quad (1.7)$$

Equations 1.6 and 1.7 show that the permittivity and the conductivity scale quadratically and linearly with the magnetic field strength (through ω), respectively. Moreover, the permittivity predominantly perturbs the $|B_1^+|$ distribution, whereas the conductivity influences the phase distribution of the B_1^+ [56]. At 1.5 and 3T, calculating the permittivity (or conductivity) from the $|B_1^+|$ (or ϕ^+) only, i.e. by neglecting the second term in the right side of Equation 1.6 (or 1.7), accounts for 10–20% reconstruction errors in most human tissues [59,60].

Research on EPT took off around 2009, when Katscher et al. [54] implemented Equation 1.5 in integral form and applied it to estimate the SAR from MR measurements. In general, Maxwell's equations and Equations 1.4 and 1.5 form the basis for many EPT reconstruction methods, but data-driven approaches using machine learning or deep learning for EP reconstruction have also recently emerged. Deep learning algorithms learn the features important for EP reconstruction from a multitude of B_1^+ maps, rather than being explicitly given physics equations to model the interaction between EPs and B_1^+ . Hereafter, a short outline of convolutional neural networks, a class of deep learning algorithms, is given (section 1.5). Then, the different techniques for B_1^+ acquisition (section 1.6) and for EP reconstruction (section 1.7) are reviewed. Next, validation of EPT methods is explained in section 1.8. Finally, the (pre-)clinical applications of EPT explored thus far are outlined (section 1.9).

1.5 Deep Learning & Convolutional Neural Networks

Deep learning (DL) is a class of machine learning algorithms based on artificial neural networks. The reader is referred to references [61–63] for more exhaustive explanations on the fundamentals of deep learning. DL algorithms are capable to automatically learn complex representations of images or data and are increasingly being employed in MRI. A review on the use of DL in MRI has recently been published [64].

Convolutional neural networks are artificial neural networks generally applied for image recognition and processing. In a nutshell, a convolutional neural network (CNN) is a series of convolutional layers constituted by multiple filters (Figure 1.4). These filters are independently convolved with the input data producing *feature maps*, which are then input for the following layer and so forth. Normally, other layers are placed between the convolutional layers to provide nonlinearities and preserve input dimensions, as well as to render the network robust and efficient. Throughout the layers, the feature maps progressively represent more complex features. The network architecture ends with a fully connected layer, which outputs a map with either the probability for a certain label for classification problems or real values for regression problems.

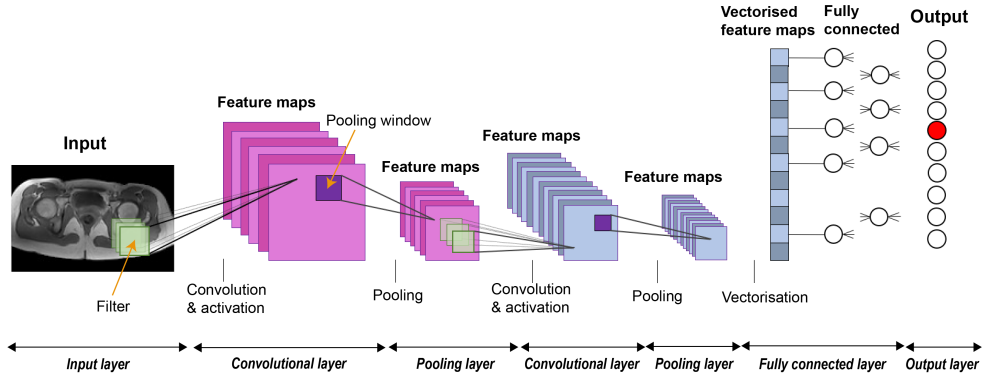


Figure 1.4. Example of a convolutional neural network. The main building blocks (layers) and operations are indicated.

Initially, the values (*weights*) of the above-mentioned filters are randomly set, thus no meaningful feature or output will be produced. The CNN needs to adjust its weights to optimize the output, which is the goal of the *training* phase. Training is an iterative optimization process requiring a lot of training data (input data and their corresponding target data for supervised learning tasks) and tuning of network parameters. During one training iteration, a large number of input data goes through the network layers ("forward pass") and the last layer predicts an output map for each input. The total error between predicted outputs and targets is evaluated with a chosen loss function and the gradients of the loss function with respect to all weights are computed to determine the contribution of each weight to the total error ("backpropagation"). A "gradient descent" optimization algorithm updates the network weights based on their error contribution in order to minimize the loss function. This procedure is performed iteratively for a fixed number of iterations and for each set of the training dataset. Once the network is trained, the CNN can be presented with new, "unseen" data to predict the output and/or to evaluate its generalization capabilities (*testing* or *inference* phase).

1.6 MR sequences for EPT

Both amplitude and phase of the B_1^+ field need to be acquired to map the tissue permittivity and conductivity (see, for example, Equations 1.6 and 1.7). The $|B_1^+|$ can be acquired with dedicated B_1^+ mapping sequences because of its non-linear influence on the MR signal. The ϕ^+ , instead, is not directly accessible because it is always summed to the ϕ^- in the MR signal (see Equation 1.3). The sum of ϕ^+ and ϕ^- is referred to as *transceive phase* (ϕ^\pm) and is measurable with commonly available MR sequences. In practice, highly accurate mapping sequences are desired since the accuracy of measured $|B_1^+|$ and ϕ^\pm maps influences the reconstruction of EP maps.

1.6.1 $|B_1^+|$ mapping sequences

The majority of $|B_1^+|$ mapping sequences acquires two MR images and encodes the $|B_1^+|$ information either in the magnitude or in the phase of such images. The $|B_1^+|$ is then reconstructed by combining these signal magnitudes or phases according to a sequence-

specific mathematical model. This mathematical model influences the accuracy and precision of the resulting $|B_1^+|$ map, since it determines the sensitivity of the technique to B_1^+ variations and the noise propagation from the MR images to the $|B_1^+|$ map.

B_1^+ mapping sequences can be divided into "magnitude-based" and "phase-based" methods, depending on whether the $|B_1^+|$ is stored in the magnitude or in the phase of the acquired images. Among magnitude-based $|B_1^+|$ mapping sequences there are, for example, the double angle methods [65–67], the actual flip angle imaging (AFI) methods [68–70], and methods exploiting stimulated echoes [71, 72]. Phase-based sequences include the phase-sensitive technique [73], the Bloch-Siegert (BS) shift technique [74] and methods exploiting adiabatic pulses [75]. Double angle and AFI $|B_1^+|$ methods have usually been utilized in EPT studies, with a few exceptions for the BS technique.

Several studies revealed that magnitude-based $|B_1^+|$ methods generally suffer from T_1 and/or T_2 sensitivity and provide a limited dynamic range for accurate $|B_1^+|$ measurements [76–78]. Phase-based methods are typically insensitive to relaxation effects, are accurate for larger ranges of $|B_1^+|$ variations and display more favourable signal-to-noise ratios than magnitude-based methods. Nonetheless, they may be sensitive to off-resonance effects and flow, and their performance may be limited by SAR restrictions. In Chapter 3 the accuracy and precision of three commonly available $|B_1^+|$ mapping sequences are examined in view of their use for EPT purposes.

1.6.2 *Transceive phase mapping sequences*

Transceive phase mapping methods must generally disentangle the desired transceive phase from other time-dependent phase terms entering the MR signal phase. Such time-dependent phase contributions are related to off-resonance variations, eddy currents caused by gradient switching and B_0 drift [39]. One strategy to minimize all the unwanted phase terms in the MR signal phase is to sample the signal right after the RF pulse, i.e. at $TE \approx 0$. This can be realized by utilizing ultra-short TE [79] and zero- TE [80] imaging methods, which allow fast acquisitions, but demand precise timing of RF and gradient pulses and therefore high-performance hardware which is not available in all scanners.

Standard MR sequences, such as the spin echo (SE), its faster version (turbo SE) [54], the spoiled gradient echo (dual-echo gradient echo [59] or a multi-echo gradient echo [81, 82]) and the balanced steady-state free precession (bSSFP) sequences have been used to map the transceive phase for EPT reconstruction. For these methods, B_0 drift can be considered negligible. Eddy currents generated during gradient switching induce a mild linear phase accrual on the signal phase, which can be minimized by averaging two identical acquisitions with opposite readout gradient polarities. The phase induced by off-resonance effects, instead, must be removed differently, depending on the sequence. In general, the transceive phase precision is linearly proportional to the image SNR for these sequences. More details on these transceive phase mapping methods can be found in Chapter 2.

1.7 Reconstruction methods for EPT

As anticipated in section 1.4, EPT reconstruction techniques can be subdivided into physics-based and learning-based methods. This section summarizes the advantages, limitations and application of several EPT reconstruction techniques belonging to these two classes. Physics-

based methods include direct and inverse EPT methods. These are extensively reviewed in [57,58].

1.7.1 Direct EPT

Direct EPT methods normally apply either Equation 1.4 or Equation 1.5 to the measured B_1^+ field, albeit with different implementation schemes. These methods do not require any particular a priori knowledge, e.g. of the RF coil setup. The most widespread EPT method is based on the homogeneous Helmholtz equation and is dubbed "Helmholtz-based EPT".

Helmholtz-based EPT Being based on Equation 1.5, Helmholtz-based EPT (H-EPT) relies on the assumption of homogeneous tissue ϵ s, which is violated at dielectric discontinuities such as tissue interfaces, where local physical errors appear [83]. Additional numerical oscillatory errors ("boundary errors") arise at tissue boundaries because the Laplacian operation is computed locally by using finite difference kernels (e.g. the kernels in [59, 84, 85]) that are convolved with measured, discretized B_1^+ field maps [86, 87]. The spatial extension and severity of boundary errors increase with the kernel size and the dielectric contrast between the adjacent tissues, respectively [86, 87]. Moreover, acting as a spatial high-pass filter, the Laplacian amplifies the noise in B_1^+ maps: the noise propagates from the $|B_1^+|$ ($/\phi^\pm$) to the H-EPT-reconstructed ϵ_r ($/\sigma$) as a function of (i) the SNR of measured inputs, (ii) the differentiation kernel shape and (iii) the kernel size, with a much more favourable propagation for conductivity reconstruction [88]. Thus, the higher the B_0 strength [89] and the larger the kernel size [87], the more precise the reconstructed ϵ map. Denoising strategies include using large kernels [90], large voxel sizes, image filters [83, 91–93], polynomial fitting to B_1^+ data [94], redesigned Laplacian kernels [95], special acquisition schemes [96] and integration-based solutions [54, 60]. Bilateral filters can be applied to constrain the differentiation to voxels with the same ϵ , thereby reducing boundary errors [81, 94].

At $B_0 < 7$ T, the necessary ϕ^+ is usually approximated with the *transceive phase assumption*, i.e. $\phi^+ \approx \phi^\pm/2$ [54, 56, 59]. The validity of this assumption deteriorates for increasing B_0 strengths [89], non-quadrature RF coils and object asymmetry, leading to larger errors at the object's periphery [97]. For 7 T and high-field MR systems, which are nowadays equipped with multi-transmit arrays, ϕ^+ is calculated from measurements of B_1^+ and B_1^- of the different channels [98, 99]. This concept has been incorporated in more sophisticated EPT approaches that, for example, include the calculation of the ϵ gradient term [93, 100].

In vivo human conductivity maps reconstructed with H-EPT were shown at 1.5, 3 and 7 T in several healthy organs, such as brain [59, 60, 93], liver [101], breast [94] and pelvis [97, 102]. On the contrary, in vivo permittivity reconstruction with H-EPT is challenging at these field strengths due to amplification of the noise in the $|B_1^+|$ map [60, 89]; permittivity mapping with H-EPT is examined extensively in Chapter 3.

Beyond Helmholtz-based EPT Advanced EPT methods, such as convection-reaction EPT [91, 103] and gradient-based EPT [93], exploit Equation 1.4 and reconstruct the three spatial gradients of the ϵ s. In gradient-based EPT, for example, the ϵ gradients are locally solved and then spatially integrated to obtain absolute ϵ maps starting from either seed points with known ϵ s [93] or an H-EPT-informed automatic seed selection [104]. Gradient-based EPT demonstrated improved boundary reconstruction and high robustness against noise, about 10 times higher than H-EPT [105]. In vivo brain conductivity maps were reconstructed at 3T with convection-reaction EPT [91, 103] and at 7 T with gradient-based EPT [93, 104]; 7 T permittivity

maps from volunteers' brain were reported with gradient-based EPT [93,104]. Other methods showing reduced boundary errors and noise sensitivity have been presented, e.g. [106–108].

1.7.2 Inverse EPT

Inverse EPT approaches are generally based on global integral forms of Maxwell's equations and obtain the EPs by iteratively minimizing a cost function measuring the discrepancy between the "measured" B_1^+ and modelled B_1^+ [109–118]. Many contributions have solved this inverse problem with the contrast source inversion (csi) method [109,114–118] and are reviewed in [119]. These integral approaches automatically account for boundary conditions, improving tissue interface reconstruction, and are less sensitive to noise because they avoid differentiation on noisy B_1^+ data. Furthermore, data consistency can be imposed and regularization terms can be included in the cost function to further mitigate the noise impact. Accurate modelling of EM fields that cannot practically be measured in MRI (e.g. electric field in an empty coil) and of the RF coil system is also often required. Because of the iterative optimization, these methods may risk to end up in local minima and are generally computationally expensive. Inverse EPT approaches demonstrated promising EP reconstructions on simulated brain and pelvis data, but in vivo EP maps have not yet been reported with such methods.

1.7.3 Learning-based EPT

Learning-based EPT methods are data-driven approaches which have emerged in the past couple of years. They use machine/deep learning techniques to reconstruct the tissue EPs from large datasets of known B_1^+ fields. Dictionary-based EPT and deep learning EPT (DL-EPT) belong to this family. In dictionary-based EPT [120], the tissue EPs are assigned with a machine learning-based matching procedure that evaluates the best match between measured B_1^+ 3D patterns and B_1^+ patterns stored in a dictionary. In DL-EPT, a CNN is trained in a supervised fashion on large datasets of measurable MR quantities, i.e. $|B_1^+|$ and ϕ^\pm , with associated EP maps. These input B_1 maps can be obtained from EM simulations, which allow to include a priori information such as the RF coil setup and the ground truth EPs [121], or from MR measurements, with EP maps reconstructed with a physic-based EPT method [122]. Training can be image-based [121] or patch-based [122], depending on the portion of the input data which is directly fed to the CNN. In principle, the EPs of any unseen B_1 measurement can be inferred once the network is trained. However, the quality and reliability of the inferred reconstruction heavily depends on the quality of the data fed to the CNN during training. This is closely linked to other key technical issues in DL-EPT, which include the generalization capability of the network and the (unknown) number of necessary training data. Brain conductivity maps of healthy volunteers were shown at 3T with dictionary-based EPT [120] and DL-EPT [121,122] and a 3T brain permittivity map was shown with DL-EPT [121].

1.8 Validation of EPT methods

Validation is intended to assess the accuracy and precision of EP maps reconstructed by a given EPT method. By *accuracy* we mean how close a reconstructed EP is to its true or reference value; deviations from the reference value are often associated with methodological imperfections. The accuracy can be calculated as long as ground truth EPs are known. True EPs are known in simulations, as they are defined a priori. In MR experiments, reference EPs are taken from independent dielectric probe measurements, which are usually carried out on phantoms. By *precision* we intend the range of values around the mean value of the reconstructed EP. This

spread is often associated with random errors caused by noise propagation. The precision can be assessed for both experimental and simulated data. Because no practical independent dielectric measurement method is available *in vivo*, knowledge of ground truth EPs for living human tissues is lacking and therefore a thorough validation on *in vivo* measured data is difficult. Taking tissue EP values reported in literature as reference EPs does not provide a strong validation considering that a large uncertainty (up to 50%) for different tissue EPs has been reported [7] and that EPs are subject-specific.

Validation differs between physic-based EPT and DL-EPT methods. A single phantom experiment is normally sufficient to validate a physics-based EPT method and guarantees the repeatability and consistency of the reconstructed EP results under the same working conditions. To date, direct EPT reconstruction techniques have generally been validated with both simulated data and MR phantom experiments. For example, H-EPT reconstructions are accurate within large homogeneous ROIs, with maximum deviations of $\sim 10\%$ from reference values [87, 89, 97], but present large standard deviations that can reach 100% of the mean reconstructed EP value [88]. Inverse EPT approaches have only been validated in simulations so far, showing deviations below 10% and much improved precision (e.g. [123]).

Because of its data-driven learning process, DL-EPT cannot be validated based on a single experiment. A gold standard procedure to validate DL models is the k -fold cross-validation [62], which allows to estimate the accuracy and precision of the method when small datasets are available. In a k -fold cross-validation the complete dataset is partitioned into k subdatasets of equal size ("folds"). The CNN is trained on $k-1$ folds and tested on the remaining fold. This process is repeated k times, such that each subdataset is tested once, serving as "validation data". The metrics for accuracy and precision are calculated on each "test" fold. Averaging the metrics over all test folds returns the overall accuracy and precision of the method. Because all data are used for training and tested once, the estimated method performance is less affected by sampling bias. Note, however, that the generalization error estimated with the cross-validation is valid as long as the test data share features with the training dataset. The accuracy and precision of DL-EPT still needs to be investigated.

1.9 Pre-clinical & clinical EPT studies

EPT can in principle be adapted and/or applied for many medical applications, which were already mentioned in section 1.2. Although initially conceived for SAR assessment in MRI, direct EPT methods have more often been used to characterize large human tumours. In this respect, preliminary EPT studies showed that the conductivity of brain tumours was higher than the conductivity of white matter [124–126]; this finding was also confirmed by Tha et al. [127], who showed that grade III and IV glioblastomas could be discerned from normal brain parenchyma based on their higher EPT conductivity. Analogously, breast tumours showed higher EPT-based conductivity than benign breast tissue [128–130]. Moreover, Balidemaj et al. [102] found that the H-EPT conductivity of cervical tumours in 20 patients was on average 13% higher than the *ex vivo* conductivity reported in literature for healthy cervical tissue [10]. Using the EPT-based conductivity values of pelvic tissues found in this last study, Balidemaj et al. [131] evaluated the added value of *in vivo* EPs in hyperthermia treatment planning (HTP). They demonstrated that using *in vivo* EPT conductivity leads to lower tumour temperatures than conventional HTP based on literature EPs, because of the higher power dissipation occurring in tissues adjacent to the tumour. All these studies were conducted for rather large neoplastic lesions ($\gtrsim 2$ cm), because the quantification would be compromised by the boundary issue otherwise.

In vivo rat experiments provided new insights into the potential of EPT as biomarker. Wang et al. [132] mapped the EPs of 11 rodent breast tumor xenograft models at 7 T and benchmarked their EP findings with probe measurements and histopathological tumour slides. They found that the conductivity elevated in tumour necrotic tissue and that the permittivity could be correlated with healing and scar formation processes. Furthermore, the preliminary results by Ko et al. [133] seem to indicate that EPT-based conductivity could be used to monitor the tissue response to radiation treatment: their in vivo experiments on a rat brain before and after radiotherapy showed that the brain conductivity was increased after the treatment, with 100% differences after 5 days of treatment. Finally, the correlation between sodium MRI and EPT-conductivity has also been studied to interpret the observed conductivity increase in tumours. Preliminary results suggested that conductivity correlates with total sodium concentration [134], and that free sodium might be the most contributing factor [135].

1.10 Outline of this thesis

Reliable quantitative measurements of subject-specific electrical properties can benefit a number of biomedical applications. The reliability of electrical properties obtained with EPT intrinsically depends on the accuracy and precision of both EPT reconstruction method and B_1^+ measurement sequence. This thesis focused on the relevant aspects of B_1^+ acquisition and EP reconstruction. The impact of accuracy and precision of commonly used ϕ^\pm and $|B_1^+|$ mapping techniques on the obtained EP maps is investigated (Chapters 2 & 3, respectively) and the performance of a newly developed DL-EPT method is explored (Chapter 4). A clinical application which benefits from accurate MR-EPT is also addressed (Chapter 5).

Chapter 2 investigates whether the recently developed PLANET method, a quantitative multi-parametric method for T_1 , T_2 and B_0 reconstruction [136], can be used for transceive phase mapping and thus for conductivity mapping. First, the MR parameters settings that minimize the errors and maximize the SNR in the transceive phase reconstructed by PLANET are predicted. Then, the transceive phase mapping performance of PLANET is compared to two other transceive phase mapping sequences (SE & bSSFP) in the brain. Next, the H-EPT conductivity reconstructions based on these three methods are compared and finally the strengths and limitations of each technique are discussed.

Chapter 3 shifts the focus to the pelvic region and the permittivity. As anticipated in section 1.7.1.1, the permittivity reconstruction is practically hampered by noise at 3T and therefore this electrical property is often "disregarded" in EPT studies. Rather than striving to denoise the measured $|B_1^+|$ map (see e.g. [92]), here the main question is whether the $|B_1^+|$ map can substantially be improved at the acquisition level. To answer this question, a framework revealing the accuracy and precision of $|B_1^+|$ sequences and their impact on H-EPT permittivity reconstruction is designed. This framework comprises Bloch simulations and MR measurements and is used to compare the impact of three $|B_1^+|$ mapping sequences (AFI, BS and DREAM) at 3T. From the accuracy and precision of Helmholtz-based permittivity maps quantified based on these sequences, this study delineates several recommendations for both sequence selection and validation of new EPT reconstruction algorithms.

In previous chapters, the conventional H-EPT implementation is used because its reconstruction errors and limitations are well-known (see section 1.7.1.1). This allows us to "isolate" the sole impact of the measurement technique on the reconstructed EPs. However, problems such as noise sensitivity and boundary errors limit the practical use of H-EPT. Hence, new EPT reconstruction methods are desired. Chapter 4 describes a new supervised DL-EPT

approach using an open-source CNN for 3D conductivity reconstruction of the pelvic region. Simulated B_1 field maps from human pelvic models with realistic EPs are used as training data; this dataset of B_1 fields is obtained by exploiting the simulation framework explained in Chapter 3. The feasibility of this DL-EPT method is demonstrated in simulated data and in MR measurements of one volunteer and two cervical cancer patients. Besides, the accuracy and precision of the method are predicted on simulated data with k -fold cross-validation.

Chapter 5 is dedicated to hyperthermia treatment planning (HTP). HTP is a planning tool to optimize the therapeutic heating of tumours with phased-arrays RF antennas. To correctly predict the heat deposition in the patient, HTP requires patient-specific EP maps, which can be obtained with EPT. This chapter first summarizes the current HTP workflow, then reviews the latest research progress made to improve the various steps of HTP and finally demonstrates the practical feasibility of an advanced patient-specific HTP workflow. This advanced workflow is illustrated for a cervical cancer patient and unifies together the DL-EPT method presented in the previous chapter and various developments that have recently been demonstrated to improve the reliability of hyperthermia treatment plans.

The pragmatic research approach and the attention for clinical applicability of the presented techniques are the common denominators of these chapters. From the acquisition perspective, a 3T clinical MR scanner is used throughout this thesis and all MR protocols are set trading between SNR, accuracy, resolution and scan time to obtain acceptable EPT reconstructions within clinically feasible times. Furthermore, new computationally efficient techniques and already established clinical tools are merged as much as possible in Chapter 5.

Transceive phase mapping using the PLANET method and its application for conductivity mapping in the brain

Soraya Gavazzi, Yulia Shcherbakova, Lambertus W. Bartels, Lukas J.A. Stalpers, Jan J.W. Lagendijk, Hans Crezee, Cornelis A.T. van den Berg, Astrid L.H.M.W. van Lier

published in:

Magnetic Resonance in Medicine 2020; 83(2):590-607, DOI:10.1002/MRM.27958

ABSTRACT

Purpose: To demonstrate the feasibility of transceive phase mapping with the PLANET method and its application for conductivity reconstruction in the brain.

Methods: Accuracy and precision of transceive phase (ϕ^\pm) estimation with PLANET, an ellipse fitting approach to phase-cycled balanced steady state free precession (bSSFP) data, were assessed with simulations and measurements and compared to standard bSSFP. Measurements were conducted on a homogeneous phantom and in the brain of healthy volunteers at 3T. Conductivity maps were reconstructed with Helmholtz-based electrical properties tomography (EPT). In measurements, PLANET was also compared to a reference technique for transceive phase mapping, i.e. spin echo (SE).

Results: Accuracy and precision of ϕ^\pm estimated with PLANET depended on the chosen flip angle (FA) and TR. PLANET-based ϕ^\pm was less sensitive to perturbations induced by off-resonance effects and partial volume (e.g. white matter + myelin) than bSSFP-based ϕ^\pm . For FA = 25° and TR = 4.6 ms, PLANET showed an accuracy comparable to that of reference SE but a higher precision than bSSFP and SE (factor of 2 and 3, respectively). The acquisition time for PLANET was 5 min; 2 min faster than SE and 8 times slower than bSSFP. However, PLANET simultaneously reconstructed T_1 , T_2 , B_0 maps besides mapping ϕ^\pm . In the phantom, PLANET-based conductivity matched the true value and had the smallest spread of the three methods. In vivo, PLANET-based conductivity was similar to SE-based conductivity.

Conclusion: Provided that appropriate sequence parameters are used, PLANET delivers accurate and precise ϕ^\pm maps, which can be used to reconstruct brain tissue conductivity while simultaneously recovering T_1 , T_2 and B_0 maps.

2.1 Introduction

In MRI the transceive phase represents the radiofrequency (RF) phase contribution to the phase of the MR signal. In principle, the MR signal phase effectively corresponds to the transceive phase when measuring at $TE = 0$: at this TE , in fact, the MR signal phase is not affected by time-dependent phase terms such as spectral shifts, off-resonance variations and gradient-induced eddy currents [39]. As the name suggests, the transceive phase originates from RF transmission and reception processes, which involve both transmit and receive chains of a MR system and the imaged sample (e.g. the human body), and is defined as the sum of the phases of the effective transmit and receive magnetic fields (B_1^+ and B_1^- , respectively) [43,47]. Ideally, the RF transmit magnetic field is circularly polarized to obtain maximum power efficiency in creating transverse magnetization. For a standard clinical MR scanner, this is typically realized by a quadrature drive of a two-channel birdcage body coil. For magnetic fields $> 1.5T$, however, eddy currents (leading to RF attenuation) and displacements currents (leading to wave propagation effects) induced in the human body become significant and result in an elliptically polarized net transmit field, the amplitude and phase of which are spatially inhomogeneous [47,137,138]. Similarly, these currents induced in the body during reception modulate the amplitude and phase of the RF receive field [45,47–49]. The transceive phase, reflecting the spatial modulations in the phase of both B_1^+ and B_1^- , is therefore characterized by a spatially-varying distribution.

The spatial modulation of the transceive phase is primarily induced by the tissue conductivity, as can be derived from Helmholtz equation [56,60,139]. This relationship has been validated in simulations [47,114,118] and experimentally with MR Electrical Properties Tomography (EPT) [54,56–60,91,95,103]. The transceive phase has been mapped extensively for conductivity reconstruction in different body sites (e.g. in brain [89,95,103,120], breast [94,129], liver [101], pelvis [97]), especially because tissue conductivity maps hold relevant information for RF safety [54,58], diagnostics [127,130] and therapeutic applications [131,140,141].

Besides conductivity mapping, transceive phase maps can also be beneficial for correction purposes in phase-based quantitative applications such as Quantitative Susceptibility Mapping (QSM) and MR thermometry. Peters and Henkelmann [142] and Salim et al. [143] showed that under certain conditions erroneous temperature measurements can occur in proton resonance frequency shift thermometry when transceive phase offsets caused by temperature-dependent tissue conductivity are not compensated for. Kim et al. [81] and Robinson et al. [144] demonstrated that more accurate susceptibility maps were obtained when the transceive phase was removed from the phase image used for QSM processing.

Different MR sequences have been proposed for transceive phase measurement, generally spurred by EPT research: dual-echo gradient echo [59], multi-echo gradient echo [81], ultra-short TE (UTE [79]) and zero- TE (ZTE [80]), the latter two being more technically demanding (e.g. requiring high-performance RF hardware to switch between transmit and receive [145]). However, the spin-echo (SE) is a more frequently used sequence for transceive phase mapping [54]. SE is available for all clinical scanners and returns accurate transceive phase estimates without the need to compensate for B_0 -related phase contribution (as in multi/dual-echo gradient-echo sequence). SE-based techniques generally have longer acquisition times than short-repetition-time gradient echo techniques. An alternative to SE is the balanced steady-state free precession (bSSFP) sequence, the signal phase of which approximately reflects the transceive phase over a large spectral range. bSSFP is characterized by relatively high acquisition speed and high SNR, crucial for differentiation-based EPT methods [101,146]. Nevertheless, its sensitivity to particular off-resonances results in banding artefacts that

compromise both the signal magnitude and phase. Methods to compensate these banding artefacts include: acquiring phase-cycled bSSFP, [147–150] dynamic bSSFP with frequency shifts coupled with B_0 map acquisition [151] and post-processing methods [152].

Recently, we have preliminarily shown a brain transceive phase map free from banding artefacts and off-resonance contamination obtained with the PLANET method, a novel ellipse fitting approach on phase-cycled bSSFP data [136,153]. Shcherbakova et al. [136] originally implemented PLANET to reconstruct T_1 , T_2 , off-resonance (Δf_0) maps and banding-free magnitude image, but recognized the potential of the method for EPT. In this study, we demonstrate how transceive phase maps can be retrieved with PLANET and investigate the attainable accuracy and precision in the human brain. To this aim, we performed numerical simulations and MR experiments on a phantom and on healthy volunteers. Moreover, we compared the transceive phase map obtained from PLANET with those acquired using conventional SE and bSSFP techniques and the conductivity maps reconstructed from these transceive phase maps.

2.2 Theory

2.2.1 The phase-cycled bSSFP signal

A mathematical expression for bSSFP signal is described in Appendix 2.A. Figure 2.1a,b shows the magnitude and phase profiles of a standard bSSFP signal (solid lines). The base period, comprised between the null points of the magnitude profile, can be defined as $[(-2TR)^{-1}, (2TR)^{-1}]$. Within this period, the region where the phase exhibits a plateau (i.e. $[(-3TR)^{-1}, (3TR)^{-1}]$) is called “pass-band” region; the narrow transition band $[\pm(3TR)^{-1}, \pm(2TR)^{-1}]$ where both magnitude and phase vary rapidly is normally known as “stop-band” region. In the stop-band, the transverse magnetization vanishes, leading to “banding artefacts” in magnitude and phase images [154].

Henceforth, we call “standard bSSFP” a bSSFP sequence with standard $(0, \pi)$ RF phase alternation scheme and “phase-cycled bSSFP” a dynamic series of standard bSSFP acquisitions where each dynamic is acquired with an extra different phase increment $\Delta\theta_n$ added to the standard RF phase cycling scheme. The steady-state, phase-cycled signal in a voxel is expressed as [150]:

$$I_n = KM \cdot e^{-\frac{TE}{2}} \cdot \frac{1 - E_2 e^{-i(\theta_0 - \Delta\theta_n)}}{1 - b \cos(\theta_0 - \Delta\theta_n)} \cdot e^{i\Omega} \quad (2.1)$$

where $\Delta\theta_n = \frac{2\pi n}{N} - \pi$ with $n = \{0, 1, 2, \dots, N-1\}$ is the user-controlled n^{th} RF phase increment and N is the total number of RF phase increments. Note that $\Delta\theta_n = -\pi$ returns the standard bSSFP signal described in Equation 2A.1. Nonetheless, for $\Delta\theta_n \neq -\pi$ both magnitude and phase of the phase-cycled bSSFP signal shift along the off-resonance spectrum (dashed lines in Figure 1a,b). In the complex plane, the phase-cycled bSSFP data lie on an ellipse for a voxel with only a single component following a Lorentzian frequency distribution (Figure 2.1c). Right after the RF pulse, this ellipse is rotated around the origin by an angle equal to the transceive phase (ϕ^\pm), whereas it is rotated by an angle Ω (Equation 2A.5) at the echo time. For completeness, we mention that the elliptical signal shape might not be maintained if multiple components with different frequency distributions are present in the voxel [155].

2.2.2 Estimation of the transceive phase ϕ^\pm with bSSFP and PLANET

bSSFP The bSSFP signal phase appears almost constant within the pass-band region and shifts vertically by a quantity corresponding to ϕ^\pm value, as shown in Figure 2.1b. Thus, the

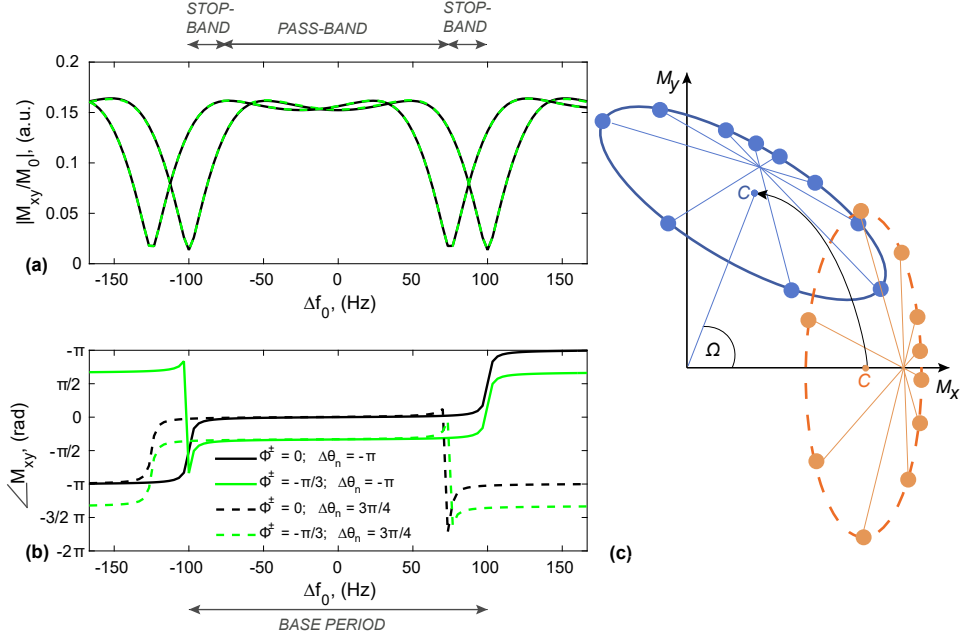


Figure 2.1. Schematic representation of bssFP and phase-cycled bssFP signals at the time point equal to TE . **(a)** Magnitude and **(b)** phase of standard bssFP signal (i.e. bssFP sequence with a $(0, \pi)$ phase cycling scheme) as a function of off-resonance frequency (Δf_0). The bssFP signal was simulated for a $FA = 25^\circ$, $TR = 5$ ms, $TE = TR/2$ and tissue properties of white matter at 3T (WM, $T_1 = 832$ ms and $T_2 = 80$ ms). Two different values of transceive phase are considered: $\phi^\pm = 0$ rad (black) and $\phi^\pm = -\pi/3$ rad (green). Moreover, two different increments ($\Delta\theta_n$) added to the phase of the RF pulse are shown: $\Delta\theta_n = -\pi$ rad (solid lines) and $\Delta\theta_n = 3\pi/4$ rad (dashed lines). Changing the transceive phase value has no effect on the signal magnitude, but it vertically translates the signal phase of a quantity corresponding to ϕ^\pm . When an increment $\Delta\theta_n \neq -\pi$ is added to the phase of the RF pulse, the magnitude and phase of bssFP signal shift with frequency. Note that an increment $\Delta\theta_n = -\pi$ rad (solid lines) corresponds to the profile of a standard bssFP signal. **(c)** Phase-cycled bssFP signal in the complex plane for a voxel with $\phi^\pm = 0$ rad, $\Delta f_0 \neq 0$ Hz and increment $\Delta\theta_n = 2n\pi/10 - \pi$ with $n = \{0,1,2 \dots 9\}$. Right after the RF pulse excitation, the phase-cycled data points (coloured dots) lie on the orange ellipse. At TE , the elliptical signal (in blue) is rotated by an angle Ω . The geometrical center of the ellipse is indicated by C .

transceive phase is generally approximated by the phase of `bssFP` signal (while all other phase contributions in the phase image $\angle I_0 = \angle(1 - E_2 e^{-i(\theta_0 + \pi)}) \cdot e^{i\Omega}$ [Equation 2A.1] are normally neglected).

PLANET `PLANET` applies a linear least squares fit, specific to ellipses, in the complex plane to steady-state phase-cycled `bssFP` data using the signal model defined in Equation 2.1 [136]. This model assumes a Lorentzian single-component relaxation model. To fit the ellipse coefficients in `PLANET`, at least $N = 6$ dynamics with different RF phase increments are required [136]. The `PLANET` method reconstructs T_1 , T_2 , a banding-free image, B_0 -related off-resonances (Δf_0) and ϕ^\pm from the shape and rotation of the ellipse (Figure 2.1c).

When B_0 drift is assumed negligible and when eddy-current effects are compensated for, the terms ϕ_{drift} and ϕ_{eddy} drop out from the rotation angle Ω in Equation 2A.5, yielding:

$$\Omega = 2\pi\Delta f_0 TE + \phi^\pm \quad (2.2)$$

Both Ω and Δf_0 in Equation 2.2 can be independently estimated from the fitting procedure (see Steps 2 and 4 in reference [136]). Hence, `PLANET`-based transceive phase can be obtained by subtracting these two terms.

2.3 Methods

We performed Bloch simulations and MR experiments on a phantom and on healthy volunteers to study the accuracy and precision of the transceive phase retrieved with `PLANET` method. `PLANET` performance to map the transceive phase was compared to the performance of a standard `bssFP` sequence. Moreover, the experimental transceive phase maps obtained with `PLANET`, `bssFP` and the reference spin echo (SE) were compared and used to reconstruct conductivity maps.

2.3.1 Simulations

A phase-cycled `bssFP` sequence with standard $(0, \pi)$ RF alternation scheme and $N = 8$ additional RF phase increment steps ($\Delta\theta_n = \frac{2\pi n}{8} - \pi$, with $n = \{0, 1, 2, \dots, 7\}$) as in reference [136] was implemented in Matlab (R2015a, the MathWorks, Natick, MA) with a Bloch simulator [156]. Input parameters for the Bloch simulation comprised sequence parameters (FA , TR) and voxel characteristics (Δf_0 , ϕ^\pm , T_1 and T_2). Rectangular-shaped RF pulses and balanced readout gradients were used. Phase encoding and slice selection gradients were not included. The simulation output was a phase-cycled `bssFP` complex signal evaluated at TE after each RF pulse. The signal was considered at steady-state after $3 \cdot T_1 / TR$ RF pulses. By applying the `PLANET` method to this simulated phase-cycled complex signal the transceive phase for `PLANET` was retrieved. The standard `bssFP` signal was obtained from phase-cycled `bssFP` data at $\Delta\theta_n = -\pi$, the phase of which returned `bssFP`-based transceive phase.

Five simulation cases were performed to study the performance of `bssFP` and `PLANET` in estimating ϕ^\pm (see Table 2.1). Four Monte Carlo simulations (Simulations I→IV) evaluated the accuracy and precision of transceive phase values obtained with `bssFP` and `PLANET` as a function of sequence settings (FA and TR in Simulations I and III; N in Simulation IV), tissue relaxation properties (T_1 and T_2 in Simulation IV), and other parameters (Δf_0 and ϕ^\pm in Simulation II). In Simulations I, II and III the relaxation times representing white matter (WM) at 3T were used ($T_1 = 832$ ms and $T_2 = 80$ ms [157]). In Simulations I, III and IV the transceive phase and off-resonance frequency (fixed parameters, Table 2.1) were selected based on the representative experimental values found at 3T in WM in a central portion of the FOV.

Simulations I and III differed in the relaxation model used: in I only the single (Lorentzian) frequency distribution of WM was present in the voxel, whereas Simulation III included also a second, smaller component, myelin water, and gives an example of a commonly used, more complex model of human WM tissue [155,158–161] (details in Table 2.1, assumed field strength: 3T). For all four cases, Gaussian noise was added independently to both real and imaginary parts of the simulated phase-cycled signal (noise standard deviation $\zeta = 10$, with $M_0 = 10000$), prior to PLANET post-processing, and the total number of Monte Carlo iterations (Z) was 10000.

Since PLANET method relies on data in the steady-state regime [136], the effect of RF dummy pulses on the transceive phase was investigated in Simulation V, where a noiseless phase-cycled bSSFP signal was simulated for a voxel containing cerebrospinal fluid (CSF) at 3T. Because of its long T_1 and T_2 , CSF demands the highest number of dummy pulses to reach steady-state.

2.3.2 Measurements

Phantom and in vivo MR experiments were performed on a 3T clinical scanner (Ingenia, Philips, Best, The Netherlands), with the body coil for transmission and a 15-channel head coil for reception. The vendor-specific CLEAR option was enabled to obtain transceive phase maps free from the complex receive sensitivity of the head coil; this emulates the situation in which the body coil was used in quadrature mode for both transmission and reception [90]. For both phantom and in vivo measurements, we used a 3D phase-cycled bSSFP sequence with the following parameters: FOV = $240 \times 240 \times 60$ mm³, voxel size = $2.5 \times 2.5 \times 2.5$ mm³, 8 phase increments ($\Delta\theta_n = \frac{2\pi n}{8} - \pi$, with $n = \{0,1,2 \dots 7\}$), FA = 25°, TE = 2.3 ms, TR = 4.6 ms. To minimize transient effects, a series of 2170 dummy pulses was applied before each phase-cycled bSSFP acquisition, thus the scan time increased from 2:46 minutes to 5:20 minutes. We employed a 2D multi-slice spin-echo (SE) sequence as a reference method for transceive phase mapping, since it is generally recognized to provide accurate ϕ^\pm values [54,139]. With the same FOV and voxel size, SE settings were: TE/TR = 5.2/1100 ms (scan time: 7:16 minutes). Both phase-cycled bSSFP and SE acquisitions were repeated with opposed readout gradient polarities to allow compensation of eddy current effects (See Post-processing). A reference Δf_0 map was acquired in each session with 3D dual-echo spoiled gradient-echo sequence (FA = 60°, TE₁/TE₂/TR = 2.3/4.6/30 ms).

Phantom experiments involved a cylindrical phantom (diameter and length: 12 cm) filled with water, 5.1 g/L NaCl and agar (2% w/v). The resulting homogeneous composition had a conductivity value within the physiologic range for the whole brain [10], $\sigma = 0.85$ Sm⁻¹, which was measured with a dielectric probe (85070E, Agilent Technologies, Santa Clara, CA).

Two independent phantom experiments were conducted by changing the B_0 shimming options to prove the robustness of PLANET-based transceive phase estimation against off-resonance effects. In the first experiment (Experiment I) a volumetric B_0 shimming within the FOV was guaranteed; in the second experiment (Experiment II) a first-order field variation was enforced by activating the y-shimming gradient (with intensity of 0.3 mT/m). A third experiment (Experiment III) investigated the effect of different RF phase increment steps ($N = 6, 8, 10$) on the transceive phase and conductivity.

In vivo brain measurements were approved by the local institutional review board. Images were obtained from three healthy volunteers, whose written informed consent was obtained.

Table 2.1. Overview of simulation cases performed. All parameters are at 3T.

Name of simulation	Type of simulation	Fixed parameters	Variable parameters	Figure	Purpose
Simulation I	Monte Carlo	$T_1 = 832$ ms $T_2 = 80$ ms $\phi^\pm = -\pi/3$ rad $N = 8$	$\Delta f_0 = [0; 15; 30]$ Hz $FA = [0 \rightarrow 90]^\circ$ $TR = [3 \rightarrow 33]$ ms	2.2, 2.3, 2B.1, 2B.2	Evaluate e_{ϕ^\pm} and ζ_{ϕ^\pm} as a function of FA and TR for a single component voxel in on-resonance and off-resonance conditions
Simulation II	Monte Carlo	$T_1 = 832$ ms $T_2 = 80$ ms $FA = 25^\circ$ $TR = 4.6$ ms $N = 8$	$\Delta f_0 = [-100 \rightarrow 100]$ Hz $\phi^\pm = [-\pi/2 \rightarrow \pi/2]$ rad	2.2	Evaluate e_{ϕ^\pm} and ζ_{ϕ^\pm} as a function of Δf_0 and ϕ^\pm for a single component voxel
Simulation III	Monte Carlo	$N = 8$ <u>1st component:</u> $T_{1,1} = 832$ ms $T_{2,1} = 80$ ms $\phi_{\pm,1} = -\pi/3$ rad $w_1 = 0.88$ <u>2nd component:</u> $T_{1,2} = 400$ ms $T_{2,2} = 20$ ms $\phi_{\pm,2} = -\pi/3$ rad $CS = 20$ Hz $w_2 = 0.12 = (1 - w_1)$	$\Delta f_{0,1} = [0; 15]$ Hz $\Delta f_{0,2} = [20; 35]$ Hz $FA = [0 \rightarrow 90]^\circ$ $TR = [3 \rightarrow 33]$ ms $(\Delta f_{0,2} = \Delta f_{0,1} + CS)$	2.2, 2.3, 2B.1, 2B.2	Evaluate e_{ϕ^\pm} and ζ_{ϕ^\pm} as a function of FA and TR for a 2-component voxel in on-resonance and off-resonance conditions. The two components considered were wm (1 st component, with wm fraction w_1) and myelin (2 nd component, with myelin fraction w_2)
Simulation IV	Monte Carlo	$\Delta f_0 = 0$ Hz $\phi^\pm = -\pi/3$ rad $FA = 25^\circ$ $TR = 4.6$ ms	$T_1 = [100 \rightarrow 4000]$ ms $T_2 = [20 \rightarrow 500]$ ms $N = [6 \rightarrow 10]$	2.4	Calculate C_{ϕ^\pm} as a function of T_1 and T_2 and as a function of N
Simulation V	Simple (Noise-free, 1 iteration)	$T_1 = 3858$ ms $T_2 = 500$ ms $\Delta f_0 = 15$ Hz $\phi^\pm = -\pi/3$ rad $FA = 25^\circ$ $TR = 4.6$ ms $N = 8$	$\#RF = [500 \rightarrow 2500]$ $\#RF$: number of RF dummy pulses	2.5	Evaluate e_{ϕ^\pm} as a function of $\#RF$

2.3.3 Post-processing

Several post-processing steps were performed in Matlab on the acquired phase-cycled bssFP and SE signals to obtain transceive phase and conductivity maps. First, a method based on local subvoxel shifts was employed to correct each signal for Gibbs ringing [162]. Then, the phase images from the two signals acquired with opposed readout gradient polarity were averaged to minimize the phase contribution due to eddy currents (ϕ_{eddy} , see Equation 2A.5). At this point, SE- and bssFP-based transceive phase maps were obtained. To retrieve PLANET-based transceive phase map, the PLANET method was applied to both phase-cycled bssFP acquisitions, and the resulting transceive phase maps were then averaged. If phase wraps appeared, the transceive phase maps were unwrapped by adding a 2π -offset to phase wraps with an in-house region-growing algorithm. Finally, the transceive phase mean value, calculated in the central slice, was subtracted from the transceive phase map for each method to exclude potential global phase constant offsets deriving arbitrarily from the scanner's data acquisition chain. Subtracting the mean value will not influence the conductivity reconstruction, the latter being a derivative-based method which neglects any global offset. For brain data, all phase-cycled images were rigidly registered to SE images after Gibbs ringing correction to reduce the impact of potential inter-scan head motion during the scan session.

Conductivity maps were reconstructed based on these experimental transceive phase maps. For conductivity reconstruction, a conventional Helmholtz-based, "phase-only" EPT method was applied (Laplacian operator: noise-robust kernel of $7 \times 7 \times 3$ voxels [59,87]), and the transceive phase assumption was used [57–59,91].

2.3.4 Accuracy

We define *accuracy* as the error between the estimate of the transceive phase and the true (or reference) transceive phase. For all Monte Carlo simulations (Simulations I→IV), the accuracy was calculated as the difference (e_{ϕ^\pm}) between bssFP- or PLANET-based transceive phase estimate averaged over all Z iterations ($\overline{\phi^\pm} = \frac{1}{Z} \sum_{i=1}^Z \phi_i^\pm$) and the true value ϕ_{true}^\pm (e_{ϕ^\pm} effectively corresponds to a systematic error [163]):

$$e_{\phi^\pm} = \left| \overline{\phi^\pm} - \phi_{true}^\pm \right| \quad (2.3)$$

In measurements knowledge on the true value is lacking. Thus, the accuracy was assessed by the difference $\Delta\phi^\pm$ between bssFP- or PLANET-based transceive phase and the transceive phase acquired with SE, which is commonly recognized as a reference sequence for transceive phase mapping [57].

2.3.5 Precision

We define *precision* as the inverse of the uncertainty of the estimated transceive phase. The uncertainty of the transceive phase is represented by its standard deviation (std). We denote the uncertainty (or std) of the transceive phase with ζ_{ϕ^\pm} , to avoid confusion with the conductivity symbol " σ ".

In Simulations I→IV, the uncertainty ζ_{ϕ^\pm} was calculated as the std of the transceive phase estimated with bssFP or PLANET over all Z iterations (ζ_{ϕ^\pm} corresponds to a random error):

$$\zeta_{\phi^\pm} = \sqrt{\frac{\sum_{i=1}^Z (\phi_i^\pm - \overline{\phi^\pm})^2}{Z}} \quad (2.4)$$

Typically, in experiments the uncertainty of a phase image Φ is approximated with $\zeta_\Phi \cong \text{SNR}_{\text{magnitude}}^{-1}$. Such approximation holds for phase images that are directly acquired with any sequence and for noise levels significantly smaller than the signal magnitude [164]. Hence, it could be applicable for *bssFP*-based transceive phase but not for *PLANET* because of the fitting procedure on the acquired signals used to retrieve ϕ^\pm . Assessing analytically the noise propagation related to *PLANET* fitting is difficult thus we followed an empirical approach that ultimately leads to determining the experimental ζ_{ϕ^\pm} . For this purpose, we performed Monte Carlo Simulation IV (Table 2.1), where we related the “true” transceive phase uncertainty calculated with Equation 2.4, which can only be assessed in simulation, to the “theoretical uncertainty $\widetilde{\zeta_{\phi^\pm}}$ ”, which was based on the aforementioned approximation by Gudbjartsson and Patz [164] and can be assessed in both simulations and measurements. The theoretical uncertainty was defined as:

$$\widetilde{\zeta_{\phi^\pm}} = \left(\sqrt{2} \cdot \text{SNR}_{\text{magnitude}} \right)^{-1} \quad (2.5)$$

where $\sqrt{2}$ accounts for the averaging operation performed to retrieve an eddy-current-free transceive phase map (see *Post-processing*). The $\text{SNR}_{\text{magnitude}}$ was calculated according to the definition of Bjork et al. [148]:

$$\text{SNR}_{\text{magnitude}} = \frac{\sum_{n=0}^{N-1} |I_n(\Delta\theta_n)|}{N \cdot \zeta} \quad (2.6)$$

where $|I_n(\Delta\theta_n)|$ is the magnitude of the n^{th} phase-cycled *bssFP* signal, ζ is the std of the Gaussian noise level ($\zeta = 10$) and N is the number of phase cycles ($N = 8$).

The simulated true and theoretical uncertainties were compared by computing their ratio $C_{\phi^\pm} = \frac{\zeta_{\phi^\pm}}{\widetilde{\zeta_{\phi^\pm}}}$. C_{ϕ^\pm} accounts for the increase/reduction in the transceive phase noise level occurring during post-processing (e.g. *PLANET* fitting), since the noise propagation attributed to the acquisition is already considered in $\widetilde{\zeta_{\phi^\pm}}$ (for which case, $C_{\phi^\pm} = 1$). For minimum uncertainty, $C_{\phi^\pm} \rightarrow 0$.

Based on the values for C_{ϕ^\pm} found in this simulation, we assessed the uncertainty ζ_{ϕ^\pm} in experiments with Equation 2.7:

$$\zeta_{\phi^\pm} = C_{\phi^\pm} \cdot \widetilde{\zeta_{\phi^\pm}} = C_{\phi^\pm} \cdot \left(\sqrt{2} \cdot \text{SNR}_{\text{magnitude}} \right)^{-1} \quad (2.7)$$

The experimental $\text{SNR}_{\text{magnitude}}$ in Equation 2.7 was calculated by averaging the *SNR* maps relative to all phase-cycled images, which conceptually corresponds to Equation 2.6. These *SNR* maps were obtained with Kellman’s method [165].

2.4 Results

2.4.1 Simulation results

Simulations I & II The accuracy of the transceive phase, identified by the error e_{ϕ^\pm} , estimated with *bssFP* and *PLANET* in a voxel containing WM tissue is illustrated in Figure 2.2 and in Figure 2B.1. In *bssFP*, the error e_{ϕ^\pm} was zero on-resonance ($\Delta f_0 = 0$ Hz, Figure 2B.1) and was independent from *FA*. Nevertheless, it varied depending on the combination of Δf_0 and *TR*: for example, $e_{\phi^\pm} \approx 0.11$ rad (i.e. $\sim 10.5\%$ of $\phi_{\text{true}}^\pm = -\pi/3$ rad) was obtained at *TR* =

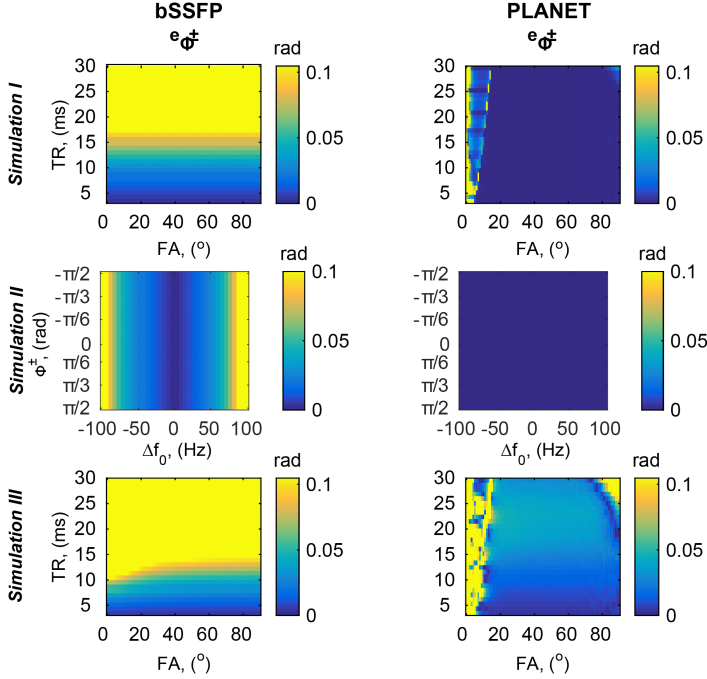


Figure 2.2. Accuracy of transceive phase estimation for bSSFP (first column) and PLANET (second column): results from simulations I (first row), II (second row) and III (third row). Simulation I: e_{ϕ^\pm} as a function of FA and TR; input $\Delta f_0 = 15$ Hz and $\phi^\pm = -\pi/3$ rad. Simulation II: e_{ϕ^\pm} as a function of Δf_0 and ϕ^\pm ; FA = 25° and TR = 4.6 ms. For both simulations I and II: single component with $T_1 = 832$ ms and $T_2 = 80$ ms. Simulation III: e_{ϕ^\pm} as a function of FA and TR for a 2-component voxel. First component: WM, input $\Delta f_{0,1} = 15$ Hz, $\phi_1^\pm = -\pi/3$ rad, $T_{1,1} = 832$ ms, $T_{2,1} = 80$ ms and $w_1 = 0.88$. Second component: myelin, input $\Delta f_{0,2} = 35$ Hz (CS = 20 Hz), $\phi_2^\pm = -\pi/3$ rad, $T_{1,2} = 400$ ms, $T_{2,2} = 20$ ms, $w_2 = 0.12$.

17 ms ($\frac{1}{4\Delta f_0}$, thus within the pass-band region, Figure 2.2) for $\Delta f_0 = 15$ Hz and at TR = 11 ms ($\frac{1}{3\Delta f_0}$, i.e. the cut-off for stop-band, Figure 2B.1) for $\Delta f_0 = 30$ Hz. In general, the error rapidly increased following a sigmoidal curve for TRs $> \frac{1}{4\Delta f_0}$. Differently, in PLANET the error was zero for any TR $< \frac{1}{2\Delta f_0}$ and any FA $> FA_{Ernst}$, where $FA_{Ernst} = \arccos(\exp(-TR/T_1))$ is the minimum FA for which the ellipse does not collapse [155], thus hindering PLANET fitting approach (Figure 2.2 and Figure 2B.1). For TRs $\approx \frac{1}{2\Delta f_0}$, the error exceeded 0.50 rad for FA $> 50^\circ$ (e.g. at TR ≈ 17 ms for $\Delta f_0 = 30$ Hz, Figure 2B.1). For the fixed parameters used in MR experiments (i.e. FA = 25° and TR = 4.6 ms, Simulation II), the following errors were obtained: $e_{\phi^\pm} \leq 0.03$ rad for $\Delta f_0 < \frac{1}{4TR} = 50$ Hz and $e_{\phi^\pm} > 0.05$ rad for $\Delta f_0 > \frac{1}{3TR} \approx 73$ Hz for bSSFP, whereas no error was observed for any Δf_0 in PLANET.

The uncertainty of the transceive phase (ζ_{ϕ^\pm}) estimated with bSSFP and PLANET is shown in Figure 2.3 and Figure 2B.2. Because of their inverse relationship, ζ_{ϕ^\pm} and SNR shared similar patterns for both methods. The uncertainty ζ_{ϕ^\pm} in bSSFP presented a TR-invariant distribution

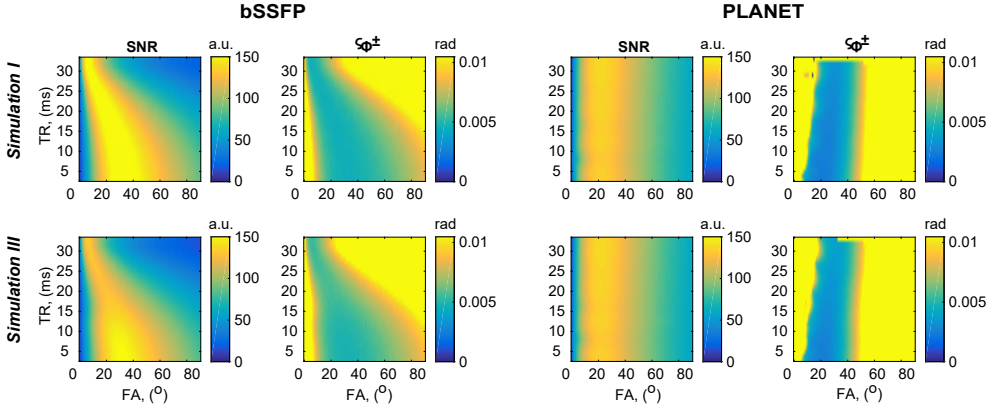


Figure 2.3. Precision of transceive phase estimation for bSSFP (left) and PLANET (right): results from simulations I (first row) and III (second row). Image SNR (as calculated in Equation 2.6) and the transceive phase uncertainty $\zeta_{\phi^{\pm}}$ (as calculated in Equation 2.4) are shown as a function of FA and TR.

at $\Delta f_0 = 0$ Hz, with lowest values for $FA = [25 - 45]^{\circ}$. A pronounced TR-dependence was observed for increasing values of Δf_0 , which reflected the transition of the signal magnitude from pass-band to stop-band region. Approaching $TR \approx \frac{1}{2\Delta f_0}$ reduced the range of FAs generating lowest $\zeta_{\phi^{\pm}}$ values (Figure 2.3 and Figure 2B.2). In PLANET an almost TR-invariant $\zeta_{\phi^{\pm}}$ was observed for any Δf_0 and the highest precision (i.e. lowest $\zeta_{\phi^{\pm}}$) was found for $FA = [18 - 30]^{\circ}$. In this FA range, the uncertainty $\zeta_{\phi^{\pm}}$ in PLANET was approximately half the uncertainty in bSSFP.

Simulation III The accuracy and precision of transceive phase estimation can change when a voxel contains multiple components with different relaxation times and frequency distributions. Results are presented for a voxel including WM as the dominant component and myelin water as the second component, in an often used ratio to model human WM tissue [155, 158–161]. With respect to the case of single WM component, the uncertainty patterns were mildly affected (Figure 2.3 and Figure 2B.2) but the error distribution varied (Figure 2.2 and Figure 2B.1). For this specific example case, $e_{\phi^{\pm}}$ increased for longer TRs in both bSSFP and PLANET, and slightly increased for smaller FAs in bSSFP. For $FA = 25^{\circ}$ and $TR = 4.6$ ms (used in experiments), bSSFP was more sensitive than PLANET to myelin presence when $\Delta f_{0,1} = 15$ Hz ($e_{\phi^{\pm}} = 1.4 \cdot 10^{-2}$ rad vs $e_{\phi^{\pm}} = 5.8 \cdot 10^{-3}$ rad, Figure 2.2), but was less sensitive when $\Delta f_{0,1} = 0$ Hz ($e_{\phi^{\pm}} = 3.8 \cdot 10^{-3}$ rad vs $e_{\phi^{\pm}} = 5.5 \cdot 10^{-3}$ rad, Figure 2B.1).

Simulation IV Figure 2.4 depicts the constant $C_{\phi^{\pm}}$, used in Equation 2.7 to estimate $\zeta_{\phi^{\pm}}$ experimentally, as a function of relaxation times. Ideally, $C_{\phi^{\pm}} \rightarrow 0$ to minimize the uncertainty in ϕ^{\pm} . Figure 2.4 shows that $C_{\phi^{\pm}} = 1$ for bSSFP, meaning that all the noise propagation in bSSFP transceive phase was explained by the theoretical uncertainty (Equation 2.5). This theoretical uncertainty holds true for phase images directly acquired from any sequence [39, 164]: a requirement fulfilled by bSSFP transceive phase. Differently, $C_{\phi^{\pm}}$ varied as a function of T_1 and T_2 in PLANET ($0.42 \leq C_{\phi^{\pm}} \leq 0.44$ for T_1 and T_2 of brain tissues at 3T, with $FA = 25^{\circ}$, $TR = 4.6$ ms and $N = 8$) and underlines that during PLANET processing the impact of noise on the transceive phase is approximately halved with respect to standard bSSFP. This agrees with the

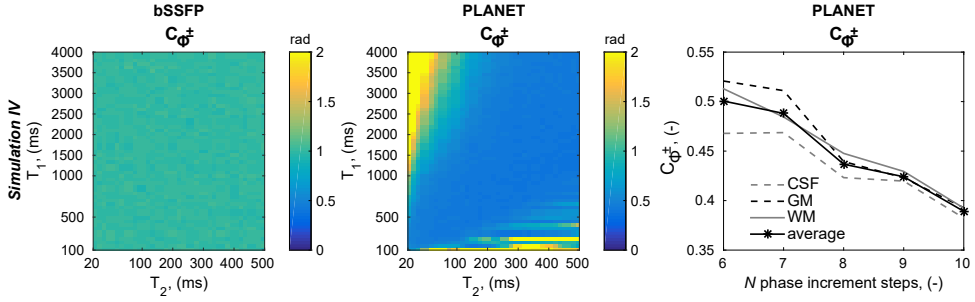


Figure 2.4. Factor C_{ϕ^\pm} : results from simulation IV. C_{ϕ^\pm} maps for bSSFP (left) and PLANET (center) as a function of T_1 and T_2 . Factor C_{ϕ^\pm} for PLANET (right) as a function of N phase increment steps for CSF, GM, WM (CSF $T_1/T_2 = 3858/500$ ms; GM $T_1/T_2 = 1331/110$ ms; WM $T_1/T_2 = 832/80$ ms [157]) and an average among these three tissues. Simulation IV: input $\Delta f_0 = 0$ Hz, $\phi^\pm = -\pi/3$ rad, $FA = 25^\circ$, $TR = 4.6$ ms and $\Delta\theta_n = 2n\pi/N - \pi$ with $n = \{0,1,2,\dots,N-1\}$. C_{ϕ^\pm} maps were obtained with $N = 8$ phase increment steps.

above-mentioned ζ_{ϕ^\pm} results found in Simulation I. Based on these results, $C_{\phi^\pm} = 1$ for bSSFP and $C_{\phi^\pm} = 0.43$ for PLANET were used to calculate the experimental uncertainty ζ_{ϕ^\pm} (Equation 2.7). Figure 2.4 also illustrates that the constant C_{ϕ^\pm} for PLANET decreased for all three brain tissues when the number of RF phase increments was increased, showing larger values and variability for $N < 8$. On average, $0.39 \leq C_{\phi^\pm} \leq 0.50$ for $6 \leq N \leq 10$ with $FA = 25^\circ$ and $TR = 4.6$ ms. Changing N did not affect PLANET accuracy ($e_{\phi^\pm} \leq 2 \cdot 10^{-4}$ rad for any N , not shown).

Simulation V Since transient effects can compromise the accuracy of ϕ^\pm , predominantly in tissues with long relaxation times such as CSF, the number of RF dummy pulses should be taken into account in bSSFP and PLANET. Figure 2.5 shows that the rotation (and shape) of the fitted ellipse changed with respect to the steady-state case (2500 pulses) when the number of dummy pulses was low. For our experimental settings, minimal variations in the ellipses were observed beyond 1250 dummy pulses. The transceive phase error right after 1250 dummy pulses was $3 \cdot 10^{-3}$ rad for PLANET and $1 \cdot 10^{-3}$ rad for bSSFP (Figure 2.5b). This error remained stable for bSSFP, whereas it decreased to $2 \cdot 10^{-4}$ rad for PLANET after 2500 pulses.

2.4.2 Measurement results

Phantom Experiments Phantom transceive phase maps are shown in Figure 2.6 for Experiments I and II. In Experiment I, a peripheral banding artefact occurred in bSSFP-based transceive phase map, in the region where $\Delta f_0 > 80$ Hz (Figure 2.6a,l). The corresponding $\Delta\phi^\pm$ map displayed a spatially varying distribution, with a 0.10 rad underestimation at the phantom periphery (Figure 2.6j). The ϕ^\pm profiles in Figure 2.6e,l,n show that in the banding-free part of the phantom the transceive phase curvature in bSSFP was slightly smaller than in SE and PLANET, which resulted from a spurious phase contamination induced by Δf_0 (in the order of ~ 0.02 rad), as already predicted in Simulation II (Figure 2.2). PLANET-based transceive phase map slightly underestimated the reference SE ϕ^\pm distribution by on average 0.03 rad (Figure 2.6b,k,l). A similar transceive phase map was obtained with PLANET when a linear Δf_0 variation was enforced using the shim gradient (Experiment II, Figure 2.6g,m), which demonstrated the robustness of PLANET against off-resonance effects. Differently, bSSFP-based

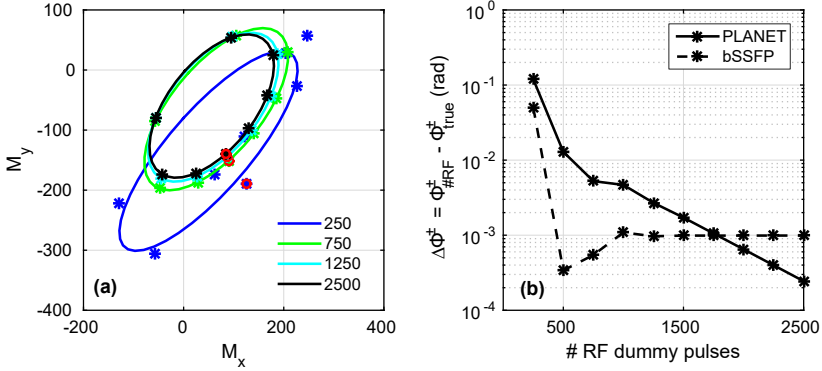


Figure 2.5. Effect of the number of RF dummy pulses. **(a)** Complex phase-cycled bSSFP signal sampled at different numbers of RF dummy pulses ($\#_{\text{RF}}$ dummy pulses: 250, 500, 750, 1250 and 2500). The phase-cycled signal was simulated for one voxel with the following parameters (Simulation V): $T_1 = 3858$ ms and $T_2 = 500$ ms (representing maximum values found in CSF from T_1 and T_2 maps obtained with PLANET); $\Delta f_0 = 15$ Hz and $\phi^\pm = -\pi/3$ rad. MR parameters settings were: $FA = 25^\circ$, $TR = 4.6$ ms, $TR = TE/2$ and $\Delta\theta_n = 2n\pi/8 - \pi$ with $n = \{0,1,2, \dots, 7\}$. The * represents the phase-cycled data corresponding to a certain $\Delta\theta_n$. The * encircled in a red circle represents the bSSFP data with $\Delta\theta_n = -\pi$ rad, i.e. the standard bSSFP. Solid lines indicate the fitted ellipses during PLANET post-processing. **(b)** Transceive phase error $\Delta\phi^\pm$ as a function of RF dummy pulses. The transceive phase error was calculated as the difference between the transceive phase estimated at a certain dummy pulse ($\phi^\pm_{\#_{\text{RF}}}$) and the true transceive phase ($\phi^\pm_{\text{true}} = -\pi/3$ rad) for both bSSFP and PLANET.

transceive phase map (after unwrapping) displayed banding artefacts in correspondence of stop-band transition regions. These artefacts could not be resolved by the unwrapping procedure (Figure 2.6f,m). Furthermore, both bSSFP- and PLANET-based transceive phase maps suffered from an offset (Figure 2.6j,k) caused by residual eddy current effects which were not fully compensated for by averaging two acquisitions with opposed readout polarity: indeed, as depicted in Figure 2B.3, the linear phase accrual (along the readout direction) induced by eddy current effects in one acquisition was slightly asymmetric with respect to the phase gradient appearing in the acquisition with reversed gradient polarity. Possible reasons for this asymmetric behaviour could be small variations of Δf_0 occurring between the two acquisitions (~ 5 minutes apart) or slight changes in the preparatory calibration steps performed before each acquisition.

Results from Experiment III, illustrated in Figure 2B.4, showed that the accuracy of PLANET-based transceive phase was unaffected by the number of RF phase increments, N . In Experiment III a banding-free bSSFP transceive phase map was obtained. The corresponding Δf_0 map resembled the Δf_0 distribution of Experiment I but showed a less pronounced variation at the phantom periphery. Nevertheless, Figure 2B.4k confirms that the transceive phase curvature in bSSFP was smaller than in SE, as already observed in Figure 2.6e,n.

The transceive phase uncertainty in PLANET was approximately half the uncertainty in bSSFP for both phantom and in vivo WM (Figure 2.7a). In Figure 2.7a also the transceive phase uncertainty for SE is reported, which was 3 and 1.5 times higher than bSSFP uncertainty for phantom and WM, respectively. Figure 2.7b shows that the acquisition time of phase-cycled

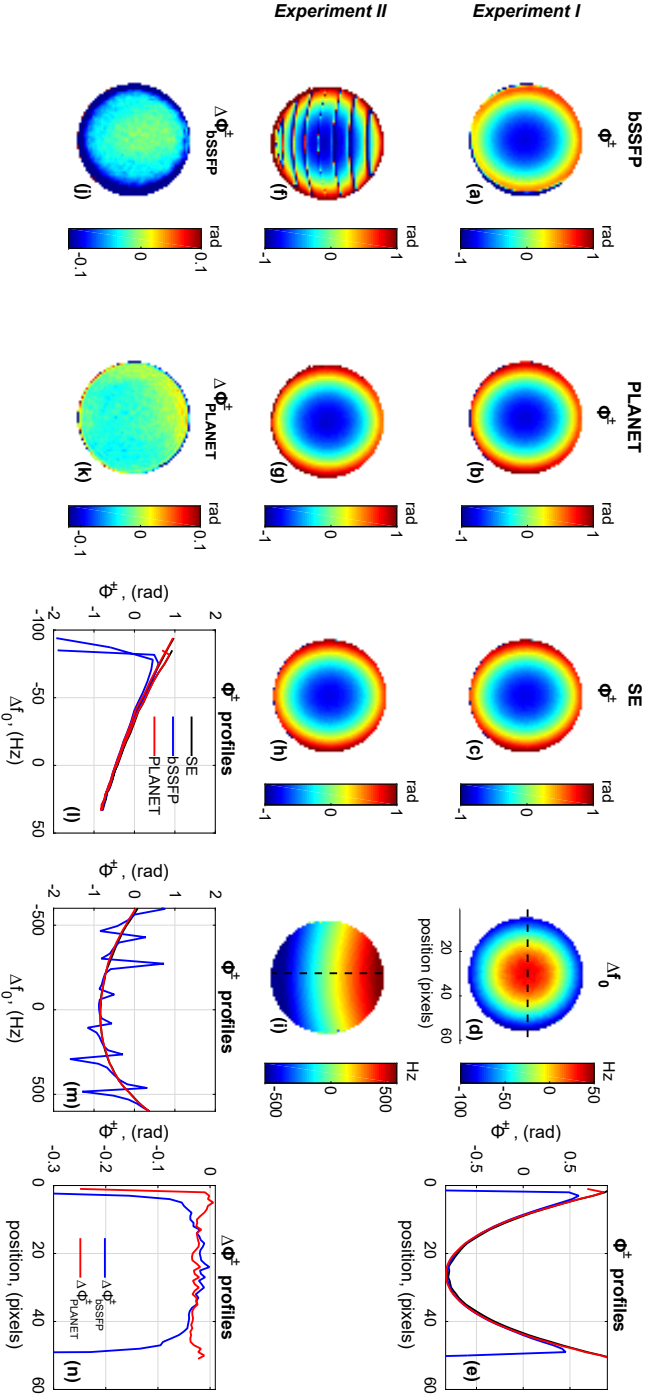


Figure 2.6. Accuracy of transceive phase estimation for bssfp and PLANET. Results from phantom MR experiments are shown. Experiment I: volume-based shimming (a-e, j-l,n); Experiment II: linear shimming of y-gradient (f-i, m). Isotropic voxel size: 2.5 mm. Transceive phase maps (ϕ^\pm) obtained from: **(a,f)** bssfp; **(b,g)** PLANET and **(c,h)** SE (reference method), after unwrapping. **(d,j)** Δf_0 maps. **(e)** Transceive phase profiles of bssfp (blue), PLANET (red) and SE (black), calculated on the central horizontal line (dashed line in (d)), for Experiment I. **(f)** $\Delta\phi^\pm$ for bssfp, defined as $\phi_{\text{bssfp}}^{\pm} - \phi_{\text{SE}}^{\pm}$, based on transceive phase maps (a) and (c). **(k)** $\Delta\phi^\pm$ for PLANET, defined as $\phi_{\text{PLANET}}^{\pm} - \phi_{\text{SE}}^{\pm}$, based on transceive phase maps (b) and (c). **(l)** Transceive phase profiles, calculated on the central horizontal line (dashed line in (d)), as a function of Δf_0 for Experiment I (a-d). **(m)** Transceive phase profiles, calculated on the central vertical line (dashed line in (i)), as a function of Δf_0 for Experiment II (f-i). The legend is the same as in (l). **(n)** $\Delta\phi^\pm$ profiles for $\Delta\phi_{\text{bssfp}}^{\pm}$ (blue) and $\Delta\phi_{\text{PLANET}}^{\pm}$ (red) calculated on the central horizontal line (dashed line in (d)) for Experiment I.

bssFP needed for PLANET was longer than bssFP of a factor N (in this case, $N = 8$). Still, this time was 2 minutes faster than SE acquisition. Using the ζ_{ϕ^\pm} reported in Figure 2.7a for WM and the scan time in Figure 2.7b we calculated the precision-per-unit-time ($(\zeta_{\phi^\pm} \cdot t)^{-1}$) shown in Figure 2.7c: the precision-per-unit-time for PLANET was 4 times lower than for bssFP and 8.5 times higher than for SE.

The ζ_{ϕ^\pm} trends in the phantom (Figure 2.7a) were also reflected in the conductivity maps presented in Figures Figure 2.8 and Figure 2B.4: SE-based conductivity map was visually noisier than bssFP-based and PLANET-based conductivity maps, whereas PLANET-based conductivity appeared least noisy. Quantitatively, the lowest conductivity std was found in PLANET, although the conductivity std values were of the same order of magnitude in all methods. Similarly, a rather mild decrease of conductivity std with increasing N was found in Figure 2B.4, which is line with the simulated trend of C_{ϕ^\pm} portrayed in Figure 2.4. Moreover, in all conductivity maps the effect of Gibbs ringing at phantom periphery was amplified. In both Figure 2.8 and Figure 2B.4 the median values (reported in the boxplot) for both PLANET-based and SE-based conductivity were close to the true value. In bssFP, the median conductivity was underestimated in both Experiments I and III: this was caused by the aforementioned smaller curvature of the observed transceive phase.

In vivo brain experiments Transceive phase and conductivity results for volunteer 1 are presented in Figures 8, 9 and Figure 2B.5. Figure 2.9 highlights that PLANET reconstructed T_1 , T_2 and Δf_0 maps, besides ϕ^\pm . The transceive phase maps from bssFP and PLANET globally resembled the reference SE map (Figure 2.9). Maps for ζ_{ϕ^\pm} showed larger uncertainty in SE, which agreed with the phantom data (Figure 2.7). The $\Delta\phi^\pm$ maps in Figure 2.10 did reveal a smoother distribution in PLANET than in bssFP. In particular, in bssFP perturbations were observed, e.g. near the genu of corpus callosum in the frontal lobe ($\Delta\phi^\pm > 0.04$ rad) and in the posterior lobe. The error in proximity of the corpus callosum could be associated with Δf_0 , which rapidly exceeded 50 Hz ($\approx \frac{1}{4TR}$), and cardiac pulsation transferred to the neighbouring CSF [166]. The origin of the slight artefact in the right posterior lobe is unclear; this artefact, nevertheless, was absent in PLANET. (Figure 2.9d). Moreover, in both methods a residual phase accumulation (with a peak value of ~ 0.06 rad) was found in the left side of the frontal lobe (Figure 2.10). Similarly to the phantom case, this residual phase appeared because the asymmetric linear phase gradients induced by eddy currents in both acquisitions did not completely cancel out when averaging was performed (Figure 2B.5). Figure 2B.5 also shows that Helmholtz-based conductivity maps reconstructed on the single acquisition with one gradient polarity differed slightly from the conductivity map retrieved from their average (as already observed in the phantom, Figure 2B.3). However, for all methods the conductivity maps had comparable quality and enhanced the errors present in the corresponding transceive phase maps, as expected. Distortions in bssFP conductivity were found in correspondence of the above-mentioned locations (Figure 2.9i and $\Delta\sigma$ in Figure 2.10). The SE-based conductivity exhibited errors in proximity of vessels, attributed to inflow artefacts appearing in its underlying transceive phase map (because of SE 2D spatial encoding). All conductivity maps showed errors in CSF; these were more prominent for bssFP and PLANET, likely because of mild phase disturbances caused by CSF pulsation [166]. Similar results were observed for the other volunteers (Figure 2.11). In volunteer 2, nonetheless, bssFP- and PLANET-based conductivity maps were almost alike (Figure 2.11e,f). Interestingly, less spatial fluctuations were found in bssFP-based ϕ^\pm and $\Delta\phi^\pm$ maps and a smooth Δf_0 map was acquired, the values of which were within the pass-band region (Figure 2.11h).

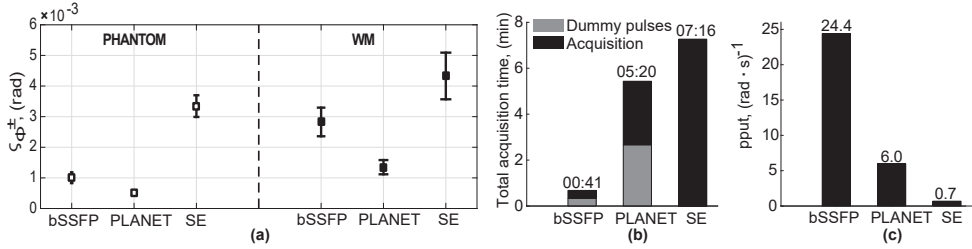


Figure 2.7. Precision, acquisition time and precision-per-unit-time of transceive phase estimation for bSSFP, PLANET and SE. **(a)** Transceive phase precision: mean values of transceive phase uncertainty ζ_{ϕ^\pm} are reported along with the std (error bars). Isotropic voxel size: 2.5 mm. The transceive phase uncertainty ζ_{ϕ^\pm} was calculated with Equation 2.7 in the phantom (empty square) and in WM (full square) of volunteer 3 ($C_{\phi^\pm} = 1$ for bSSFP and SE, $C_{\phi^\pm} = 0.43$ for PLANET). WM was segmented using MICO segmentation method [167]. Voxels of the central slice were used for ζ_{ϕ^\pm} calculation in both cases. **(b)** Total acquisition time for the three methods (i.e. including both acquisitions with opposite readout gradient polarity). In bSSFP and PLANET the time spent for both the dummy pulses and the actual acquisition is shown (a series of ~ 2170 dummy RF pulses — corresponding to ~ 10 seconds — was added before each phase-cycled bSSFP acquisition). **(c)** Precision-per-unit-time (pput) for the three methods, where $\text{pput} = (\zeta_{\phi^\pm} \cdot t)^{-1}$, calculated by using ζ_{ϕ^\pm} values for WM in (a) and the total time t in (b).

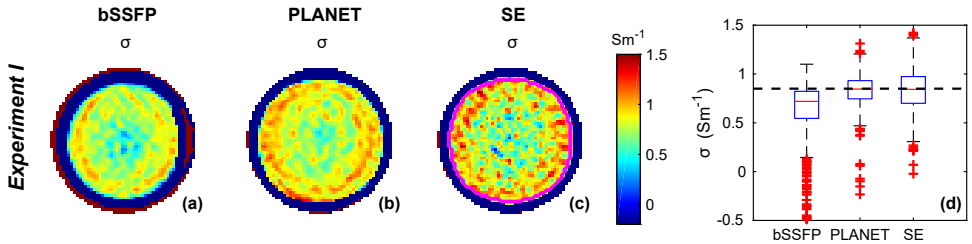


Figure 2.8. Phantom conductivity based on bSSFP, PLANET and SE (reference) methods from Experiment I. Conductivity maps reconstructed from transceive phase maps estimated with **(a)** bSSFP; **(b)** PLANET and **(c)** SE in Experiment I. The transceive phase maps used for conductivity reconstruction are shown in Figure 2.6 (a-c). **(d)** Boxplot of conductivity values, evaluated in the circular ROI (shown in magenta color in (c)) in the central slice of the phantom. The ROI was based on thresholding on SE magnitude image followed by erosion to exclude EPT boundary errors. The true conductivity value, as measured by the dielectric probe, is shown with a black dashed line.

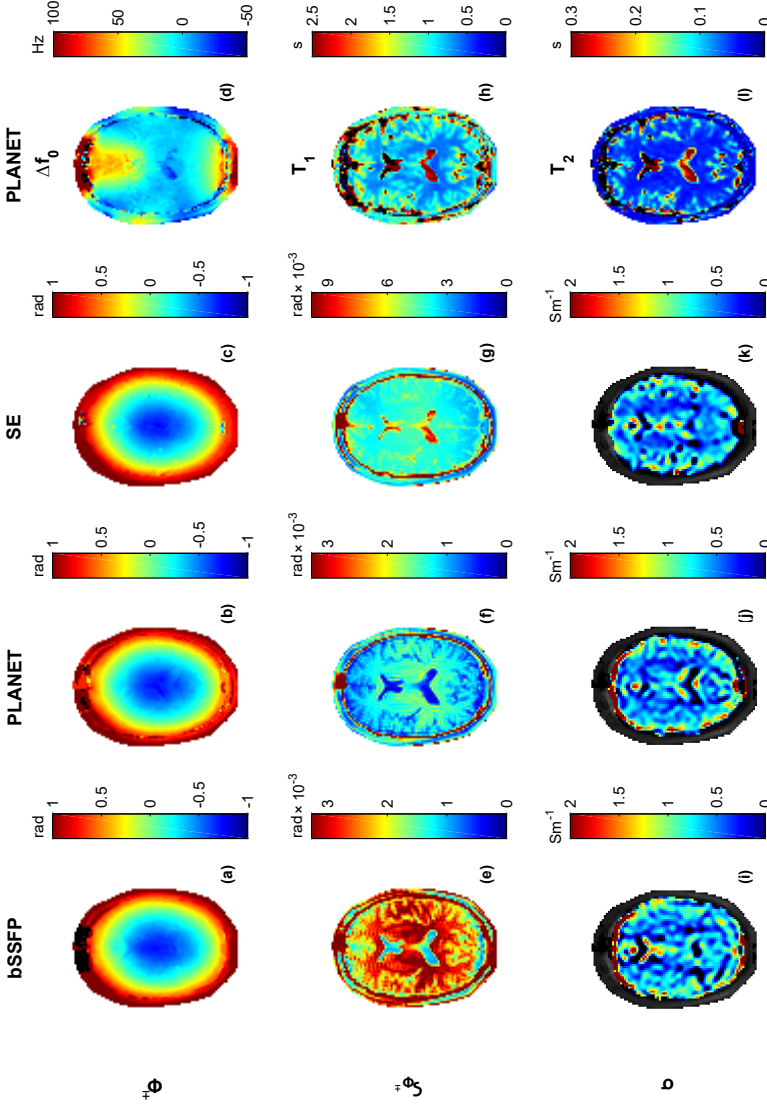


Figure 2.9. In vivo brain results for volunteer 1, obtained with bSSFP (first column), PLANET (second column) and SE (reference, third column) methods. Transceive phase maps (ϕ^\pm) obtained from (a) bSSFP; (b) PLANET and (c) SE, after unwrapping. (d) Δf_0 map obtained with PLANET. Maps of the transceive phase uncertainty (ς_{ϕ^\pm}) for (e) bSSFP; (f) PLANET and (g) SE. The ς_{ϕ^\pm} for SE was calculated with Equation 2.7, $C_{\phi^\pm} = 1$, being SE-based ϕ^\pm -map directly acquired. Note the different colorbar in (g) with respect to (e) and (f). (h) T_1 map obtained with PLANET. Conductivity maps based on (i) bSSFP; (j) PLANET and (k) SE, reconstructed from ϕ^\pm maps shown in (a-c) respectively. (l) T_2 map obtained with PLANET. Note that T_1 and T_2 maps are expected to suffer a ~ 20 – 25% bias, because the TR used in this study (4.6 ms) was specifically chosen for transceive phase mapping but was suboptimal for T_1 and T_2 mapping [155].

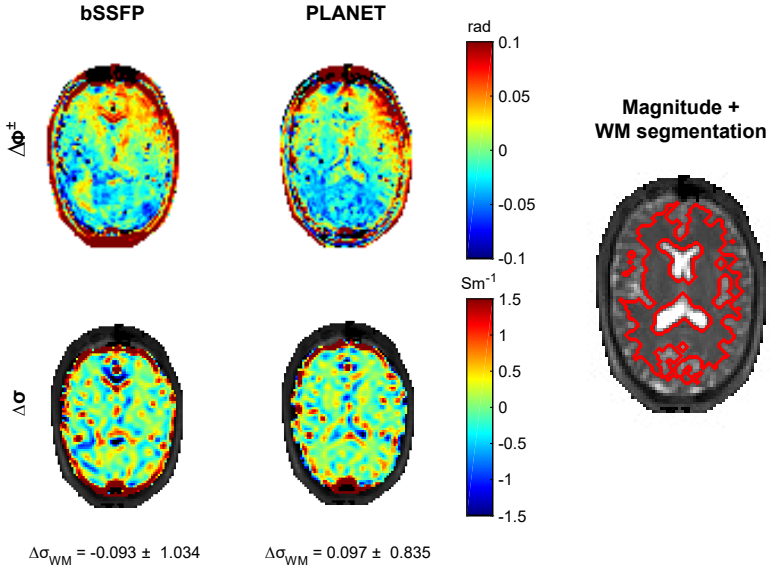


Figure 2.10. Transceive phase difference maps ($\Delta\phi^\pm$, *top*) and conductivity difference maps ($\Delta\sigma$, *bottom*) for both bSSFP (*left*) and PLANET (*right*) for volunteer 1. Difference maps were performed with respect to SE-based ϕ^\pm and σ ($\Delta\phi_{\text{bSSFP/PLANET}}^\pm = \phi_{\text{bSSFP/PLANET}}^\pm - \phi_{\text{SE}}^\pm$ and $\Delta\sigma_{\text{bSSFP/PLANET}} = \sigma_{\text{bSSFP/PLANET}} - \sigma_{\text{SE}}$). Transceive phase and conductivity maps are shown in Figure 2.9. Mean \pm std $\Delta\sigma$ values in WM are reported below the corresponding map. WM segmentation was performed with MICO segmentation method [167] and is shown in red on the banding-free magnitude image obtained with PLANET method.

2.5 Discussion

In this study, we introduced a novel technique to map the transceive phase ϕ^\pm , the PLANET method, an ellipse fitting approach to phase-cycled bSSFP data. We studied accuracy and precision of its ϕ^\pm estimates in brain with simulations and MR measurements and compared these to ϕ^\pm acquired with standardly-used transceive phase mapping sequences (bSSFP and spin echo (SE)). To the best of the authors' knowledge, this is the first study comparing transceive phase mapping methods. Furthermore, based on experimental ϕ^\pm maps, we reconstructed Helmholtz-based conductivity maps to provide an example of an application which depends on transceive phase information. Our analysis demonstrated that PLANET can reconstruct accurate and precise transceive phase maps in the brain, therefore allowing reliable reconstruction of brain tissue conductivity.

A fundamental benefit offered by the PLANET method is that it retrieves transceive phase maps free from off-resonance effects that generally contaminate the transceive phase acquired with bSSFP. The superior "robustness" of PLANET against off-resonance variations was proven in both simulations (Figure 2.2 and Figure 2B.1) and phantom measurements (Figure 2.6 and Figure 2B.4), and is particularly advantageous for large off-resonances which result in banding artefacts in bSSFP-based transceive phase (see, for example, Experiment II, when a linear field variation was artificially induced; Figure 2.6i). This different robustness against off-resonance effects depends on how both methods estimate ϕ^\pm : as detailed in the *Theory*, in standard

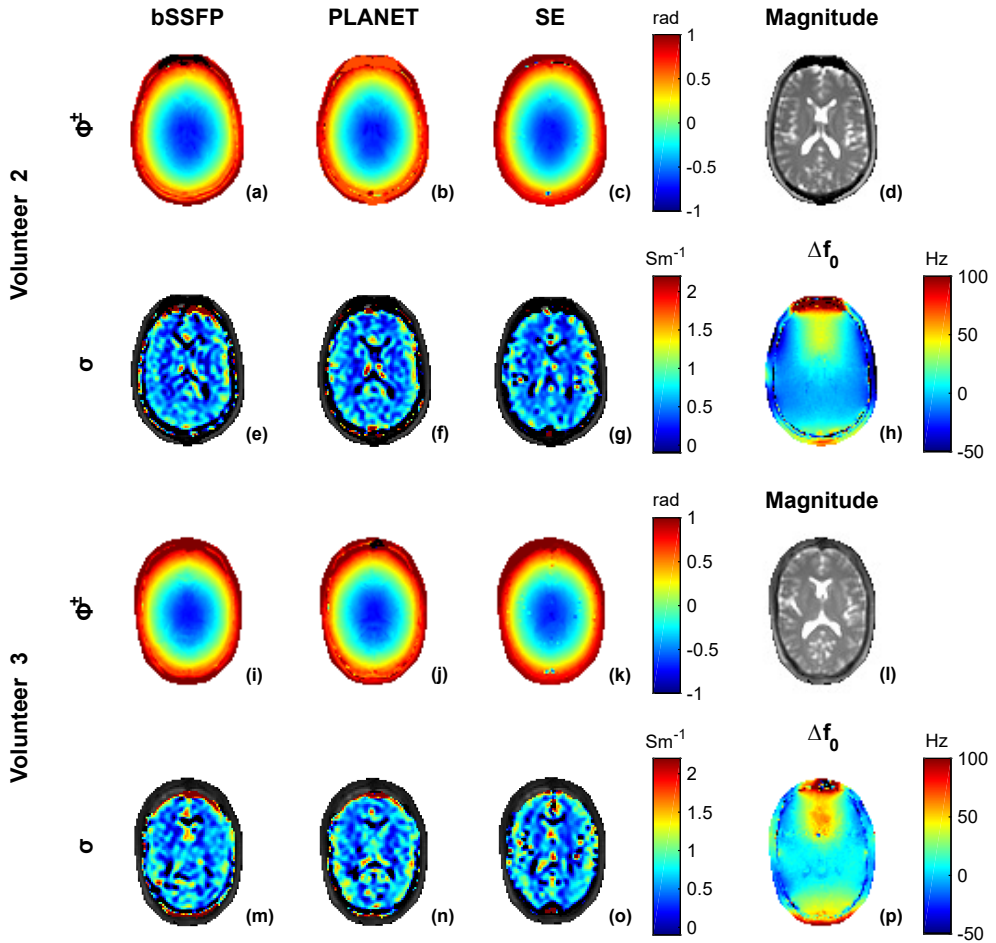


Figure 2.11. In vivo brain results for volunteer 2 (a-h) and 3 (i-p), obtained with bSSFP (first column), PLANET (second column) and SE (reference, third column) methods. Transceive phase maps (ϕ^\pm) obtained from (a,i) bSSFP; (b,j) PLANET and (c,k) SE, after unwrapping. (d,l) Banding-free magnitude image obtained with PLANET method. Conductivity maps based on (e,m) bSSFP; (f,n) PLANET and (g,o) SE, reconstructed from transceive phase maps shown in (a-c, i-k) respectively. (h,p) Δf_0 map.

bSSFP the signal phase is commonly associated with the transceive phase. Considering that the signal phase $\angle I_0 = \angle(1 - E_2 e^{-i(\theta_0 + \pi)}) \cdot e^{i\Omega}$ is mainly influenced by the transceive phase (in Ω), the off-resonance (in Ω and θ_0) and T_2 (in E_2), the equivalence “ $\phi^\pm = \text{signal phase}$ ” is a suitable approximation when all other phase contributions are negligible. Banding artefacts and T_2 effects, for instance, occur when $|\Delta f_0| > (3TR)^{-1}$ [151]. Ideally, these effects could be eliminated by combining appropriate B_0 shimming with short TR s, two options that depend on the available MR system’s hardware and software tools and the imaged object. Within the pass-band region, however, bSSFP-based ϕ^\pm can still be contaminated by Δf_0 -induced “phase leakage”, which can mildly modify the ϕ^\pm curvature (e.g. Figure 2.6e,j,n Figure 2B.4k). Differently, in PLANET the transceive phase is intrinsically corrected for Δf_0 (and T_2) effects because it results directly from the difference between the off-resonance-driven phase and the rotation angle Ω (Equation 2.2), and these two parameters are estimated independently from the shape of the ellipse.

Besides PLANET, other techniques have been proposed specifically to remove bandings from bSSFP transceive phase. A post-processing pipeline for 2D phase “unbanding” was reported by Kim et al. [152]. The recent correction technique by Ozdemir and Ider [151] relies on two bSSFP dynamics with a $(2TR)^{-1}$ frequency shift; this is conceptually similar to employing a phase-cycling scheme. Their methodology does require extra Δf_0 and T_2 measurements to correct bSSFP-based ϕ^\pm for the above-mentioned effects, hence elongating the total scanning time to > 15 minutes. Compared with this last technique, PLANET bypasses the need for additional acquisitions, because it estimates simultaneously ϕ^\pm , Δf_0 , T_2 and T_1 within shorter times [136] (Figure 2.9).

Shcherbakova et al. [155] have already shown that accuracy and precision in T_1 and T_2 in WM estimated with PLANET depend on appropriate selection of sequence settings. Similarly, our simulation results demonstrated that the choice of FA , TR and N (number of RF phase increments) influence the accuracy and precision of PLANET transceive phase estimates. Unsurprisingly, increasing N benefitted the transceive phase precision (Figure 2.4), at the cost of longer acquisition times. Unlike when optimizing T_1 and T_2 accuracy [155], using $TR < 10$ ms was beneficial for transceive phase accuracy in PLANET, but mostly in bSSFP, especially when a second component such as myelin was present in the voxel (Figure 2.2 and Figure 2B.1). The FA choice was relevant for the precision: in both PLANET and bSSFP the lowest uncertainty (ζ_{ϕ^\pm}) was found for $FA = [20 - 30]^\circ$ (Figure 2.3 and Figure 2B.2). Hence, FA and TR should be carefully selected in voxels with mixed content.

Based on all simulation predictions for ϕ^\pm , we selected $FA = 25^\circ$, $TR = 4.6$ ms, and $N = 8$ for all our MR measurements. We also acquired and averaged two phase maps obtained with identical settings but reversed readout gradient polarity, in order to reduce the impact of eddy-currents on the transceive phase. In the volunteer study, both PLANET and bSSFP showed similar $\Delta\phi^\pm$ spatial distributions, with mild perturbations in WM. Besides residual errors caused by eddy currents effects in both methods and by off-resonance effects in bSSFP (which we have already discussed), we hypothesize that bias in WM, albeit small, could originate from partial volume that is likely to occur for the voxel size chosen (2.5 mm isotropic). This is supported by the fact that multiple species with different susceptibilities or chemical shifts are present in human WM (myelin, proteins, lipids, iron, deoxyhemoglobin, etc.) [158,168]. Characterizing the effect of such species in the transceive phase estimated with PLANET or bSSFP was beyond the scope of this study, but the example of a common 2-component relaxation model for human brain (i.e. WM as dominant component and myelin as second component) reported in Figure 2.2 and Figure 2B.1 already demonstrated that myelin properties caused ζ_{ϕ^\pm} errors in both methods, with bSSFP being increasingly more sensitive

than PLANET to myelin presence when the dominant component was no longer on resonance. These errors, as already explained by e.g. Miller [169] and Miller et al. [158], arise because multiple components with different frequency distribution within the same voxel distort the symmetry of bSSFP profile. As a result, in phase-cycled bSSFP data these asymmetries can modify rotation and shape of the ellipse corresponding to the main signal (dominant WM component) on which PLANET fitting is applied [155].

Besides the aforementioned lower sensitivity to off-resonance effects and partial volume, we observed a lower ζ_{ϕ^\pm} for PLANET than for bSSFP and SE (of a factor 2 and 3, respectively, for our sequence settings, Figure 2.7a). Nonetheless, the acquisition of phase-cycled bSSFP data needed for PLANET was 8 times slower than the standard bSSFP acquisition (because $N = 8$). Thus the precision-per-unit-time was higher for bSSFP than for PLANET: overall, bSSFP was 4 times more “efficient” than PLANET (Figure 2.7c). Note also that if precision in the transceive phase were of primary importance rather than accuracy, averaging 8 standard bSSFP acquisitions would produce a $2\sqrt{2}$ precision increase in ϕ^\pm , which is $\sqrt{2}$ times higher than the precision gain obtained in PLANET-based transceive phase with respect to single bSSFP-based transceive phase. In brain experiments, however, acquiring two phase-cycled bSSFP scans with opposed gradient polarity was 2 minutes faster than the conventional SE and took in total 5 minutes, a duration we deemed (already) clinically acceptable, especially in light of the simultaneous reconstruction of T_1 , T_2 , Δf_0 . Although we did not consider accelerating the acquisition in this work, decreasing the number of dummy pulses and the number of RF phase increments N might serve this purpose. For example, decreasing the number of dummy pulses from ~ 2100 to ~ 1300 would save ~ 1 minute for our sequence settings, at the cost of reduced accuracy in all parameters reconstructed with PLANET [155]. However, the resulting transceive phase error would be rather small ($e_{\phi^\pm} \approx 2.7 \cdot 10^{-3}$ rad, Figure 2.5). Reducing N to the minimum ($N = 6$) would additionally shorten the acquisition by 1:20 minutes (corresponding to -25% of the total time reported in Figure 2.7b) and a $\sim 15\%$ reduction in transceive phase precision would be paid (Figure 2.4). Furthermore, using acceleration techniques such as parallel imaging (e.g. SENSE [170]) or compressed sensing (e.g. [171]), would also be recommendable, but their effect on transceive phase reconstruction should be critically evaluated.

An example of an application for which accurate transceive phase maps are important is conductivity mapping with EPT, and precise maps are especially indicated for differentiation-based EPT methods, which are typically more sensitive to noise than integration-based methods [57]. Although multiple EPT reconstruction methods to map brain conductivity have been proposed previously (e.g. references [59, 60, 91, 103, 120]), here we employed the conventional (“phase-only”) Helmholtz-based approach because of its known linear noise propagation from transceive phase to conductivity [88] that allows comparison of ϕ^\pm mapping methods. In the homogeneous phantom, the conductivity std was on the same order of magnitude for all methods, despite their different ζ_{ϕ^\pm} . This reveals a low linear coefficient (or slope) in the above-mentioned noise propagation relationship of this EPT method and is in line with the theoretical model by Lee et al. [88]. PLANET and SE had comparable median conductivity values, whereas bSSFP underestimated the conductivity because of a slightly altered shape of its transceive phase (Figure 2.8 and Figure 2B.4). Our conductivity findings also suggest that the acquisition duration could be more than halved in PLANET (from $\sim 05:20$ minutes with the settings used in this study to 02:03 minutes) if conductivity retrieval alone were of interest, because mapping ϕ^\pm from a single polarity acquisition (Figures 2B.3 and 2B.5, both PLANET and bSSFP) and reducing N to 6 for PLANET (Figure 2B.4) had little impact on the accuracy and precision of Helmholtz-based conductivity. Nonetheless, whether this impact remains little for conductivity maps obtained with other EPT methods should be verified. In vivo, the small disturbances present in transceive phase

maps of PLANET, bSSFP and also SE were unsurprisingly enhanced in the corresponding conductivity maps. Overall, PLANET-based conductivity qualitatively resembled the reference SE-based conductivity for all volunteers (Figure 2.9 and Figure 2.11). Thus, we expect that using any other EPT reconstruction algorithms on PLANET-based transceive phase map would produce conductivity maps at least comparable to the conductivity maps reconstructed with presently-used sequences.

2.6 Conclusion

The newly-introduced PLANET method reconstructs accurate and precise transceive phase maps when appropriate sequence settings are chosen and is therefore a valid technique to map brain transceive phase and conductivity. PLANET retrieves transceive phase maps free from off-resonances effects, which typically corrupt bSSFP maps. This renders PLANET suitable for situations in which stronger B_0 inhomogeneity comes into play (e.g. for field strengths $> 1.5T$) and/or with limited B_0 shimming control. Furthermore, sensitivity to partial volume effects is better attenuated in PLANET than in bSSFP. Despite its longer acquisition time and lower time-efficiency than bSSFP, PLANET simultaneously retrieves banding-free magnitude image, T_1 , T_2 , Δf_0 , [136] transceive phase and can be exploited for reconstruction of conductivity and magnetization transfer parameters [172] within clinically feasible times, which could be useful for quantitative brain tissue characterization.

2.A Appendix A: The bSSFP signal

The complex bSSFP signal inside a voxel in the steady-state regime is expressed as [150]

$$I_0 = KM \cdot e^{-\frac{TE}{T_2}} \cdot \frac{1 - E_2 e^{-i(\theta_0 + \pi)}}{1 - b \cos(\theta_0 + \pi)} \cdot e^{i\Omega}, \text{ for } E_{1,2} = e^{-\frac{TR}{T_{1,2}}} \quad (2A.1)$$

where K is a proportionality constant which includes the magnitude of the receive coil sensitivity. Definition of M and b is as follows:

$$M = \frac{M_0 (1 - E_1) \sin(FA)}{1 - E_1 \cos(FA) - E_2^2 (E_1 - \cos(FA))} \quad (2A.2)$$

$$b = \frac{E_2 (1 - E_1) (1 + \cos(FA))}{1 - E_1 \cos(FA) - E_2^2 (E_1 - \cos(FA))} \quad (2A.3)$$

which both depend on TR , relaxation times T_1 and T_2 through $E_{1,2} = e^{-\frac{TR}{T_{1,2}}}$ and FA . The phase components θ_0 and Ω depend on: chemical shift (CS, in Hz), off-resonance caused by B_0 field variations (Δf_0 , in Hz), transceive phase (ϕ^\pm), eddy currents due to ramping of readout gradient G (ϕ_{eddy}), the gradient polarity ($sign(G)$) and B_0 drift (ϕ_{drift}):

$$\theta_0 = 2\pi (CS + \Delta f_0) TR \quad (2A.4)$$

$$\Omega = 2\pi (CS + \Delta f_0) TE + \phi^\pm + \phi_{drift} + sign(G) \cdot \phi_{eddy} \quad (2A.5)$$

2.B Appendix B: Supplementary figures

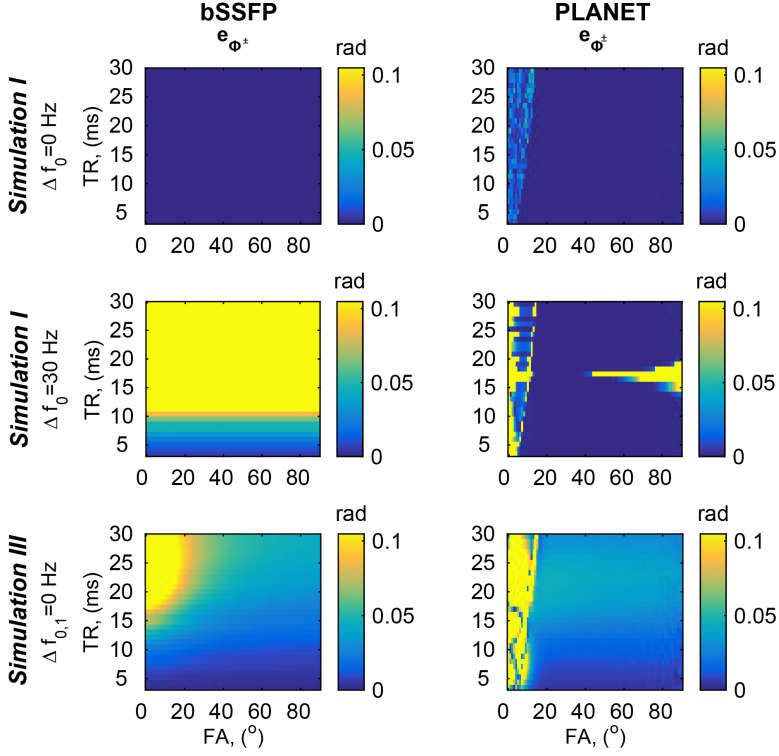


Figure 2B.1. Accuracy of transceive phase estimation for bSSFP (*first column*) and PLANET (*second column*): results from simulation I and III.

Simulation I: $e_{\phi^{\pm}}$ as a function of FA and TR for a single-component voxel at $\Delta f_0 = 0$ Hz (*first row*) and at $\Delta f_0 = 30$ Hz (*second row*). WM: $T_1 = 832$ ms, $T_2 = 80$ ms and $\phi^{\pm} = -\pi/3$ rad. Simulation III: $e_{\phi^{\pm}}$ as a function of FA and TR for a 2-component voxel (*third row*). First component: WM, input $\Delta f_{0,1} = 0$ Hz, $\phi^{\pm}_1 = -\pi/3$ rad, $T_{1,1} = 832$ ms, $T_{2,1} = 80$ ms and $w_1 = 0.88$. Second component: myelin, input $\Delta f_{0,2} = 35$ Hz (CS = 20 Hz), $\phi^{\pm}_2 = -\pi/3$ rad, $T_{1,2} = 400$ ms, $T_{2,2} = 20$ ms, $w_2 = 0.12$.

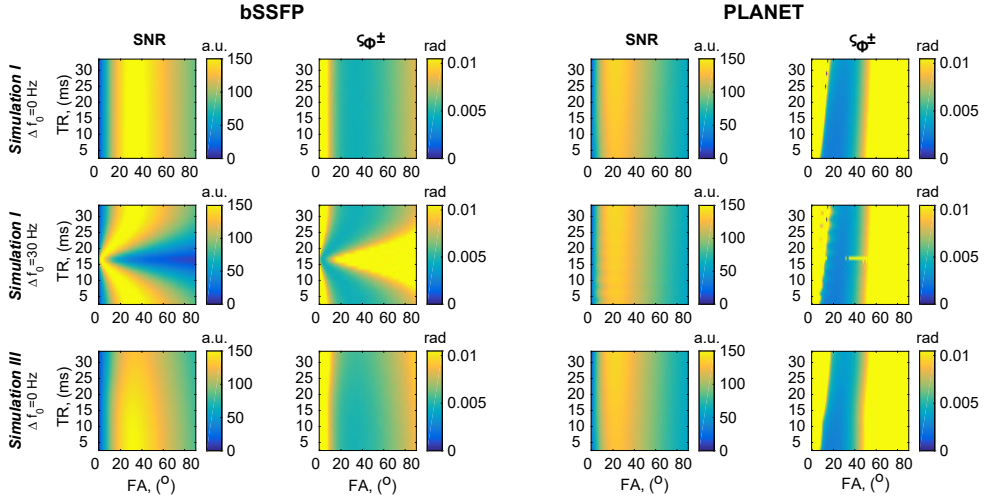


Figure 2B.2. Precision of transceive phase estimation for bSSFP (*left*) and PLANET (*right*): results from simulation I and III. Image SNR (as calculated in Equation 2.6) and the transceive phase uncertainty ζ_{ϕ^\pm} (as calculated in Equation 2.4) are shown as a function of FA and TR. Simulation I: image SNR and ζ_{ϕ^\pm} for a single-component voxel at $\Delta f_0 = 0$ Hz (*first row*) and at $\Delta f_0 = 30$ Hz (*second row*). Simulation III: image SNR and ζ_{ϕ^\pm} for a 2-component voxel at $\Delta f_{0,1} = 0$ Hz (*third row*).

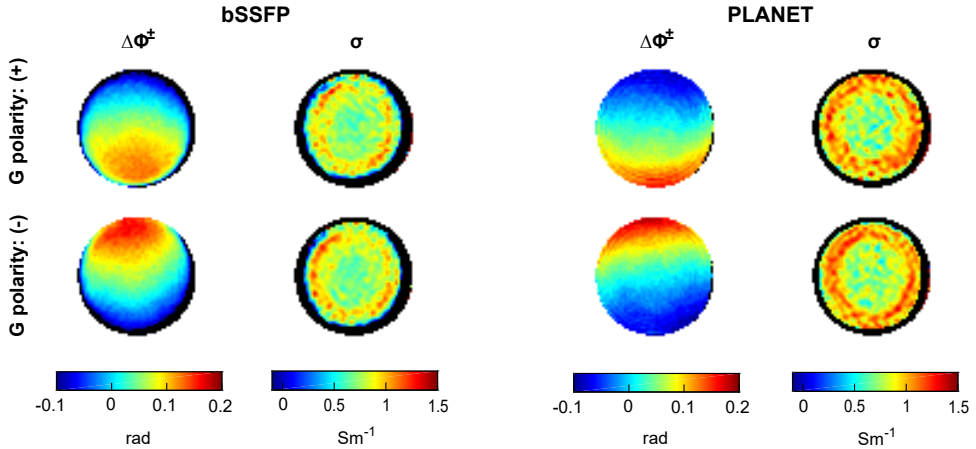


Figure 2B.3. Effect of eddy-current-induced phase accumulation on the phantom transceive phase and conductivity for bSSFP (*left*) and PLANET (*right*). The effect on the transceive phase is shown with a difference map calculated as $\Delta\phi_{\text{bSSFP/PLANET}}^\pm = \phi_{(+/-)}^\pm \text{bSSFP/PLANET} - \phi_{\text{SE}}^\pm$ where the subscripts “(+/-)” refer to the single acquisition with either positive “(+)” or negative “(-)” gradient polarity G . A linear phase gradient with reverse direction is visible along the readout direction (anterior-posterior in this case) according to the gradient polarity considered. Results are displayed for Experiment I and can be compared with maps shown in Figures 2.6 and 2.8.

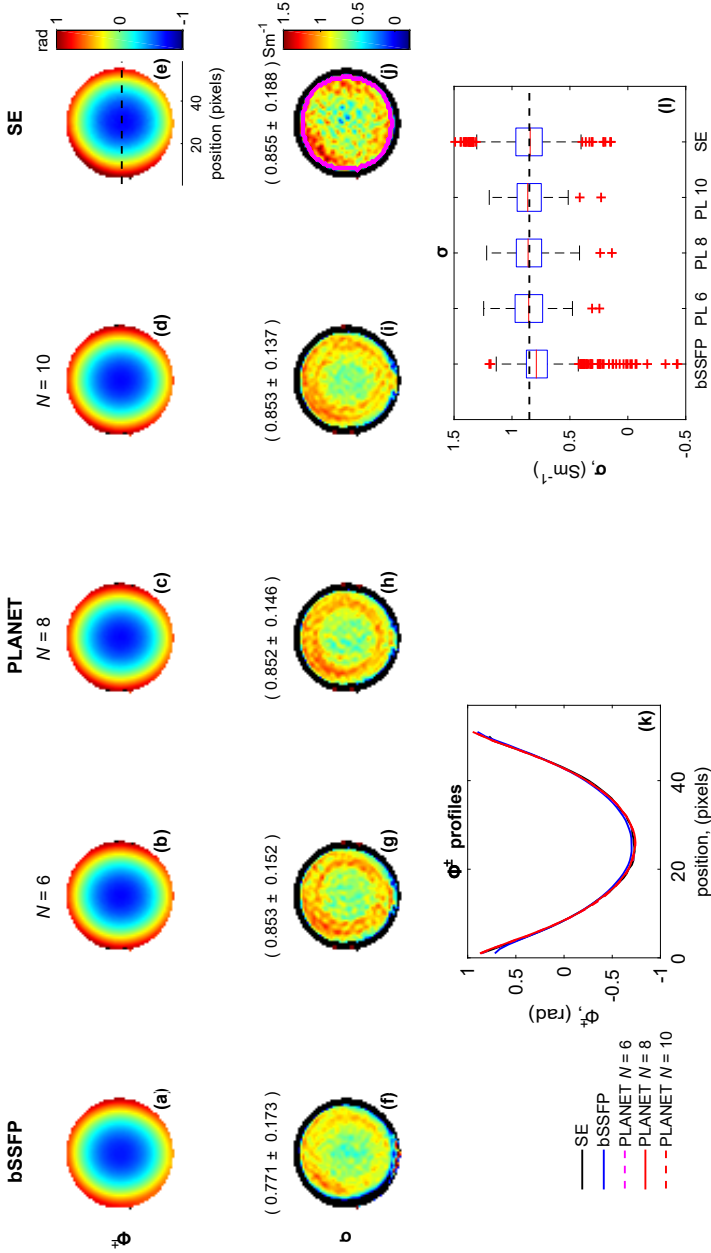


Figure 2B.4. Phantom transceive phase and conductivity for all methods from Experiment III, where volume-based shimming was performed. For PLANET, the effect of using different N phase step increments on the transceive phase and conductivity is shown. Transceive phase maps for: (a) bSSFP; (b) PLANET with $N = 6$ (scan time: 04:04 min); (c) PLANET with $N = 8$ (scan time: 05:20 min); (d) PLANET with $N = 10$ (scan time: 06:47 min); (e) SE (reference method), after unwrapping. Conductivity maps reconstructed from transceive phase maps estimated with (f) bSSFP; (g) PLANET with $N = 6$; (h) PLANET with $N = 8$; (i) PLANET with $N = 10$; (j) SE. Conductivity (mean \pm std) values are reported above the maps. Mean and std were calculated within the circular ROI (shown in magenta color in (j)) in the central slice of the phantom. (k) Transceive phase profiles of bSSFP, PLANET (with the three different N) and SE, calculated on the central horizontal line (dashed line in (e)). (l) Boxplot of conductivity values, evaluated in the circular ROI. The true conductivity value, as measured by the dielectric probe, is shown with a black dashed line.

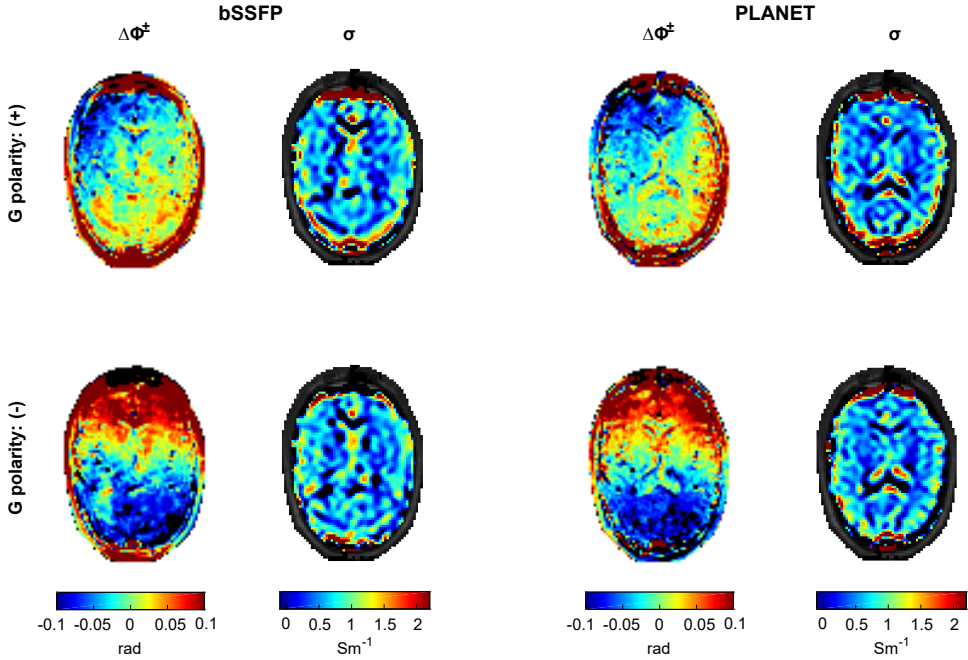


Figure 2B.5. Effect of eddy current-induced phase accumulation on the transceive phase and the conductivity for bSSFP (*left*) and PLANET (*right*). Results are displayed for volunteer 1 and can be compared with maps shown in Figures 2.9 and 2.10. The effect on the transceive phase is shown with a difference map calculated as $\Delta\phi_{\text{bSSFP/PLANET}}^\pm = \phi_{(+/-)\text{ bSSFP/PLANET}}^\pm - \phi_{\text{SE}}^\pm$ where the subscripts “(+/-)” refer to the single acquisition with either positive “(+)” or negative “(-)” gradient polarity G . Reversed linear phase gradients occur along the readout direction (anterior-posterior in this case) according to the gradient polarity considered; these gradients, however, were not perfectly “mirrored” thus a residual eddy-current-induced phase remains visible when the two phase images are averaged to obtain the transceive phase (e.g. on the left side of frontal lobe, Figure 2.10).

Accuracy & precision of electrical permittivity mapping at 3T: the impact of three B_1^+ mapping techniques

Soraya Gavazzi, Cornelis A.T. van den Berg, Alessandro Sbrizzi, H. Petra Kok, Lukas J.A. Stalpers, Jan J.W. Lagendijk, Hans Crezee, Astrid L.H.M.W. van Lier

published in:

Magnetic Resonance in Medicine 2019; 81(6):3628-3642, DOI:10.1002/MRM.27675

ABSTRACT

Purpose: To investigate the sequence-specific impact of B_1^+ amplitude mapping on the accuracy and precision of permittivity reconstruction at 3T in the pelvic region.

Methods: B_1^+ maps obtained with AFI, Bloch-Siegert (BS) and DREAM sequences, set to a clinically feasible scan time of 5 minutes, were compared in terms of accuracy and precision with electromagnetic and Bloch simulations and MR measurements. Permittivity maps were reconstructed based on these B_1^+ maps with Helmholtz-based EPT. Accuracy and precision in the permittivity were assessed. A two-compartment phantom with properties and size similar to the human pelvis was used for both simulations and measurements. Measurements were also performed on a female volunteer's pelvis.

Results: Accuracy was evaluated with noiseless simulations on the phantom. The maximum B_1^+ bias relative to the true B_1^+ distribution was 1% for AFI and BS and 6%–15% for DREAM. This caused an average permittivity bias relative to the true permittivity of 7%–20% for AFI and BS and 12%–35% for DREAM. Precision was assessed in MR experiments. The lowest standard deviation in permittivity, found in the phantom for BS, measured 22.4 relative units and corresponded to a standard deviation in B_1^+ of 0.2% of the B_1^+ average value. As regards B_1^+ precision, in vivo and phantom measurements were comparable.

Conclusion: Our simulation framework quantitatively predicts the different impact of B_1^+ mapping techniques on the permittivity reconstruction and shows high sensitivity of permittivity reconstructions to sequence-specific bias and noise perturbation in the B_1^+ map. These findings are supported by the experimental results.

3.1 Introduction

Knowledge of the electrical properties of tissues is necessary to build patient-specific electromagnetic (EM) models, which are fundamental for radiofrequency (RF) safety [54, 173] and for treatment planning for therapeutic heating of malignant tissues using RF or microwave antennas [131, 140, 174–176]. For example, patient-specific electrical properties may be used as input for planning in locoregional hyperthermia treatment of patients with pelvic tumors (e.g. cervix) with phased arrays of 70–130 MHz antennas [131, 140]. In this frequency range, however, electrical properties might vary (e.g. the permittivity variation is 11% in muscle and 15% in the cervix) due to their dispersive nature [10]; thus, electrical properties should be characterized at a frequency near the frequency used for treatment in order to improve the reliability of treatment planning. Moreover, a great body of literature has shown differences between the electrical properties of healthy and malignant human tissues [9, 13, 14, 17, 127, 129, 177–179]; such differences could potentially be exploited for diagnostic purposes. Therefore, measuring the electrical properties of tissues, being permittivity (ϵ_r) and conductivity (σ), has since long been an important research question [3, 10, 20, 27].

A relatively recent Magnetic Resonance (MR)-based technique, called Electrical Properties Tomography (EPT) [54, 57, 58], extracts non-invasively the tissue *in vivo* electrical properties from the spatial modulation of the circularly polarized component (B_1^+) of the transverse RF transmit field, which is responsible for spin excitation. This spatial modulation in the complex B_1^+ field is determined by induced conduction and displacement currents (which are governed by the tissue conductivity and permittivity distributions), the applied RF frequency (e.g. 128 MHz at 3T proton imaging) and the incident RF field [45, 47, 49]. To the leading order, the permittivity is encoded in the amplitude of the B_1^+ field ($|B_1^+|$), while the conductivity is reflected in the phase of such field [47, 56, 59, 60]. Therefore, measuring accurate and precise B_1^+ amplitude and phase maps is essential in EPT, as the quality of these maps intrinsically influences the quality of both property estimates. Indeed, Lee et al theoretically demonstrated that the precision of permittivity and conductivity reconstructed with a Helmholtz-based algorithm depends linearly on the precision of B_1^+ amplitude (or $\text{SNR}_{B_1^+}$) and phase maps, respectively [88]. Seemingly, the accuracy of both properties is expected to be proportional to the accuracy of the measured B_1^+ amplitude and phase maps [57, 180], although it has never been verified.

To date, several techniques for B_1^+ field mapping have been used in EPT studies (e.g. standard spin echo, gradient echo and bSSFP for phase mapping, and AFI [68] and double-angle methods [67] for $|B_1^+|$ mapping) and numerous algorithms have been proposed to disentangle both properties from the B_1^+ field [54, 59, 60, 84, 88, 91, 93, 106, 109, 113–116, 120, 181–183]. Based on measured field maps, *in vivo* conductivity maps have been derived (e.g. [54, 59, 60, 84, 93, 120, 181]) and also preliminarily tested for clinical oncologic applications, for example in brain [124–127], breast [128, 129] and uterine cervix [102]. At the same time, few studies have reported *in vivo* permittivity maps [60, 89, 92, 93] but no study has exploited permittivity maps in clinical scenarios. Regardless of the chosen EPT reconstruction algorithm, the precision of these permittivity maps was poorer than that of conductivity images. These inferior results were attributed to higher noise levels in experimental $|B_1^+|$ maps [60, 89, 92].

The underlying precision of B_1^+ amplitude and phase maps is dissimilar because both maps are measured independently and differently. The B_1^+ phase distribution is typically approximated with the phase image acquired with standard MR sequences. Thus, its precision is linearly proportional to the SNR of the MR image [39]. On the other hand, the $|B_1^+|$ is mapped with

dedicated B_1^+ mapping sequences (e.g. [67, 68, 72–74]). These sequences employ a model describing the sequence-specific B_1^+ encoding mechanism to derive the $|B_1^+|$ information from acquired MR images. This model regulates the noise propagation that leads to finite precision in the B_1^+ map. Moreover, the B_1^+ encoding model, which normally relies on approximations or assumptions, might degrade the accuracy of the $|B_1^+|$ calculation and therefore bias the estimated $|B_1^+|$ distribution.

B_1^+ mapping sequences that share similar encoding mechanisms, e.g. the double-angle and AFI-based techniques, are expected to have comparable accuracy and precision in the $|B_1^+|$ and consequently similar influence on the permittivity. However, while the accuracy and precision of $|B_1^+|$ maps obtained with some B_1^+ mapping sequences have already been assessed in studies unrelated to EPT [76–78, 184], the impact of the $|B_1^+|$ acquisition on the accuracy and precision of the permittivity map remains still unknown.

Hence, in this study, we investigate the specific impact of the $|B_1^+|$ sequence on permittivity mapping. To this aim, we examined three commonly commercially available sequences (namely, AFI [68], Bloch-Siebert shift (BS, [74]), and DREAM [72]) which have distinct B_1^+ encoding mechanisms. Clinically acceptable scanning times are essential and therefore the three B_1^+ techniques were set to image the $|B_1^+|$ in the pelvic region within 5 minutes. B_1^+ maps of the pelvic region at 3T were of interest to estimate the permittivity at ~ 128 MHz, which falls within the frequency range (70–130 MHz) applied for locoregional hyperthermia treatments of cervical cancers [185]. By designing a methodological framework consisting of (i) mathematical models, (ii) numerical simulations and (iii) MR measurements that take the sequence-specific generation of the $|B_1^+|$ distribution into account, we quantified to what extent the quality of the different B_1^+ amplitude maps affects the accuracy and precision of the resulting permittivity maps. Comparing these permittivity maps highlighted the impact of sequence-specific $|B_1^+|$ accuracy and precision on the permittivity.

3.2 Methods

Phantom MR simulations and measurements and *in vivo* measurements were performed with AFI, BS and DREAM techniques, which were set to map the B_1^+ amplitude distribution in the pelvic region within 5 minutes at 3T. From these $|B_1^+|$ data, permittivity maps were obtained. Figure 3.1 illustrates the complete workflow of our study. Subsequently, the accuracy and precision of both $|B_1^+|$ and permittivity maps have been evaluated and compared. Hereafter, we define the *accuracy* as the bias caused by model imperfections between the estimate of the quantity and the true quantity (in our case, this quantity could be the B_1^+ amplitude or the permittivity), in the absence of noise. The *precision*, instead, is inversely related to the standard deviation (std) of the estimate (i.e. $\text{precision} = (\text{std})^{-2}$) and generally reflects the propagation of noise. Moreover, we will use the term “ B_1^+ map” to refer to the B_1^+ amplitude map, unless explicitly stated otherwise.

3.2.1 Phantom and *in vivo*

For simulations and measurements, a pelvic-sized phantom was used consisting of two compartments [97]: an elliptically shaped cylinder and an inner sphere (Figure 3.2). The outer cylinder was made of poly(methyl methacrylate). The inner sphere was ~ 7.5 mm thick and was made of polystyrene. Phantom composition, dielectric properties and relaxation times are listed in Table 3.1. Dielectric properties of the solutions contained in the inner and outer compartments were measured with a dielectric probe (85070E, Agilent Technologies) and

3. ϵ_r mapping at 3T: impact of three B_1^+ mapping techniques

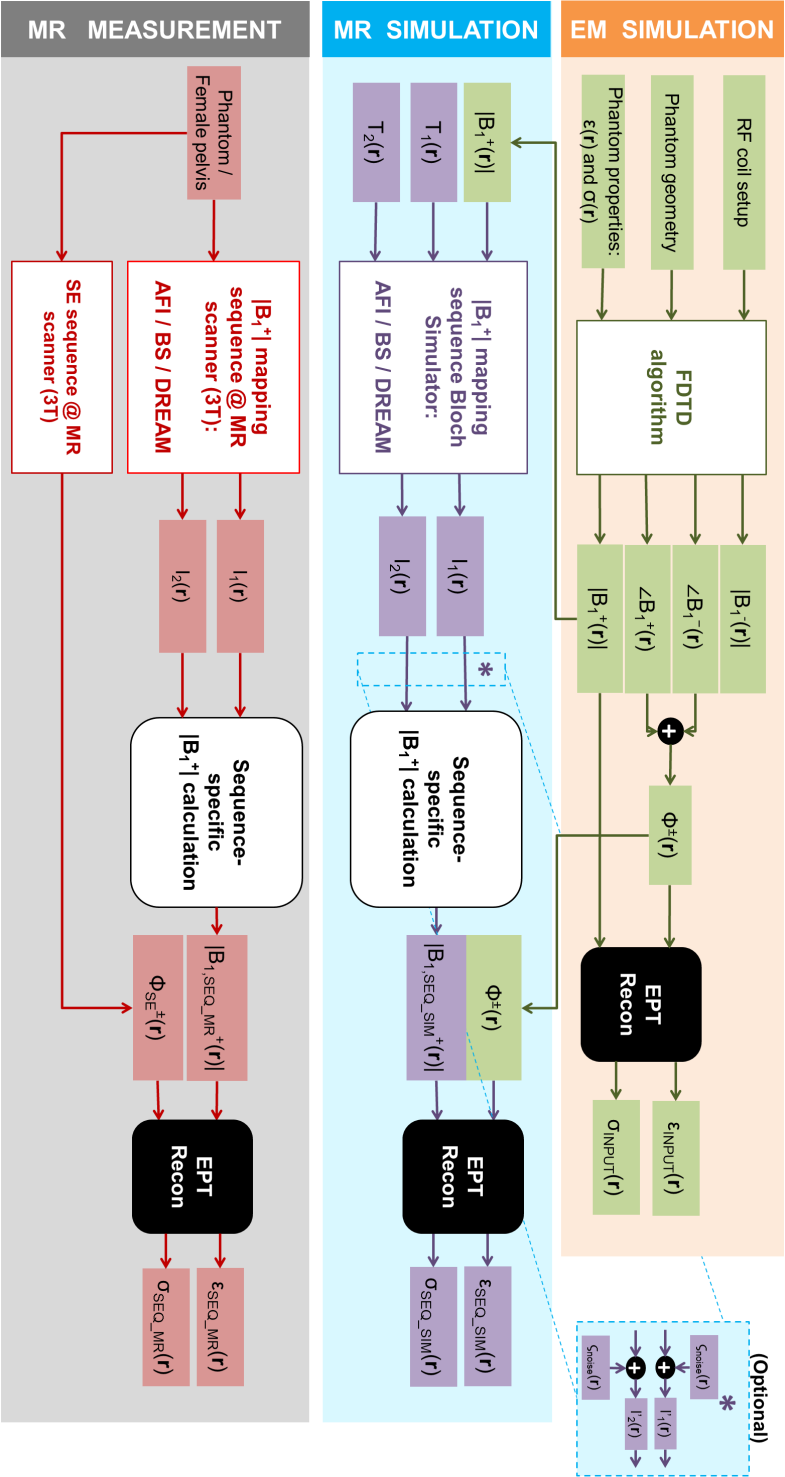


Figure 3.1. From B_1^+ generation to permittivity (ϵ_r) reconstruction: workflow of our study, consisting of an electromagnetic (EM) simulation, MR simulations and MR measurements on a phantom and in vivo MR measurements on a female pelvis. For the MR simulations, Gaussian noise ϵ_{noise} could be optionally added separately to both real and imaginary parts of the signals I_1 and I_2 (denoted by the asterisk and the block “Optional”). In the MR measurements, a separate SE sequence was performed to retrieve a transceive phase map (Φ_{SE^+}) needed for EPT reconstruction. The sequence-specific calculations were performed according to the formulas reported in the Appendix. The subscript “SEQ” refers to any sequence among AFI, BS and DREAM.

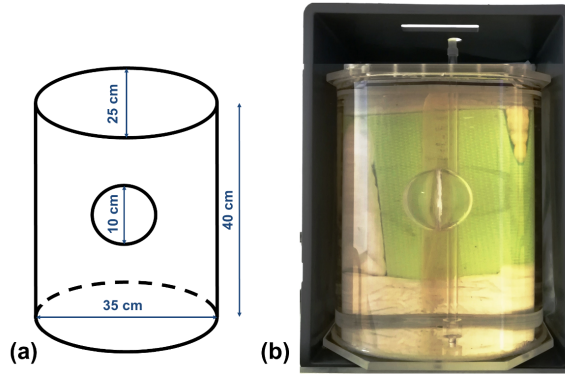


Figure 3.2. Phantom used for simulations and measurements. **(a)** Schematic view of the phantom, with its dimensions. **(b)** Picture of the phantom.

Table 3.1. Phantom characteristics

	Inner compartment	Outer compartment
Composition	6 g/L NaCl	Ethylene glycol + 64 g/L NaCl
ϵ_r (rel. units) ^a	80	36
σ (Sm^{-1})	0.99	0.47
T_1 (ms) ^b	3929	500
T_2 (ms)	433	74

^a Values for permittivity ϵ_r and conductivity σ were measured with a dielectric probe (85070E, Agilent Technologies) from samples of both solutions.

^b T_1 and T_2 values are average values taken from T_1 and T_2 maps measured with a vendor-specific “mix-rSE” sequence (single slice, isotropic voxel size = 5 mm).

matched those of the uterus and the average female pelvis, respectively, based on literature values [10]. Measurements were also conducted on the pelvis of a female volunteer (whose written informed consent was obtained).

3.2.2 MR Experiments

All experiments were performed on a 3T scanner (Ingenia, Philips Healthcare, Best, Netherlands), using a 28-channel torso array for reception. For all three techniques, a 3D acquisition was chosen due to its inherently higher SNR compared to 2D acquisition, essential for EPT. For each sequence, settings were chosen to achieve a scan length of 5 minutes for a FOV = $480 \times 260 \times 80 \text{ mm}^3$ with voxel size $2.5 \times 2.5 \times 5 \text{ mm}^3$ (transverse orientation, Table 3.2). A multi-slice spin echo sequence was used to map the transceive phase. To obtain an eddy current-free transceive phase map, two identical spin echo scans with opposed gradient polarity were acquired [54]. For all MR scans, the vendor-specific CLEAR option was enabled [90]. With CLEAR the combined transceive phase of the body coil and the torso array is converted to the transceive phase of the body coil only.

Table 3.2. Protocol parameter settings for both simulations and measurements. Settings apply for both phantom and in vivo cases.

	AFI	BLOCH-SIEGERT (BS)	DREAM	SE ^a
FOV (mm ³)	480 × 260 × 80	480 × 260 × 80	480 × 260 × 80	480 × 260 × 80
Voxel size (mm ³)	2.5 × 2.5 × 5	2.5 × 2.5 × 5	2.5 × 2.5 × 5	2.5 × 2.5 × 5
Spatial Encoding	3D	3D	3D	2D Multi-Slice
Imaging flip angle (°)	60	60	15	90
TE (ms)	2.5	12	TE ₁ /TE ₂ = 2.1/4.6	6
TR (ms)	TR ₁ /TR ₂ = 30/155	93	7.7	1000
Fast imaging mode	None	None	Ultrafast GRE, 2 shots	None
Sequence-specific options	N.A.	Fermi pulse angle: 725° Fermi pulse duration: 8 ms Fermi pulse offset freq: 4 KHz K _{gs} : 90.2 rad/G ²	STE-first scheme STEAM flip angle: 40° STEAM slice thickness: 20 mm Shot interval length: 3900 ms	N.A.
Pixel BW (Hz)	409.8	479.4	790.5	586.5
NSA ^b	1	1	2	1
Scan duration (min : s)	5:00	5:02	5:05	7:06

^a The SE technique was used only for MR measurements to map the transceive phase. Its scan time duration refers to the time needed to acquire two identical SE scans with opposed gradient polarity for compensation of eddy-currents).

^b NSA = Number of signal averages

3.2.3 MR Simulations

The complex B_1^+ field pattern in the phantom, as generated by a 16-rod birdcage RF coil, was simulated using an in-house developed FDTD (finite-difference-time-domain) algorithm [186]. The coil was tuned at 128 MHz (3T) and driven in quadrature mode. A resolution of $2.5 \times 2.5 \times 5 \text{ mm}^3$ was used for the simulation. The resulting components of the magnetic field were combined to obtain the complex magnetic transmit field (B_1^+) and complex magnetic receive field (B_1^-) (Figure 3.1).

Subsequently, the MR experiment for each B_1^+ mapping sequence was emulated in Matlab (R2015a, The MathWorks, Natick, MA) by using a Bloch simulator [156]. Input for these simulations were the geometry of the phantom model, the B_1^+ amplitude map from the FDTD simulation (also called “input B_1^+ ” in this study), T_1 and T_2 values (see Figure 3.1 and Table 3.1). The input B_1^+ map was normalized to the average $|B_1^+|$ value in the central slice. Therefore, all values relating to B_1^+ are reported as relative units.

Rectangular-shaped RF excitation pulses were employed, except for the off-resonant Fermi pulse in bs. All pulses were set to achieve an average flip angle equal to the chosen nominal flip angle in the experiments (Table 3.2) and were scaled by the input transmit field. Imaging gradients were also approximated as rectangular blocks. Furthermore, we assumed ideal spoiling of the transverse magnetization at the end of each TR . Two different simulation approaches were used according to the acquisition regime of each sequence. For the steady-state sequences (AFI and bs) the voxel signal corresponded to the signal value at TE , i.e. the value at the center of k-space. Differently, to mimic the multi-shot imaging modality of DREAM, the full readout and phase-encoding gradient schemes were implemented. Thus, the full k-space was collected and then Fourier-transformed into the image domain to obtain the MR image.

For each sequence, the output of each simulation was two MR images (I_1 and I_2 , Figure 3.1). These images were combined to form the B_1^+ map according to the sequence-specific B_1^+ encoding mechanism, as outlined in Appendix 3.A. To simulate the full phantom volume, the sequence simulation was looped over all slices.

3.2.4 Permittivity reconstruction

Permittivity maps were reconstructed with a Helmholtz-based EPT method. This method is based on a finite-difference Laplacian implementation: specifically, the noise-robust kernel was employed for the Laplacian operator [59]. The kernel size was $7 \times 7 \times 5$ voxels.

The EPT reconstruction requires the complex B_1^+ field as input data, i.e. both the amplitude and phase distribution maps. As the phase of the transmit field (ϕ^+) is not directly measurable in MR, the transceive phase assumption [56] was used. The transceive phase assumption approximates the B_1^+ phase as half of the *transceive phase* (ϕ^\pm), namely the sum of the B_1^+ and B_1^- phases. Van Lier et al. [59] and Balidemaj et al. [97] showed that this approximation introduced a minor phase error in both the brain at 7T and the pelvis at 3T.

We reconstructed permittivity maps based on complex B_1^+ data from both simulations and experiments. The B_1^+ amplitude map was derived from AFI, bs and DREAM measurements or simulations. The transceive phase was derived from the spin echo-based transceive phase map (measurements) and from the sum of B_1^+ and B_1^- phases obtained in the EM simulation

(Figure 3.1). We also reconstructed the permittivity from the true " B_1^+ " amplitude and transceive phase, i.e. the maps without influence of the B_1^+ mapping technique. We called this permittivity map "input permittivity". Note that this "input permittivity" represents the best permittivity that could be obtained with the above-mentioned reconstruction method.

3.2.5 Effect of transceive phase assumption

To assess the impact of the transceive phase assumption on permittivity, we simulated two types of permittivity: the first permittivity was reconstructed from the B_1^+ amplitude map and the transceive phase map and the second was based on the B_1^+ amplitude and phase maps.

3.2.6 ROI delineation

For both measurements and simulations, two regions of interest (ROIs) corresponding to the two compartments were manually delineated. All ROI delineations did not include the boundary errors caused by Helmholtz-based EPT reconstruction. In vivo, three ROIs were defined corresponding to the whole pelvis, bladder and fat tissues. These ROIs were based on thresholding on magnitude images followed by further erosion to exclude the aforementioned EPT boundary errors.

3.2.7 Accuracy assessment

As there is no reference technique ('golden standard') for B_1^+ mapping in experiments, the accuracy (bias) of B_1^+ was assessed on noiseless simulated B_1^+ maps of the phantom. The bias in the B_1^+ pattern was illustrated by an error map representing the difference between the sequence B_1^+ map and the true B_1^+ distribution. To evaluate the isolated impact of the sequence-specific B_1^+ bias on the accuracy in the permittivity, we first reconstructed the permittivity maps on the above-mentioned simulated B_1^+ maps. Then, we calculated the permittivity error maps, i.e. difference maps between the sequence-based permittivity and the input permittivity. Moreover, an average accuracy for the permittivity was estimated in both phantom simulations and measurements by calculating the permittivity mean values in the ROIs.

3.2.8 Precision assessment

Since precision and std are inversely related, we will use the std of the quantity under consideration as a measure for its precision. To avoid confusion with the conductivity symbol, we will denote the std with " ζ ". Hence, we will indicate hereafter the noise level, the std in the B_1^+ amplitude and the std in permittivity with ζ_{noise} , $\zeta_{B_1^+}$ and ζ_{ϵ_r} respectively.

An analytical expression for the std in the B_1^+ map, $\zeta_{B_1^+}$, was determined via error propagation [187] for each B_1^+ mapping sequence (see Appendix 3.A for more details) and used to generate $\zeta_{B_1^+}$ -maps in measurements and simulations. As shown in Appendix 3.A, $\zeta_{B_1^+}$ depends on sequence settings, the magnitudes or phases of the original images I_1 and I_2 and their SNRs (SNR_1 and SNR_2). To obtain the $\zeta_{B_1^+}$ map from measured data, SNR maps corresponding to the images I_1 and I_2 were calculated with Kellman's method [165]. The implementation of Kellman's method was validated with the temporal SNR method (SNR_{mult} in [188]) in prior

experiments (not shown). For both phantom and in vivo experiments, mean and std values for $\zeta_{B_1^+}$ were calculated in the respective aforementioned ROIs.

In the MR simulations (phantom only), instead, the real and imaginary parts of the images I_1 and I_2 were corrupted independently with a Gaussian noise level ζ_{noise} . Subsequently, fictitious SNR_1 and SNR_2 , maps were generated from the ratio of the noiseless image amplitude maps and ζ_{noise} . Finally, a single map for $\zeta_{B_1^+}$ was obtained. This procedure was repeated by using a range of realistic noise levels common to each technique. For each sequence and ζ_{noise} , the resulting simulated maps for SNR_1 (and SNR_2) and $\zeta_{B_1^+}$ were then spatially averaged inside the phantom. With these average values, we predicted the relationship between $\zeta_{B_1^+}$ and the image SNR_s for the three sequences.

To determine the effect of realistic B_1^+ precision on the reconstructed permittivity, we performed a Monte Carlo-based simulation (1000 iterations). In this case, the noise level used to corrupt the images in each technique was chosen such that the simulated image SNR_s approximated the sequence-specific experimental image SNR_s . In each iteration, a B_1^+ map was retrieved from these noisy images and used to reconstruct the permittivity. Subsequently, the permittivity mean and std maps over all iterations were calculated and eventually averaged inside the ROIs.

The std in permittivity, ζ_{ϵ_r} , was calculated on measured permittivity data in the ROIs corresponding to both compartments. The permittivity precision was then correlated with the B_1^+ precision found experimentally in the phantom.

3.3 Results

3.3.1 Simulation results

Accuracy Noiseless simulations showed that all the techniques were able to reveal the B_1^+ field in the phantom (Figure 3.3a). Although these maps appeared to have perfect resemblance with the input field, difference maps exposed the subtle sequence-specific errors (Figure 3.3b). The maximum relative accuracy (i.e. $bias_{B_1^+} = \left| \left(B_{1,sequence}^+ - B_{1,input}^+ \right) / B_{1,input}^+ \right|$) was 0.2% for AFI, 0.3% for BS, and 6.1% for DREAM in the inner compartment. In the outer compartment the maximum relative accuracy was 1.5% for AFI, 0.3% for BS, and 15.4% for DREAM. Figure 3.3c depicts the permittivity maps reconstructed on these sequence-specific B_1^+ maps and the permittivity reconstructed on the input B_1^+ , dubbed “input permittivity”. For all these cases, the transceive phase obtained from the EM simulation was used together with the B_1^+ amplitude. The difference between the *sequence-specific* and *input* permittivity is reported in Figure 3.3d. This difference revealed the inaccuracies introduced by the B_1^+ mapping technique. The seemingly small bias in B_1^+ obtained with AFI and BS led to substantial errors in the permittivity maps. In the inner compartment, the relative bias for the permittivity (defined as $bias_{\epsilon_r} = \left| \left(\epsilon_{r,sequence} - \epsilon_{r,input} \right) / \epsilon_{r,input} \right|$) was on average 7.4% for AFI and BS; in the outer compartment it was 19.5% for AFI and 17.9% for BS. In the case of DREAM, the higher B_1^+ inaccuracies caused a further distorted permittivity map (e.g. the rim around the phantom perimeter and mild spurious fluctuations in Figure 3.3d). In this case, average relative errors of 12% in the inner compartment and 35.4% in the outer compartment were observed, with peak errors up to 264% around the phantom perimeter. In general, the mean permittivity was

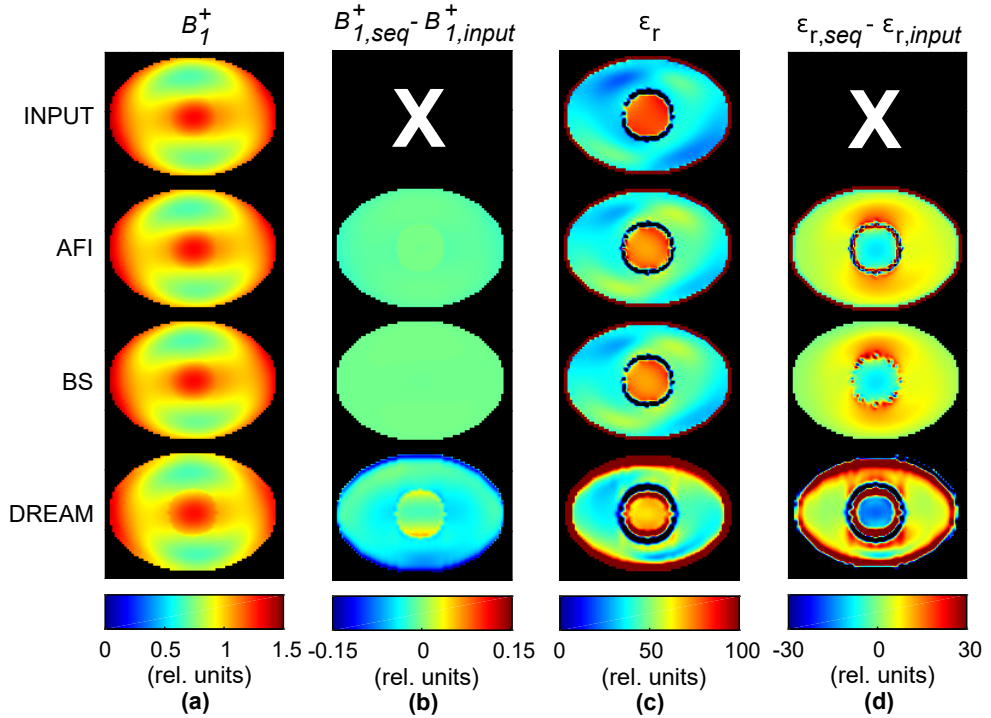


Figure 3.3. Phantom simulation study to assess the accuracy of both B_1^+ and ϵ_r , which were obtained with the EM simulation (“input”, first row), AFI (second row), BS (third row) and DREAM (fourth row). No noise was added. (a) B_1^+ maps. Values for the B_1^+ maps were normalized to the average value in the central slice. (b) Map of the error in B_1^+ ($B_{1,sequence}^+ - B_{1,input}^+$). (c) Permittivity maps, which were reconstructed from the maps shown in (a) and the simulated transceive phase. (d) Map of the error in ϵ_r ($\epsilon_{r,sequence} - \epsilon_{r,input}$). Note that the input permittivity ($\epsilon_{r,input}$) accounts for the transceive phase assumption and is therefore the best permittivity that can be obtained with this EPT reconstruction method.

offset from the input permittivity of ~ 6 units for both AFI and BS and of ~ 13 – 15 units for DREAM in both compartments (Table 3.3).

Effect of transceive phase assumption The effect of the transceive phase assumption on permittivity is illustrated in Figure 3.4 for our phantom. The transceive phase error ($\phi^\pm/2 - \phi^+$, Figure 3.4a) appeared as left-right anti-symmetry and was larger in the outer compartment, where the validity of the assumption degrades. The maximum error was 0.15 rad. A peripheral anti-symmetric pattern was also reflected in the permittivity reconstructed with the transceive phase combined with the B_1^+ amplitude (Figure 3.4c). This led to a maximum bias of 15% with respect to the permittivity calculated based on the B_1^+ phase and amplitude. In general, using the transceive phase contributed mostly to the spread of permittivity values (Table 3.3). Similar effects have been observed for the conductivity in previous studies [59, 97].

Table 3.3. Phantom permittivity (in relative units) obtained from simulations and measurements. Mean \pm std values were calculated in two ROIs corresponding to both compartments. The boundary errors due to EPT reconstruction were excluded from the ROIs.

	Simulations						Measurements			
	$ B_1^+ $ and B_1^+ phase (noiseless)		$ B_1^+ $ and transceive phase (noiseless)		$ B_1^+ ^a$ and transceive phase		$ B_1^+ $ and transceive phase			
	Inner compartment	Outer compartment	Inner compartment	Outer compartment	Inner compartment	Outer compartment	Inner compartment	Outer compartment	Inner compartment	Outer compartment
TRUE ^b	80	36	80	36	80	36	80	36	80	36
INPUT ^c	80.64 \pm 0.59	36.42 \pm 0.76	80.45 \pm 2.76	36.21 \pm 5.94	—	—	—	—	—	—
AFI	74.69 \pm 2.28	43.28 \pm 3.46	74.49 \pm 3.13	43.07 \pm 6.66	73.79 \pm 95.75	43.04 \pm 26.14	83.77 \pm 103.00	38.65 \pm 31.85		
BS	74.71 \pm 2.26	42.74 \pm 3.63	74.52 \pm 3.11	42.52 \pm 6.78	74.52 \pm 44.02	42.57 \pm 12.48	72.34 \pm 47.65	38.40 \pm 22.38		
DREAM	65.02 \pm 10.68	49.03 \pm 13.86	64.81 \pm 10.76	48.80 \pm 14.86	63.52 \pm 17.00	47.98 \pm 28.93	56.87 \pm 48.71	55.31 \pm 46.69		

^a Montecarlo simulation to emulate the MR measurements. B_1^+ maps were affected by noise, which corrupted the original images I_1 and I_2 .

^b TRUE refers to the permittivity values measured with the dielectric probe and already reported in Table 3.1.

^c INPUT refers to the permittivity values calculated from the input permittivity reconstructed directly from the EM simulation data.

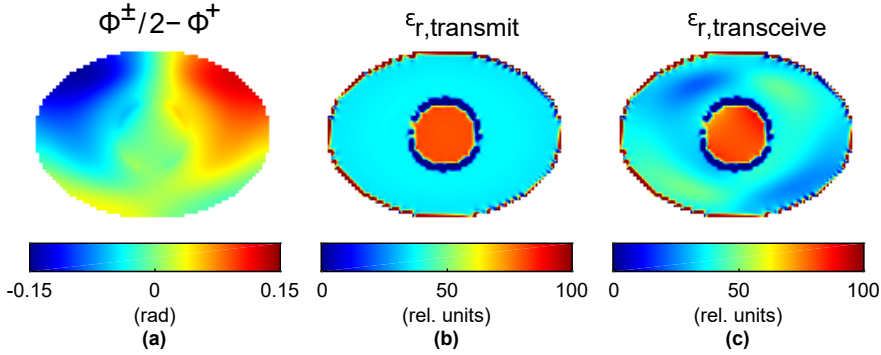


Figure 3.4. Effect of the transceive phase assumption on the permittivity, for the phantom case. (a) Transceive phase error map, calculated as the difference between half of the transceive phase, $\phi^\pm/2$, and the transmit phase ϕ^+ ; (b) permittivity map reconstructed with the transmit phase; (c) permittivity map reconstructed with the transceive phase. An anti-symmetric pattern appears in the permittivity when the transceive phase assumption is used. In (b) and (c) the input B_1^+ amplitude map was used.

3.3.2 Measurement results

Figure 3.5 presents the measurement results in the phantom for all B_1^+ methods. First, the SNR_1 , i.e. the SNR of the first image (the highest in magnitude between the two signals) is shown. Second, the measured B_1^+ map is reported. Overall, each technique showed similar B_1^+ spatial distributions. Comparing B_1^+ maps from AFI and DREAM with respect to BS-based B_1^+ map resulted into differences of $< \pm 0.15$ rel. units, similar to the accuracy found in simulations (not shown). Third, maps for the std in B_1^+ ($\zeta_{B_1^+}$) are shown, which were calculated from measured data as described in Appendix 3.A. Despite its lowest SNR_1 , DREAM introduced the smallest $\zeta_{B_1^+}$ in the inner compartment (average $\zeta_{B_1^+} = 4.3 \cdot 10^{-3}$ rel. units). BS had a slightly higher $\zeta_{B_1^+}$ ($5.9 \cdot 10^{-3}$ rel. units), and AFI had almost two-fold $\zeta_{B_1^+}$ ($1.1 \cdot 10^{-2}$ rel. units). In the outer compartment, the average $\zeta_{B_1^+}$ for DREAM was slightly lower than for AFI ($3.5 \cdot 10^{-3}$ vs $4.9 \cdot 10^{-3}$ rel. units), but higher than BS ($\zeta_{B_1^+} = 2.2 \cdot 10^{-3}$ rel. units). Finally, the corresponding permittivity maps are reported. Although affected by noise, BS- and DREAM-based permittivity maps displayed a bias pattern which resembles the permittivity reconstructions on simulated B_1^+ maps (Figure 3.3c): note, for instance, the rim of higher values and spurious fluctuations in the outer compartment periphery in DREAM-based permittivity. The measured permittivity mean values were, nonetheless, biased with respect to the values predicted with noisy simulations (~ 5 units in the outer compartment for all sequences, and $\sim 10, 2$, and 8 units for AFI, BS and DREAM respectively in the inner sphere). Also permittivity std values were offset. These offsets were likely caused by experimental factors that were not simulated, such as ringing and ghosting due to fluid motion as a result of gradient switching.

Figure 3.6 presents in vivo results, which can be compared to the phantom results. In terms of B_1^+ precision (Figure 3.6c), the phantom inner sphere and the bladder were alike: the std in B_1^+ (average $\zeta_{B_1^+} = 2.1 \cdot 10^{-2}$ rel. units) was considerably poorer in AFI than for the

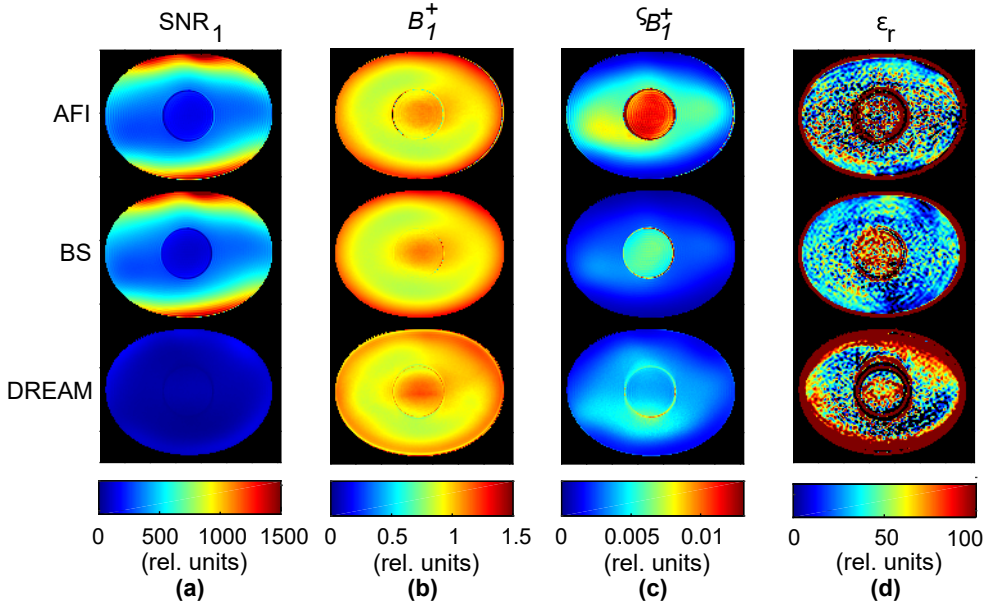


Figure 3.5. Phantom MR measurements. For each B_1^+ mapping technique (AFI: *top row*, BS: *centre row*, DREAM: *bottom row*) the following maps are reported: **(a)** SNR_1 , namely the SNR relative to the image I_1 ; **(b)** the B_1^+ field distribution. Values for the B_1^+ maps were normalized to the average value in the central slice; **(c)** the B_1^+ standard deviation $\zeta_{B_1^+}$, as calculated in Appendix 3.A; **(d)** the permittivity ϵ_r .

other two methods ($4.4 \cdot 10^{-3}$ and $5.1 \cdot 10^{-3}$ rel. units for BS and DREAM respectively). With respect to the outer compartment, on average slightly lower $\zeta_{B_1^+}$ values were measured in fat ($2.2 \cdot 10^{-3}$, $1.1 \cdot 10^{-3}$ and $4.0 \cdot 10^{-3}$ rel. units for AFI, BS and DREAM, respectively). Overall, the $\zeta_{B_1^+}$ averaged over the whole pelvis was $5.3 \cdot 10^{-3}$, $4.7 \cdot 10^{-3}$ and $5.1 \cdot 10^{-3}$ rel. units for AFI, BS and DREAM. On the other hand, the measured B_1^+ maps (Figure 3.6b) exhibited different types of disturbances than the phantom measurements. AFI B_1^+ map was hampered by bowel motion. DREAM B_1^+ map showed sharp transitions at tissue interfaces (e.g. hip bone/muscle). In BS B_1^+ map, ghosting due to the flowing blood in iliac vessels appeared between hip bone and bladder. As expected, these disturbances were enhanced by the derivative kernel used for EPT reconstruction and generally corrupted the permittivity distribution. Nevertheless, the posterior part in BS-based permittivity map was unaffected by the above-mentioned artifact. For the fat in that particular region, a permittivity of 5.3 ± 26.3 rel. units (mean \pm std) was calculated, by excluding EPT boundary errors. The average value found was close to the literature value (5.9 rel.units [10]).

Precision In Figure 3.7 the relationship between the SNR_1 and $\zeta_{B_1^+}$ is shown for the three sequences. In all cases, the simulated curves predicted the measured trends. The most favorable $\zeta_{B_1^+}$ - SNR_1 curve was found for DREAM, i.e. high B_1^+ precision was achieved for a relatively low image SNR. Note, however, that the measured SNR_1 range for DREAM was rather limited (measured max $\text{SNR}_1 < 350$) in comparison to the SNR_1 obtained with AFI and

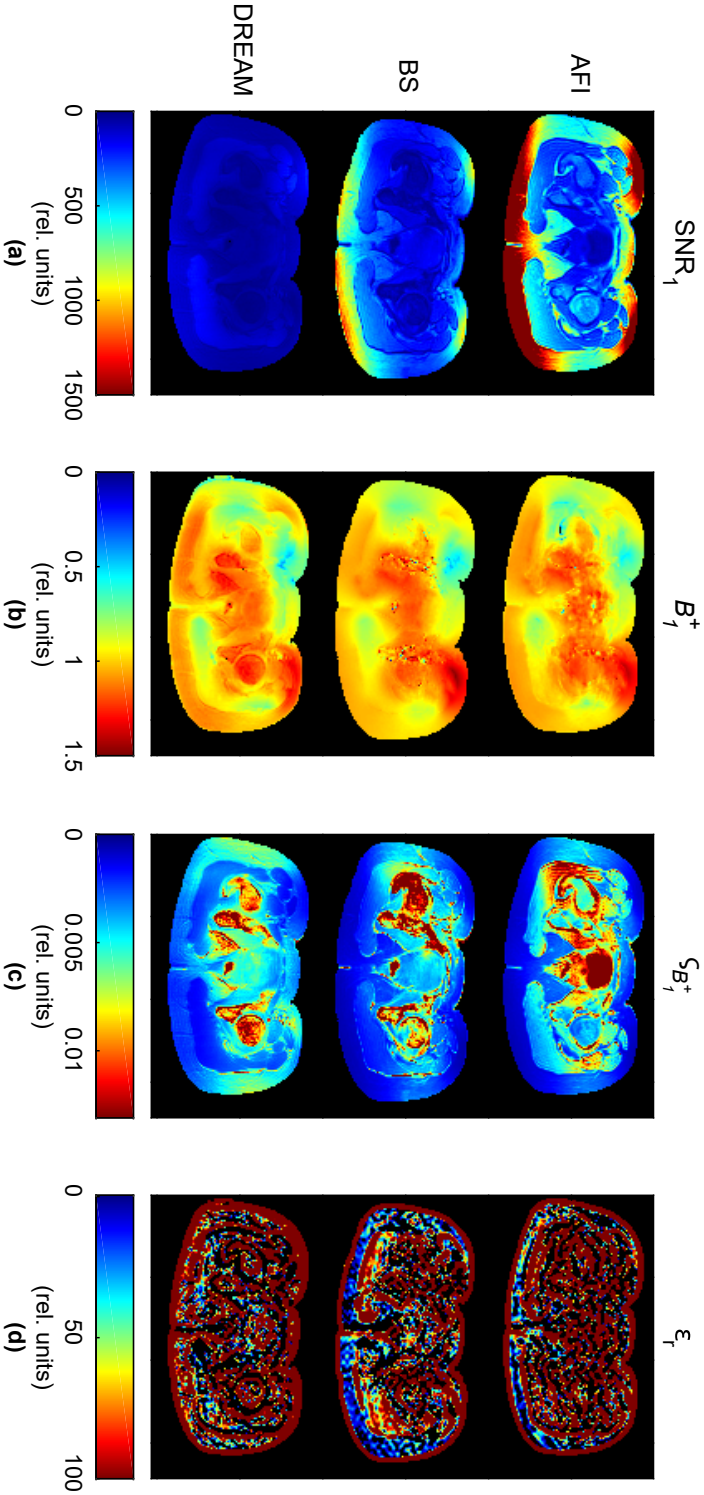


Figure 3.6. In vivo MR measurements on a female pelvis. For each B_1^+ mapping technique (AFI: top row, BS: centre row, DREAM: bottom row) the following maps are reported: (a) SNR_1 , namely the SNR relative to the image I_1 ; (b) the B_1^+ field distribution. Values for the B_1^+ maps were normalized to the average value in the central slice; (c) the B_1^+ standard deviation $S_{B_1^+}$, as calculated in Appendix 3.A; (d) the permittivity ϵ_r .

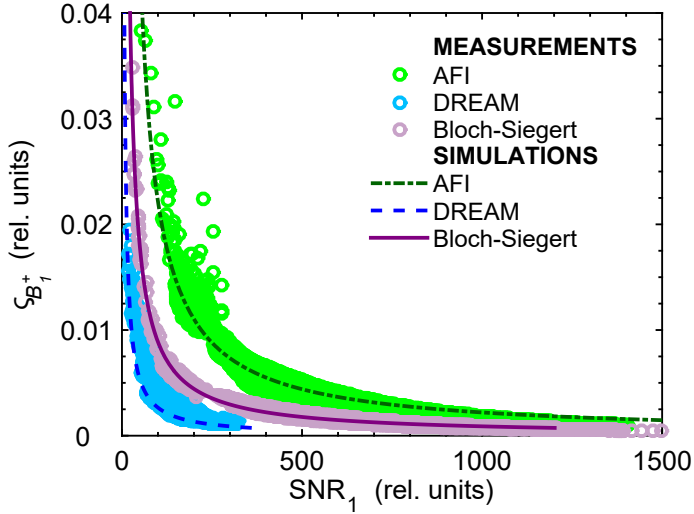


Figure 3.7. $\zeta_{B_1^+}$ as a function of SNR_1 , the SNR of the 1st image (I_1) for each technique, plotted for the central slice. The circles and lines represent the measured and the simulated data, respectively. In simulations, different maps for SNR_1 and $\zeta_{B_1^+}$, corresponding to different levels of ζ_{noise} , were generated. For each ζ_{noise} , SNR_1 and $\zeta_{B_1^+}$ maps were averaged inside the phantom. The simulated trends shown in this figure are the result of the averaging operation. In the measured data, the voxels related to the plastic borders of both compartments were excluded. The simulated curves predicted well the behaviour found in measurements.

BS (measured max $\text{SNR}_1 > 1000$). Figure 3.7 also displays the asymptotic behavior of $\zeta_{B_1^+}$, which implies that large jumps of image SNR would be necessary for rather small gains in B_1^+ precision.

Figure 3.8 illustrates our phantom experimental findings on the relationship between the B_1^+ precision and permittivity precision. Also shown is the relationship for the EPT kernel employed in this study, as theorized by Lee et al. [88]. We found that BS achieved the smallest ζ_{ϵ_r} in both compartments (22.4 and 47.6 rel. units in the inner and outer compartment, respectively) and that AFI-derived permittivity had the greatest ζ_{ϵ_r} values (103.0 and 31.8 rel. units in the inner and outer compartments, respectively). Regarding DREAM, ζ_{ϵ_r} was biased by the distorted permittivity distribution caused by sequence-related inaccuracies affecting the B_1^+ map. Overall, our results agreed well with Lee's theoretical model. Note that experimental factors, as mentioned earlier, might have slightly biased ζ_{ϵ_r} values. Nonetheless, it is worth noticing that deviations of the same order of magnitude from the theoretical model were reported in [88] for an analytical complex B_1^+ map (i.e. no sequence dependence, transceive phase assumption and experimental factors).

3.4 Discussion

We investigated, for the first time, the impact of B_1^+ acquisition on permittivity mapping. To this end, we designed a framework to predict and validate the sensitivity of the permittivity reconstruction to the sequence-specific accuracy and precision effectively achieved by the B_1^+

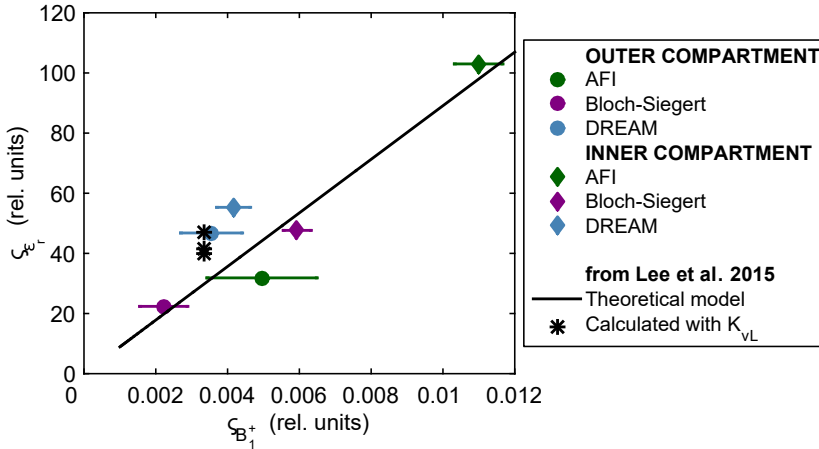


Figure 3.8. Experimental relationship between $\zeta_{B_1^+}$ and ζ_{ϵ_r} . Both $\zeta_{B_1^+}$ and ζ_{ϵ_r} were evaluated in two manually delineated ROIs matching the phantom inner and outer compartments. For $\zeta_{B_1^+}$ the average value is displayed. The horizontal bars indicate the spread (std) of the $\zeta_{B_1^+}$ in both ROIs. The black line represents the theoretical model [88] relating ζ_{ϵ_r} and $\zeta_{B_1^+}$ for the noise-robust kernel K_{vL} (Equation 18 in ref. [88], where $N_{tot} = 117$, $L = \sqrt{67}$, $G = 290.2$ and $\zeta_{B_1^+} \approx 1/\text{SNR}_{B_1^+}$). The black asterisks refer to the std values of the permittivity calculated by Lee et al. [88] inside three ROIs, for a simulated phantom B_1^+ map with fictitious $\text{SNR}_{B_1^+} = 300$.

amplitude map at 3T. Moreover, we compared the accuracy and precision of Helmholtz-based permittivity maps reconstructed on B_1^+ maps measured with AFI, Bloch-Siebert (bs) and DREAM sequences. According to our definition, accuracy was associated with imperfections specific to the employed sequence whereas precision (inverse of variance) was related to noise propagation. Our analysis demonstrated how the permittivity reconstruction is influenced by the sequence-specific error and noise propagation in the $|B_1^+|$ depending on which B_1^+ mapping sequence is used. More generally, we found that Helmholtz-based permittivity is extremely sensitive to both bias and noise in the B_1^+ map.

Regarding the accuracy, bs-based and AFI-based permittivity maps were comparably accurate in our phantom (Figures 3.3, 3.5 and Table 3.3). The B_1^+ maps from which these permittivity maps were reconstructed were also comparably accurate, which is in line with other studies [77,78,184]. The DREAM-based permittivity, instead, deviated from the expected permittivity distribution because of inaccuracies in the B_1^+ map, which were larger at compartment interfaces. In vivo, permittivity maps were corrupted by under- and over-shooting errors (also called “boundary errors”) arising in correspondence of discontinuities in the B_1^+ distribution (Figure 3.6). These discontinuities manifested evidently at tissue interfaces in DREAM B_1^+ map and were likely caused by imperfect T_1 or T_2 decay of the stimulated echo [72,189]. Analogously, in vivo bs B_1^+ distributions were disturbed by ghosting artifacts due to sensitivity to flow, as a result of its “phase-based” B_1^+ encoding mechanism [74].

Considering the precision, we found that the permittivity std (ζ_{ϵ_r}) differed when the permittivity was derived from different B_1^+ sequences. For the most commonly used AFI technique, for example, the permittivity std was 1.5-2 times greater than for bs (Figure 3.8 and Table 3.3).

Note that, on average, the underlying std in B_1^+ ($\zeta_{B_1^+} \approx \text{SNR}_{B_1^+}^{-1}$) for AFI was double the std in B_1^+ for BS. Similar findings on B_1^+ precision of AFI and BS were reported in [78, 190]. Although permittivity precision in the pelvis was not estimated because of the aforementioned boundary errors disturbing the permittivity map, the B_1^+ precision trends found in the phantom were also observed in the female pelvis, particularly in bladder, uterus and fat (Figure 3.6). Thus, we expect the in vivo permittivity precision to be in the same order of magnitude as the phantom permittivity precision, because the noise propagation from the B_1^+ to Helmholtz-based permittivity is linear, as theoretically demonstrated by Lee et al. [88]. Furthermore, by comparing the precision of the three sequences, our results experimentally validated Lee’s theoretical model for the noise propagation from the B_1^+ to the permittivity (Figure 3.8).

Overall, extremely small errors in the B_1^+ map created considerable deviations in the permittivity distribution reconstructed with Helmholtz-based EPT. For example, BS results in the outer compartment showed that a less than 1% deviation in accuracy (or bias) in the simulated B_1^+ map (Figure 3.3b) resulted in 20% relative bias in the permittivity (Figure 3.3d) and that a $\zeta_{B_1^+} = 2.0 \cdot 10^{-3}$ rel. units, i.e. 0.2% of the average measured B_1^+ , led to $\zeta_{\epsilon_r} = 22.4$ rel. units (Figure 3.8). In the pelvis, the std in B_1^+ measured on average 0.5% at 3T for all the sequences, with values as low as 0.1% in fat for BS and peaks higher than 2% in the bladder for AFI (Figure 3.6d). All these values, nevertheless, were far from the B_1^+ precision required to achieve $\zeta_{\epsilon_r} = 5$ units ($\zeta_{B_1^+} \approx 0.05\%$, (Figure 3.8), which we deem a considerable improvement for the permittivity precision, in relation to the range of tissue permittivity (i.e. $20 \leq \epsilon_r \leq 85$ rel. units for the majority of tissues at 128 MHz, except fat; see e.g. [3, 10, 20, 27]). Such a low std in B_1^+ would be reached only for image $\text{SNR}_1 \geq 2500, 1500$ and 500 rel. units for AFI, BS and DREAM, respectively (Figure 3.7), but these SNRs were not achieved in our experimental setup (pelvis FOV in 5 minutes at 3T). Hence, we deduce that a Helmholtz-based approach cannot reconstruct precise permittivity maps for the B_1^+ precision clinically achieved by three commonly available sequences (at 3T for scan times ≤ 5 minutes).

Investigating more noise-robust solutions for permittivity mapping was beyond the scope of this study, but brain permittivity maps with superior quality were shown at 7T for Helmholtz-based EPT [89] and gradient-based EPT combined with multi-channel systems [93]. Higher fields strengths, in fact, benefit permittivity mapping not only for the intrinsic SNR gain but also because the imprint of the displacement currents on the B_1^+ is stronger [88, 89]. Moreover, improved permittivity results have very recently been reported by using newly-formulated EPT reconstruction methods on B_1^+ maps from EM simulations. For example, using a quasi-Newton approach, Rahimov et al. have shown a permittivity precision of $\sim 20\%$ in the brain [113]. In Guo et al. the std in permittivity, converted from the reported interquartile ranges according to the procedure in [191], was ~ 8 rel. units in white and gray matters, and ~ 17 rel. units in cerebrospinal fluid [115]. In both studies, the simulated B_1^+ was directly corrupted with a noise level $\zeta_{B_1^+} = 3.1 \cdot 10^{-3}$ (i.e. $\text{SNR}_{B_1^+} = 316$). Provided that these results are experimentally corroborated, using such less noise-sensitive EPT reconstruction methods or denoising techniques [92] could be preferred when precise permittivity maps obtained with clinical MR scanners (1.5 or 3T) are desired.

Our findings on the accuracy also revealed that the slight perturbations of the B_1^+ field resulting from realistic permittivity variations (already studied in e.g. [47, 192]) can be in the same order of magnitude as the sequence-specific errors in the B_1^+ maps. Thus, although the severity of these errors on the permittivity accuracy may vary depending on the chosen reconstruction technique and on the imaged body geometry, we conclude that using only

electromagnetic simulations of the B_1^+ field is insufficient to fully investigate the accuracy of a permittivity reconstruction.

Despite the fact that our in vivo permittivity maps did not provide reliable quantitative estimates, we remark that we pragmatically tackled the unprecedented problem of assessing to what extent the B_1^+ acquisition influences the permittivity reconstruction. In light of all our results, we cannot give definitive solutions but we can propose several directions for improvement, ranging from recommendations on sequence selection for permittivity mapping to suggestions on how to fully assess the quality of the reconstructed permittivity map. BS and AFI techniques should be preferred over DREAM for clinical applications where accurate permittivity estimates are of utmost importance, as is the case of hyperthermia treatment planning [174]. Strategies to mitigate some sequence-specific imperfections contaminating in vivo B_1^+ and permittivity distributions were beyond the scope of this study, but are worthy of further investigation (e.g. using flow compensation for BS or acceleration techniques to reduce motion artifacts for AFI). Alternatively, when precise reconstruction of the permittivity of certain tissues is desired, for example for tissue contrast visualization purposes, bear in mind that DREAM or BS had more favorable “ B_1^+ precision-to-image SNR” performance than AFI. This recommendation is also valid when EPT algorithms prone to noise amplification (e.g. derivative-based methods) are employed for permittivity reconstruction. Besides, if shorter scan durations are intended, then DREAM could allow the greatest time reduction (of ~ 3 min for our FOV), due to a higher flexibility in parameter settings; however, this might come at a cost of accuracy (e.g. by decreasing the shot interval length [189]) and loss of precision (e.g. by reducing the number of averages). More generally, to validate or predict the permittivity accuracy obtained with any new reconstruction method, or even to train a neural network [121], we recommend taking the used B_1^+ mapping technique into account, for example by running Bloch simulations emulating the sequence, in addition to electromagnetic simulations of the B_1^+ field. Likewise, in order to predict or validate the method performance under clinically realistic noise levels valid for the majority of body tissues, we advise testing newly-developed reconstruction methods against noise levels between 0.5–2.5% of the average B_1^+ (i.e. $40 \leq \text{SNR}_{B_1^+} \leq 200$).

3.5 Conclusion

In conclusion, the merit of our work is to provide a methodology to assess the sensitivity of permittivity reconstruction to bias and noise in B_1^+ maps. Despite addressing only one reconstruction method and three B_1^+ mapping sequences, we emphasize that our framework, outlined in Figure 3.1, is reproducible for any type of B_1^+ mapping sequence (but also phase mapping sequence, if conductivity were of interest) and EPT reconstruction algorithm. By using this framework, two major findings were obtained. Firstly, the B_1^+ mapping sequence affects the accuracy and precision of the permittivity reconstruction according to the sequence-specific error propagation determined by its B_1^+ encoding mechanism. This implies that attention should be paid to select the most appropriate B_1^+ mapping sequence in relation to the accuracy and precision desired in the final permittivity map. Secondly, the B_1^+ precision achieved by commonly available B_1^+ mapping techniques was below the precision needed to decrease the permittivity standard deviation to only 5–10 units, which means that the extreme sensitivity of Helmholtz-based EPT to noise perturbations, together with boundary errors, renders permittivity reconstruction not feasible at 3T in clinically acceptable times.

3.A Appendix: Derivation of error propagation (precision) in the B_1^+ , $\zeta_{B_1^+}$

In each examined B_1^+ technique, two images, I_1 and I_2 , are acquired. Their magnitude/phase representation is $I_1 = S_1 \cdot \exp(i \cdot \theta_1)$ and $I_2 = S_2 \cdot \exp(i \cdot \theta_2)$. Either the amplitudes or the phases of such images are then combined to form a B_1^+ map according to a sequence-specific function $f(x_1, x_2)$ where x_1 and x_2 are the input data (either magnitude or phase, depending on the mapping technique). In this section, a short summary and the sequence-specific function $f(x_1, x_2)$ are presented for each technique. Next, as a measure for precision, the std in the B_1^+ amplitude, $\zeta_{B_1^+}$, for all the three methods is derived by applying the law of error propagation [187]:

$$\zeta_{B_1^+} = \sqrt{\left(\frac{\partial B_1^+}{\partial x_1}\right)^2 \cdot \zeta_{x_1}^2 + \left(\frac{\partial B_1^+}{\partial x_2}\right)^2 \cdot \zeta_{x_2}^2} \quad (3A.1)$$

Where ζ_{x_1} and ζ_{x_2} are the standard deviations of the noise corresponding to, respectively, the signals x_1 and x_2 .

Note that in the following expressions the B_1^+ represents the (dimensionless) spatial modulation of the transmit field, $B_1^+(\mathbf{r})$. Also known in literature as *transmit sensitivity*, $B_1^+(\mathbf{r})$ corresponds to the absolute B_1^+ field (in Tesla) normalized by the nominal B_1^+ value in Tesla.

3.A.1 AFI

The AFI technique is a steady-state spoiled gradient-echo sequence with two interleaved repetition times TR_1 and TR_2 after an imaging pulse with constant nominal tip angle α_{nom} . Two images are acquired in each TR interval. Under the assumptions of perfect spoiling and repetition times shorter than T_1 , the ratio of the magnitude images is related to the transmit field as follows [68]:

$$B_{1,AFI}^+(\mathbf{r}) = \frac{1}{\alpha_{nom}} \cdot \arccos\left(\frac{n \frac{S_2(\mathbf{r})}{S_1(\mathbf{r})} - 1}{n - \frac{S_2(\mathbf{r})}{S_1(\mathbf{r})}}\right) \quad (3A.2)$$

where $n = TR_1/TR_2$. Note that $x_1 = S_1$ and $x_2 = S_2$.

The expression for the B_1^+ std, $\zeta_{B_1^+}$, is:

$$\zeta_{B_{1,AFI}^+} = \sqrt{\frac{1}{\alpha_{nom}^2} \cdot \frac{n^2 - 1}{(S_1^2 - S_2^2)(nS_1 - S_2)^2} \cdot (S_2^2 \cdot \zeta_{S_1}^2 + S_1^2 \cdot \zeta_{S_2}^2)} \quad (3A.3)$$

where ζ_{S_i} is the std of the noise in the magnitude data. Note that this quantity is related to the SNR as $\zeta_{S_i} = \frac{S_i}{SNR_i}$, for $i = 1, 2$.

3.A.2 BLOCH-SIEGERT SHIFT (BS)

The BS technique is a steady-state spoiled gradient echo sequence with an off-resonance pulse (in this case a Fermi pulse) inserted between the excitation and acquisition. The off-resonance pulse induces a B_1 -dependent frequency shift which is translated into a phase shift in the

3. ε_r mapping at 3T: impact of three B_1^+ mapping techniques

image. Acquiring two signals with opposite offset frequencies and subtracting their phase images leads to a phase shift difference that is related to the B_1^+ amplitude [74], as expressed below:

$$B_{1,BS}^+(\mathbf{r}) = \frac{1}{A_{peak,Fermi}} \cdot \sqrt{\frac{\theta_1(\mathbf{r}) - \theta_2(\mathbf{r})}{2 \cdot K_{BS}}} \quad (3A.4)$$

with $x_1 = \theta_1$ and $x_2 = \theta_2$. $A_{peak,Fermi}$ is the Fermi pulse peak value. K_{BS} is a pulse-related constant that depends on the pulse waveform $B_{1,normalized}(t)$, its duration T_{Fermi} and its offset frequency ω_{Fermi} , as in Equation 3A.5:

$$K_{BS} = \int_0^{T_{Fermi}} \frac{(\gamma \cdot B_{1,normalized}(t))^2}{2\omega_{Fermi}} \quad (3A.5)$$

The std $\varsigma_{B_1^+}$ for BS is expressed by:

$$\varsigma_{B_{1,BS}^+} = \sqrt{\frac{1}{8 \cdot (A_{peak,Fermi})^2} \cdot \frac{\varsigma_{\theta_1}^2 + \varsigma_{\theta_2}^2}{K_{BS} \cdot (\theta_1 - \theta_2)}} \quad (3A.6)$$

where ς_{θ_i} is the std of the phase data θ_i , and is related to the image SNR by formula 15.84 in Haacke et al. [39], i.e. $\varsigma_{\theta_i} = \text{SNR}^{-1}$ (radians), for $i = 1, 2$.

Note that Equation 3A.6 coincides with Equation 20 of reference [78] if $A_{peak,Fermi}$ is replaced by the expression of a (fictitious) block pulse with nominal flip angle α_{nom} , peak value $A_{peak,Fermi}$ and duration τ .

3.A.3 DREAM

In DREAM, a STEAM sequence [193] is utilized to encode the B_1^+ information. The STEAM segment serves as a magnetization-preparation before an imaging step composed by a train of RF pulses (also called shot) with gradient echo readout. A stimulated echo and a free-induction decay signals are acquired quasi-simultaneously in a single acquisition. The ratio of their magnitudes ($x_1 = S_1$ and $x_2 = S_2$) is related to B_1^+ as indicated below [72]:

$$B_{1,DREAM}^+(\mathbf{r}) = \frac{1}{\alpha_{nom}} \cdot \arctan \left(\sqrt{\frac{2 \cdot S_1(\mathbf{r})}{S_2(\mathbf{r})}} \right) \quad (3A.7)$$

Note that $x_1 = S_1$ and $x_2 = S_2$. Applying Equation 3A.1 for DREAM yields the following $\varsigma_{B_1^+}$ expression:

$$\varsigma_{B_{1,DREAM}^+} = \sqrt{\frac{1}{\alpha_{nom}^2} \cdot \frac{1}{2 \cdot (2S_1 - S_2)^2} \cdot \left(\frac{S_2}{S_1} \cdot \varsigma_{S_1}^2 + \frac{S_1}{S_2} \cdot \varsigma_{S_2}^2 \right)} \quad (3A.8)$$

where ς_{S_i} is the std of the noise in the magnitude data and is related to the image SNR as $\varsigma_{S_i} = \frac{S_i}{\text{SNR}_i}$, for $i = 1, 2$.

Deep learning-based reconstruction of in vivo pelvis conductivity with a 3D patch-based CNN trained on simulated MR data

Soraya Gavazzi, Cornelis A.T. van den Berg, Mark H.F. Savenije, H. Petra Kok, Peter de Boer, Lukas J.A. Stalpers, Jan J.W. Legendijk, Hans Crezee, Astrid L.H.M.W. van Lier

published in:

Magnetic Resonance in Medicine 2020; 84(5):2772-2787, DOI:10.1002/MRM.28285

ABSTRACT

Purpose: To demonstrate that pelvis conductivity mapping at 3T with deep learning (DL) is feasible.

Methods: 210 dielectric pelvic models were generated based on CT scans of 42 cervical cancer patients. For all dielectric models, electromagnetic and MR simulations with realistic accuracy and precision were performed to obtain $|B_1^+|$ and transceive phase (ϕ^\pm). Simulated $|B_1^+|$ and ϕ^\pm served as input to a 3D patch-based convolutional neural network (CNN), which was trained in a supervised fashion to retrieve the conductivity. The same network architecture was retrained using only ϕ^\pm in input. Both network configurations were tested on simulated MR data and their conductivity reconstruction accuracy and precision were assessed. Furthermore, both network configurations were used to reconstruct conductivity maps from a healthy volunteer and two cervical cancer patients. DL-based conductivity was compared in vivo and in silico to Helmholtz-based (H-EPT) conductivity.

Results: Conductivity maps obtained from both network configurations were comparable. Accuracy was assessed by mean error (ME) with respect to ground truth conductivity. On average, $ME < 0.1 \text{ Sm}^{-1}$ for all tissues. Maximum MEs were 0.2 Sm^{-1} for muscle and tumour, and 0.4 Sm^{-1} for bladder. Precision was indicated with the difference between 90th and 10th conductivity percentiles, and was below 0.1 Sm^{-1} for fat, bone and muscle, 0.2 Sm^{-1} for tumour and 0.3 Sm^{-1} for bladder. In vivo, DL-based conductivity had median values in agreement with literature and H-EPT values, and higher precision than H-EPT.

Conclusion: Anatomically-detailed, noise-robust and relatively accurate conductivity maps were reconstructed in the pelvis with DL.

4.1 Introduction

The omnipresence of electromagnetic (EM) technologies in telecommunication and medical applications has increasingly stimulated research on the electrical properties (EPs) of the human body. Electrical properties (permittivity and conductivity) regulate the interaction between EM fields and human tissues. Accurate dielectric models of the human body are crucial in EM dosimetry [194–196] (e.g. for safety purposes in telecommunication and MR scanning) and in treatment planning for therapeutic heating of cancer [174,197]. At RF frequencies, these properties reflect tissue water content and ionic concentration [3,20] and have been shown to change between healthy and pathologic tissues [9,13,14,17,198], suggesting potential use as a biomarker.

The majority of these EP studies and current computational dielectric models are based on ex vivo EP measurements [10]. However, differences between ex vivo and in vivo EPs were reported [14,179]. Hence, non-invasive techniques for patient-specific EP detection were developed [33,54,57]. One such technique, termed “MR Electrical Properties Tomography” (EPT), measures in vivo EPs at the Larmor frequency of the MR system (e.g. at 128 MHz for a 3T MR scanner). EPT exploits the fact that a subject’s EPs perturb the spatial distribution of the transverse magnetic field produced by the RF coil system for spin excitation, the B_1^+ field. The B_1^+ field is measurable with MR sequences. Therefore, tissue EPs can be reconstructed from B_1^+ measurements [54,57,58].

EPT reconstruction algorithms to disentangle EPs from B_1^+ field measurements include physics-based direct and inverse methods, and learning-based techniques. Direct methods retrieve EPs by applying Maxwell’s equations to the measured B_1^+ field [57,58]. Second order spatial derivatives in these equations are typically computed as finite difference kernels, which are convolved with B_1^+ maps. Despite this straightforward implementation, the differentiation operation - normally a Laplacian kernel - is extremely sensitive to noise in measured B_1^+ fields and introduces numerical errors at physical tissue interfaces and/or acquisition artefacts [57,58,88]. Moreover, several direct EPT methods rely on piece-wise constant EPs and transceive phase assumptions [57–59]. Denoising strategies, e.g. [92,94,95], were proposed and magnitude-driven bilateral filters [81,94] or reformulations of full Helmholtz equation [91,93] were used to reduce boundary errors. Direct EPT techniques were employed in recent clinical studies evaluating the potential value of EPT-based conductivity in discriminating tumours [127,129] and in hyperthermia treatment planning [131]. Reconstructing good quality permittivity maps with clinical scanners and within acceptable times remains challenging: the necessary high precision requirements [88] are unmet with standard B_1^+ mapping techniques [199].

Inverse approaches reconstruct EPs by iteratively minimizing a cost function comparing the true B_1^+ with a modelled B_1^+ field [109,113,116–118]. These reconstruction techniques bypass the assumption of piece-wise constant properties, reduce boundary errors and mitigate noise impact on EP maps by avoiding differentiation on measured data. Their challenges are represented by accurate modelling of 3D incident magnetic and electric fields and high computational cost, e.g. to update the contrast source in CSI-EPT [109]. Promising reconstructions with inverse approaches were shown on simulated data, but no study to date has reported in vivo EP maps reconstructed with these techniques.

Learning-based methods, namely dictionary-based EPT [120] and deep learning EPT (DL-EPT), infer EPs from large datasets of B_1^+ fields and their corresponding EPs via machine/deep learning. The basic idea of DL-EPT, for example, is to train a convolutional neural network (CNN) to learn the mapping relation between B_1^+ and EPs. Typically, the CNN is trained in a

supervised fashion with multiple B_1^+ data and their corresponding EP distributions as input. So far, CNNs were trained on image [121] or local [122] level based on directly accessible MR quantities (B_1^+ amplitude, $|B_1^+|$ and/or transceive phase, ϕ^\pm) from simulations [121] or in vivo measurements [122]. When tested in brain at 3T, the trained network produced conductivity [121, 122] and permittivity [121] maps with higher precision than in direct EPT maps. Nonetheless, an additional anatomical input (e.g. an MR magnitude image) was required besides the B_1^+ map for accurate EP reconstruction in [121]. In Hampe et al. [122] the reliability of conductivity reconstruction in diverse brain geometries was strongly limited by the lack of large representative datasets for training.

Building on the challenges of previous DL-EPT works, we introduce new methodological aspects for DL-based conductivity mapping at 3T. Our DL-EPT method employs a novel 3D patch-based CNN which was trained exclusively on simulated B_1 fields with realistic accuracy and precision. Realistic accuracy and precision in B_1 fields were reproduced by implementing the framework developed in our previous study [199] which combines EM and MR simulations. This enables training on realistic measurable datasets for which ground truth EPs are available, and stands as a valid alternative to training on in vivo MR measurements for which the true EP values are not available. In this study, we consider DL-EPT for female pelvic anatomies with and without cervical cancer, because patient-specific conductivity maps in this region would be relevant for hyperthermia treatment planning of cervical cancer patients. Thus, the training dataset comprised in silico B_1^+ fields of diversified human pelvic models. These pelvic models were derived from segmentation of CT scans of cervical cancer patients who underwent hyperthermia treatment and possessed realistic tissue EPs variations at 128 MHz, including EPs of both healthy and malignant cervical tissues. By examining two network configurations, i.e. using complex B_1 data ($|B_1^+|$ and ϕ^\pm) or only transceive phase information as input, we assess the conductivity reconstruction accuracy and precision of the proposed method in silico. We also discuss its performance regarding typical challenges for pelvis conductivity mapping: (i) greater size, which limits the validity of transceive phase assumption already at 3T [97]; (ii) high degree of anatomical variations (e.g. bladder filling, different inter-patient organ positions, inter-patient variation in body mass index); (iii) organ motion (bowel peristalsis and breathing); (iv) low SNR. Finally, we show DL-based in vivo conductivity maps and compare them to the status-quo EPT method for pelvis, i.e. Helmholtz-based EPT.

4.2 Methods

4.2.1 Database construction

Human pelvic models Forty-two human models were built from CT scans of 42 cervical cancer patients who had undergone hyperthermia treatments. Patients' CT scans were semi-automatically segmented based on Hounsfield unit intensity with an in-house developed software [175], resulting into fat, muscle, bone, and air segmentations. Tumour and bladder were manually segmented for all pelvic models by a radiation oncologist.

Construction of dielectric models Tissue-specific uniform distributions of realistic conductivity, σ , and permittivity, ϵ_r , values at 128 MHz (see Table 4.1) were defined for each tissue as explained in Appendix 4.A. Then, a total of 210 dielectrically different human models were generated out of the 42 anatomically segmented models. For every anatomy, 5 different combinations of piece-wise constant conductivity and permittivity were randomly assigned to each segmented tissue from the predefined tissue-specific EP uniform distributions.

Table 4.1. Electrical properties and relaxation times of tissues in pelvic models. Minimum and maximum values for the uniform distributions of both conductivity and permittivity are reported. T_1 and T_2 values assigned as input to MR simulations are listed as well. T_1 and T_2 values were taken from the following references: [201] for fat, bone and tumour; [22] for muscle; [202] for bladder.

Segmented tissue	Tissue in dielectric model	σ (Sm^{-1}) [min, max]	ϵ_r (rel. units) [min, max]	T_1 (ms)	T_2 (ms)
Air	Air	0	1	20	1
Fat	Fat	[0.04, 0.08]	[5.92, 8.89]	382	68
Muscle					
Metal clips*					
Plastic catheter*	Muscle	[0.73, 1.07]	[49.77, 73.21]	1233	37.2
Empty bladder					
Full bladder	Bladder content	[1.35, 2.60]	[69.60, 72.62]	2400	100
Bone	Cancellous	[0.14, 0.18]	[21.03, 26.28]	586	49
	Cortical	[0.07, 0.08]	[14.72, 17.66]	586	49
Tumour	Tumour	[0.66, 1.45]	[37.35, 82.34]	1616	83

* Non-biological materials (metal clips and plastic catheters), present during CT scan session in some cervical cancer patients and manually segmented in the corresponding pelvic model, were considered dielectrically equivalent to muscle, because their segmentations were physically surrounded by muscle. These non-biological materials are typically absent in human body.

To represent both healthy subjects and cancer patients in our dataset, one out of five tumour EP permutations was enforced to have muscle EPs for every anatomical model. Both empty and full bladder cases were included in the dataset. Empty bladders (present in 70/210 dielectric models) were given muscle EPs, as commonly adopted in hyperthermia treatment planning studies [131,200]. Full bladders were assigned bladder content EPs [102]. Figure 4.1 illustrates the final EP distributions for each tissue in our complete dataset.

EM simulations EM simulations with realistic MR setup and patient positioning were performed in Sim4Life (v3.4, ZTM AG, Zurich, Switzerland) for all 210 dielectric models. First, a 3T birdcage coil (bore diameter = 70 cm) was modelled and tuned at 128 MHz. Subsequently, each dielectric model was positioned inside the birdcage coil such that the cervix/tumour location was axially centred with the isocenter. Furthermore, the model's back was 13.5 cm distant from the isocenter, to mimic a patient lying on the MR table. A $2.5 \times 2.5 \times 2.5 \text{ mm}^3$ mesh-grid was enforced within a volume of $550 \times 360 \times 260 \text{ mm}^3$ centred at the isocenter. This volume was chosen based on the models with largest dimensions, such that it contained the anatomy between L3-4 vertebra to the perineum for each model. Outside this volume, the rest of the human model and the body coil were voxelized with a default resolution. Two FDTD simulations, i.e. in quadrature and anti-quadrature modes, were run per dielectric model ($15.755 \cdot 10^6$ cells) on a GPU (NVIDIA Titan X Pascal, 12 GB RAM) to calculate both transmit, B_1^+ , and receive, B_1^- , fields [43]. From these complex fields, B_1^+ amplitude, $|B_1^{+,em}|$, and transceive phase, $\phi^{\pm,em}$, were retrieved for all 210 dielectric models. $|B_1^{+,em}|$ was normalized to its mean value in the central slice. The total simulation time per model was 3.25 hours.

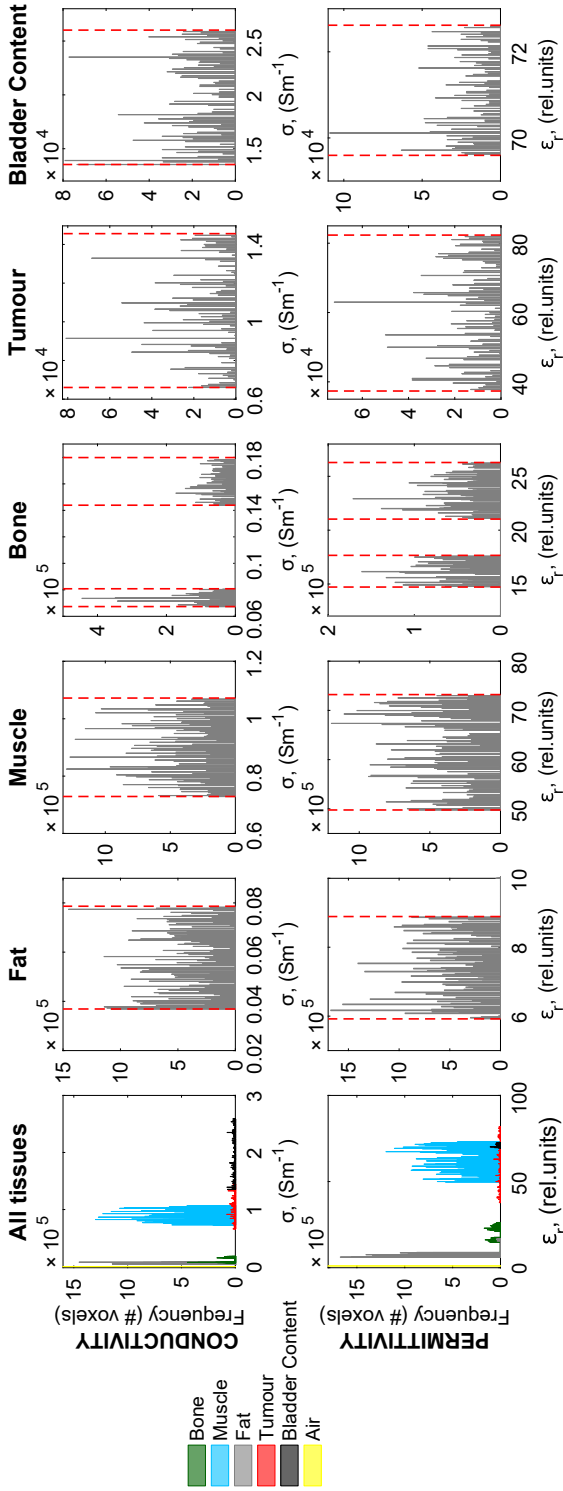


Figure 4.1. Final distribution of both conductivity (*top row*) and permittivity (*bottom row*) for all pelvic tissues in the complete dataset, after EPs were randomly assigned to all 210 dielectric pelvic models. Tissue-specific conductivity and permittivity distributions are displayed together in “All tissues” (*first column*), and separately in the remaining columns. Red dashed lines represent EP limits (maximum and minimum of uniform distribution, also reported in Table 4.1) imposed a priori for every tissue. Note that the resulting EP distributions for muscle and fat were higher than for bone, tumour and bladder content, because of their higher number of voxels and presence in pelvic models.

MR simulations MR simulations emulating $|B_1^+|$ and ϕ^\pm acquisitions used in MR experiments were run as described in Chapter 3 [199] to account for sequence-specific accuracy and precision. We implemented AFI [68] and SE sequences in a Bloch simulator adopting experimental MR parameters (see MR experiments) and using T_1, T_2 (Table 4.1), $|B_1^{+,em}|$ and $\phi^{\pm,em}$ as inputs. In AFI, the nominal flip angle was scaled by $|B_1^{+,em}|$. In SE, $\phi^{\pm,em}$ was applied as a phase shift to the RF pulses. Spatial encoding gradients were not included. MR signals were computed voxel-wise at TE . For both AFI and SE, the resulting noiseless MR signals were used to retrieve noiseless $|B_1^{+,mr}|$ and $\phi^{\pm,mr}$. $|B_1^{+,mr}|$ was calculated from AFI signals as described in Yarnick [68] and $\phi^{\pm,mr}$ corresponded to the phase of SE signal.

To mimic a realistic image precision, real and imaginary parts of AFI and SE noiseless signals were corrupted by realistic Gaussian noise levels, and subsequently used to reconstruct noisy $|B_1^{+,mr}|$ and $\phi^{\pm,mr}$ [199]. Realistic noise levels were chosen such that the simulated image SNR for both AFI and SE closely resembled experimental image SNRs obtained in the volunteer experiment for most tissues (see e.g. muscle, bladder and bone SNRs in Figure 4.2).

MR simulations were performed on dielectric models of dimensions $550 \times 360 \times 130 \text{ mm}^3$, which consisted of the pelvic region only. Such smaller axial dimension was based on the FOV used for MR experiments and was adopted to reduce the computational cost when training the network. Both AFI and SE simulations were run in Matlab (R2015a; The MathWorks, Inc., Natick, MA) on a workstation with Intel Xeon CPU E3-1220 v3 at 3.1 GHz and lasted in total 2 minutes per model.

4.2.2 MR experiments

A healthy volunteer and two cervical cancer patients were scanned on a 3T clinical MR scanner (Ingenia, Philips, The Netherlands) with a 28-channel torso coil for reception. Patient 1 was diagnosed with IIB squamous cell carcinoma. Patient 2 had IIA2 neuroendocrine cervical carcinoma. Our imaging protocol was approved by the local ethical committee and all subjects gave written informed consent. The $|B_1^+|$ was acquired with AFI sequence [68] (flip angle = 60° , $TE/TR_1/TR_2 = 2.5/30/210 \text{ ms}$). The transceive phase was obtained by averaging phase images from two SE acquisitions with opposed gradient polarities to minimize eddy current effects. [54, 203] SE settings were: imaging flip angle = 90° , $TE/TR = 6.2/12000 \text{ ms}$. FOV was $370 \times 259 \times 120 \text{ mm}^3$ for volunteer and $400 \times 280 \times 120 \text{ mm}^3$ for patients. Resolution was $2.5 \times 2.5 \times 7.5 \text{ mm}^3$ for volunteer and patient 1 and $5 \times 5 \times 7.5 \text{ mm}^3$ for patient 2 (due to scan time limitations). In all scans, the vendor-specific CLEAR option [90] was used to replace the phase contribution of receive array with the receive phase of the body coil operated in anti-quadrature.

For both patients, the tumour was delineated by a radiation oncologist on an ADC map aided by a T_2 -weighted image [204, 205]. For all subjects, muscle and bladder ROIs were manually delineated on 5 and 3 adjacent slices of SE magnitude image, respectively. Tumour delineation was transferred to SE magnitude image too.

4.2.3 Conductivity mapping

DL-EPT EPs locally distort the RF magnetic field in all three dimensions. To handle this physical problem, we sought a 3D network architecture for regression tasks trainable at a patch level. The compact, 3D CNN architecture by Li et al. [206] satisfied these requirements, thus was used for DL-EPT conductivity reconstruction. Li et al.'s network consists of 20 convolutional

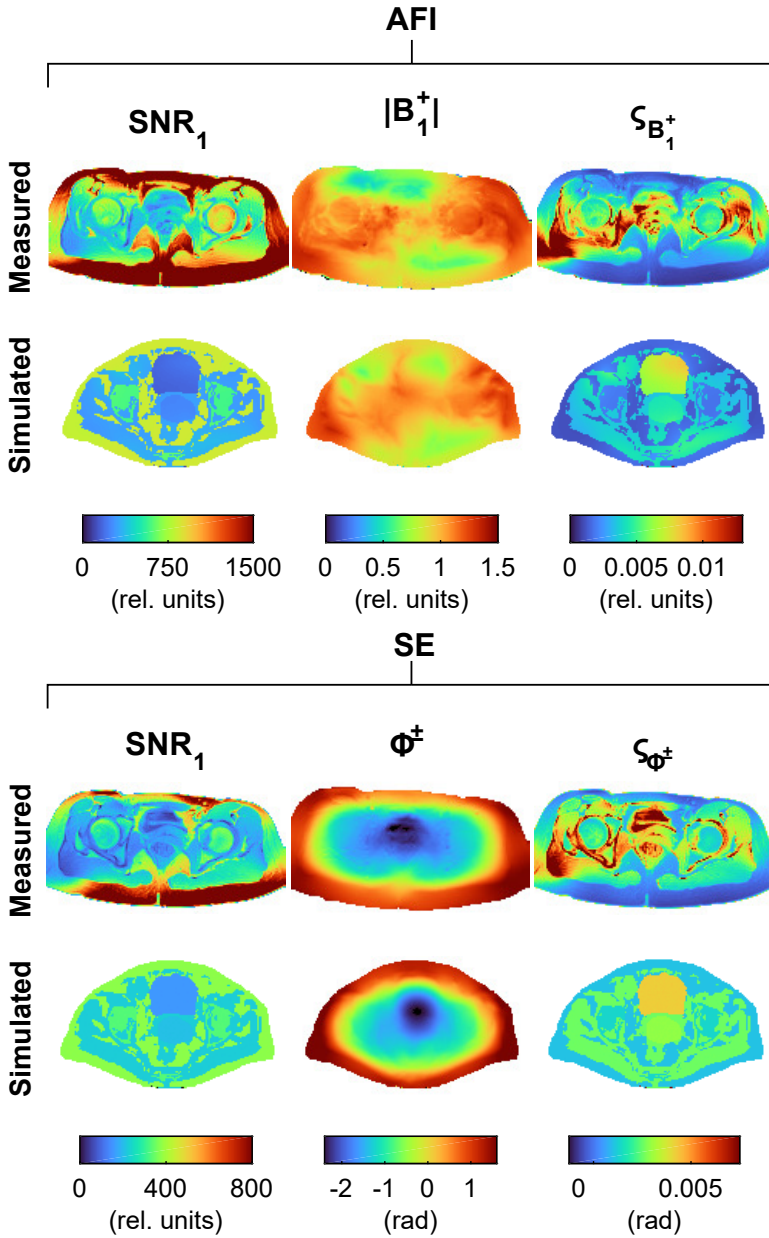


Figure 4.2. Comparison between measured and simulated MR data with realistic noise levels, for both AFI (*top*) and SE (*bottom*) sequences. Image SNR for both sequences is shown in first column. For measured data image SNR were retrieved with Kellman and McWeigh’s method [165]. $|B_1^+|$ for AFI and ϕ^\pm for SE are shown in second column. The standard deviations in $|B_1^+|$ ($\zeta_{B_1^+}$) and in ϕ^\pm (ζ_{ϕ^\pm}), derived as described in Chapters 2 and 3 [199,203], are shown in third column.

4. DL-based reconstruction of in vivo pelvis conductivity

layers of $3 \times 3 \times 3$ voxels, which are residually-connected in pairs and are progressively dilated with increasing dilation factors (for more details on network architecture, see [206]). The last layer had no activation function, differently from the original design in [206] which was meant for classification problems. This network is currently implemented under the name of “*highres3dnet*” in NiftyNet, an open-source TensorFlow-based platform with modular structure for DL research in medical imaging (<https://niftynet.io/>) [207].

Tissue conductivity perturbs both $|B_1^+|$ and transceive phase, but it is predominantly encoded in the curvature of the latter [57–59]. Based on this prior knowledge, we trained *highres3dnet* in both ‘full B_1^+ ’ and ‘transceive phase only’ configurations in order to assess whether differences in conductivity reconstruction exist between configurations. In ‘full B_1^+ ’ configuration, input data comprised real and imaginary parts of a complex B_1^+ field calculated as $|B_1^+| \cdot \exp(i \cdot \phi^\pm)$. We refer to “*Net_{EM}-B1*” when these input data were derived from (noiseless) EM simulations (i.e. $|B_1^{+,em}| \cdot \exp(i \cdot \phi^{\pm,em})$) and “*Net_{MR}-B1*” when they came from MR simulations (i.e. $|B_1^{+,mr}| \cdot \exp(i \cdot \phi^{\pm,mr})$) corrupted by noise. The ‘transceive phase only’ variant employed $\phi^{\pm,mr}$ from noisy MR simulations as input and is indicated hereafter with “*Net_{MR}- ϕ^\pm ””. In both configurations, a binary mask of the pelvis was provided as additional input. Ground truth conductivity (σ_{GT}) was given in input as regression target during training.*

Before entering the network, input data were rescaled by subtracting their mean value, which resulted in input data with values not exceeding $[-3, 3]$ units. Physically, removing this mean value has no effect on conductivity estimation with EPT [57,58]. Unlike usual DL endeavours, the standard deviation of input magnetic field data was not normalised to 1, because it holds information on spatial modulations from which the conductivity is retrieved in EPT. Before performing the aforementioned pre-processing steps, in vivo B_1^+ and ϕ^\pm were interpolated to $2.5 \times 2.5 \times 2.5 \text{ mm}^3$ (same resolution of in silico models used in training). Target conductivity σ_{GT} was normalized within $[-3, 3]$ units with fixed factors before training ($\sigma_{scaled} = \frac{\sigma_{GT} - a}{b}$, $a = 1.5$, $b = 0.5$). These factors were used at inference (or test) stage to convert the inferred conductivity map from normalized to absolute values.

For both configurations, *highres3dnet* was trained and tested in 7-fold cross-validation¹ on 180 (36 pelvic models \times 5 EP permutations) and 30 simulated data, respectively. All 210 dielectric models were tested once among all 7 folds. Training was performed with mean absolute error (MAE) loss function, L1 regularization with weight decay of $5.0 \cdot 10^{-5}$ and Adam optimisation. MAE loss function and L1 regularization on network weights were chosen to reduce sensitivity to outliers and promote sparsity. During training, input data were randomly sampled into patches of $80 \times 80 \times 24$ voxels. We chose this patch size after preliminary empirical tests with different sizes, taking also into consideration the FOV of input data and the depth of the network, which benefitted from relatively big patches for accurate reconstruction [206]. The learning rate was $5 \cdot 10^{-3}$ for 10000 iterations and was decreased to $8 \cdot 10^{-4}$ thereafter. Training was stopped after 42500 iterations for *Net_{EM/MR}-B1* and after 35000 iterations for *Net_{MR}- ϕ^\pm* because the loss function had converged and the conductivity MAE averaged over all 7 folds was smaller than in other iterations for the majority of pelvic tissues. Training and testing were run on a GPU (NVIDIA Tesla P100, 16 GB RAM). Training lasted 1-2 days. Inference time was ~ 10 s for a single model/subject. Further details regarding parameter tuning are listed in Table 4.2.

The accuracy and precision of conductivity reconstruction were evaluated for *Net_{MR}-B1* and

1. For a definition of k -fold cross-validation, see section 1.8.

Table 4.2. Parameters used to tune both full B_1^+ (“Net_{EM/MR}-B1”) and transceive phase only (“Net_{MR}- ϕ^\pm ”) network configurations. This table is shown in the form of the configuration file as provided in NiftyNet for this study (for more details on configuration file, see https://niftynet.readthedocs.io/en/dev/config_spec.html).

	“Net _{EM/MR} -B1”	“Net _{MR} - ϕ^\pm ”
INPUT	$[B1REAL] = \Re\{ B_1^{+,mr} \cdot \exp(i\phi^{\pm,mr})\}$ $[B1IMAG] = \Im\{ B_1^{+,mr} \cdot \exp(i\phi^{\pm,mr})\}$ [MASK] = binary pelvic mask [CONDUCTIVITY] = σ_{GT} [SAMPLINGWEIGHT] = binary pelvic mask <i>spatial_window_size</i> = (80, 80, 24)	[TRANSCIVEPHASE] = $\phi^{\pm,mr}$ [MASK] = binary pelvic mask [CONDUCTIVITY] = σ_{GT} [SAMPLINGWEIGHT] = binary pelvic mask <i>spatial_window_size</i> = (80, 80, 24)
NETWORK	<i>volume_padding_size</i> = (4, 4, 4) <i>volume_padding_mode</i> = symmetric <i>name</i> = highres3dnet <i>decay</i> = $5 \cdot 10^{-5}$ <i>activation_function</i> = prelu <i>reg_type</i> = L1 <i>batch_size</i> = 2 <i>window_sampling</i> = weighted <i>whitening</i> = False <i>normalisation</i> = False	<i>volume_padding_size</i> = (4, 4, 4) <i>volume_padding_mode</i> = symmetric <i>name</i> = highres3dnet <i>decay</i> = $5 \cdot 10^{-5}$ <i>activation_function</i> = prelu <i>reg_type</i> = L1 <i>batch_size</i> = 2 <i>window_sampling</i> = weighted <i>whitening</i> = False <i>normalisation</i> = False
TRAINING	<i>loss_type</i> = MAE <i>sample_per_volume</i> = 24 <i>optimizer</i> = adam <i>lr</i> = 0.005 (till 10000 th iteration) <i>lr</i> = 0.008 (from 10000 th to 42500 th iteration)	<i>loss_type</i> = MAE <i>sample_per_volume</i> = 24 <i>optimizer</i> = adam <i>lr</i> = 0.005 (till 10000 th iteration) <i>lr</i> = 0.008 (from 10000 th to 35000 th iteration)
INFERENCE	<i>border</i> = (16, 16, 4) <i>spatial_window_size</i> = (80, 80, 24) <i>inference_iter</i> = 42500	<i>border</i> = (16, 16, 4) <i>spatial_window_size</i> = (80, 80, 24) <i>inference_iter</i> = 35000
REGRESSION	<i>image</i> = B1REAL, B1IMAG, MASK <i>output</i> = CONDUCTIVITY <i>loss_border</i> = 4 <i>sampler</i> = SAMPLINGWEIGHT <i>error_map</i> = False	<i>image</i> = TRANSCIVEPHASE, MASK <i>output</i> = CONDUCTIVITY <i>loss_border</i> = 4 <i>sampler</i> = SAMPLINGWEIGHT <i>error_map</i> = False

Net_{MR}- ϕ^\pm with the 7-fold cross-validation. Accuracy and precision were calculated for each pelvic tissue. The accuracy was indicated by the mean error (ME), defined as:

$$ME = \sum_{i=1}^N \frac{\sigma_{GT} - \sigma_i}{N} \quad (4.1)$$

where N is the number of voxels within the tissue. The precision was denoted by the difference between conductivity 90th and 10th percentiles, S_{90-10} :

$$S_{90-10} = |\sigma(P_{90}) - \sigma(P_{10})| \quad (4.2)$$

where $\sigma(P_i)$ indicates the i^{th} percentile for conductivity.

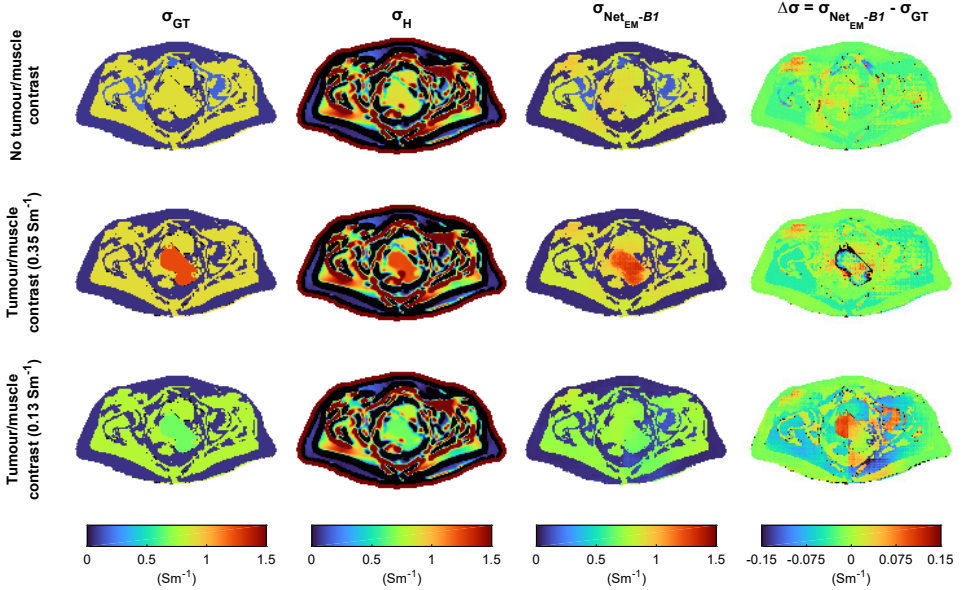


Figure 4.3. Conductivity reconstruction for three in silico pelvic models (that share same anatomy but different tissue conductivity, pelvic model #15). Pelvis conductivity from a healthy subject (i.e. no tumour/muscle contrast) is displayed in top row. The conductivity from two cervical cancer patients is also shown: one with good tumour/muscle contrast (0.35 Sm^{-1} , middle row) and one with poor tumour/muscle contrast (0.13 Sm^{-1} , bottom row). Maps for ground truth conductivity (first column), Helmholtz-based conductivity (σ_H , second column), DL-EPT conductivity tested with $\text{Net}_{\text{EM-B1}}$ (third column) and the difference between $\text{Net}_{\text{EM-B1}}$ conductivity and ground truth conductivity (fourth column) are reported.

Helmholtz-based EPT (H-EPT) For comparison, Helmholtz-based conductivity was reconstructed by convolving a noise-robust Laplacian kernel ($7 \times 7 \times 5$ voxels) [59] with simulated and measured data. The transceive phase assumption was used [57–59].

4.3 Results

4.3.1 In silico results

Conductivity maps reconstructed with $\text{Net}_{\text{EM-B1}}$ on noiseless simulated EM data displayed detailed pelvic anatomy (Figures 4.3 and 4.4b). In particular, tissue interfaces were sharply reconstructed. Only a few boundary voxels were assigned an incorrect conductivity value. This is a striking improvement over conventional Helmholtz-based conductivity, which exhibited the well-known “boundary errors” at tissue interfaces. These boundary errors prevented correct estimation in small tissue volumes, e.g. bone in Figure 4.3. Moreover, anti-symmetric errors in Helmholtz-based conductivity (e.g. muscle) caused by degradation of the transceive phase assumption [97] were absent in DL-based conductivity. Nevertheless, DL-based conductivity could display slight over-/under-estimation within a tissue: in the test model in Figure 4.4b, for example, conductivity was underestimated by $0.23 \pm 0.27 \text{ Sm}^{-1}$

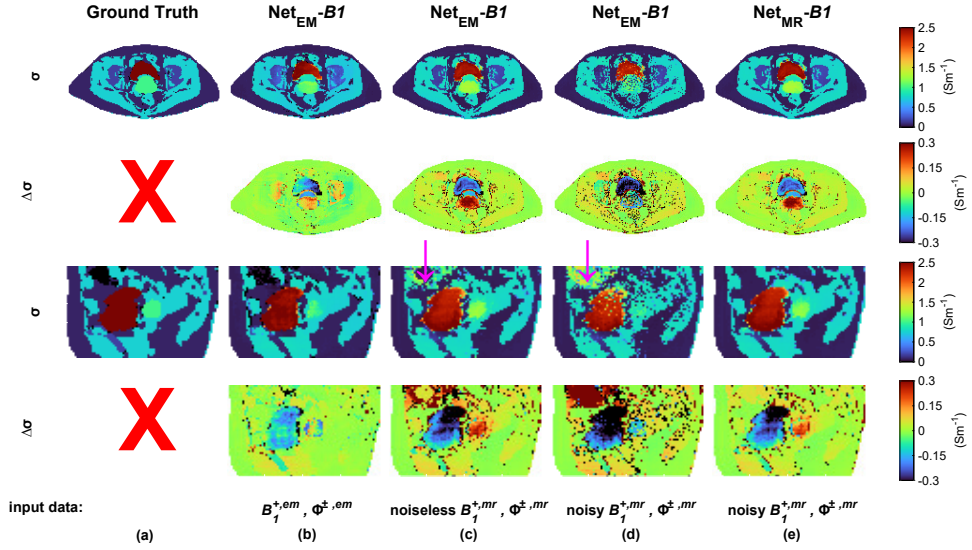


Figure 4.4. Impact of noiseless and noisy MR simulated input data on DL-EPT conductivity reconstructed with $\text{Net}_{\text{EM}}\text{-}B1$, the network trained on EM simulations ($|B_1^{+,em}|$ and $\phi^{\pm,em}$). **(a)** Ground truth conductivity. DL-EPT conductivity maps tested with $\text{Net}_{\text{EM}}\text{-}B1$ by using input data obtained from: **(b)** (noiseless) EM simulations ($|B_1^{+,em}|$ and $\phi^{\pm,em}$). This is similar to the result reported in Figure 4.3; **(c)** noiseless MR simulations (noiseless $|B_1^{+,mr}|$ and $\phi^{\pm,mr}$), to determine the impact of sequence accuracy on DL-EPT reconstruction; **(d)** noisy MR simulations with realistic noise level on MR images (noisy $|B_1^{+,mr}|$ and $\phi^{\pm,mr}$), to determine the impact of sequence noise propagation on DL-EPT reconstruction. **(e)** Conductivity map reconstructed with $\text{Net}_{\text{MR}}\text{-}B1$, the network trained on noisy MR simulated data (noisy $|B_1^{+,mr}|$ and $\phi^{\pm,mr}$), to show the impact of retraining with realistic MR simulated data. Magenta arrows in (c) and (d) point to an air pocket, the conductivity reconstruction of which is disturbed.

(mean \pm std) in the bladder volume. Note that the general reconstruction performance, assessed with the cross-validation, is discussed below. Figure 4.3 also shows that the tumour embedded in muscle was correctly “detected” when muscle/tumour conductivity contrast was sufficiently high (0.35 Sm^{-1}) but was partly assigned muscle conductivity for low contrast (0.13 Sm^{-1}).

Figure 4.4 illustrates the impact of using $|B_1^+|$ and ϕ^\pm simulated with AFI and SE sequences on DL-EPT conductivity reconstruction with $\text{Net}_{\text{EM}}\text{-}B1$. Figure 4.4c shows that the reconstructed conductivity was disturbed by the strong B_1^+ underestimation in air (e.g. in bowel, Figure 4B.1) when noiseless simulated MR data were given in input. However, small B_1^+ errors, occurring in fat and bone due to their low T_1 to which AFI is sensitive [68,199] (Figure 4B.1), did not influence the conductivity. Using noisy simulated data as input for $\text{Net}_{\text{EM}}\text{-}B1$ further perturbed the conductivity reconstruction (Figure 4.4d), especially in tissues with low precision, e.g. air, muscle and bladder (see Figure 4.2). Conductivity reconstructions robust to both sequence-specific errors and noise (Figure 4.4e) were shown when the CNN was trained with input noisy simulated MR data (i.e., $\text{Net}_{\text{MR}}\text{-}B1$).

4. DL-based reconstruction of in vivo pelvis conductivity

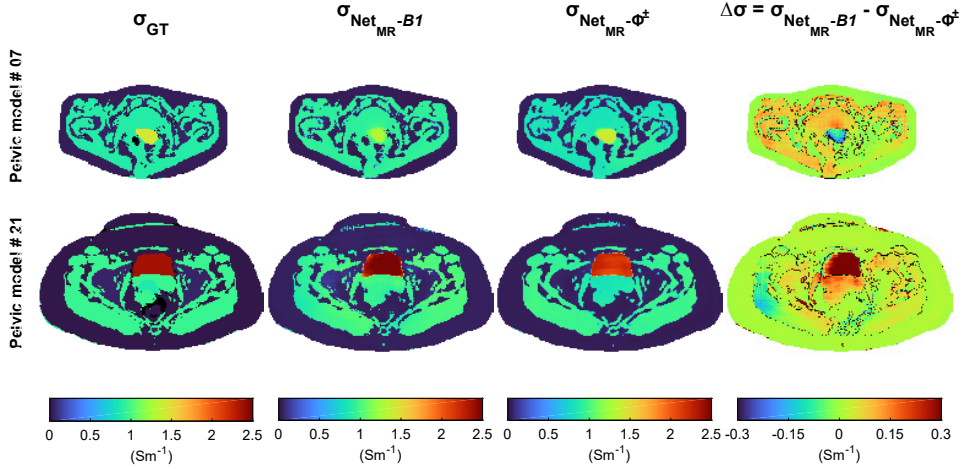


Figure 4.5. Comparison between conductivity maps reconstructed with $\text{Net}_{\text{MR}}\text{-}B1$ and $\text{Net}_{\text{MR}}\text{-}\phi^{\pm}$, the networks trained on noisy MR simulated data using both $|B_1^{+,mr}|$ and $\phi^{\pm,mr}$ or only $\phi^{\pm,mr}$, respectively. Maps for ground truth conductivity (*first column*), DL-EPT conductivity reconstructed by $\text{Net}_{\text{MR}}\text{-}B1$ (*second column*), DL-EPT conductivity reconstructed by $\text{Net}_{\text{MR}}\text{-}\phi^{\pm}$ (*third column*) and the conductivity difference between $\text{Net}_{\text{MR}}\text{-}B1$ and $\text{Net}_{\text{MR}}\text{-}\phi^{\pm}$ (*fourth column*) are shown for two pelvic models with different anatomies (one thin patient, model #07, and one fat patient, model #21).

Figure 4.5 shows that both $\text{Net}_{\text{MR}}\text{-}B1$ and $\text{Net}_{\text{MR}}\text{-}\phi^{\pm}$ reconstructed comparable conductivity maps in two patients with distinct anatomies. This finding was also confirmed by the results of 7-fold cross-validation: as reported in Table 4.3, conductivity reconstruction accuracy (ME) and precision (S_{90-10}) in all tissues were comparable for both network configurations. ME and S_{90-10} are also visualized for all test data and for all tissues in Figure 4.6: on average, ME was below 0.1 Sm^{-1} in all pelvic tissues, with minimum/maximum ME of approximately $\pm 2.5 \cdot 10^{-3} \text{ Sm}^{-1}$ for fat, $\pm 5.0 \cdot 10^{-3} \text{ Sm}^{-1}$ for bone, $\pm 0.15 \text{ Sm}^{-1}$ for muscle, $\pm 0.23 \text{ Sm}^{-1}$ for tumour and $\pm 0.4 \text{ Sm}^{-1}$ for bladder content. In general, S_{90-10} was below 0.1 Sm^{-1} for fat, bone and muscle. For tumour and bladder content, S_{90-10} was on average 0.2 and 0.3 Sm^{-1} , respectively, with maximum peaks of 0.5 Sm^{-1} for tumour and 0.6 Sm^{-1} for bladder content. Interestingly, bladder content and tumour displayed the highest absolute values for ME and S_{90-10} (Table 4.3). Note that they were the least represented tissues in our dataset (140/210 and 168/210 dielectric models showed bladder content and tumour EPs, respectively). Moreover, the comparable ME and S_{90-10} among all test folds in Figure 4.6 denote that both network configurations were robust to data with different geometries and EPs. It is also worth mentioning that $\text{Net}_{\text{MR}}\text{-}B1$ retrieved sharper anatomical details, such as tissue infiltrations and interfaces, than $\text{Net}_{\text{MR}}\text{-}\phi^{\pm}$ (as can be appreciated in Figure 4.5). This was not accounted for in ME and S_{90-10} calculations, as these metrics were calculated in tissue ROIs obtained by erosion of 1 voxel from the original tissue segmentation.

Figure 4.7 explores the reconstruction capability of $\text{Net}_{\text{MR}}\text{-}B1$ in presence of tissues with conductivity values outside the predefined tissue conductivity ranges (outliers). For example, the tumour in outlier 1 ($\sigma_{\text{GT}} = 2.9 \text{ Sm}^{-1}$) was assigned a mean $\sigma = 2.2 \text{ Sm}^{-1}$, belonging

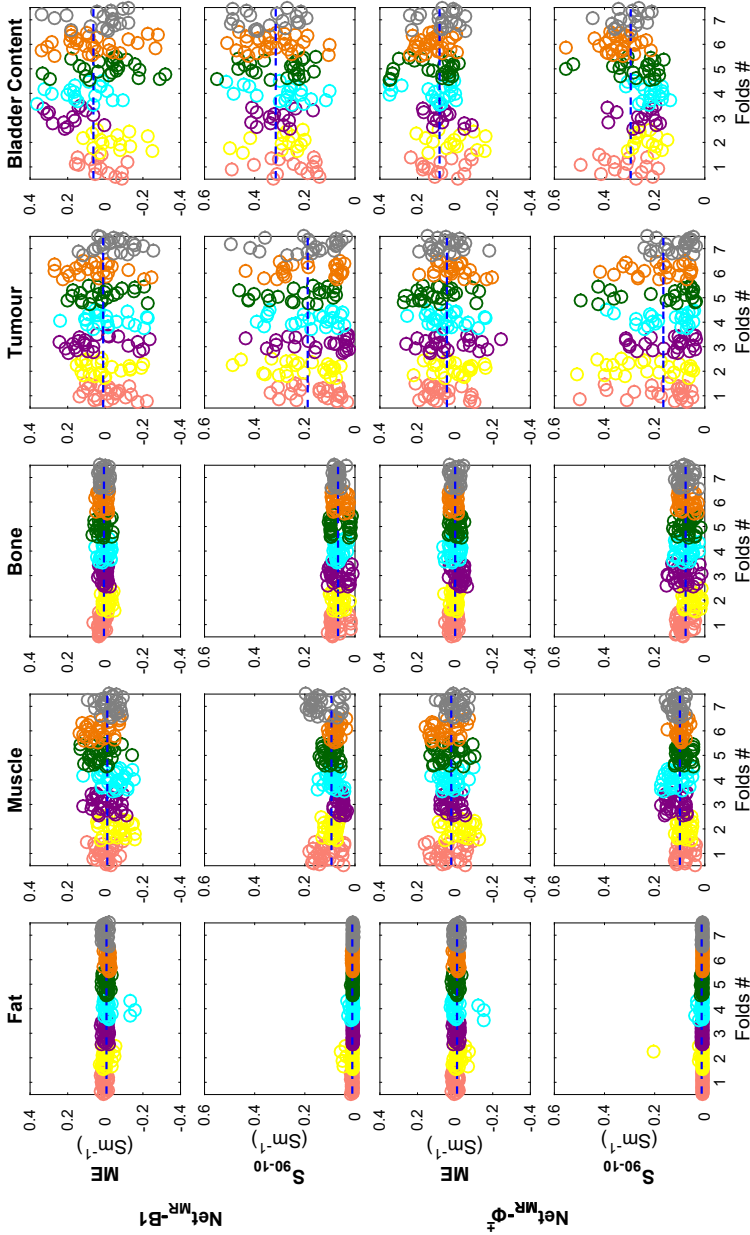


Figure 4.6. Mean error (ME) and spread S_{90-10} for all pelvic tissues, resulting from 7-fold cross-validation for $\text{Net}_{\text{MR}}\text{-B1}$ (first and second rows) and $\text{Net}_{\text{MR}}\text{-}\phi^{\pm}$ (third and fourth rows). ME and S_{90-10} in every tissue were calculated within a tissue roi that corresponded to the tissue segmentation without the outermost voxels (i.e. 1 voxel was eroded from the original segmentation). Each colour represents one fold, where 30 dielectric models were used as test data. Each circle represents one dielectric model belonging to the test dataset. All 210 dielectric models were tested once within all 7 folds. The dashed blue lines represent the average bias and S_{90-10} (over all folds) for each pelvic tissue.

Table 4.3. Mean \pm std values for global ME and S_{90-10} over all dielectric models in all 7 folds for both $\text{Net}_{\text{MR}}\text{-}B1$ and $\text{Net}_{\text{MR}}\text{-}\phi^\pm$.

	$\text{Net}_{\text{MR}}\text{-}B1$		$\text{Net}_{\text{MR}}\text{-}\phi^\pm$	
	ME (Sm^{-1})	$S_{90-10}(\text{Sm}^{-1})$	ME (Sm^{-1})	$S_{90-10}(\text{Sm}^{-1})$
Fat	$-6.28 \cdot 10^{-3} \pm 0.0260$	0.0107 ± 0.0063	-0.0101 ± 0.0246	0.0126 ± 0.0248
Muscle	-0.0106 ± 0.0663	0.0938 ± 0.0374	0.0207 ± 0.0620	0.0994 ± 0.0307
Bone	$7.16 \cdot 10^{-3} \pm 0.0228$	0.0676 ± 0.0262	$-1.03 \cdot 10^{-4} \pm 0.0242$	0.0766 ± 0.0308
Tumour	0.0113 ± 0.1292	0.1886 ± 0.1360	0.0437 ± 0.1061	0.1654 ± 0.1171
Bladder Content	0.0607 ± 0.1593	0.3160 ± 0.1430	0.0912 ± 0.1107	0.3037 ± 0.1211

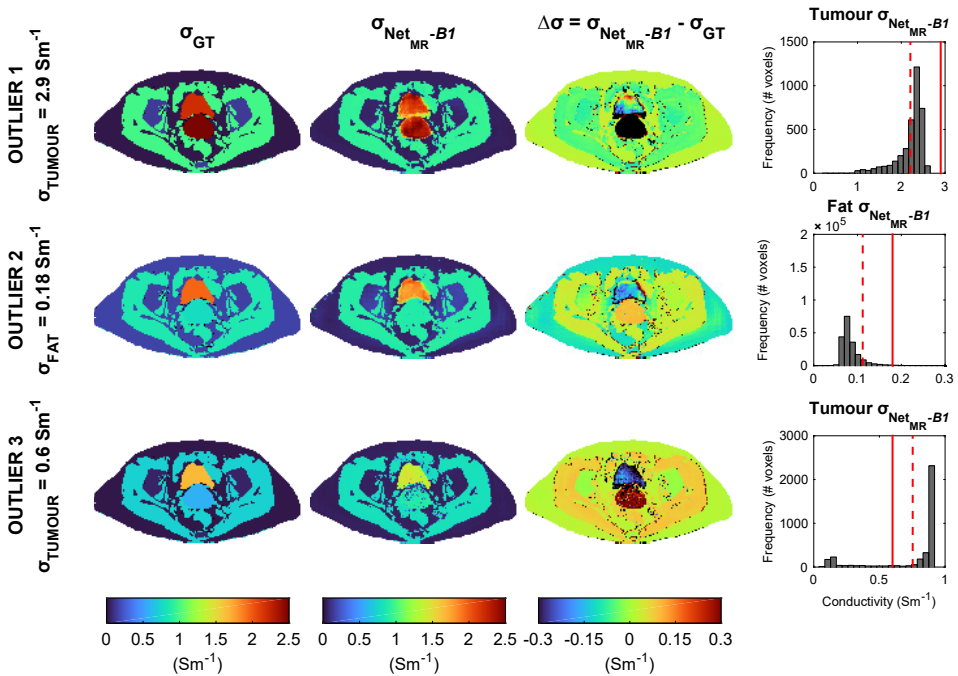


Figure 4.7. DL-EPT conductivity reconstruction (with $\text{Net}_{\text{MR}}\text{-}B1$) in presence of outlier EP values, i.e. values that were not included in our EP database. Three outlier cases are presented: outlier 1 (top row), with tumour $\sigma = 2.9 \text{ Sm}^{-1}$ and $\epsilon_r = 85$ rel. units; outlier 2 (middle row), with fat $\sigma = 0.18 \text{ Sm}^{-1}$ and $\epsilon_r = 8.27$ rel. units; outlier 3 (bottom row), with tumour $\sigma = 0.6 \text{ Sm}^{-1}$ and $\epsilon_r = 35$ rel. units. Maps for ground truth conductivity (first column), DL-EPT conductivity retrieved with $\text{Net}_{\text{MR}}\text{-}B1$ (second column) and their conductivity difference (third column) are reported. Conductivity histograms for the tissue with outlier EPs are shown in fourth column. Solid and dashed lines in red colour represent ground truth conductivity and mean DL-EPT conductivity value in the tissue, respectively.

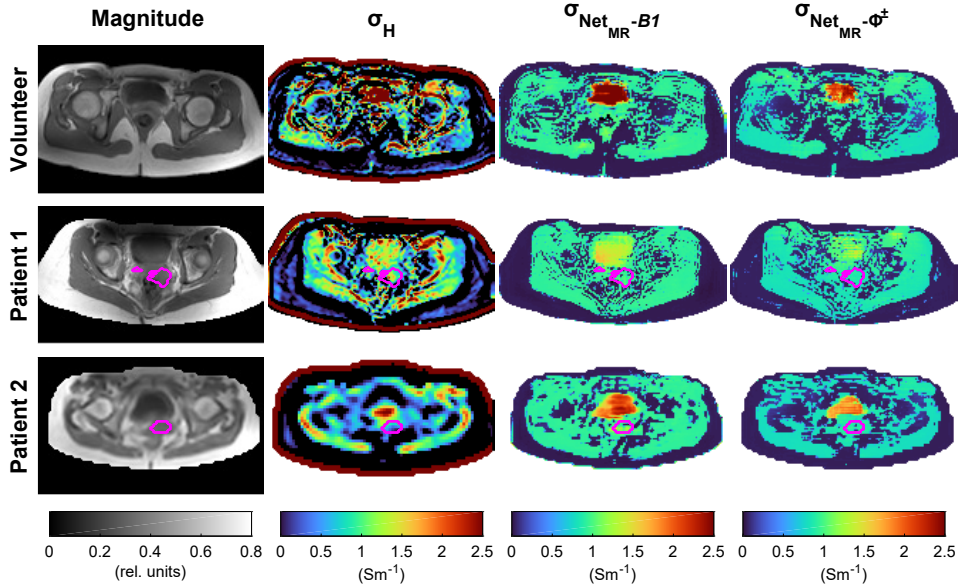


Figure 4.8. In vivo conductivity results on a healthy volunteer and two cervical cancer patients (transversal view). Magnitude image from SE acquisition (*first column*), Helmholtz-based conductivity map (σ_H , *second column*), DL-EPT conductivity map reconstructed with $\text{Net}_{\text{MR}}\text{-}B1$ (*third column*) and DL-EPT conductivity map reconstructed with $\text{Net}_{\text{MR}}\text{-}\phi^\pm$ (*fourth column*) are shown. The tumour delineation is displayed in magenta colour.

to bladder distribution (Figure 4.1). The tumour in outlier 3 ($\sigma_{\text{GT}} = 0.6 \text{ Sm}^{-1}$, a value in between bone and muscle conductivity distributions, Figure 4.1) was predominantly assigned muscle-like conductivity although conductivity values of cancellous bone were also present. In outlier 2, fat tissue presented fat-like conductivity values, with a mean $\sigma \approx 0.1 \text{ Sm}^{-1}$ (vs $\sigma_{\text{GT}} = 0.18 \text{ Sm}^{-1}$). In all examples, the conductivity of adjacent tissues was reconstructed within the above-mentioned accuracy and precision.

4.3.2 In vivo results

Conductivity maps obtained with $\text{Net}_{\text{MR}}\text{-}B1$ and $\text{Net}_{\text{MR}}\text{-}\phi^\pm$ are shown in Figure 4.8 (transversal view) and Figure 4B.2 (sagittal view). In vivo conductivity maps reconstructed with DL-EPT confirmed in silico results: first, the underlying anatomy was clearly reconstructed (Figure 4.8 and Figure 4.9 for a zoomed view); second, conductivity values were quite homogeneous within tissues. For both $\text{Net}_{\text{MR}}\text{-}B1$ and $\text{Net}_{\text{MR}}\text{-}\phi^\pm$, erroneous conductivity values were predominantly caused by imaging artefacts in the underlying B_1^+ and ϕ^\pm (Figure 4.10), such as ghosting arising from motion (e.g. breathing and flow) during acquisition. These were visible, for example, in proximity of bladder and bone. Note that ghosting artefacts were not included in training data.

The quality of DL-based conductivity outperformed that of Helmholtz-based EPT conductivity (Figures 4.8 and 4.9), as already observed in silico. Figure 4.11 reports a quantitative comparison of $\text{Net}_{\text{MR}}\text{-}B1$ and $\text{Net}_{\text{MR}}\text{-}\phi^\pm$ with H-EPT, depicting median conductivity values calculated

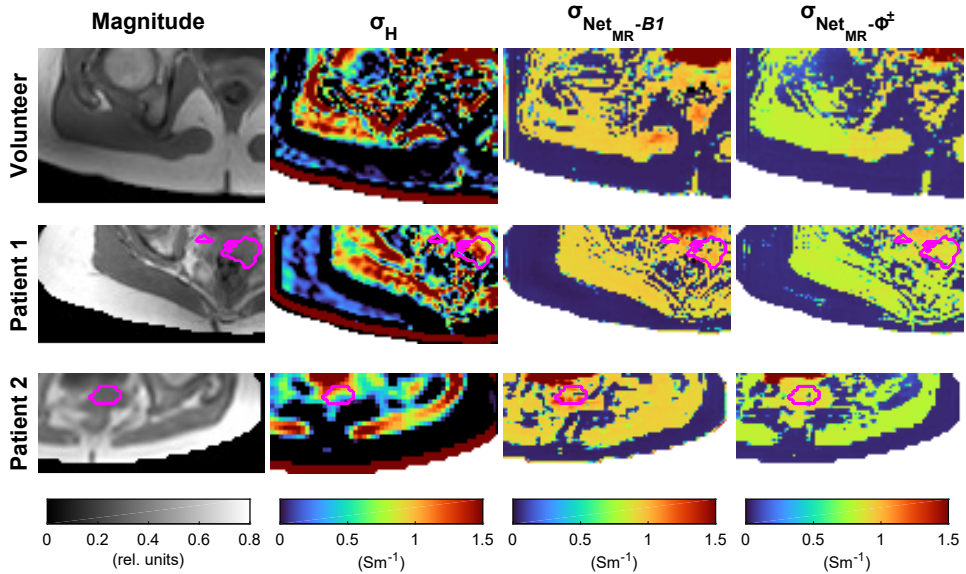


Figure 4.9. Zoomed view of in vivo conductivity results on a healthy volunteer and two cervical cancer patients shown in Figure 4.8. Magnitude image from SE acquisition (*first column*), Helmholtz-based conductivity map (σ_H , *second column*), DL-EPT conductivity map reconstructed with $\text{Net}_{\text{MR}-B1}$ (*third column*) and DL-EPT conductivity map reconstructed with $\text{Net}_{\text{MR}-\phi^\pm}$ (*fourth column*) are shown. The tumour delineation is displayed in magenta colour.

in 3D tissue ROIs (illustrated in Figure 4.10), together with 10th and 90th percentiles. Previous simulation and experimental studies [87, 97] showed that accurate H-EPT estimates can be obtained within boundary-free ROIs. Because the broad boundary errors in H-EPT in fat and muscle did not leave enough voxels for reliable statistics, the comparison was not reported for these tissues. For all three subjects, median conductivity values differed from H-EPT median values by less than 8% in $\text{Net}_{\text{MR}-\phi^\pm}$ and ~11% in $\text{Net}_{\text{MR}-B1}$ in muscle and tumour. In bladder, differences in median values up to 35% were found in $\text{Net}_{\text{MR}-\phi^\pm}$ for all subjects, whereas in $\text{Net}_{\text{MR}-B1}$ differences were less than 5% for volunteer and patient 2, and 40% for patient 1. DL-EPT values were also in the range of values found in an earlier study [102]. Moreover, the conductivity spread in DL-EPT was smaller than in H-EPT. The relatively low 10th percentiles found for DL-EPT in the tumour were caused by aforementioned motion-related errors entering the tumour ROI (Figure 4.8).

4.4 Discussion

A novel deep learning-based method for reconstruction of subject-specific conductivity in the pelvic region was presented. This method comprises a fully open-source three-dimensional (3D) patch-based convolutional neural network (CNN) architecture (*highres3dnet*) and an in silico training dataset of MR accessible quantities ($|B_1^+|$ and transceive phase, $\text{Net}_{\text{MR}-B1}$, or transceive phase only, $\text{Net}_{\text{MR}-\phi^\pm}$), which were obtained from realistic MR simulations at 3T of pelvic models with representative anatomies and electrical properties. Accuracy and precision of conductivity reconstruction were validated in silico. The trained network reconstructs in

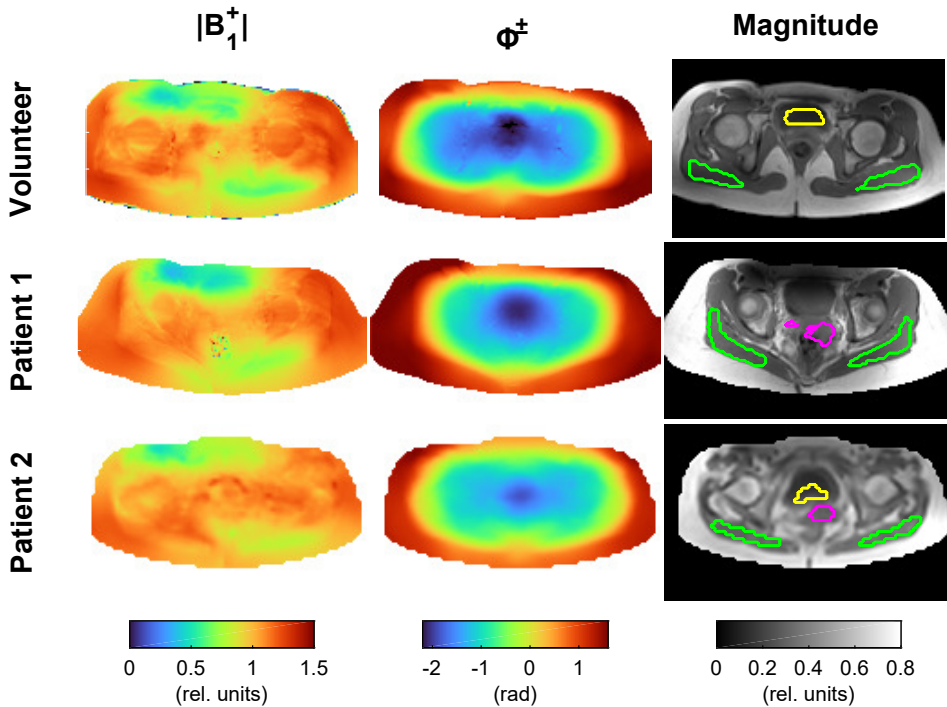


Figure 4.10. In vivo $|B_1^+|$ (first column) and ϕ^\pm (second column) maps of both healthy volunteer and cervical cancer patients. Tissue ROIs used for statistics were manually delineated by avoiding visible Helmholtz-based EPT boundary errors and are displayed on a slice of the magnitude image (third column).

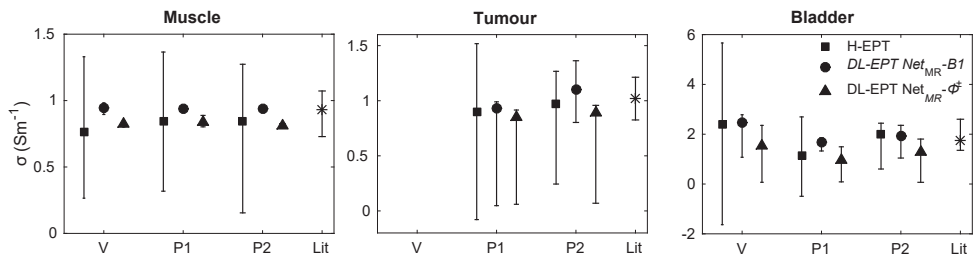


Figure 4.11. Quantification of pelvic tissue conductivity reconstructed with Helmholtz-based EPT and DL-EPT (both $\text{Net}_{\text{MR}}-B1$ and $\text{Net}_{\text{MR}}-\phi^\pm$) for both healthy volunteer and cervical cancer patients. Median values are reported. Error bars denote 10th and 90th percentiles. These values were calculated within 3D tissue ROIs (illustrated in Figure 4.10 for one slice). Literature mean values, along with maximum and minimum values found in the population examined in [102], are also shown. V = volunteer; P1 = patient 1; P2 = patient 2; Lit = literature.

few seconds a 3D pelvis conductivity map with sharp tissue interfaces, robust to experimental noise levels and relatively sensitive to tissue conductivity variations. When tested in vivo, the CNN produces conductivity maps with similar quality as in silico conductivity maps, demonstrating that the adopted simulation-based training dataset sufficiently represents measured B_1 fields.

A merit of our approach is the ability to accurately reconstruct the conductivity at tissues interfaces, revealing the underlying pelvic anatomy (Figures 4.5 and 4.8). This shows that the network learnt to extract the anatomical information directly from the input B_1 data alone, unlike a previous study, where an MR magnitude image was required in input to obtain 2D conductivity maps with correct brain anatomy [121]. Anatomically-detailed conductivity maps, as achieved by the proposed DL-based method, are particularly appealing for MR-based hyperthermia treatment planning of cervical cancer patients: for example, to enable localization of hot spots, which typically occur at muscle/fat interfaces [174].

Conceptually, the capability of accurate boundary reconstruction is attributable to highres3dnet architecture, and in particular to the synergic combination of (i) patch-based training and (ii) dilated convolutions. Highres3dnet was initially chosen for conductivity reconstruction because of its flexibility in dealing with 3D regression problems in patch-based fashion, which we expected to capture the 3D, local nature of the EPT problem. Patch-based approaches allow to capture local features from input data, while diminishing the risk of overfitting global spatial context. Besides, they reduce the computational cost on GPU memory. Dilated convolutions in our CNN architecture efficiently expand the receptive fields, which relate to wider spatial contexts of the input patch, while preserving the spatial resolution of features in the input patch throughout the layers [206]. This appears to be more advantageous than using down- and up-sampling layers, as found, for instance, in the U-net architecture employed by Hampe et al. [122]. Down-sampling layers reduce the resolution of the input features, which is only partially recovered by the subsequent up-sampling layers. This might potentially explain the smoother boundaries in [122].

Our approach does not depend on geometrical similarities among training human models and tested subjects, as supported by the consistent DL-EPT results for diverse pelvic tissue anatomies (Figures 4.3–4.5, 4.8): all the relevant information is recovered from the B_1^+ . This is a substantial difference with a recent DL-EPT finding, where only test geometries similar to training geometries were well reconstructed [122]. The network from this prior study likely over-fitted the anatomical information in training from the input transceive phase. This issue was attributed to the lack of geometrical variability in training, being the training dataset based on geometrical transformations of few human brain models. Differently, we expect that our CNN properly exploited the diversified training dataset to learn the mapping function between input magnetic field and conductivity in the pelvis.

The training of our supervised DL-based method was deliberately founded on simulated data, as simulations intrinsically connect the ground truth EP_s to $|B_1^+|$ and ϕ^\pm and can reproduce the magnetic field with high fidelity. Direct training on MR data, as explored in reference [122], is another viable option, which could be motivated by the final practical application of the method on in vivo MR measurements. Nonetheless, in vivo MR data lack ground truth EP information, thus target EP_s must be obtained by an arbitrarily chosen EPT reconstruction method (e.g. processed H-EPT [122]). A possible downside of training on in vivo MR data is that potential inaccuracies in these EP maps deriving from the selected EPT algorithm would be incorrectly learnt as true values. Furthermore, simulations allow to include knowledge of the RF coil system and to expand the training samples: for instance, by creating several

EP permutations and/or by retrieving anatomies from different imaging modalities. In this study, CT scans of real patients were used to create human models but segmenting clinical MR images, which offer greater tissue contrast, might also be considered. In that case, we believe that `highres3dnet` would be able to reconstruct most of the tissues' anatomy for the reasons discussed above. Moreover, the EP permutations were intended to cover the spectrum of possible inter-subject EP variations as much as possible (see Appendix 4.A) but, for simplicity, each pelvic tissue was assigned a single EP value from the predefined EP distributions. Thus, our *in silico* training dataset currently does not account for intra-tissue EP variations, which instead would be naturally encoded in measured B_1 data, even though B_1 maps from a rather large population should be acquired to sufficiently sample the inter-subject EP variability. Finally, simulations permit to emulate the accuracy, precision and acquisition artifacts of the $|B_1^+|$ and ϕ^\pm maps measured with different MR sequences, which could be learnt and potentially compensated by the CNN.

Based on a framework using EM and MR simulations [199], the propagation of sequence-specific systematic deviations (accuracy) and noise (precision) occurring from MR images to $|B_1^+|$ and ϕ^\pm during the acquisition is realistically included in our training $|B_1^+|$ and ϕ^\pm maps. On the contrary, it is "common practice" in DL-EPT to train on simulated EM data of magnetic fields to which Gaussian noise is directly superimposed [121]. This does not account for sequence-related inaccuracies and it implicitly assumes a possibly unrealistic noise distribution in the $|B_1^+|$ and ϕ^\pm maps (which, in fact, is regulated by the mapping sequence), although it might approximate the noise level obtainable in measurements. However, our results demonstrated that the conductivity reconstruction with $\text{Net}_{\text{MR}}\text{-}B1$, i.e. the network trained on simulated MR data, was more robust to errors (e.g. in air, Figure 4.4c) than the reconstruction performed with the network trained on EM simulations alone ($\text{Net}_{\text{EM}}\text{-}B1$). DL-based reconstruction with $\text{Net}_{\text{MR}}\text{-}B1$ was also noise-robust.

The comparable performance of the two network configurations ($\text{Net}_{\text{MR}}\text{-}B1$ and $\text{Net}_{\text{MR}}\text{-}\phi^\pm$) suggests that the CNN can reliably reconstruct the conductivity from the transceive phase alone (Table 4.3 and Figure 4.6). $\text{Net}_{\text{MR}}\text{-}B1$ better reconstructed the tissue interfaces *in silico*; this advantage was not clear *in vivo*. In general, the contribution of $|B_1^+|$ for DL-based conductivity mapping seems minor; the two configurations differed only noticeably in the bladder for two subjects. A transceive phase-only approach would save scan time and avoid artefacts strictly related to $|B_1^+|$ acquisitions.

All the technical aspects discussed thus far alleviated some problems of pelvis conductivity mapping at 3T. For example, the validity of the transceive phase assumption, adopted in many EPT methods, degrades at 3T for large body sizes such as the pelvis (see e.g. H-EPT in Figure 4.3) [97]. Training with the transceive phase circumvents this limitation. Furthermore, the low pelvis SNR, which is typically compensated by using large voxel sizes [97], was mitigated in this study by training on simulated MR data with SNRs predicting the experimental precision at a desired resolution (Figure 4.2). Nevertheless, our DL-based method does not currently handle the imaging artifacts caused by motion (breathing, bowel peristalsis, flowing blood) that inevitably affect $|B_1^+|$ and ϕ^\pm maps (Figure 4.8). Handling these motion-induced artefacts is still an unresolved challenge in EPT. We envisage that including these artefacts in the simulated training dataset would improve *in vivo* DL-based pelvis reconstructions.

The network performs consistently when presented with unseen pelvic data, as confirmed by its stable behaviour with respect to test data of different folds (Figure 4.6), which gives confidence on the reliability of the overall accuracy and precision predicted by the *in silico* cross-validation. The cross-validation revealed on average a low mean error (ME) in all

tissues (Table 4.3), which indicates an overall good sensitivity to conductivity variations. Nevertheless, MEs up to $\sim 20\%$ from the ground truth conductivity could occur for muscle, bladder and tumour, therefore further optimization is necessary to render our method competitive with the accuracy of other physics-based EPT reconstruction methods (e.g. CSI-EPT approaches [109,117] exhibiting errors below 10% in simulated pelvis conductivity maps). Those MEs might be possibly decreased by manipulating the loss function or augmenting the number of EP permutations; yet, we cannot predict the number of training samples needed for this improvement. Moreover, bladder content and tumour were less represented in our database (\sim approximately one order of magnitude lower than the other tissue types, Figure 4.1), which likely explains the higher uncertainty in ME and S_{90-10} in absolute values in these two tissues (Figure 4.6). Solutions to the issue of imbalanced data were proposed for DL classification problems, but they are still focus of research in regression problems. [208] We expect that the accuracy in these tissues will be enhanced by handling the problem of imbalanced data.

Our data-driven approach retrieves the conductivity for the specific body region, body coil and field strength, because this knowledge is imprinted during training. Its applicability to other body sites or field strengths cannot be assured yet. Moreover, Figure 4.7 suggests that the network tends to favour anatomically realistic conductivity values (seen in training) if outlier conductivity values, i.e. outside the training range, are present. Thus, we deduce that training with a larger range of conductivity values would likely be more appropriate to generalize our method. We acknowledge also that the current implementation fails to indicate such type of error. We believe that combining our DL-based reconstruction with an inverse EPT reconstruction method (which guarantees data consistency), similarly to the hybrid approach adopted by Leijssen et al. [209], could increase the confidence in the accuracy of reconstruction of outlier cases.

To emphasize the feasibility of the proposed DL-EPT method, we also reported conductivity maps reconstructed on experimental in vivo data. These maps reproduce the quality observed in the simulation study, thus we conclude that our training simulated B_1^+ fields are sufficiently representative of realistic B_1^+ (excluding imaging artefacts, which were not simulated). Furthermore, we compared in vivo DL-EPT conductivity maps with Helmholtz-based EPT (H-EPT) conductivity maps. Note that H-EPT is currently the only method shown in vivo for pelvis conductivity mapping; the aforementioned CSI-EPT approaches [109,117], despite showing good accuracy and precision in pelvis conductivity simulations, have not yet been presented for measured pelvic data. In vivo, DL-based conductivity represents a remarkable improvement over the state-of-art H-EPT conductivity (Figure 4.8), presenting no boundary errors, higher precision and rather small differences with H-EPT values in boundary-free tissue ROIs (Figure 4.11). However, we do realize that the presented comparison does not provide validation for our in vivo results, since H-EPT values cannot be considered as ground truth. Therefore, we advise caution in interpreting quantitative in vivo values obtained with DL-EPT without additional validation. We surmise that the accuracy predicted with the cross-validation also applies experimentally, but a separate study is warranted to validate this. Similar to previous conductivity works, an effective validation could be performed, for example by testing the CNN on phantoms with known EPs, although the network might need re-training on different digital phantoms for this scope.

In the perspective of oncologic applications, several implications ensue from the fact that MEs up to $\sim 0.20 \text{ Sm}^{-1}$ could occur in tumour conductivity with $\text{Net}_{\text{MR}}\text{-}B1$ and $\text{Net}_{\text{MR}}\text{-}\phi^\pm$. In the context of hyperthermia treatment planning, for example, an under-/over-estimation of this magnitude in the conductivity of a deep-seated tumour like cervical cancer has a

limited effect on the tumour temperature [131]. Nevertheless, the tumour temperature is also affected by the conductivity of tissues surrounding the tumour, like muscle and bladder [131]. Thus, errors up to 0.15 and 0.4 Sm^{-1} in muscle and bladder, respectively (Figure 4.6), might profoundly affect the tumour temperature achieved during the treatment. Moreover, it is currently unclear whether this reconstruction accuracy would prohibit usage in longitudinal studies to monitor the response of a treatment because inter-treatment tumour conductivity changes are unknown. For diagnostic applications based on conductivity, the tumour volume would be detected only if the dielectric contrast of normal/cancerous tissues were above $\sim 0.25 \text{Sm}^{-1}$. For lower conductivity contrasts, we observed that tumour and muscle (/healthy) tissues were generally given the same conductivity value (Figure 4.3).

4.5 Conclusion

We showed, for the first time, that in vivo conductivity maps in the human pelvis characterized by anatomical details, robustness to noise and relatively good sensitivity to tissue conductivity variations are feasible at 3T by using deep learning. In particular, we demonstrated that the combination of (i) a broad training dataset, with realistic pelvic anatomies and EPs, (ii) a 3D, compact, high resolution CNN architecture (the implementation and configuration of which are made publicly available) trained at a patch level on (iii) only measurable $|B_1^+|$ and ϕ^\pm quantities obtained from MR simulations with realistic accuracy and precision was sufficient to guarantee good quality, 3D maps of pelvis conductivity.

The quality of DL-based conductivity maps shown in this work represents a dramatic improvement over the status quo methodology used for pelvis EPT, i.e., conventional Helmholtz-based EPT, and may prove useful for clinical oncological applications.

4.A Appendix A: Determining tissue-specific EP uniform distributions

Tissue EPs in all dielectric models were randomly selected from uniform distributions of tissue-specific conductivity and permittivity at 128 MHz. These EP distributions were designed to account for possible inter-subject EP variations within each tissue and were determined with one of the following strategies, unless explicitly stated otherwise:

- (i) When reported in literature, conductivity (/permittivity) variations recorded at 128 MHz for a certain tissue were used to define conductivity (/permittivity) distributions for that tissue.
- (ii) If variations of only one property (e.g. σ) were found in literature, these were used to define the range for the other property (e.g. ϵ_r) as follows: the known maximum and minimum values (e.g. σ_{\min} and σ_{\max}), were used to calculate ratios relative to the mean value (e.g. $\sigma_{\min}/\sigma_{\text{avg}}$ and $\sigma_{\max}/\sigma_{\text{avg}}$, where σ_{avg} is mean σ value), expressed in %. These relative ratios were then applied to the literature mean value of the other property. We employed the same ratios for both EPs under the assumption that conductivity and permittivity vary in a linearly-dependent fashion. This assumption was supported by the fact that pelvic tissues fall within the region where a quasi-linear relationship exists between permittivity and conductivity at 128 MHz (Figure 4A.1).
- (iii) When ranges were not found for either EP, a 20% variation around EP mean value was assumed, because the majority of human EPs at 128 MHz can be described by a permittivity-to-conductivity trend $\pm 20\%$ variation (Figure 4A.1).

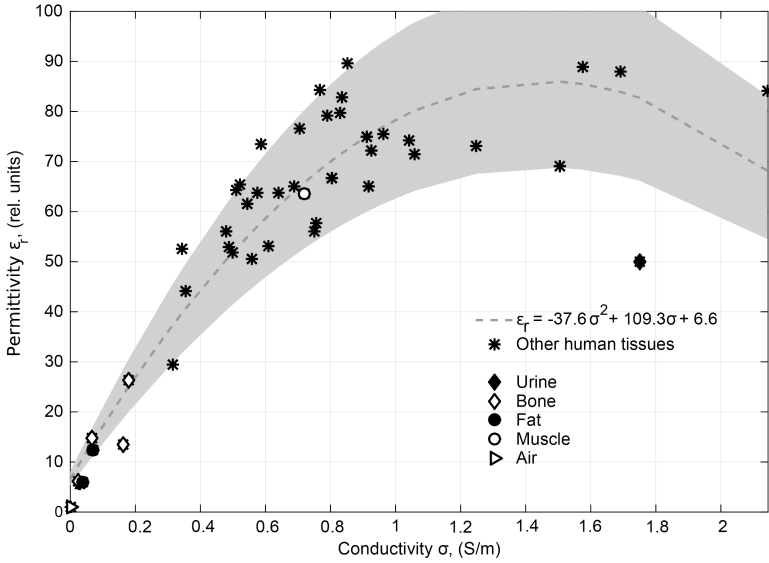


Figure 4A.1. Permittivity-Conductivity scatterplot of human tissues at 128 MHz. The values for electrical properties of tissues were taken from [22]. The dash grey line represents the polynomial fit to the data and the shaded area represents the $\pm 20\%$ error.

Note that we preferred using in vivo σ and ϵ_r values, when available in literature, over common tabulated mean values [10,22]. Hereafter, we explain how EP ranges were determined for each segmented tissue:

- Fat: minimum values for both σ and ϵ_r distributions were taken from Gabriel et al. [10], whereas maximum values were based on Peyman et al. [32].
- Muscle: Minimum, mean and maximum σ values were selected from Balidemaj et al. [102]. No in vivo ϵ_r variability was found in literature, therefore strategy (ii) was adopted. Gabriel et al.'s [10] mean ϵ_r was used.
- Bone: EPs in bone segmentation were randomly selected from two different EP distributions, i.e. cortical or cancellous tissues. Including these two tissues was a compromise between MRI and hyperthermia treatment planning: on the one hand, EPs of cancellous bone, a voluminous tissue, are expected to greatly influence the measured B_1^+ field; on the other hand, EPs of cortical bone, a thin interfacial layer, may prove critical in hyperthermia treatment planning to correctly assess the magnitude of hot spots. Conductivity and permittivity ranges were defined as in (iii). In particular, cancellous EP range = $[0.8, 1]$ ·literature EPs; cortical EP range = $[1, 1.2]$ ·literature EPs, where the corresponding literature EPs were taken from Gabriel et al. [10].
- Bladder: Empty and full bladders had different EPs. Empty bladders were given muscle EPs. Full bladders were assigned bladder content EPs: σ distribution was based on Balidemaj et al. [102], whereas ϵ_r distribution was taken from Fu et al. [12]'s values for urinary bladder at 128 MHz at 36°C.
- Tumour: Minimum, mean and maximum σ values were selected from Balidemaj et al. [102]. No in vivo ϵ_r range was found in literature, thus strategy (ii) was applied. Gabriel et al. [10]'s mean ϵ_r for cervix was used. Both EP maximum (/minimum) values were further increased (/decreased) by 20%.

- Metal and plastic catheters: these non-biological materials were manually segmented in some pelvic models. Because their segmentations were physically surrounded by muscle (and because they are typically absent in the human body), they were considered dielectrically equivalent to muscle.

4.B Appendix B: Supplementary figures

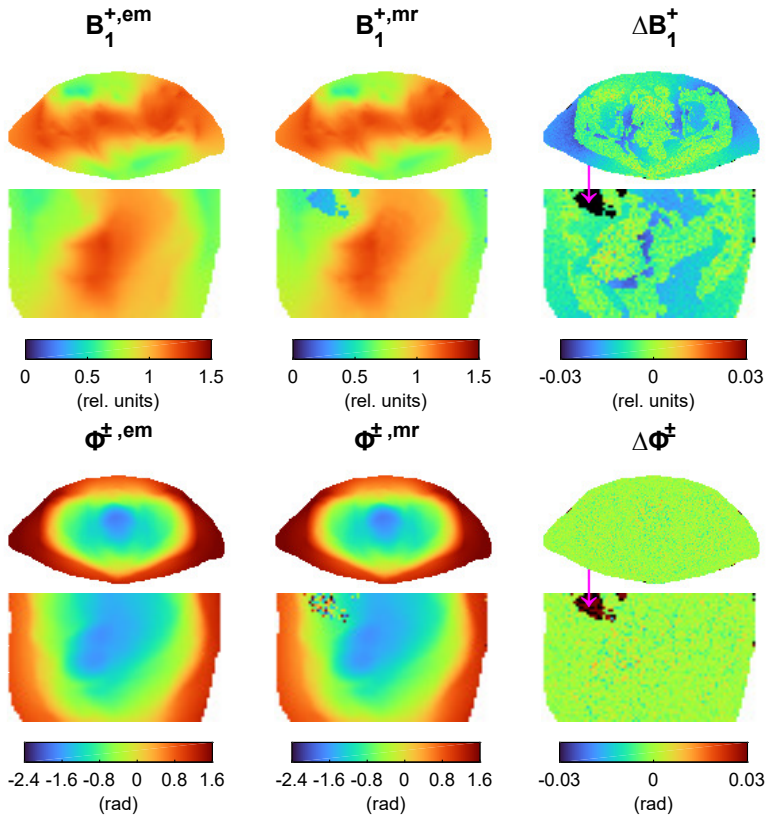


Figure 4B.1. Comparison between $|B_1^+|$ (top row) and ϕ^\pm (bottom row) obtained from EM and noisy MR simulations. First column: $|B_1^{+,em}|$ and $\phi^{\pm,em}$ maps. Second column: $|B_1^{+,mr}|$ and $\phi^{\pm,mr}$ maps. Third column: Difference maps ΔB_1^+ and $\Delta \phi^\pm$, obtained as difference between data from noisy MR simulations (in second column) and data from EM simulations (in first column). Magenta arrows in difference maps point to an air pocket.

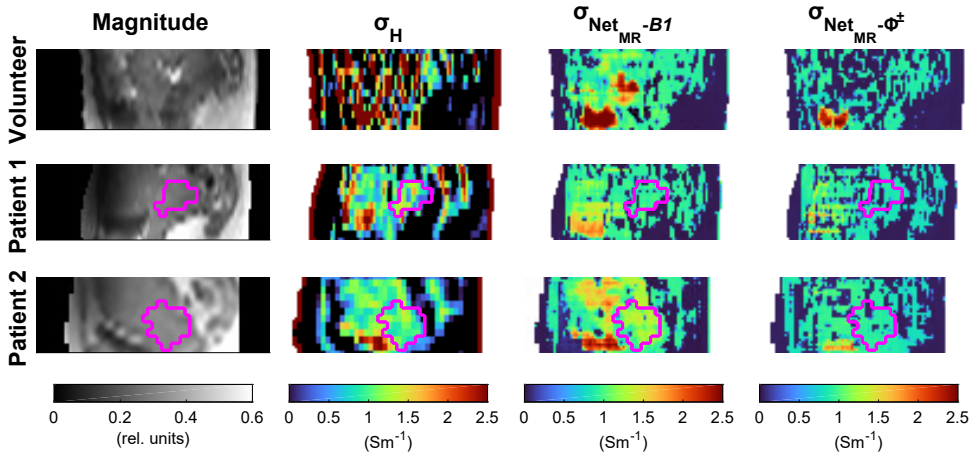


Figure 4B.2. In vivo conductivity results on a healthy volunteer and two cervical cancer patients (sagittal view). Magnitude image from SE acquisition (*first column*), Helmholtz-based conductivity map (σ_H , *second column*), DL-EPT conductivity map reconstructed with $\text{Net}_{\text{MR}-B1}$ (*third column*) and DL-EPT conductivity map reconstructed with $\text{Net}_{\text{MR}-\phi^\pm}$ (*fourth column*) are shown. The tumour delineation is displayed in magenta colour. (Transversal view is shown in Figure 4.8).

Advanced patient-specific hyperthermia treatment planning

Soraya Gavazzi, Astrid L.H.M.W. van Lier, Cornel Zachiu, Eric Jansen, Lukas J.A. Stalpers, Jan J.W. Lagendijk, Hans Crezee, H. Petra Kok

published in:

International Journal of Hyperthermia 2020; 37(1):992-1007, doi:10.1080/02656736.2020.1806361

ABSTRACT

Hyperthermia treatment planning (HTP) is valuable to optimize tumour heating during thermal therapy delivery. Yet, clinical hyperthermia treatment plans lack quantitative accuracy due to uncertainties in tissue properties and modelling, and report tumour absorbed power and temperature distributions which cannot be linked directly to treatment outcome. Over the last decade, considerable progress has been made to address these inaccuracies and therefore improve the reliability of hyperthermia treatment planning. Patient-specific electrical conductivity of tissues derived from MR measurements has been introduced to accurately model the power deposition in the patient. Thermodynamic fluid modelling has been developed to account for the convective heat transport in fluids such as urine in the bladder. Moreover, discrete vasculature trees have been included in thermal models to account for the impact of thermally significant large blood vessels. Computationally efficient optimization strategies based on SAR and temperature distributions have been established to calculate the phase-amplitude settings that provide the best tumour thermal dose while avoiding hot spots in normal tissue. Finally, biological modelling has been developed to quantify the hyperthermic radiosensitization effect in terms of equivalent radiation dose of the combined radiotherapy and hyperthermia treatment. In this paper, we review the present status of these developments and illustrate the most relevant advanced elements within a single treatment planning example of a cervical cancer patient. The resulting advanced HTP workflow paves the way for a clinically feasible and more reliable patient-specific hyperthermia treatment planning.

5.1 Introduction

Clinical hyperthermia aims at heating the tumour to a temperature of 39–43°C in order to increase the therapeutic effect of radiotherapy and/or chemotherapy. Several clinical trials have demonstrated that complementing these two standard oncological treatments with hyperthermia improves the tumour response and patient survival for different tumour sites (e.g. cervix [210,211], breast [212], bladder [213], soft tissue sarcoma [214]). In general, a therapeutic thermal dose of 43°C for 1 hour is pursued in the tumour [215,216], in view of the demonstrated thermal dose-effect relationship [217–219]. This desired tumour thermal dose is often not achieved because of treatment limiting hot spots exceeding 45°C in normal tissue. Achieving optimal tumour heating while avoiding hot spots in healthy tissues is a clinical challenge. Hyperthermia treatment planning (HTP) can be helpful to improve treatment quality, especially for locoregional hyperthermia as applied to deep-seated (pelvic) tumours, for which the use of HTP is recommended by the most recent quality assurance guidelines [220]. Locoregional hyperthermia is usually applied by heating systems consisting of phased-arrays of radiofrequency (RF) antennas, operating at frequencies between 60–130 MHz for deep-seated pelvic tumours [221,222], between 300–600 MHz for brain tumours [223] and at 434 MHz for head and neck tumours [224]. Thus, some extent of normal tissue heating is inevitable and several degrees of freedom (i.e. the amplitudes and phases of the individual antennas) are available to optimize the temperature distribution. In this respect, HTP can be very useful to predict optimal settings for effective tumour heating during thermal therapy delivery [197,225,226]. In this introduction, we review the current practice in HTP workflow and the recent research progress made to improve HTP accuracy.

In the typical clinical HTP workflow, an anatomical patient model is generated by segmenting a pre-treatment CT or MR image [197,227,228]. For each segmented tissue, dielectric (or electrical) and thermal tissue properties are normally assigned from tabulated literature data. Then, electromagnetic and thermal simulations are performed to obtain the electric field, power absorption and temperature distribution in the patient's body for selected phase-amplitude settings. Thermal modelling is generally based on Pennes' bioheat equation [229], which models the heat transfer from blood to tissue as a heat sink term proportional to the local volumetric blood perfusion and the difference between local tissue temperature and the assumed blood temperature. Subsequently, automatic optimization techniques [225,230–233] predict the phase-amplitude settings for the individual antennas to realize optimal heat deposition in the tumour while preventing overheating of normal tissue. Notwithstanding various studies reported good qualitative agreement between HTP simulations and clinical observations during treatment [234–237], present hyperthermia treatment plans lack quantitative accuracy because of uncertainties in dielectric [174,185,238] and thermal [233] parameters and because of approximate heat transport modelling of blood flow and heat convection in fluids [200,239,240]. Furthermore, these hyperthermia treatment plans report only power and temperature distributions, but do not allow easy interpretation of the increased radiosensitization and therefore of the added clinical benefit to the primary treatment. Over the past years, substantial effort has been put into research to improve the reliability of hyperthermia treatment planning.

An important advancement is the measurement and inclusion of patient-specific electrical tissue properties. Indeed, uncertainties (up to 50%) in dielectric properties, in particular in the electrical conductivity, can cause average errors of 20% in the predicted power deposition [174], therefore leading to suboptimal prediction of tumour heating and hot spots outside the target region. Permittivity and conductivity maps were initially obtained from the water and fat content determined using standard MRI sequences [51, 52]. A shortcoming of these

methods is that they are calibrated on literature values and thus they neglect the impact of heterogeneities in ionic concentration, blood content and tumour pathophysiology in the calculation of the electrical properties. Subject-specific maps of the electrical conductivity were later reconstructed with another MR-based technique, called MR Electrical Properties Tomography (EPT), which relies on measurements of the RF magnetic transmit field, also called B_1^+ , generated within the body during an MR scan [57,58]. Balidemaj et al. [131] reported a substantial effect of including EPT conductivity values in the patient models for HTP, compared to using literature values: differences in the predicted temperature ranged from 0.6°C to 1.5°C in five patients. However, the accuracy of EPT at tissue interfaces and its robustness against noise are limited. Lately, Mandija et al. [121] have pioneered an EPT technique exploiting Deep Learning (DL-EPT). In DL-EPT, electrical properties of a body site at a specific field strength are reconstructed by a convolutional neural network trained on large datasets of simulated B_1^+ distributions. Very recently, a novel DL-EPT method has been developed for reconstruction of in vivo 3D conductivity maps in the pelvic region [241]. Both the in silico validation and the in vivo comparison with a conventional EPT technique demonstrated that this DL-EPT method is able to reconstruct pelvis conductivity maps with high noise-robustness and accuracy at tissue interfaces.

Sophisticated modelling of the thermal impact of blood flow, urine and cerebrospinal fluid has been developed to calculate more accurate temperature distributions during hyperthermia for various tumour sites. Since the substantial heat exchange between individual large blood vessels and the surrounding tissues is ignored in the Pennes heatsink model, thermal models including discrete vessels have been proposed [242–244]. The discrete vasculature model (DIVA) by Kotte et al. [245,246] efficiently represents 3D patient-specific vessel trees within a 3D thermal model. Raaymakers et al. [247] experimentally validated the DIVA temperature prediction, demonstrating that temperature profiles in the vicinity of a large vessel in the heated area corresponded well to the measured temperature profiles, in contrast to the temperature profiles predicted by the simple Pennes model [239,240,248]. Sumser et al. [248] reported maximum temperature differences of $\sim 1^\circ\text{C}$ between DIVA and Pennes models for target volumes close to large vessels. In case unbound body fluids, e.g. urine and cerebrospinal fluid, are present in the heated region, convection will influence the temperature distribution. Schooneveldt et al. developed convective fluid models of the bladder [200,249] and cerebrospinal fluid [250] to accurately represent the fluid dynamics during hyperthermia. In the bladder, for example, more realistic and homogeneous temperatures were predicted by the complete fluid thermodynamic model. Compared to the default model, in which the bladder was modelled as a solid perfused (muscle) tissue, mean deviations between temperature predictions and measurements during treatment reduced from 4°C to 0.6°C [200].

Several phase-amplitude optimization techniques have been developed to efficiently calculate the effective phase-amplitude steering settings for modern phased-array systems. These techniques are normally referred to as SAR-based [225,231,251,252] or temperature-based [233,253] optimization strategies, depending on whether their optimization principle is applied to the SAR distribution or the temperature distribution. SAR-based optimization typically maximizes the quotient of the absorbed power in the tumour and a weighted energy norm outside the tumour [230]. Additional weight functions can be defined to account for potential hot spot locations, or regions which are known to have a significantly different perfusion. Nonetheless, temperature hot spots can still occur after SAR-based optimization. Temperature-based optimization allows for direct constraints to normal tissue temperatures, but fast thermal computations are essential since many temperature evaluations need to be performed during optimization. For this purpose, Cheng et al. [254] proposed a concept called “virtual sources”, which uses a weighted combination of pre-calculated phase-amplitude

configurations. Das et al. [255] formulated a method based on superposition of pre-calculated temperature distributions, based on Pennes' bioheat equation. By extending the concept of temperature superposition to DRVA thermal modelling, Kok et al. [256] enabled efficient temperature-based optimization accounting for discrete vasculature.

Recently, biological modelling has been introduced to quantify the radiosensitization effect of hyperthermia. In this regard, Kok et al. [257] presented a method to predict the effect of hyperthermic radiosensitization in terms of equivalent enhanced radiation dose, i.e. the radiation dose yielding the same biological effect as the combined radiotherapy plus hyperthermia treatment. In this model, the equivalent dose calculation is based on an extended version of the linear-quadratic (LQ) model with temperature-dependent radiosensitivity parameters α and β reflecting the radio-sensitizing effect of hyperthermia. Literature data on the radiobiological parameters of different tumour and normal tissues at hyperthermic temperatures are scarce, therefore α and β are normally determined based on few studies reporting the α and β values for some specific tumour cell lines at specific temperatures [258,259]. Myerson et al. [260] and van Leeuwen et al. [261] went a step further: Myerson et al. [260] modelled the heat-induced radiosensitization as changes in the α parameter based on results from in vitro hyperthermia studies; van Leeuwen et al. [261] derived the α and β behaviour from mathematical modelling based on biological experiments on cervical cancer cell lines. Furthermore, Franken et al. [259] and Datta and Bodis [262] concluded that the rise in tumour temperature during hyperthermia significantly changes the tumour α/β ratio, based on cell survival experiments and on clinical data. Studies in in vivo tumour models [263,264] also demonstrated that hyperthermia is tumour-selective as it does not cause significant radiosensitization in normal tissues, provided radiotherapy and hyperthermia are given sequentially. Hence, normal tissue α and β values are assumed to be much less temperature-dependent. In general, results from biological modelling in prostate [257], cervical cancer [265], and recurrent paediatric sarcoma patients [266] demonstrated considerable dose escalations for the combined treatment, highlighting the importance to take the synergistic action of radiotherapy and hyperthermia into account during the treatment planning.

Thus, substantial improvements on various aspects of hyperthermia treatment planning have been realized, but these elements should be integrated into a single HTP workflow to fully exploit the benefits of this research. Hence, in this paper we demonstrate how to integrate the most relevant advanced developments in this field into a single workflow, thereby illustrating an example for advanced patient-specific hyperthermia treatment planning.

5.2 Hyperthermia Treatment Planning workflow

We demonstrate the advanced workflow for hyperthermia treatment planning on a cervical cancer patient. The patient underwent a diagnostic MRI examination, after which she was diagnosed with stage IIIB adenosquamous carcinoma of the cervix. The patient received a combined radiotherapy (RT) + hyperthermia (HT) treatment. An external beam radiation dose of 46 Gy (23×2 Gy) was given, followed by a 24 Gy brachytherapy boost using pulse dose rate (PDR) brachytherapy. Five weekly hyperthermia treatments were delivered after an external beam RT session, by using the 70 MHz AMC-4/ALBA-4D locoregional hyperthermia system. According to the clinical protocol, a planning CT scan was made for both external beam radiotherapy and hyperthermia. The external beam dose distribution was calculated using Oncentra External Beam (Elekta AB, Stockholm, Sweden). Hyperthermia treatment planning was performed using Plan2Heat [175].

Hereafter, we outline first the clinical imaging acquisition protocols, then we describe the

methodologies used for advanced hyperthermia treatment planning, which include DL-EPT patient-specific tissue conductivity values, modelling of large vasculature, an effective thermal conductivity accounting for convection within the urine in the bladder, phase-amplitude optimization and biological modelling. The advanced hyperthermia treatment planning workflow is also schematically illustrated in Figure 5.1.

5.2.1 Imaging protocols

MR The diagnostic MRI examination was carried out with a 3T clinical scanner (Ingenia, Philips Healthcare, Best, the Netherlands) with a 26-channel torso receive coil. A 3D spoiled gradient echo was acquired with flip angle (FA) = 10° , TR = 5.6 ms, echo train length = 3, SENSE accelerator factor = 1.5 for both phase encoding directions, FOV = $350 \times 350 \times 98 \text{ mm}^3$, resolution = $1.22 \times 1.22 \times 1.3 \text{ mm}^3$, scan time = 1:51 minutes, and processed according to a generalized two-point Dixon's method [267]. The resulting water-only image was used for vascular segmentation.

Additionally, a 3D AFI sequence [68] and a 2D multi-slice spin echo (SE) sequence were performed to reconstruct the amplitude of the B_1^+ field, $|B_1^+|$, and the transceive phase, ϕ^\pm , respectively, which are necessary for EPT reconstruction. AFI was performed with $FA = 65^\circ$, $TR_1 = 30 \text{ ms}$, $TR_2 = 120 \text{ ms}$, $TE = 2.5 \text{ ms}$, total scan time = 3:30 minutes. SE parameters were: imaging $FA = 90^\circ$, $TR = 1200 \text{ ms}$, $TE = 6.2 \text{ ms}$. SE was performed twice with opposing readout gradient polarities to acquire an eddy current-free transceive phase map (total scan time = 6:57 minutes). A $FOV = 400 \times 280 \times 120 \text{ mm}^3$ and resolution = $5 \times 5 \times 7.5 \text{ mm}^3$ were used for both AFI and SE.

The duration of the entire MR examination for this patient was $\sim 50 \text{ min}$. This includes 5–10 min of patient preparation time and 27 min of standard diagnostic MRI. The additional MR-EPT protocol took 10 min.

CT The planning CT image for external beam RT treatment (RT-CT) was obtained with a Philips Gemini TF 16 PET/CT scanner (Philips, Best, The Netherlands). The RT-CT image was acquired with $FOV = 600 \times 600 \times 363 \text{ mm}^3$ and resolution = $1.17 \times 1.17 \times 3.0 \text{ mm}^3$ with the patient in supine position. As part of the clinical protocol, a bowel contrast agent was used during RT-CT scan session in order to allow bowel delineation and sparing during the following radiotherapy treatment planning.

The planning CT image for hyperthermia treatment (HT-CT) was acquired mimicking the hyperthermia treatment setup, i.e. with the patient in supine position on a water bolus and mattresses and with the intravaginal plastic pelotte for temperature monitoring during treatment in situ. The HT-CT image was acquired with a GE LightSpeed RT16 CT scanner (GE Healthcare, USA) with $FOV = 650 \times 650 \times 680 \text{ mm}^3$ and resolution = $1.27 \times 1.27 \times 2.5 \text{ mm}^3$.

The durations of the RT-CT and HT-CT examinations were 10–15 min each. For logistic reasons, the HT-CT scan was performed in a separate imaging session after the first hyperthermia treatment. Both the RT-CT and HT-CT could be obtained within a single session; in that case, the HT-CT image should be acquired first, to avoid Hounsfield unit-based tissue segmentation (see next section) being complicated by the presence of bowel contrast.

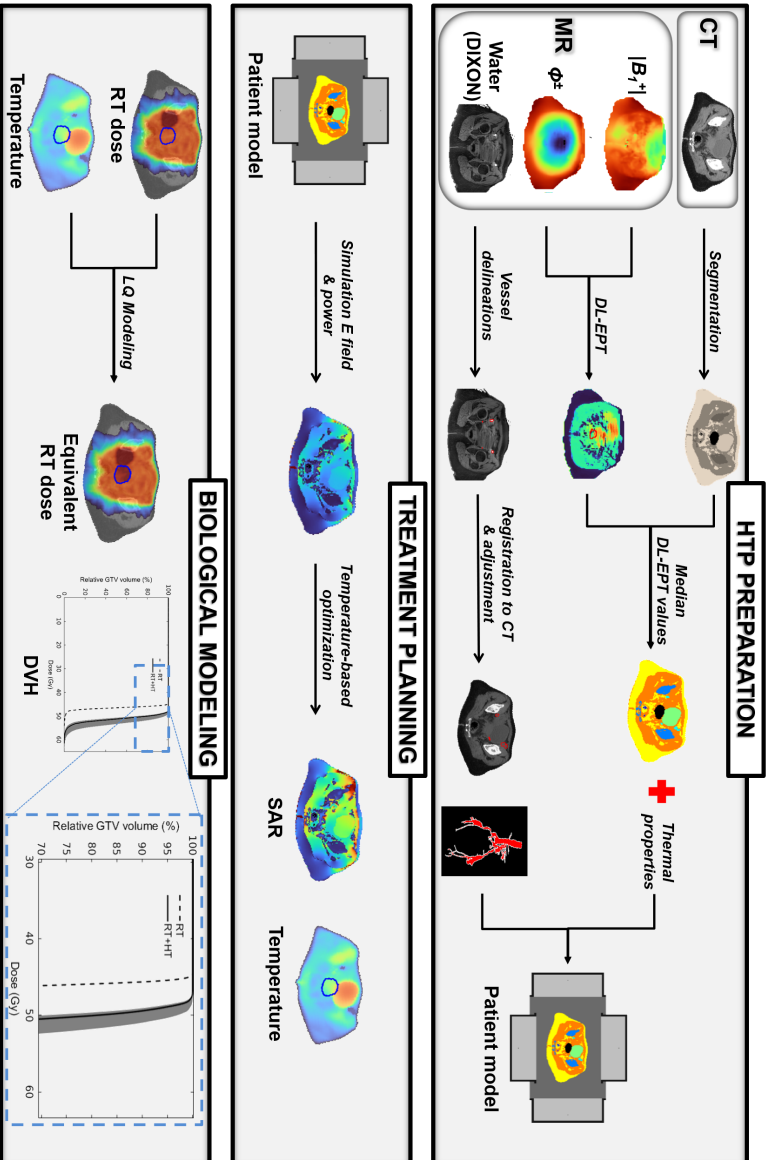


Figure 5.1. Workflow describing schematically all the methodological steps performed for advanced HTP. In HTP preparation, the patient anatomical model is obtained from CT segmentation. The vasculature, reconstructed from an MR scan and registered to the CT, is also included in this model. The dielectric properties are assigned to each tissue type based on the median DL-EPT values. The thermal properties are assigned from literature values, but an effective thermal conductivity accounting for convective heat transfer in the bladder is assigned. Next, treatment planning is performed, in which the electric field distribution is calculated and phase-amplitude settings for effective tumour heating are optimized. Finally, biological modelling predicts the radiosensitizing effect of hyperthermia in terms of an equivalent enhanced radiation dose.

5.2.2 Preparation of the patient model for HTP

Tissue geometry The HT-CT scan was semi-automatically segmented based on Hounsfield units with an in-house developed software package, Plan2Heat [175], resulting into fat, muscle, bone and air segmentations. Gross tumour volume (GTV), bladder and the intra-vaginal plastic pelotte were segmented manually (delineation time: ~ 20 min).

Vascular structures with diameters $\gtrsim 3$ mm were included explicitly in the patient model. External/internal iliac arteries and veins, as well as small blood vessels (with diameter $\gtrsim 3$ mm), were manually delineated on the water-only Dixon image, by exploiting the high contrast of vessels with respect to surrounding tissues. Subsequently, these delineations were mapped onto the HT-CT image by deformable registration between the Dixon and CT images. The multi-modal EVOlution registration algorithm [268] was used, which maximizes edge alignment between the images being registered. This algorithm requires only contrast between anatomical tissues, preferably present in both image modalities, and assumes deformable/elastic tissues or volumetric tissue changes. The multi-modal EVOlution registration algorithm provides a high accuracy in mapping contours between CT and MR images, as demonstrated in a previous abdominal imaging study [269].

The contours of the registered vessels were slightly adjusted on the CT to match the vessel shape in the CT. Furthermore, the vessels registered on the CT only partially covered the patient's pelvis volume due to the smaller FOV of water-only Dixon image (~ 100 mm in cranio-caudal direction) with respect to the FOV of the HT-CT scan. Thus, the aorta, the renal arteries, the left inferior mesenteric artery, and the common iliac arteries which were identifiable only on the HT-CT image were delineated manually. The common iliac vessels were then manually connected to the registered delineations of the subordinate iliac arteries and veins.

Manual vessel delineation on the MR water-only image takes about 1.5–2.5 hours, whereas vessel delineation and adjustment on the HT-CT image may require 3–5 hours. Exact times depend on the quality of the image contrast, the image FOV and resolution, the desired minimum diameter of the vascular structures to include in the patient model and the operator's experience.

Electrical properties of tissues Recently, Gavazzi et al. [241] have developed a DL-EPT approach for pelvis conductivity mapping where a convolutional neural network infers the conductivity of pelvic tissues from $|B_1^+|$ and ϕ^\pm maps measured with MRI, after being trained on in silico dielectric pelvic models with realistic conductivity values at 128 MHz. For implementation details, validation and comparison with a conventional EPT method, the reader is referred to Chapter 4. The conductivity is reconstructed in ~ 10 seconds on an NVIDIA Tesla P100 GPU with 16 GB RAM.

Electrical properties of tissues were assigned a single value for each tissue type in the segmented patient model. The conductivity of fat, muscle, bone, tumour and bladder corresponded to the median DL-EPT conductivity value calculated in manually delineated 3D regions of interest (ROIs) per tissue. Tissue ROI delineation took approximately 30 min. These conductivity values, measured at 128 MHz (the Larmor frequency of the 3T MR system), were decreased by 3% to obtain conductivity values at 70 MHz (the operating frequency of our hyperthermia system) [131]. The tissue permittivity was taken from literature for two main reasons: first, retrieving the permittivity with EPT at 128 MHz has proven challenging for conventional EPT [57, 199], and has not been shown yet in the pelvis with DL; second, even large changes in permittivity (e.g. in muscle) affect very little the temperatures predicted by

Table 5.1. Electrical and thermal properties of pelvic tissues at 70 MHz. Bold font indicates the parameters that were introduced in this study and differing from literature values (in normal font). σ : Conductivity; ϵ_r : Permittivity; ρ : Density; c_t : Specific heat capacity; k_t : Thermal conductivity; W_b : Perfusion.

	σ ($S \cdot m^{-1}$) ^a	ϵ_r (rel. units)	ρ ($kg \cdot m^{-3}$)	c_t ($J \cdot kg^{-1} K^{-1}$)	k_t ($W \cdot m^{-1} K^{-1}$)	W_b ($kg \cdot m^{-3} s^{-1}$)
Air	0	1	1.29	10000 ^b	0.024	0
Bladder	1.22	50	1024	4178	5.6^c	0
Blood	0.83	84.1	1050	3617	0.52	-
Bone	0.12	16.4	1908	1313	0.32	0.12
Fat	0.04	13.4	911	2348	0.21	1.1
Muscle	0.91	70.8	1090	3421	0.49	3.6
Cervical tumour	1.02	70.8	1090	3421	0.49	1.8

^a The values of σ obtained with DL-EPT at 128 MHz were decreased by 3% to determine the values at 70 MHz.

^b The value of c for air is ten times higher to permit larger time steps in thermal computations. This has a negligible effect on the steady state temperature.

^c The value of k for bladder was ten times higher than the literature value to account for convection phenomena in the bladder.

HTP [131]. The electrical properties of blood were also assigned from literature [10,22]. This is justified, since *ex vivo* electrical properties of blood can be expected to be rather similar to *in vivo* values. Electrical properties of tissues are reported in Table 5.1, along with thermal properties.

Thermal properties of tissues Thermal properties of tissues were derived from the literature [22,270]. A constant perfusion model was used, with enhanced perfusion values to account for the effect of hyperthermic temperatures based on experimental data [271]. A dedicated modelling approach was adopted for the bladder. Recent studies have shown that modelling fluid convection has a large impact on the final temperature distribution, yielding more accurate hyperthermia treatment planning [200,249,250,272]. However, modelling convective heat transfer is computationally time-consuming at this moment, which makes it impractical for routine clinical use. A practical and time-efficient alternative is to increase the effective thermal conductivity of the fluid. This strategy was shown to approximate the thermal effect of fluid dynamics fairly well [250,272]. We included this strategy to account for convective heat transfer in the urinary bladder, which we modelled to have zero perfusion and thermal conductivity 10 times higher than the literature value [200,250,272].

5.2.3 Hyperthermia Treatment Planning

Simulation of the electric field The dielectric patient model was down-sampled to a resolution of $2.5 \times 2.5 \times 2.5 \text{ mm}^3$ based on the winner-takes-all principle [273]. The patient model was then placed within a model of the ALBA-4D hyperthermia system (Medlogix, Rome, Italy) [274], consisting of 1 ring with 4 waveguides operating at 70 MHz (Figure 5.1). Finite Difference Time Domain (FDTD) simulations of the electric field (E-field) were performed with perfectly matched layer boundary conditions [275]. The E-field was computed separately for each antenna with unit amplitude and zero phase and takes 1–1.5 hours per antenna on an NVIDIA GeForce GTX 760 GPU. The exact computation time depends on the computational volume, which is determined by the patient size. The electric field maps were used as input for the optimization of amplitude-phase antenna settings. Superposition can be used to calculate the SAR distributions for specified antenna settings.

Thermal modelling and temperature-based optimization Thermal modelling was based on Pennes' bioheat equation [229]:

$$c_t \rho_t \frac{\partial T}{\partial t} = \nabla \cdot (k_t \nabla T) - \omega c_b (T - T_{art}) + Q + \rho \cdot \text{SAR} \quad (5.1)$$

In Equation 5.1 the temperature change over time in the tissue lies on the left-hand side, with c_t ($\text{J} \cdot \text{kg}^{-1} \text{K}^{-1}$) the tissue's specific heat per mass, ρ_t ($\text{kg} \cdot \text{m}^{-3}$) its mass density, T (K) the temperature, and t (s) the time. On the right side of Equation 5.1 the first term represents the thermal conduction, with k_t ($\text{W} \cdot \text{m}^{-1} \text{K}^{-1}$) the tissue thermal conductivity; the second term models the perfusion, with c_b ($\text{J} \cdot \text{kg}^{-1} \text{K}^{-1}$) the specific heat per mass of blood, ω ($\text{kg} \cdot \text{m}^{-3} \text{s}^{-1}$) the volumetric perfusion rate, and T_{art} the arterial blood temperature; Q ($\text{W} \cdot \text{m}^{-3}$) is the metabolic heat rate, which is negligible during hyperthermia; the last term is the power absorption induced by the heating system, which is proportional to the SAR.

The delineated blood vessels, representing arteries and veins visible on the water-only Dixon and HT-CT images, have a large diameter ($\gtrsim 3$ mm) and thus also a high flow velocity ($\geq 15 \text{ cm} \cdot \text{s}^{-1}$ [276]). This implies that these vessels do not reach thermal equilibrium with surrounding tissue when reaching and traversing the heated region [276]. Therefore, modelling a constant temperature boundary condition is justified and a 37°C temperature was imposed to the vessel delineations during the thermal computation.

Based on this thermal model, phase-amplitude antenna settings were optimized to realize a favourable 3D steady state temperature distribution for optimal tumour heating. For efficient calculations during optimization, temperature super-positioning was used to calculate the temperature distribution for any arbitrary set of phases and amplitudes by a vector-matrix-vector multiplication [255,256]. The vector represents the antenna settings and the matrix elements are pre-calculated by decomposition of Equation 5.1. Quadratic programming was used to maximize the cost function, which was defined as the tumour T90 (i.e. the temperature exceeded in 90% of the tumour volume), while constraining the maximum temperature for normal tissues to 45°C . Further constraints were imposed on the antenna contributions to avoid clinically unrealistic power settings: in particular, each antenna was set to deliver at least 10% and at most 40% of the total power. Calculation of the 11 $(\frac{N^2+N}{2} + 1; N$ number of antennas, with $N = 4$) temperature distributions needed for superposition takes about 30 seconds each, using an NVIDIA GeForce GTX 760 GPU. The actual optimization takes less than 5 min on an Intel Xeon E5-1650 v3 3.5 GHz running CentOS 6.8.

5.2.4 Biological modelling

Biological modelling was performed to obtain insight into the radiosensitizing effect induced by hyperthermia, assuming hyperthermia is applied for 1 hour once a week, directly after external beam radiotherapy. This effect was expressed in terms of equivalent radiation dose EQD_{RT} , i.e. the radiation dose yielding the same effect as the combined RT + HT treatment. The EQD_{RT} calculation is based on an extended linear-quadratic (LQ) model, which includes temperature-dependent radiosensitivity parameters $\alpha(T)$ and $\beta(T)$ [257,265]. Calculations were performed using the in-house developed software package, X-Term [277], which determines the EQD_{RT} per voxel from the radiotherapy dose distribution and the temperature distribution. Calculation of the EQD_{RT} is described more in detail in the following sections.

Preparation Because the equivalent radiation dose is calculated on a voxel-by-voxel basis from the RT dose distribution and from the temperature distribution, these two maps need

to be matched on the same reference frame. Therefore, the RT-CT and HT-CT scans were registered with an intensity-based deformable image registration algorithm embedded in Velocity Medical Solutions (Varian Medical Systems, Palo Alto, CA). First, the bony anatomy was rigidly registered between both scans, followed by a deformable registration as described by Crezee et al. [265]. The resulting deformation vector field was then applied to resample the RT dose distribution onto the HT-CT image. This process takes up to 0.5–1 hour, including corrections and fine-tuning of the (structure-guided) deformable image registration.

Equivalent radiation dose calculation The equivalent radiation dose for RT + HT treatments was calculated instantly, by using the following equation [261]:

$$EQD_{RT} = D \cdot \frac{\alpha(T) + G \cdot \beta(T) \cdot D}{\alpha(37) + d_{ref} \cdot \beta(37)} + \frac{7.38 \cdot 10^{13} \cdot (T + 273.15) \cdot \exp\left(\frac{\delta S}{2} - \frac{\delta H}{2 \cdot (T + 273.15)}\right)}{\alpha(37) + d_{ref} \cdot \beta(37)} \quad (5.2)$$

where $\alpha(T)$ and $\beta(T)$ are the temperature-dependent radiosensitivity parameters, $\alpha(37)$ (Gy^{-1}) and $\beta(37)$ (Gy^{-2}) are the radiosensitivity parameters at $37^\circ C$, G is the Lea-Catcheside protraction factor accounting for repair during irradiation, D (Gy) is the total dose, d_{ref} (Gy) is the fraction dose of the RT treatment (i.e. 2 Gy), δS ($cal/^\circ C/mol$) is the entropy of inactivation and δH is the inactivation energy of the critical rate-limiting molecules causing cell death.

The temperature-dependent tumour LQ parameters α and β were applied only within the GTV region, whereas α and β were kept at their normothermic value in the surrounding normal tissue regions. Similar equivalent dose calculations could be applied to normal tissue, but here we calculated only the EQD_{RT} in the tumour region to evaluate the possible effect of the combined treatment. This was motivated by the fact that radiosensitization in normal tissue is much lower compared to the tumour region, not only when hyperthermia is applied within 1-4 hours after radiotherapy [263,264], but also for time intervals shorter than 1 hour [278].

Similar to [261], the temperature-dependent LQ parameters were obtained from extensive SiHa cervical cancer cell line experiments and increased exponentially with the temperature according to the following expressions:

$$\alpha(T) = \alpha(37) \cdot \exp\left[\frac{T - 37}{41 - 37} \cdot \ln\left(\frac{\alpha(41)}{\alpha(37)}\right)\right] \quad (5.3)$$

$$\beta(T) = \beta(37) \cdot \exp\left[\frac{T - 37}{41 - 37} \cdot \ln\left(\frac{\beta(41)}{\beta(37)}\right)\right] \quad (5.4)$$

After inserting Equations 5.3 and 5.2 within Equation 5.2 and substituting $\beta(37) = \alpha(37)/[\alpha(37)/\beta(37)]$, the equivalent radiation dose becomes:

$$EQD_{RT} = D \cdot \frac{\frac{\alpha(37)}{\beta(37)} \cdot \exp\left[\frac{T - 37}{41 - 37} \cdot \ln\left(\frac{\alpha(41)}{\alpha(37)}\right)\right] + G \cdot D \cdot \exp\left[\frac{T - 37}{41 - 37} \cdot \ln\left(\frac{\beta(41)}{\beta(37)}\right)\right]}{\frac{\alpha(37)}{\beta(37)} + d_{ref}} + \frac{\frac{\alpha(37)}{\beta(37)} \cdot \left[7.38 \cdot 10^{13} \cdot (T + 273.15) \cdot \exp\left(\frac{\delta S}{2} - \frac{\delta H}{2 \cdot (T + 273.15)}\right)\right]}{\alpha(37) \cdot \left(\frac{\alpha(37)}{\beta(37)} + d_{ref}\right)} \quad (5.5)$$

where the values for each parameter in Equation 5.5 are summarised in Table 5.2. The tumour α/β ratio at 37°C was 17.9 Gy. A confidence interval for the equivalent dose was also calculated as explained by van Leeuwen et al. [261].

Table 5.2. Parameters and 95% confidence intervals (within brackets) used in the EQD_{RT} calculation expressed in Equation 5.5. These values were obtained from SiHa cervical cancer cell line experiments [261].

Parameter (measure unit)	Value
$\alpha(37)$ (Gy ⁻¹)	0.386 (0.364 – 0.409)
$\alpha(37)/\beta(37)$ (Gy)	17.9 (14.6 – 22.5)
$\alpha(41)/\alpha(37)$ (-)	1.73 (1.64 – 1.83)
$\beta(41)/\beta(37)$ (-)	0.41 (0.28 – 0.59)
δS (cal/°C/mol)	392.08 (391.62 – 392.46)
δH (cal/mol)	147907.8 (NA) ^a

^a δH has no confidence interval since it is a fixed parameter.

5.3 HTP workflow results

5.3.1 HTP preparation results

Figure 5.2 presents the MR-based reconstruction of the patient-specific conductivity by using DL-EPT. The $|B_1^+|$ and ϕ^\pm maps given as input to the trained convolutional neural network are shown along with an MR magnitude image. These maps displayed characteristic patterns in the pelvis at 3T. The reconstructed DL-EPT conductivity map exhibited clear tissue conductivity contrasts, noise-robust estimation and sharp muscle/fat interfaces.

Figure 5.3 illustrates the conductivity histograms obtained within the 3D tissue ROIs. Narrow conductivity histograms were observed in muscle and fat, indicating a precise estimation. Median conductivity values for muscle and fat were 0.933 Sm⁻¹ and 0.044 Sm⁻¹, respectively. Moreover, muscle conductivity agreed with the in vivo mean value found in a previous study where 20 patients were analysed with Helmholtz-based EPT [102], whereas it was 29% higher than the tabulated value by Gabriel et al. [10]. Fat conductivity was 19% higher than the literature value for non-infiltrated fat [10]. Figure 5.3 also depicts the conductivity histograms for bladder, bone and tumour. Bone presented a median conductivity of 0.123 Sm⁻¹, a value in between the average literature conductivity values of cortical and cancellous bone (0.067 Sm⁻¹ vs 0.180 Sm⁻¹, respectively) [10]. However, the bone conductivity histogram was skewed towards lower values, possibly reflecting the heterogeneity of bone tissues. The tumour and bladder median conductivities were 1.050 Sm⁻¹ and 1.255 Sm⁻¹, respectively. A similar conductivity value for cervical cancer was found by Balidemaj et al. (1.02 Sm⁻¹) [102]. The small side tails of tumour conductivity histogram were likely caused by inaccuracies due to motion artefacts, which entered the 3D tumour delineation. Analogously, the broader histogram for bladder content could be explained by breathing ghosts and bowel motion artefacts. Hence, the bladder median conductivity was 28% lower than previously reported urine conductivity [11, 102], but still close to the range reported for 10 different patients (1.35 Sm⁻¹ to 2.60 Sm⁻¹) [102]. Such variation in bladder electrical conductivity predominantly

depends on urine salinity concentration. Note that the median conductivity values obtained with DL-EPT were obtained at 128 MHz (the Larmor frequency at 3T MR proton imaging). These values were converted to values at 70 MHz and then assigned to the corresponding tissue in the patient model (Table 5.1).

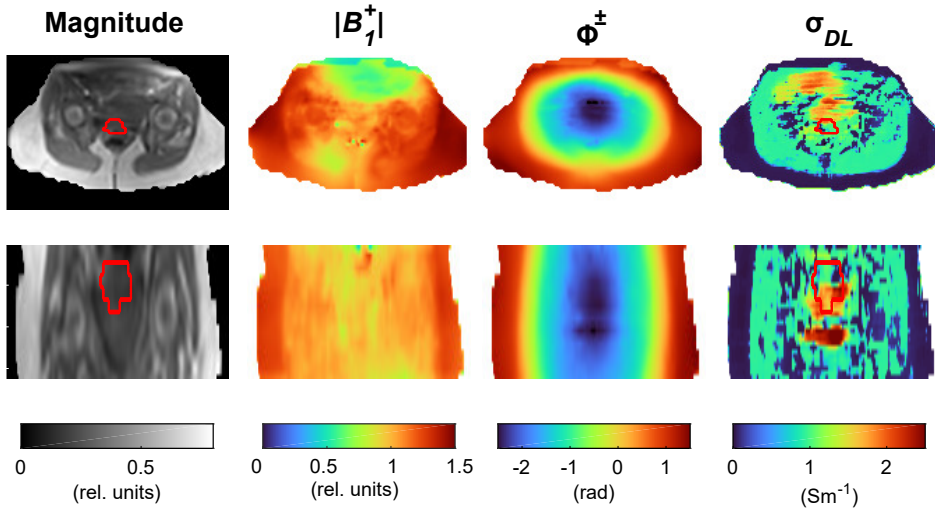


Figure 5.2. DL-EPT. Transverse and coronal cross-sections of MR magnitude image from AFI sequence, $|B_1^+|$ map, transceive phase (ϕ^\pm) map, conductivity map obtained with DL-EPT (σ_{DL}). $|B_1^+|$ and ϕ^\pm maps are given as input to the trained network, which infers σ_{DL} . The tumour contour is shown in red. The tumour was delineated by a radiation oncologist on an ADC map (part of the diagnostic MRI protocol) [204,205]. The tumour delineation was then rigidly transferred to the frame of reference of AFI image.

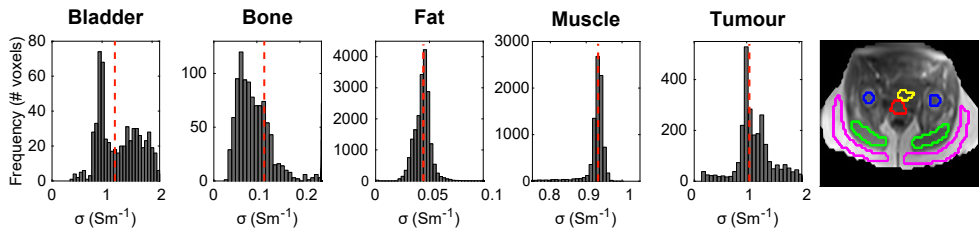


Figure 5.3. Histograms of DL-based conductivity in pelvic tissues. Conductivity histograms are reported for each tissue along with the median value (red dashed line). Conductivity histograms were based on conductivity values within manually delineated tissue ROIs, depicted on the MR magnitude image (bladder: yellow; bone: blue; fat: magenta; muscle: green; tumour: red).

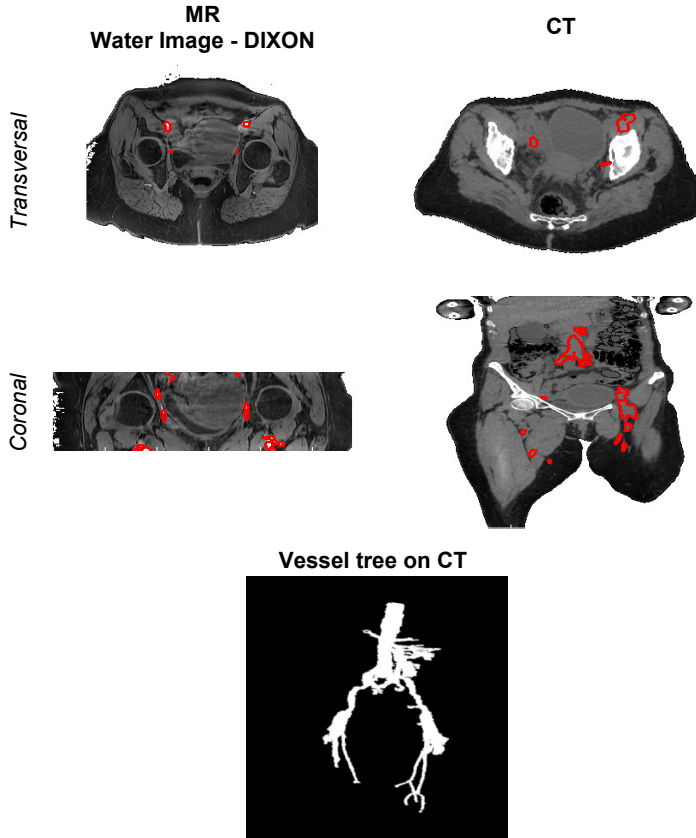


Figure 5.4. Vessel definition on MR and CT scans. Vessel delineations are shown on the transverse and coronal cross-sections of both water-only Dixon image (*left*) and HT-CT scan (*right*). These delineations were manually adjusted after MR to CT registration (not shown). At the bottom, a 3D rendering of the final vessel tree is shown.

Figure 5.4 depicts the vessels reconstructed from the water-only Dixon MR image and the HT-CT scan. Figure 5.4 clearly shows that iliac arteries and veins have high MR signal intensity with respect to the surrounding muscle in the water-only image, which was therefore exploited for vessel delineation. This benefit of using water-only Dixon scan for vascular imaging was also demonstrated in a previous study, highlighting the better image quality and ~30% higher vessel-to-background contrast provided by water-only Dixon-based contrast-enhanced MR angiography than a conventional MR angiographic technique [279]. After the multi-modal deformable registration with EVolution registering the MR image to the HT-CT frame of reference, the iliac vessel contours were manually adjusted to accurately fit the vessel shape on the HT-CT image. This is represented in the transverse view of HT-CT image. The coronal views of both MR and CT scans in Figure 5.4 also reveal the different cranio-caudal dimensions in both scans. Because of this, vessels that were outside the MR image FOV, such as the aorta, the renal arteries and common iliac arteries, were manually delineated directly on the HT-CT image. A 3D rendering of the final reconstructed vessel tree is also reported in Figure 5.4.

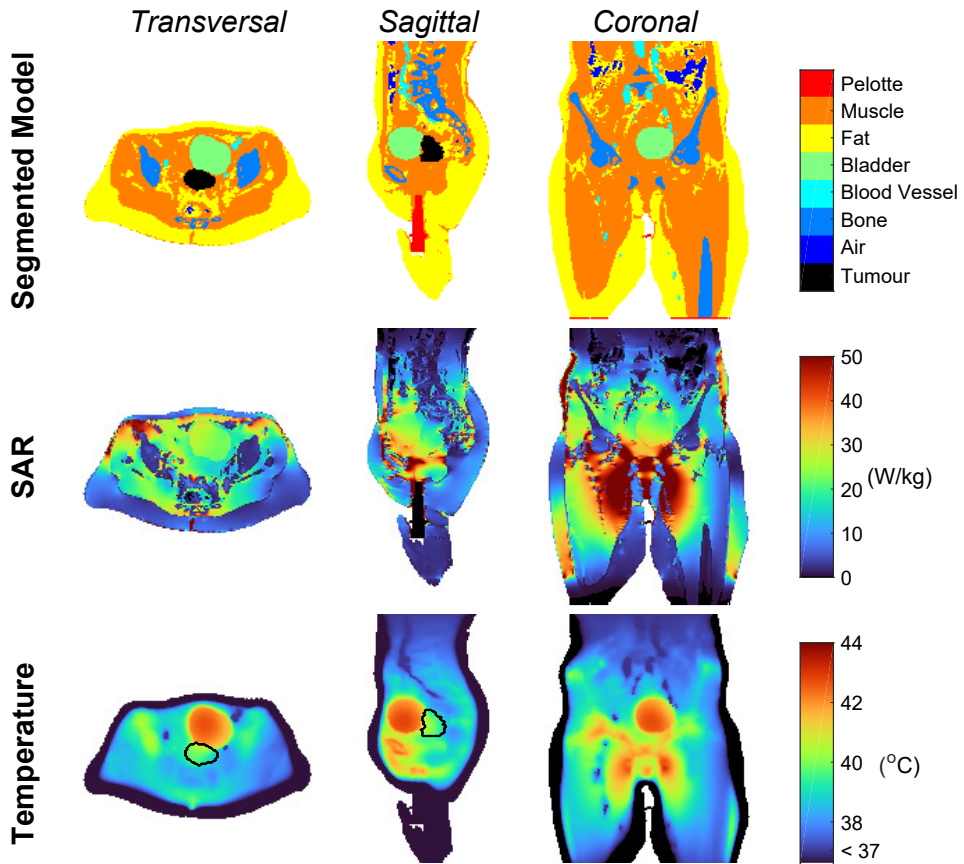


Figure 5.5. Patient model, SAR and Temperature maps. Transverse, sagittal and coronal cross-sections of the segmented model (*first row*), showing all the tissues included in the patient model, the SAR distribution (*second row*) and the temperature distribution (*third row*) in the patient. The GTV contour is indicated in black.

5.3.2 Hyperthermia treatment planning results

Figure 5.5 shows the SAR and temperature distribution after temperature-based optimization. The optimized phase settings were top/bottom/left/right = $0^{\circ}/-23^{\circ}/92^{\circ}/72^{\circ}$, and the power ratios were top/bottom/left/right = 0.23/0.10/0.28/0.39. The total power absorbed by the patient was 314 W, of which ~ 3.9 W were absorbed by the bladder (149 ml volume), whereas the tumour absorbed 1.77 W (82.6 ml volume). This is caused by the higher bladder electrical conductivity with respect to the tumour conductivity. As far as temperature is concerned, the predicted tumour T90, T50 and T10 (i.e. the temperature exceeded in 90%, 50% and 10% of the tumour volume) were 39.0°C , 39.8°C and 40.5°C respectively. The temperature map shows that the average bladder temperature was 42.15°C , which is 2.35°C higher than the tumour average temperature, reflecting the negative impact of urine on the achieved tumour thermal dose. Higher tumour temperatures could not be achieved without overheating normal tissue, since hot spots were arising outside the target region, in particular at muscle/bone and/or

muscle/fat interfaces (see, for example, close to the ischium in the sagittal view of Figure 5.5), where tissue temperatures reached the 45°C constraint. Moreover, the cold tracks induced by the flowing blood in the vessels did not influence the tumour temperature because of their distant location. However, the external iliac artery and vein, as well as the internal iliac artery (visible in the transverse view), contributed to lowering the temperature in the bladder periphery. Furthermore, the external iliac vessels, running down towards the legs (coronal view of Figure 5.5), affected the temperature of potential hot spots occurring around the pubic bone.

5.3.3 Biological modelling results

Figure 5.6 displays the dose distribution related to external beam radiotherapy treatment alone, the temperature distribution and the equivalent radiation dose distribution for the combined treatment (with an assumed fraction dose of 2 Gy, as for RT). The mean RT dose in the GTV was 46.6 Gy. The equivalent radiation dose to the tumour increased on average by 5 Gy when hyperthermia was added, leading to a mean dose value of 51.4 Gy. This 10% increase in dose is attributed to the relatively mild temperature increase achieved in the tumour during HTP. The Dose Volume Histogram (DVH, Figure 5.7) in the GTV indicates that the D95% (i.e. the dose obtained in 95% of the tumour volume) was 45.45 Gy for radiotherapy alone, and 48.9 Gy for the combined RT + HT treatment, with an uncertainty range of 48.6–50.3 Gy reflecting the uncertainty in temperature-dependent LQ parameters. The D0.01cc (the maximum dose received by at least 0.01 cm³ of the tumour volume) was 53.8 Gy and 60.8 Gy for RT alone and RT + HT combination, respectively. In addition, Figure 5.7 displays the DVH of the effective biological equivalent dose predicted when a routine HTP workflow was performed (RT + HT_{lit}, with literature-based electrical and thermal properties [10,22,270], bladder modelled as perfused muscle tissue, and no inclusion of blood vessels). This literature-based prediction led to a ~1 Gy higher mean dose with respect to the advanced RT + HT prediction. The D95% and D0.01cc for RT + HT_{lit} were 50.0 Gy (uncertainty range: 48.6–51.8 Gy) and 58.9 Gy, respectively. The impact of the advanced elements introduced in the proposed HTP workflow is thus also reflected in the predicted equivalent dose. The dose to normal tissue and organs at risk did not change, since radiosensitization in normal tissue was considered negligible [278].

5.4 Discussion

We presented a framework for advanced patient-specific hyperthermia treatment planning (HTP) in which we integrated, for the first time, the clinical HTP workflow with all currently available advanced features of HTP: (i) *in vivo* MR-based conductivity information, (ii) heat transfer modelling of the vasculature, (iii) modelling of heat convection in urine and (iv) modelling of the hyperthermia treatment effect in terms of equivalent radiation dose. As demonstrated in earlier research papers [131,240,247,248,257,265,277], each of these advanced modelling steps influences HTP predictions and ultimately contributes to reliable patient-specific treatment planning. This makes it important to include all developed advanced features into a single clinical workflow. The presented framework fulfilled this scope without excessive additional computational effort compared to the current state-of-art planning procedure. The E-field calculations of 4–6 h are unchanged and remain the most time-consuming computational part of the workflow. Also the computation time of other parts of the HTP process, e.g. temperature based optimization, did not change. For this advanced workflow, an additional 10 min of MRI scanning time is required for the MR-EPT protocol and the following DL-EPT reconstruction takes only few seconds. Manual delineation of tissues to generate the dielectric model (i.e. for tissue segmentation on the HT-CT image or for DL-EPT

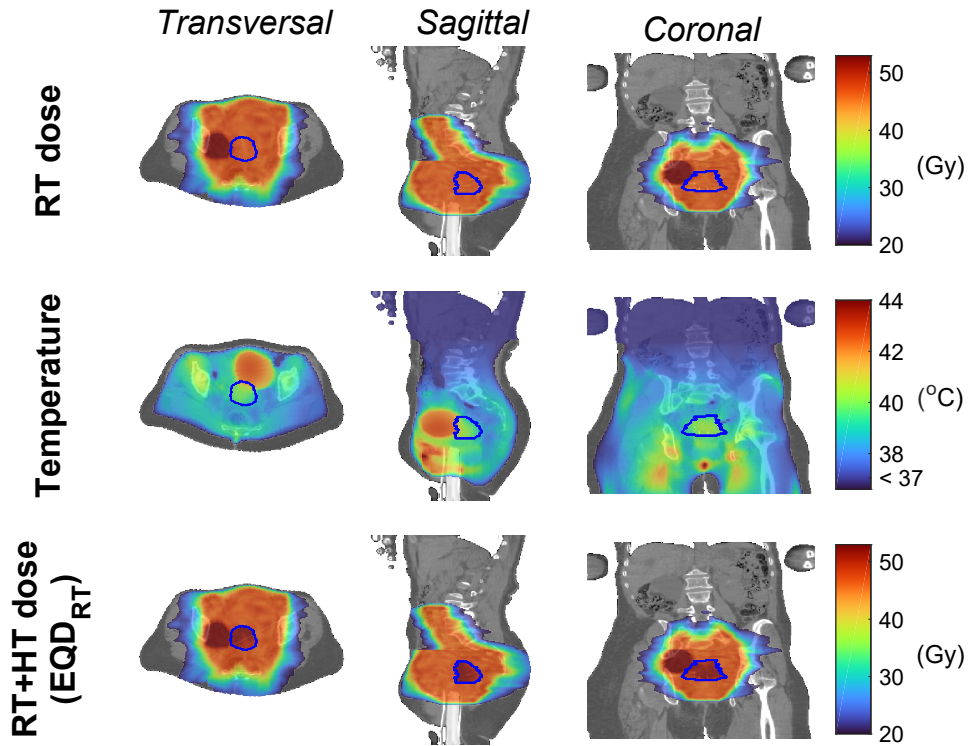


Figure 5.6. Equivalent dose distributions in radiotherapy and radiotherapy plus hyperthermia. Transverse, sagittal and coronal cross-sections of the radiotherapy (RT) dose distribution (*first row*), the temperature distribution obtained from hyperthermia treatment planning (*second row*), and the equivalent dose distribution deriving from combining radiotherapy and hyperthermia (*third row*). The equivalent radiation dose was calculated within the GTV, which is denoted with blue contours. NB: The high-dose region adjacent to the GTV reflects an additional lymph node boost (with mean dose of 54.59 Gy).

median value calculation) did not exceed 30 min. Manual delineation of blood vessels is more time-consuming (on the order of hours) and varies predominantly with image quality, desired vessel diameter and operator’s experience. These manual delineations could be automated in the future, as discussed later. The workflow was illustrated for locoregional hyperthermia of a cervical cancer patient, but a similar pipeline including patient-specific conductivity reconstruction, vasculature modelling and equivalent dose calculation could also be applied for superficial hyperthermia treatment planning.

Including DL-EPT to obtain the patient-specific conductivity represents an important progress towards reliable hyperthermia treatment planning. We have recently shown that DL-based pelvis conductivity maps display high reconstruction accuracy at tissue interfaces, robustness against noise in measured B_1^+ maps and acceptable sensitivity to conductivity variations [241]. In contrast to DL-EPT, the present state-of-art method for *in vivo* pelvis conductivity mapping [57, 102, 131], i.e. conventional Helmholtz-based EPT (H-EPT), suffers from high

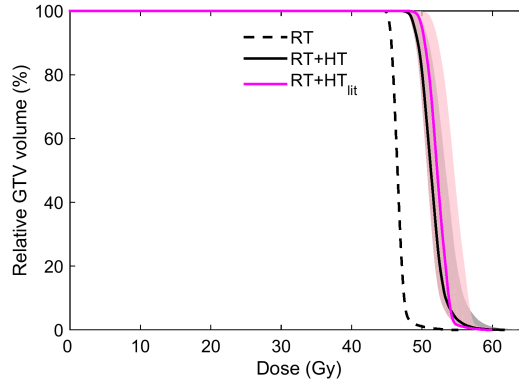


Figure 5.7. Dose Volume Histogram (DVH). DVH reflecting the dose distribution in the GTV for radiotherapy alone (RT, dashed line) and the combined radiotherapy and hyperthermia treatment as predicted with the advanced HTP workflow (RT + HT, solid line). For comparison, the DVH predicted using a routine HTP workflow based on literature dielectric properties is also shown (RT + HT_{lit}, solid magenta line). The shaded area around the DVH for RT + HT and RT + HT_{lit} corresponds to confidence intervals resulting from uncertainty in LQ parameters.

sensitivity to noise and so-called “boundary errors” at tissue interfaces, which limit its practical use. Among the numerous EPT approaches [57], inverse methods such as CSI-EPT demonstrated reduced noise sensitivity and good accuracy, also at tissue boundaries, in pelvis conductivity simulations [109, 117]; nonetheless, *in vivo* pelvis conductivity maps have not been reported yet. In principle, electrical properties could be obtained with any EPT reconstruction method, but the quality of conductivity maps demonstrated *in vivo* by DL-EPT is appealing for direct use as input to HTP, thus eventually eliminating the need for Hounsfield-based thresholding of CT scans to create the patient dielectric model. Nevertheless, direct input to HTP is not yet feasible because bowel peristalsis, breathing and pulsatile flow occurring in the pelvis during the MRI acquisition produce imaging artefacts which affect the $|B_1^+|$ and ϕ^\pm maps (Figure 5.2). At locations where these artefacts appear, DL-EPT retrieves an erroneous conductivity value. To date, no EPT method is capable to counterbalance these motion-induced artefacts. Therefore, we implemented a hybrid alternative where median DL-EPT conductivity values were calculated in tissue 3D ROIs and then assigned to a Hounsfield unit-based segmented model. A deterministic EPT approach as the one suggested by Bevacqua et al. [117], where the tissue segmentation serves as representation basis of the unknown electrical properties, may conceptually be simpler than our hybrid strategy if only median EPT values are desired. In this regard, a convolutional neural network could probably be trained to combine segmentation with learning of an average EPT value for each tissue, for the specific use in HTP. Note, however, that our DL-EPT method was originally developed as an EPT approach aiming at a wide range of clinical scopes [57], with HTP as one of the possible applications. Thus, our network was trained to directly reconstruct the whole 3D electrical conductivity distribution. To aim for full 3D conductivity maps as input for HTP, future work in DL-EPT should focus on compensating these motion patterns. Furthermore, an

in vivo pelvis permittivity map would also be necessary for fully MR-based HTP. EPT-based in vivo permittivity mapping has been proven more challenging than conductivity mapping in the frequency range of 64–128 MHz, corresponding to clinical MR field strengths [57, 199]. However, preliminary results from a recent study [121] have shown that a good quality permittivity map could be reconstructed in the brain at 3T with a DL-EPT method. Further research is required to establish whether DL-EPT could reproduce good quality permittivity maps also in the pelvis.

A previous study [131] showed that the true in vivo electrical conductivity values, which are higher than literature values used in clinical HTP, have a profound impact on the power absorbed by the tumour and its achieved thermal dose with optimized antenna settings. This demonstrates the clinical relevance of using DL-EPT in vivo conductivity values in this workflow (Figure 5.5). In particular, the tumour SAR was ~25% lower than the bladder SAR, which was caused by the bladder having a 20% higher electrical conductivity than the tumour. In the present example, the bladder absorbed twice as much power as the tumour, due to its relatively large volume and high conductivity. For a conservative fixed bladder electrical conductivity (1.80 Sm^{-1}), Balidemaj et al. [131] showed that increasing bladder volumes negatively affected the tumour SAR. They further reported that the resulting predicted tumour temperature T90 was diminished by 0.57°C – 1.37°C from the temperature predicted with the conventional HTP for bladder volumes between 33 ml – 497 ml. Considering that similar conditions apply for the patient examined here (augmented bladder electrical conductivity and 149 ml of volume), a negative impact on the tumour temperature of a similar magnitude is expected. Moreover, the in vivo electrical conductivity of the surrounding muscle tissue, which differed by -8% from that of tumour, negatively influenced the tumour SAR. The resulting decrease in tumour temperature can be estimated around 0.40°C [131].

Another important advantage of using patient-specific conductivity information yielding trustworthy SAR predictions is that the location and magnitude of hot spots will be predicted more accurately, since temperature is correlated with SAR. The electrical conductivity of muscle, being higher than the average literature value, contributed to increase the dielectric contrast at muscle/fat and/or muscle/bone interfaces, therefore aggravating the severity of energy deposition at these locations. Figure 5.5 illustrates that high SAR values, resulting in potential hot spots, occurred at such tissue interfaces outside the heated region. These predicted arising hot spots, reaching the 45°C constraint for normal tissue during phase-amplitude optimization, limited a further increase of the tumour temperature.

The effect of convective heat transfer in the urinary bladder was integrated to account for its impact on the tumour temperature distribution, owing to the bladder's vicinity to the cervical tumour. For a clinically acceptable computation time, fluid heat convection in the urine was accounted for by a higher bladder thermal conductivity, which we set to a value 10 times higher than the literature value. Previous works on bladder HTP showed that using a ten-fold thermal conductivity value approximates the thermal effect of fluid heat convection that can be modelled by a computationally intensive thermophysical model of the bladder [200, 272]. As a result of this improved modelling, the mean predicted bladder temperature increases with respect to current clinical HT plans where the bladder is typically modelled as solid perfused tissue. Modelling the bladder as solid tissue was shown to yield errors of 3.8°C in the median predicted bladder temperature [131, 200]. Furthermore, 1°C temperature differences can be expected also at 1–1.5 cm distance from the bladder [200, 249], therefore affecting adjacent tissues such as the cervical tumour and muscle. Considering the realistic bladder electrical conductivity and convection, hyperthermia delivery for cervical cancer patients could be expected to benefit from an empty bladder. A previous study modelling only the

electrical in vivo conductivity of urine already suggested this [131]. However, during a 1-hour treatment some bladder filling would be unavoidable.

Incorporating a patient-specific network of large blood vessels traversing the heated region in Pennes' bioheat transfer model represents a further advance in HTP. The Pennes model is commonly used and proved to be valuable but neglects the direction of blood flow and the local heat exchange of vasculature, resulting in deviations in temperature estimations of $\sim 1\text{--}2^\circ\text{C}$ [240,256]. Explicit modelling of large blood vessels is thus required for accurate temperature predictions. Here we combined manual delineations of blood vessels $\gtrsim 3$ mm in the pelvic region based on the contrast of water-only Dixon scan with vessel delineations outside the pelvic region directly on the HT-CT image to enable modelling of the largest thermally significant arteries and veins. Further improvements would also include smaller thermally significant blood vessels using the more sophisticated DIVA thermal model [245,246]. This requires a patient-specific discrete vasculature model, knowledge on blood flowrates and directionality, and a 3D perfusion map in input. Hence, for future routine applications, additional vessel visualization methods should be acquired, for example angiograms which are typically realized with contrast-enhanced MRI, and (automatic) reconstruction of vessel networks from these angiograms should be incorporated in the clinical workflow [248]. If necessary, available realistic vessel generation software could be used to update incomplete vessel branches automatically [280]. Moreover, flow imaging could be included in the workflow, for example within the MRI protocol, to retrieve functional information on blood flow parameters. Ideally, a quantitative 3D map of the perfusion in the patient would also be required for accurate temperature predictions. It was previously shown that a 25% uncertainty in perfusion parameters of muscle and fat affected the optimized tumour T90 by $0.2\text{--}0.4^\circ\text{C}$ [185]. Furthermore, van den Berg et al. [240] found that the temperature in the prostate was $\sim 1\text{--}2^\circ\text{C}$ lower when a 3D heterogeneous perfusion was modelled, compared to a homogeneous perfusion model. However, perfusion maps acquired with perfusion CT or MR imaging techniques cannot be obtained during hyperthermia and therefore the increase in perfusion levels at hyperthermic conditions, which can be up to a factor of 10 [281], is not accounted for. Alternatively, thermal decay measurements with standard clinical thermometry probes could be used to estimate the perfusion level [282], but these measurements can only be performed off treatment (i.e. while the power is off, e.g. right after the treatment). The disadvantage of thermal decay measurements is that they provide an indication of the perfusion only at a certain point in time and at the specific locations of these probes (generally within the bladder, the cervix and the rectum).

A temperature-based optimization strategy was applied to predict the antenna settings for optimal tumour heating, while limiting the incidence of treatment limiting hot spots [253,255,256]. However, the proposed workflow can also be combined with SAR-based optimization, if desired [225,231,232,251,252]. SAR-based optimization techniques generally yield a lower computational cost compared to temperature-based optimization techniques, since the latter typically involve many temperature evaluations for which the Pennes bioheat equation should be solved. Nevertheless, an efficient temperature-based optimization method based on superposition of pre-calculated temperature distributions [255] was used in this workflow. This method allows for temperature-optimization within a few minutes. Here, a temperature-based optimization was preferred as it accounts for physiologically important cooling mechanisms such as perfusion and conduction, as well as bolus cooling. Previous HTP studies in the pelvic region demonstrated that temperature-based optimization is robust to perfusion uncertainty [233] and that simulated temperature changes after phase-amplitude steering correlate with measured temperature changes during HT [283]. Moreover, since tumour temperature and treatment-limiting normal tissue hot spots, which are related to

treatment effect, are inherently accounted in the optimization cost function, a temperature-based optimization was also a straightforward choice in light of the subsequent biological modelling.

Biological modelling of the combined radiotherapy and hyperthermia treatment is a beneficial step towards a patient-tailored treatment plan for this treatment combination. We assessed the radiosensitization induced by hyperthermia in terms of equivalent dose by exploiting the extended LQ model [257]. The equivalent dose was calculated for the GTV only, because the radiosensitization in the tumour was shown to be higher than in normal tissue for hyperthermia delivery immediately after radiotherapy [278]. Figure 5.7 shows that the tumour temperature achieved in this patient escalated the equivalent radiation dose in the GTV by, on average, an extra 5 Gy. Besides, Figure 5.7 indicates that the advanced modelling steps influencing HTP predictions, as discussed above, also influence the predicted equivalent dose. The hyperthermic radiosensitization effect is reflected in the temperature-dependent α and β parameters. These parameters, obtained from extensive cell line experiments [261], relate to the inhibiting effect of hyperthermia on DNA damage repair and to direct cell kill, but do not account for other mechanisms such as reoxygenation [261,264]. Further (in vivo) research is needed to acquire knowledge on how these physiological effects influence the α and β values [278]. Moreover, LQ parameters for normal tissues should still be investigated, for example by extensive in vivo measurements at different radiation doses, temperature and time intervals [278], especially for organs at risk such as bladder, rectum and bowels. A previous planning study concluded that the hyperthermic radiosensitization in these organs at risk is negligible compared to the tumour region, also because the temperatures were lower [278]. However, a significantly higher bladder temperature is predicted by the advanced HTP. Although in clinical studies for pelvic tumours no enhanced bladder toxicity is observed [284], these higher temperatures might influence the equivalent bladder dose to some extent. In the future, reliable equivalent dose computations in both tumour and normal tissues and prediction of the potential cytotoxicity to organs at risk would become possible with more extensive knowledge on the behavior of LQ parameters under hyperthermic conditions. A next, though very challenging, step in patient-tailored treatment planning would be to directly optimize the equivalent dose distribution of the combined treatment, rather than optimizing the individual treatment modalities separately.

Even though there are still some uncertainties and challenges left in HTP, as discussed above, the advancements achieved with this sophisticated HTP framework will improve the reliability of pre-treatment plans compared to the present clinical HTP procedure. Therefore, they are also likely to improve the treatment quality. A previous study demonstrated that, even for clinical pre-treatment plans which are only qualitatively reliable, the treatment plan can be adapted on-line in response to patient's hot spot-induced complaints without significantly diminishing the thermal dose to the tumour [285]. This treatment plan re-optimization is referred to as adaptive HTP. Adaptive HTP can be valuable for both hyperthermia treatments guided by standard thermometry probe feedback and locoregional MR-guided hyperthermia (e.g. using the BSD Sigma Eye MR or the Sigma 30 MR applicator). Instead of thermometry probe feedback, MR-guided hyperthermia uses more detailed MR thermometry information to re-optimize treatment settings. This is feasible for large fixated tumours, as shown for example for treatment of extremity sarcomas [286]. In case of pelvic hyperthermia, nevertheless, MR thermometry information is less reliable due to motion artefacts and standard probe thermometry feedback is still preferable [287]. Ongoing research aims to close the gap towards quantitative temperature monitoring in the pelvic region [288]. In general, it is expected that adaptive HTP will benefit from advanced pre-treatment plans, since these plans more accurately predict the magnitude and locations of potential hot spots, which means that

the pre-treatment plan will be closer to the real optimum. Furthermore, the correlation between the simulated and measured temperature changes during hyperthermia as a result of phase-amplitude steering would be improved [283], which will render adaptive HTP strategies more effective.

5.5 Conclusion

A patient-tailored advanced hyperthermia treatment planning workflow was presented, integrating the following novel research elements in the current clinical practice of hyperthermia treatment planning: (i) patient-specific in vivo tissue conductivity reconstructed with DL-EPT from MR measurements; (ii) patient-specific modelling of the thermal influence of large blood vessels; (iii) modelling of the effects of heat convection in urine; (iv) patient-specific assessment of the radiosensitizing effect induced by hyperthermia in equivalent radiotherapy dose. The proposed workflow ensures more accurate predictions of the power deposition and temperature in the patient, as well as a more realistic prognosis of the expected tumour control (through the equivalent radiation dose of the combined treatment) without requiring excessive computational effort.

General Discussion

The electrical properties of tissues (permittivity ϵ_r and conductivity σ) regulate the effects of EM fields in the human body and hold the promise of being endogenous biomarkers. MR-based Electrical Properties Tomography (EPT) is a powerful technique to measure such properties non-invasively [57, 58]. This is possible because the electrical properties (EPs) perturb the spatial distribution of the complex B_1^+ field, i.e. the magnetic field responsible for spin excitation in MRI. MR-EPT requires the acquisition of both amplitude and phase of the complex B_1^+ field, from which the ϵ_r and σ distributions are reconstructed. Both B_1^+ acquisition and EP reconstruction can be performed in different ways, as outlined in sections 1.6 and 1.7, and ultimately influence the accuracy and precision of EP maps.

Assessing the accuracy and precision of EP maps is a central theme in this thesis. These characteristics determine the validity of EPT as a quantitative mapping tool for clinical applications. The preceding chapters specifically explored different aspects of an MR-EPT experiment that define the accuracy and precision of EPT-based maps: the MR acquisition, the EPT reconstruction and the intended clinical application. First, the impact of acquisition techniques on EPT was quantified: in particular, Chapter 2 focused on transceive phase mapping methods (i.e. PLANET [136], bSSFP and SE) and their impact on Helmholtz-based EPT (H-EPT) conductivity mapping, and Chapter 3 dealt with the influence of three commonly available $|B_1^+|$ mapping sequences (AFI [68], Bloch-Siegert [74] and DREAM [72]) on H-EPT permittivity reconstruction. Then, Chapter 4 presented a new deep learning-based EPT (DL-EPT) approach for conductivity reconstruction in the pelvic region and analyzed its reconstruction performance. Finally, Chapter 5 was extensively dedicated to hyperthermia treatment planning (HTP), the medical application of interest in this thesis. Here, DL-EPT and advanced HTP elements were combined within a single workflow to enable more reliable hyperthermia treatment plans.

In this chapter, the salient contributions of this thesis to the general knowledge on EPT are contextualized and discussed, and directions for future EPT research are outlined. Hereafter, the term " B_1^+ " will be used to indicate a "surrogate" magnetic field with measurable amplitude and phase, therefore with amplitude $|B_1^+|$ and phase corresponding to the transceive phase ϕ^\pm , unless explicitly stated otherwise.

6.1 B_1^+ acquisition & EPT

The sequence and MR settings used to acquire the $|B_1^+|$ and ϕ^\pm influence the quality of the complex B_1^+ map. The measured B_1^+ map, in turn, affects the quality of EPT reconstructions. Although this has generally been recognized, the impact of B_1^+ acquisition on accuracy and precision of EPT reconstructions has long been ignored. This thesis investigated this impact for the first time by making use of simulations for error prediction and MR measurements for experimental assessment.

6.1.1 Error quantification in EPT

Chapter 3 presented a simulation framework to quantitatively predict the error propagation from MR acquisition to EPT reconstruction. This same framework was also used in Chapter 4 to construct the training database of magnetic fields fed to the CNN (see section 4.2.1), and can be used to optimize sequence settings or reconstruction parameters during prototyping of new MR-EPT methodologies. This simulation framework comprises electromagnetic (EM) simulations followed by MR sequence simulations. The concept of MR sequence simulation introduced here is new in EPT, whereas EM simulations have already been used to estimate the reconstruction performance of EPT algorithms (for example, reconstruction-specific intrinsic bias, introduction of potential artifacts and effect of assumptions, as shown in e.g. [54, 89, 93, 109]).

The added value of MR sequence simulations in EPT MR simulations of $|B_1^+|$ and ϕ^\pm mapping sequences intrinsically model how sequence-specific errors and noise propagate from the acquired MR signals into the reconstructed magnetic field maps. Thus, EP maps reconstructed from these simulated $|B_1^+|$ and ϕ^\pm fields contain the impact of the acquisition technique. MR simulations permit to emulate the $|B_1^+|$ and/or ϕ^\pm distribution resulting from an MR-EPT experiment for a specific body region, since the sequence parameters (e.g. FA , TR), the tissue properties (e.g. proton density, T_1, T_2 , Δf_0) and the true B_1^+ distribution at a specific Larmor frequency, obtained from EM simulations, must be given in input.

The difference between the true $|B_1^+|$ (or ϕ^\pm) and the $|B_1^+|$ (or ϕ^\pm) "observed" through the sequence, i.e. the final output of the MR simulation, exposes the impact of sequence-specific imperfections, thus the accuracy of the acquisition technique. Comparing the EP maps reconstructed with a given EPT algorithm on both true and observed magnetic field maps reveals the deviations caused by those imperfections. Furthermore, reconstructing the EP maps on $|B_1^+|$ and ϕ^\pm maps with realistic SNR reveals the impact of noise.

Until now, white Gaussian noise was directly superimposed to the (true) $|B_1^+|$ and ϕ^\pm maps to reproduce their experimental SNRs. This procedure implicitly assumes that the noise level is homogeneous in these maps and does not account that the SNR is affected by both the tissue properties and the noise propagation of the measuring sequence. As shown in Chapters 2 and 3, the effective noise distribution in the $|B_1^+|$ ($\zeta_{B_1^+}$) and ϕ^\pm (ζ_{ϕ^\pm}) is spatially distributed. The realistic impact of noise on these fields can be modelled by MR simulations when the noise is added independently to the real and imaginary channels of the MR signal. In this thesis, noise in the MR images used for B_1^+ reconstruction was assumed to be Gaussian. This is valid for Cartesian sampling and single coil acquisition [289], however coil sensitivity maps or other sampling schemes could be included to render the noise distribution more realistic, if deemed necessary.

The discussion above illustrates the importance of using MR sequence simulations to complement EM simulations, as the latter do not fully account for the errors occurring in an MR-EPT experiment. In short, MR simulations allow to model the sequence-specific contribution to the accuracy and precision of the reconstructed EP map. By varying the sequence parameters and noise levels in input to the MR simulation, the sensitivity of the EPT reconstruction method to sequence-related errors and noise could be derived, which is useful when modelling this sensitivity analytically becomes difficult. In this thesis, Hargreaves' Bloch simulator [156] was used to perform MR simulations, but there are also other simulation environments. Pulseq [290] and JEMRIS [291] are interesting open-source environments for sequence prototyping and can also be interfaced with the MR scanner to automatically import the sequence diagram.

6.1.2 The impact of B_1^+ acquisition on Helmholtz-based EPT

In this thesis, the accuracy and precision of different acquisition methods were quantitatively assessed and related to the bias and standard deviation of the EP map reconstructed with H-EPT. In this context, the accuracy was indicated by the difference between the reconstructed and the true (or reference) variable x , whereas the precision of x was related to the inverse of its standard deviation (std, ζ_x), which was principally dominated by the impact of noise. In essence, the results revealed the sensitivity of H-EPT to errors and noise that can realistically occur during the acquisition.

Accuracy Chapter 2 showed that slight distortions of the ϕ^\pm curvature, caused by a mild contamination from off-resonance effects (of ~ 0.02 - 0.03 rad) in *bssFP*, resulted in $\sim 10\%$ underestimation in H-EPT conductivity reconstruction. Similarly, noiseless simulations in Chapter 3 highlighted that $|B_1^+|$ maps with less than 1% bias from the true $|B_1^+|$, as was the case for *BS*, resulted in an average permittivity error between 7% and 17% of the true permittivity. These findings revealed for the first time that H-EPT reconstruction is particularly sensitive to errors in the B_1^+ distribution. Such small errors can simply be caused by sequence-related imperfections in the reconstruction of $|B_1^+|$ and ϕ^\pm maps (e.g. due to T_1 sensitivity, as in *AFI*, or Δf_0 effects as in *bssFP*). Thus, extremely accurate acquisitions are required for H-EPT.

Precision A substantial difference in precision between conductivity and permittivity was observed ($\zeta_\sigma = 16\% - 21\%$ of the true σ value vs $\zeta_{\epsilon_r} = 60\% - 89\%$ of the true ϵ_r value) despite the fact that the precision practically achieved in both ϕ^\pm and $|B_1^+|$ maps was on the same order of magnitude ($\zeta_{\phi^\pm} = 0.1\% - 0.4\%$ of an unitary ϕ^\pm vs $\zeta_{B_1^+} = 0.2\% - 0.6\%$ of the average $|B_1^+|$). These findings clearly highlighted the realistic noise sensitivity of H-EPT at 3T, showing for the first time which SNRs (in both magnetic fields and EPs) should be expected from different MR-EPT acquisitions. Furthermore, they provided de facto an experimental validation of the theoretical model derived by Lee et al. [88] for the noise propagation in H-EPT (this is explicitly shown, for instance, in Figure 3.8).

Taken collectively, these precision results confirm the general conclusion of previous studies [60, 88, 89], i.e. that the noise propagation in H-EPT is more favourable for the conductivity reconstruction, which implies that a higher $|B_1^+|$ precision is required to achieve a permittivity precision comparable to that of conductivity. However, they also point to the significant conclusion that permittivity mapping with H-EPT is practically not feasible at 3T within clinically acceptable times, because the $|B_1^+|$ precision effectively achieved by commonly available B_1^+ mapping sequences is overall too low to obtain meaningful precision in the permittivity (Figure 3.8).

6.1.3 The impact of B_1^+ acquisition on DL-EPT

Although the error and noise propagation in DL-EPT were not assessed, a preview on the impact of the acquisition on DL-EPT was simulated in Chapter 4 (Figure 4.4). Using input magnetic fields observed through AFI and SE sequences influenced the accuracy of the conductivity fields reconstructed by $\text{Net}_{\text{EM-B1}}$, i.e. the CNN trained on pure simulated EM data: comparing Figure 4.4b and Figure 4.4c demonstrated evident errors around an air pocket (where an obvious underestimation in $|B_1^+|$ was found) and mild differences in the nearby muscle tissue and bladder apex, although no particular sequence-specific bias was observed in these locations. The reason why the observed errors also extended to regions with accurate $|B_1^+|$ and ϕ^\pm might hypothetically be related to the conductivity being evaluated within each window (or patch) during inference. Thus, intra-patch conductivity errors might arise due to local inaccuracies in input data. Moreover, the impact of noise on the conductivity map reconstructed by $\text{Net}_{\text{EM-B1}}$ was evident (Figure 4.4d). These observations motivated the inclusion of the sequence accuracy and precision within the training dataset (accomplished by using the simulation framework outlined in Chapter 3), as these characteristics are expected to be learnt and compensated for by the network. The conductivity reconstruction obtained with $\text{Net}_{\text{MR-B1}}$ (trained on simulated MR data) demonstrated a partial improvement of above-mentioned errors and an effective noise mitigation (Figure 4.4e). Please note that both $\text{Net}_{\text{EM-B1}}$ and $\text{Net}_{\text{MR-B1}}$ were trained with the same parameters, due to time constraints; further parameter optimization is likely required for $\text{Net}_{\text{MR-B1}}$ to fully compensate for the bias in the input magnetic fields.

6.1.4 Future perspectives

This section outlines some prospects for future research stemming from the results, limitations and conclusions of both Chapters 2 and 3.

Permittivity mapping From a precision perspective, permittivity mapping with H-EPT is not clinically feasible at clinical MR field strengths but it is worth of investigation at MR field strengths higher than 3T, which bring intrinsic SNR gain [39] and stronger permittivity-related perturbations in the transmit field [56]. Few H-EPT permittivity results with improved precision have already been demonstrated, for example at 7 T [89] and at 21.1 T [292]. At clinical field strengths, nevertheless, permittivity mapping is better pursued by using inverse EPT and DL-EPT approaches. In this sense, a simulation study reported that CSI-EPT could achieve $\zeta_{\epsilon_r} \approx 20\text{--}25\%$ in WM for a $\zeta_{B_1^+} = 0.5\%$ ($\text{SNR}_{B_1^+} = 200$) after 300 iterations [123]. A recent preliminary study has shown that the permittivity map from a 3T volunteer's brain MR scan could be reconstructed with improved precision ($\zeta_{\epsilon_r} \approx 7\text{--}15\%$) with DL [121].

Accuracy in EPT Assessing the sensitivity of EPT reconstruction methods to spatial errors in the underlying complex B_1^+ distribution should be subject of future research, as these errors can occur during the MR acquisition and vary per MR sequence. The simulation framework discussed above is a practical tool that already proved useful for this task. Such research will reveal the severity of the acquisition-related impact on the accuracy of EPT maps, and consequently whether the accuracy requirements for the acquisition methods might be relaxed for a specific EPT reconstruction method, which implies that accuracy could be traded, for example, for faster acquisition.

Faster acquisition The MR sequence protocols in Chapters 2 and 3 were devised to enable $|B_1^+|$ and ϕ^\pm acquisitions in the pelvis ($\text{FOV} = 480 \times 260 \times 80 \text{ mm}^3$) within 5 minutes. Nevertheless, acceleration strategies will be required to obtain EP reconstructions for larger FOVs or

for voxel sizes < 2.5 mm within clinically acceptable times. For example, larger FOVs could be demanded for HTP and voxel sizes < 2.5 mm could be required for clinical visualization. In this respect, faster implementations for some of the examined mapping techniques have been published (e.g. [171,293]). Acceleration techniques such as (multi-)shot acquisition (e.g. turbo-SE), parallel imaging (e.g. SENSE [294], GRAPPA [295]) and compressed sensing might also be incorporated in some of these mapping methods. Furthermore, different k-space sampling schemes and flow compensation strategies could be explored to reduce the impact of artifacts induced by physiologic motion. Obviously, these additions would influence the accuracy and precision of the measured magnetic fields, therefore it would be interesting to evaluate whether this influence is quantitatively relevant for EPT reconstructions.

Simultaneous $|B_1^+|$ and ϕ^\pm acquisition The modified multi-echo AFI [70] and DREAM [72] sequences permit to simultaneously map both $|B_1^+|$ and ϕ^\pm , thus they are undeniably appealing for EPT. Chapter 3 evaluated DREAM [72] only as a $|B_1^+|$ mapping modality, showing that its $|B_1^+|$ map exhibited blurring and ringing artifacts, with errors up to 6%-15% from the true $|B_1^+|$ distribution. These inaccuracies are mainly caused by differences in signal evolution between FID and STE. Ehses et al. [296] have recently corroborated the observations of Chapter 3. Furthermore, they designed a compensation strategy to minimize blurring and ringing artifacts which could be implemented to improve the accuracy of DREAM-based $|B_1^+|$ maps. More generally, future research might be aimed at comparing and/or optimizing these two sequences for use in EPT.

6.2 Deep Learning & EPT

In this thesis, DL-EPT was explored. The concept of DL-EPT has recently been introduced by Mandija et al. [121] and refers to a DL-based end-to-end EPT reconstruction approach in which a convolutional neural network (CNN) learns the mapping relation between the EPs and the B_1^+ distribution in a supervised fashion, i.e. by using paired inputs-outputs training data. This section discusses the open challenges and opportunities of DL-EPT starting from the results obtained in Chapter 4. Furthermore, it anticipates alternative uses of DL for EPT reconstruction.

6.2.1 DL-EPT

In Chapter 4, an open-source 3D CNN architecture (*highres3dnet* [206]) was trained on synthetic pelvic B_1^+ fields with known tissue EPs to reconstruct the conductivity in the human pelvis at 3T. This novel DL-EPT method could reconstruct in silico and in vivo 3D pelvis conductivity maps with detailed anatomical structures, noise-robustness and different tissue conductivity variations solely from the input $|B_1^+|$ and ϕ^\pm maps. This suggests that the network learned the mapping relation linking B_1^+ and σ in the pelvis at 3T, unlike two previous DL-EPT works where the brain tissue geometry could not be recovered accurately from input brain B_1^+ fields alone [121,122]. The fact that the reconstruction properties predicted in the simulation study were also maintained in measurement-based conductivity maps suggests that the training simulated B_1^+ fields were already representative enough of the measured $|B_1^+|$ and ϕ^\pm maps. Overall, the quality of DL-based pelvis conductivity reconstruction was superior to that of conventional H-EPT.

The network trained on simulated ϕ^\pm data alone – the "transceive phase only" configuration – was sufficient to reconstruct the conductivity, with mild differences in performance

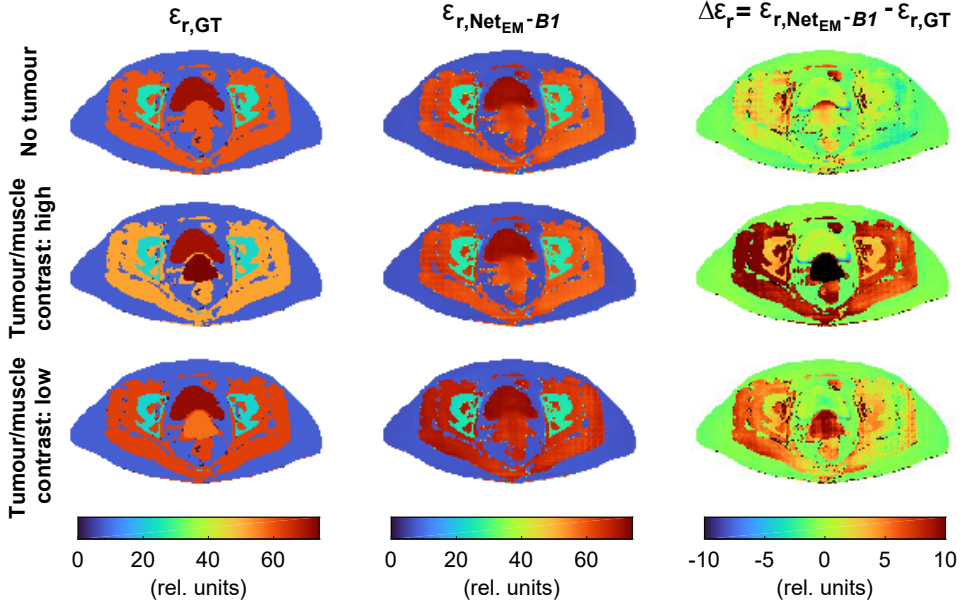


Figure 6.1. Permittivity maps reconstructed with DL-EPT in three *in silico* pelvic models (sharing the same anatomy but different tissue permittivity, pelvic model #01). Pelvis permittivity from a healthy subject (i.e. no tumour/muscle contrast) is displayed in top row. Permittivity from two cervical cancer patients is also shown: one with high tumour/muscle contrast (28.7 rel. units, *middle row*) and one with poor tumour/muscle contrast (5.3 rel. units, *bottom row*). Maps for ground truth permittivity and DL-EPT permittivity inferred with $\text{Net}_{\text{EM}-B1}$ are shown in first and second columns, respectively. Their difference is shown in third column. Note how the permittivity reconstruction by $\text{Net}_{\text{EM}-B1}$ is poorly sensitive to the tissue permittivity variations. $\text{Net}_{\text{EM}-B1}$ was trained with the same parameters of the conductivity study (see Table 4.2).

with respect to the "full B_1 " configuration (i.e. the CNN trained on both ϕ^\pm and $|B_1^+|$ data, " $\text{Net}_{\text{EM}/\text{MR}-B1}$ "). However, the full B_1 configuration is useful to reconstruct the permittivity too. At the moment, the permittivity map reconstructed by $\text{Net}_{\text{EM}-B1}$ displays the same anatomical detail already shown in the conductivity map (Figure 4.3), but appears to be much less sensitive to permittivity variations. This is clearly illustrated in Figure 6.1: the same permittivity values are reconstructed despite the different ground truth permittivity distributions. The lower sensitivity of this DL-EPT method to permittivity changes may partially be attributed to the weaker imprint of the permittivity on the B_1^+ distribution at 3T [56], but the chosen training and/or network specifications may also play a role. Thus, further research is necessary to verify whether *highres3dnet* could retrieve more accurate permittivity distributions; alternatively, another CNN architecture must be investigated.

Hereafter, several aspects related to the performance and applicability of the proposed DL-EPT method are analyzed.

Reconstruction accuracy & precision In Chapter 4 the mean error (ME) and the difference between the 90th and 10th percentiles of the inferred conductivity (S_{90-10}) were used as metrics for the accuracy and precision of DL-EPT reconstruction, respectively. These metrics were assessed on simulated data with a 7-fold cross-validation (with randomly chosen folds). The ME of DL-based conductivity reconstruction was, on average, acceptable but presented variability over the whole database of 210 dielectric models (see Table 4.3). Thus, for example, the ME can generally be expected to fall between -0.15 and 0.15 Sm^{-1} for muscle conductivity and between -0.23 and 0.23 Sm^{-1} for tumour conductivity (Figure 4.6). As already discussed in Chapter 4, increasing the number of training samples and/or manipulating the regularization and loss function might reduce such error ranges.

This variability arises because of the data-driven learning of DL-EPT. It is also likely connected to the problem of imbalanced data, since the training conductivity dataset was randomly chosen from a database in which the tissue conductivity distributions were by design imbalanced (see Figure 4.1 and section 4.2.1). The CNN is intuitively expected to correctly infer the tissue conductivity values that were more frequent in the training dataset; these probably corresponded to the more represented tissue conductivity values in the database. Moreover, data imbalance existed among pelvic tissues, with tumour and bladder being under-represented with respect to the other tissues. This explains, at least in part, why the standard deviation of ME in bladder and tumour was higher than that of another high-conductivity tissue, i.e. muscle. Thus, resolving the problem of imbalanced data will probably increase the reconstruction accuracy. To this aim, oversampling of under-represented tissues was attempted by assigning them a higher weight than the remaining tissues during training; nevertheless, a tenfold increase in the weight for tumour tissue, for example, did not substantially improve the accuracy in tumour conductivity estimation. Another possibility to tackle data imbalance could be to evaluate the loss function on patches with equalized tissue conductivity histograms; this might be accomplished by weighting the already present loss function by the inverse of number of voxels with a particular tissue conductivity value.

The discussion above also holds for the precision parameter. In general, a large S_{90-10} described a heterogeneous conductivity estimation within a tissue. The highest S_{90-10} values occurred in the under-represented tumour and bladder tissues. Visually inspecting these results revealed that the network often did not correctly reconstruct the conductivity for the entire tissue volume, as "spurious" conductivity contamination from the surrounding tissue (for instance, muscle) occurred in part of the volume. Unlike the precision of H-EPT conductivity which largely depends on noise propagation, the precision metric S_{90-10} was probably marginally affected by the impact of noise in the input data. The higher noise-robustness of DL-EPT was associated with the inclusion of noise within the training B_1^+ fields.

Generalization The term "generalization" refers to the network's ability to accurately predict new, unseen data. In this respect, the trained CNN generalized fairly well when presented with unknown pelvic B_1^+ distributions obtained at 3T with fixed resolution, EPs and acquisition modalities, i.e. unseen data drawn from the same domain as the one used for training (*in-domain* data). This can be deduced from the conductivity reconstruction performance in the different test data, which was summarized, for example, in the cross-validation results. Nevertheless, the generalization power of DL-EPT cannot be assured for *out-of-domain* test data, taken for example at different body sites, B_0 field strengths, SNR, or having out-of-distribution conductivity values.

Exploring the performance of the CNN with respect to test data with out-of-distribution conductivity values ("outliers") revealed a tendency to reconstruct values from the input training conductivity distribution (Figure 4.7). Although these tissue conductivity distributions were methodologically intended to cover as realistically as possible the spectrum of inter-subject tissue conductivity variations, training on broader tissue conductivity ranges or on a continuous range might improve the generalization. Furthermore, it is possible that the DL-based reconstruction was implicitly "biased" by the predefined conductivity distributions assigned to each pelvic tissue in the database (Figure 4.1). This could be deduced from the example of outlier conductivity in fat tissue ("outlier 2", Figure 4.7), but should be further investigated. Adding dielectric models with different compartments and shapes to the training dataset may avoid this potential reconstruction bias.

The in vivo feasibility of the proposed DL-EPT method was demonstrated but its generalization to pelvic MR measurements is not yet fully guaranteed, since only the conductivity of the main pelvic tissues (fat, muscle, bone, cervix/tumour and bladder) was learnt and reconstructed by the network. This is attributed to the training database construction, which allowed to electrically characterize only the main pelvic tissues resulting from the segmentation of patients' CT scans. To enable superior soft-tissue contrast in the reconstructed conductivity maps, two training databases could be considered:

- (i) a database based on in vivo $|B_1^+|$ and ϕ^\pm measurements, which naturally encode the inter- and intra-tissue conductivity variations. This approach was explored by Hampe et al. [122], who claimed an improved DL-EPT reconstruction performance against experimental artifacts (e.g. pulsatile flow) compared to an in silico-based training. However, in vivo B_1^+ fields lack the ground truth conductivity information necessary to correctly learn the mapping relation between B_1^+ fields and σ . The practical solution proposed by Hampe et al. [122] was to reconstruct a surrogate of the ground truth conductivity with a physics-based EPT algorithm (in their case, a processed version of H-EPT). As argued in section 4.4, this automatically includes inaccuracies and assumptions characterizing the adopted EPT reconstruction method (e.g. inaccurate boundary reconstruction and tranceive phase assumption for H-EPT) within the supervised learning process of DL-EPT.
- (ii) a synthetic database of B_1^+ fields pertaining to human models built from MR image segmentation. In this approach, the superior tissue contrast can be represented by the MR-based segmentation and the ground truth EPs are known, as these can be defined a priori. Still, the acquisition process of $|B_1^+|$ and ϕ^\pm fields should be realistically emulated to appropriately represent the measured magnetic fields: beyond simulating the sequence-specific accuracy and precision, experimental imaging artifacts related, for instance, to physiologic motion (flow, breathing, bowel peristalsis, etc...) need to be included in the MR signals before reconstructing the synthetic $|B_1^+|$ and ϕ^\pm maps.

The first option is more practical and less time-consuming than the second, because less modelling is involved to build the training dataset. However, one should ponder what the advantage is of a DL-EPT method which intrinsically learns the reconstruction performance of another physics-based EPT processing, considering that an end-to-end DL-based EPT approach is specifically intended to bypass the inaccuracies and assumptions limiting the performance of current EPT algorithms.

Confidence Because of its deterministic model parameters and inference, the CNN does not inform about its prediction confidence (or uncertainty) for the inferred conductivity map. Estimating the predictive uncertainty of the network allows to increase the trust in the generated output: for example, out-of-domain data could be detected on the basis of a low confidence level (high uncertainty).

The confidence estimation for deep learning models typically revolves around the formalism of Bayesian modelling, whereby the network parameters are modelled as probability distributions and the predictive uncertainty can be quantified based on the posterior distribution computed over the parameters given the training data [297,298]. Among the different techniques for Bayesian inference approximation, perhaps Monte Carlo dropout [299], i.e. temporarily removing a random number of nodes from the network at both training and test times, is the most practical to model the uncertainty for the existing CNN, since the predictive uncertainty can simply be calculated from the variance of N stochastic forward passes through the network. Alternatively, the model uncertainty could be predicted by the variance of predictions obtained from "deep ensembles", i.e. ensembles of different multiple neural networks trained on the same dataset [300]. Deep ensembles were shown to have a better accuracy-to-confidence curve than practising Monte Carlo dropout, which means that they were more robust against overconfident wrong predictions [300,301].

Experimental validation Conductivity deviations of $\sim 10\%$ were found in muscle, bladder and tumour ROIs between $\text{Net}_{\text{MR-B1}}$ and H-EPT, but this preliminary experimental comparison was not sufficient to prove the accuracy of DL-EPT in MR measurements, being based on only three human subjects. As a form of experimental validation, a correlation study between DL-EPT and a reference EPT algorithm could be performed based on MR measurements on multiple volunteers and patients. In the pelvis, in particular, attention should be paid to quantitatively analyze the conductivity in trustworthy tissue ROIs (e.g. artifacts-free regions). However, note that no "gold standard" EPT reconstruction method has been recognized, thus the tissue conductivity values measured with the arbitrarily chosen reference EPT algorithm cannot be taken as safe ground truth. A phantom study may arguably be an effective experimental validation for DL-EPT, since ground truth EPs of phantoms can independently be measured with a dielectric probe. To this end, the CNN should be tested on MR measurements of several phantoms with different known EPs, unlike physics-based EPT methods for which a single phantom experiment is sufficient for performance assessment. Nevertheless, the network likely needs re-training on a dataset containing additional phantom data, similarly to the training database used in [121]. In any case, an average metric describing the global reconstruction performance should be deduced from the different in vivo or phantom MR experiments.

DL-EPT conductivity as a biomarker? The simulation study of Chapter 4 showed that DL-EPT could discriminate a malignant cervical lesion from the surrounding healthy muscle tissue if the conductivity contrast between these two tissues exceeded $\sim 0.25 \text{ Sm}^{-1}$. Based on this observation, a few conjectures on the potential use of DL-based conductivity as a biomarker can be made. When the tumour/healthy contrast is greater than 0.25 Sm^{-1} , the conductivity inferred by the current DL-EPT approach might facilitate tumour visualization with respect to other MRI contrasts, but it might only complement the MR images (e.g. ADC) already used for tumour delineation. This is because DL-EPT could not always correctly reconstruct the conductivity of the entire tumour volume, as previously discussed for high- S_{90-10} dielectric models. Nevertheless, the DL-based conductivity map could not yet be used as a general diagnostic marker, because conductivity differences between malignant and benign tissues might also be smaller than $\sim 0.25 \text{ Sm}^{-1}$ in reality. This seems supported by the H-EPT conductivity values found by Balidemaj et al. [102] in a small-scale patient study ($\sigma_{\text{tumour}} = 1.02 \pm 0.29 \text{ Sm}^{-1}$ vs $\sigma_{\text{muscle}} = 0.93 \pm 0.26 \text{ Sm}^{-1}$). Finally, preliminary rat experiments showed conductivity differences of at least 0.20 Sm^{-1} in the rat brain after 1 day of radiation treatment, and these differences increased to $0.30\text{--}0.5 \text{ Sm}^{-1}$ after 5 days of treatment [133]. Conductivity differences of this magnitude would be revealed by DL-EPT conductivity; this implies that a conductivity-based tumour response monitoring might be feasible already from

early days. Nevertheless, the treatment-induced conductivity changes vary per treatment type (radiotherapy, chemotherapy, hyperthermia) and are tissue dependent. For cervical cancer, these inter-treatment conductivity changes are unknown, thus the potential of DL-EPT conductivity as a biomarker for monitoring of cancer treatment response in longitudinal studies remains unclear.

6.2.2 *New frontiers for deep learning in EPT*

As discussed in the previous section, an end-to-end DL-EPT approach learns the function from B_1^+ to EP_s in a supervised fashion, bypassing all the processing steps of physics-based EPT reconstruction, but it requires exhaustive training datasets and may raise doubts over generalization power and confidence. This section moves beyond the concept of DL-EPT and anticipates how DL could be employed to complement existing EPT reconstruction algorithms in the future. The synergy between DL and EPT algorithm is expected to improve generalization and trust on EP reconstructions while reducing the need for rich training datasets.

A first research option could be to implement a DL-based pre- or post-processing to minimize the impact of noise and/or remove inaccuracies and artifacts in EP maps reconstructed with physics-based EPT algorithms. To this end, DL approaches which have already emerged for image denoising, segmentation and artifact detection in MRI [64] may be applied. Alternatively, learned iterative reconstruction schemes could be investigated for use in inverse EPT approaches. In learned iterative reconstruction, the updating function of a specific iterative method is learned by a CNN from the training data rather than being mathematically defined a priori [302,303]. In this way, the effect of the regularization term, which relates to prior knowledge on the data and is often empirically determined, can be learned automatically as well. The learned updating function can then be used to solve the inverse problem at hand. Recent studies have shown that the learned iterative reconstruction reduced the number of iterations for convergence, thus enabling substantially faster computations, and achieved comparable reconstruction accuracy with respect to standard optimization procedures [302,303].

6.3 Hyperthermia treatment planning

In locoregional hyperthermia of deep-seated pelvic tumours, phased-arrays of RF antennas operating at 60–130 MHz are used to focus the RF energy deposition (i.e. SAR) in the tumour in order to produce localized therapeutic tumour heating. To generate focused heating in the tumour while minimizing the incidence of treatment-limiting hot spots in normal tissue, the phase and amplitude settings of each RF antenna need to be optimized. The best settings for effective hyperthermia therapy can be predicted prior to the treatment with a procedure called *hyperthermia treatment planning* (HTP), which is the focus of Chapter 5.

6.3.1 *Advanced hyperthermia treatment planning*

Chapter 5 reviewed the routine HTP workflow and the latest methodological developments introduced in this field. These methodological developments include using EPT to determine the patient-specific EP_s , modelling the thermal impact of the patient's vasculature and of convection in body fluids (e.g. urine in bladder), and modelling the radiosensitization induced by hyperthermia.

Since these advanced aspects, taken separately, improved the reliability of the hyperthermia treatment plan, in Chapter 5 these research developments were combined and integrated with

the routine HTP infrastructure. The rationale here was that leveraging such developments should ultimately increase the accuracy of HTP predictions. The resulting advanced HTP workflow was illustrated for a cervical cancer patient and its practical feasibility was proved. Note that the current single-patient study could not demonstrate whether the temperature prediction from this advanced HTP was actually accurate; this would have required a detailed analysis of dynamic temperature changes during treatment and additional imaging of anatomy and perfusion. As validation, a future study on multiple patients might compare the temperature output of the proposed advanced HTP with thermal decay measurements obtained while administering the planned treatment, as well as compare the predicted potential hot spot locations with potential patient’s complaints.

6.3.2 The role of EPT in hyperthermia treatment planning

Knowing the patient-specific tissue ϵ_p s is essential in HTP to model the SAR distribution in the patient used for thermal modelling and phase-amplitude optimization. In the current HTP practice, literature ϵ_p s [10,22] are assigned to a segmented model of the patient’s body. Typically, segmentation is semi-automatically performed on the patient’s CT scan based on Hounsfield units. MRI-based segmentation is also possible and offers greater anatomical detail due to the superior soft-tissue contrast of MRI [197]. Studies comparing CT- and MRI-based segmentation in hyperthermia simulations reported small differences in SAR calculations, but resulting in more significant differences in temperature distributions [227,304].

In principle, EPT represents an incredible opportunity for HTP, as it reconstructs patient-specific EP maps with the same anatomical detail of MRI, avoiding segmentation faults in the first place and enabling the realization of an MR-based HTP workflow. Nevertheless, patient-specific EPT maps have not yet been used as direct input for HTP because differentiation-based EPT algorithms still reconstruct inaccurate EP values at tissue boundaries and do not reliably map the permittivity at MR field strengths close to the operating frequency of several heating devices (e.g. for pelvic hyperthermia, $f = 60\text{--}130$ MHz). At the same time, *in vivo* EP mapping with inverse EPT approaches still needs to be demonstrated. In the following, alternative EP mapping solutions are discussed.

Earlier this year, Rashed et al. [305] published a DL-based method that infers both ϵ_p s (at different frequencies) and the tissue density ρ from T_1 and T_2 -weighted MR images, which are commonly acquired in the clinics. Although the three output maps exhibit the same anatomical information of input T_1 and T_2 weighted MRI data, this method is most likely not capable to retrieve the subject-specific ϵ_p s, since the CNN was trained only on fixed, literature EP values. In general, even if a relation between the water content in T_1 -weighted MR images and the electrical properties were modelled, for example based on the fact that water content is the main factor in determining the ϵ_p s at MRI frequencies — basically, the same concept of water-based EPT [53] —, this DL-based method would not accurately quantify the ϵ_p s because this underlying relation excludes other factors contributing to the ϵ_p s, such as ion concentration and/or pathological conditions. Hence, it would not be suited for personalized planning of hyperthermia treatment.

The DL-EPT method proposed in this thesis preserves the subject-specific EP information by inferring the ϵ_p s from B_1^+ measurements and reconstructs EP maps with accurate tissue interfaces and robust to experimental noise. These characteristics render this DL-EPT method an appealing candidate for direct use in hyperthermia simulations, as recognized in Chapter 5. Nevertheless, a fully MR-based HTP is not yet possible because the current implementation of DL-EPT only provides conductivity maps. At present, good quality DL-based conductivity

maps at the spatial resolution used in HTP ($2.5 \times 2.5 \times 2.5 \text{ mm}^3$) can be reconstructed in the pelvis only if motion-related artifacts are mild (Figure 4.8). Otherwise, the safest option for use in HTP is to assign median DL-EPT conductivity values to tissues in a patient model, as performed in Chapter 5. Moreover, in both Chapters 4 and 5, DL-EPT was quantitatively compared to H-EPT in carefully delineated ROIs to estimate the experimental accuracy of DL-based conductivity reconstruction for an individual subject. It is expected that the technical improvements discussed in the previous section relative to reconstruction accuracy, network uncertainty and experimental validation will increase the confidence in the quantitative capability of DL-EPT, whereas training the CNN with imaging artifacts will probably facilitate the practical use of DL-EPT conductivity maps in HTP for deep seated pelvic tumours.

6.3.3 Future perspectives

This section identifies two research opportunities which may prove useful in the perspective of MR-based HTP.

Deep learning for hyperthermia treatment planning Meliaddò et al. [306] have very recently presented an unconventional approach in which the patient's local SAR distribution at 7 T MRI could be predicted with DL directly from the measured complex B_1^+ map (based on $|B_1^+|$ and ϕ^\pm), bypassing the need of EPT and electric field simulations. Inspired by this work, future research in HTP might investigate whether a CNN could be used to learn the mapping relation between the patient's B_1^+ field measured with MRI and the electric field components at each individual antenna of an hyperthermia applicator (with arbitrary phase-amplitude settings). Such a DL-based method would substantially speed up the retrieval of electric field maps, which currently requires $\approx 1\text{--}1.5$ hours for each antenna. Furthermore, the reconstructed electric field maps could directly be used as input to the efficient optimization techniques already described and employed in Chapter 5. However, knowledge of the patient's conductivity distribution would still be required to calculate the intermediate SAR ($\text{sAR} = \sigma|E|^2/2\rho$) during the optimization, for which any EPT processing could in theory be used. This would implicitly bypass the need for permittivity maps that are typically challenging to obtain in vivo in the frequency range of interest.

Several methodological aspects described in Chapter 4 might be recycled for training such a network, for example the database of pelvic models with realistic EPs, as well as the simulation framework to reproduce the sequence-specific accuracy and precision in the simulated B_1^+ fields. At the same time, many technical improvements already discussed for DL-EPT in the previous section would also be valuable for this task. Note that the current implementation of highres3dnet in NiftyNet does not allow multiple outputs (the electric field components related to the antennas), therefore modifications to the CNN architecture would need to be implemented or another CNN architecture should be investigated.

Field of view in MR-based HTP In treatment planning of locoregional hyperthermia, cranio-caudal FOVs as large as 40–50 cm are necessary to predict the location of hot spots, which can occur outside the heated target region. This implies that current B_1^+ acquisitions, which normally map the target region, should be significantly accelerated to cover such large FOVs in order to enable an MR-based HTP workflow. Alternatively, average anatomical templates could be built to cover the extreme parts of the FOV that are not acquired with MRI. The reliability of using these templates for treatment planning should thoroughly be assessed.

6.4 Conclusion

The technical developments presented in this thesis were specifically focused on MR acquisition and reconstruction aspects contributing to the accuracy, precision and clinical applicability of EPT-based electrical property maps. The first two chapters found that the accuracy and precision of conductivity and permittivity reconstructed with conventional H-EPT were considerably affected by sequence-specific systematic errors and noise in the complex B_1^+ , and could vary sensibly depending on the adopted measurement technique. Based on these results, the general recommendation for the EPT community is to account for the impact of $|B_1^+|$ and ϕ^\pm mapping techniques on EPT reconstructions. The simulation framework presented in Chapter 3 could be useful for this purpose, as it predicts both acquisition-related and reconstruction-related errors in EPT maps. Knowing such errors would potentially enable correction strategies and could guide the selection of a $|B_1^+|$ (or ϕ^\pm) mapping sequence (and/or reconstruction method) that can guarantee the required accuracy and precision in EPT maps. Considering the plethora of EPT reconstruction algorithms and B_1^+ mapping techniques available, as well as the number of emerging clinical EPT studies, the author of this thesis anticipates that a combined assessment of acquisition- and reconstruction-related errors will become increasingly important for those applications that rely on quantitative absolute values of tissue EPs, for example hyperthermia treatment planning and therapy response monitoring in longitudinal follow up studies. Such an assessment will also enable fair comparison of EPT maps obtained from different groups or multi-centre trials.

Furthermore, a novel DL-based EPT reconstruction method for conductivity mapping in the pelvic region was developed and its in vivo feasibility was demonstrated. The resulting pelvis conductivity maps displayed superior image quality over conductivity reconstructions obtained with a conventional EPT algorithm, especially in terms of tissue boundary reconstruction and robustness against noise. Although a number of new challenges still need to be solved to guarantee accurate and trustworthy results, DL-based conductivity maps already seem appealing for direct use in hyperthermia treatment planning. Put in a wider perspective, this work represents an initial step in the emerging field of DL-based MR-EPT and provides technical foundations as well as directions upon which future research may build to fully exploit the opportunities that DL can offer for electrical property mapping.

Bibliography

- [1] H. Fricke, "The Electric Capacity of Suspensions with Special Reference to Blood," *The Journal of General Physiology*, vol. 9, no. 2, pp. 137–152, 1925.
- [2] H. Fricke, "The Maxwell-Wagner Dispersion in a Suspension of Ellipsoids," *The Journal of Physical Chemistry*, vol. 57, no. 9, pp. 934–937, 1953.
- [3] H. P. Schwan, "Electrical Properties of Tissue and Cell Suspensions," in *Advances in biological and medical physics*, vol. 5, pp. 147–209, New York, NY, USA: Academic Press, 1957.
- [4] E. H. Grant, "The Structure of Water Neighboring Proteins, Peptides and Amino Acids as Deduced from Dielectric Measurements," *Annals of the New York Academy of Sciences*, vol. 125, no. 2, pp. 418–427, 1965.
- [5] K. S. Cole and R. H. Cole, "Dispersion and Absorption in Dielectrics I. Alternating Current Characteristics," *The Journal of Chemical Physics*, vol. 9, no. 4, pp. 341–351, 1941.
- [6] C. Gabriel, "Summary of session B: The Dielectric Properties of Tissues," in *Radio Frequency Radiation Dosimetry and Its Relationship to the Biological Effects of Electromagnetic Fields*, pp. 73–74, Dordrecht, The Netherlands: Springer, 2000.
- [7] C. Gabriel, S. Gabriel, and E. Corthout, "The dielectric properties of biological tissues: I. Literature survey," *Physics in Medicine and Biology*, vol. 41, no. 11, pp. 2231–2249, 1996.
- [8] A. J. Surowiec, S. S. Stuchly, J. R. Barr, and A. Swarup, "Dielectric properties of breast carcinoma and the surrounding tissues," *IEEE Transactions on Biomedical Engineering*, vol. 35, no. 4, pp. 257–263, 1988.
- [9] W. T. Joines, Y. Zhang, C. Li, and R. L. Jirtle, "The measured electrical properties of normal and malignant human tissues from 50 to 900 MHz," *Medical Physics*, vol. 21, no. 4, pp. 547–550, 1994.
- [10] C. Gabriel, "Compilation of the Dielectric Properties of Body Tissues at RF and Microwave Frequencies.," tech. rep., London, UK, 1996.
- [11] A. Peyman and C. Gabriel, "Dielectric properties of porcine glands, gonads and body fluids," *Physics in Medicine and Biology*, vol. 57, no. 19, pp. N339–N344, 2012.
- [12] F. Fu, S. X. Xin, and W. Chen, "Temperature-and frequency-dependent dielectric properties of biological tissues within the temperature and frequency ranges typically used for magnetic resonance imaging-guided focused ultrasound surgery," *International Journal of Hyperthermia*, vol. 30, no. 1, pp. 56–65, 2014.
- [13] M. Lazebnik, D. Popovic, L. McCartney, C. B. Watkins, M. J. Lindstrom, J. Harter, S. Sewall, T. Ogilvie, A. Magliocco, T. M. Breslin, W. Temple, D. Mew, J. H. Booske, M. Okoniewski, and S. C. Hagness, "A large-scale study of the ultrawideband microwave dielectric properties of normal, benign and malignant breast tissues obtained from cancer surgeries," *Physics in Medicine and Biology*, vol. 52, no. 20, pp. 6093–6115, 2007.

- [14] A. P. O'Rourke, M. Lazebnik, J. M. Bertram, M. C. Converse, S. C. Hagness, J. G. Webster, and D. M. Mahvi, "Dielectric properties of human normal, malignant and cirrhotic liver tissue: in vivo and ex vivo measurements from 0.5 to 20 GHz using a precision open-ended coaxial probe," *Physics in Medicine and Biology*, vol. 52, no. 15, pp. 4707–4719, 2007.
- [15] A. Peyman, B. Kos, M. Djokić, B. Trotošek, C. Limbaeck-Stokin, G. Serša, and D. Miklavčič, "Variation in dielectric properties due to pathological changes in human liver," *Bioelectromagnetics*, vol. 36, no. 8, pp. 603–612, 2015.
- [16] A. Fornes-Leal, C. Garcia-Pardo, M. Frasson, V. Pons Beltran, and N. Cardona, "Dielectric characterization of healthy and malignant colon tissues in the 0.5-18 GHz frequency band," *Physics in Medicine and Biology*, vol. 61, no. 20, pp. 7334–7346, 2016.
- [17] S. Gavazzi, P. Limone, G. De Rosa, F. Molinari, and G. Vecchi, "Comparison of microwave dielectric properties of human normal, benign and malignant thyroid tissues obtained from surgeries: a preliminary study," *Biomedical Physics & Engineering Express*, vol. 4, no. 4, p. 047003, 2018.
- [18] S. Semenov, T. Huynh, T. Williams, B. Nicholson, and A. Vasilenko, "Dielectric properties of brain tissue at 1 GHz in acute ischemic stroke: Experimental study on swine," *Bioelectromagnetics*, vol. 38, no. 2, pp. 158–163, 2017.
- [19] G. Vecchi, "Electromagnetics for Medical Applications: New Paradigms?," in *7th European Conference on Antennas and Propagation (EUCAP)*, (Gothenburg, Sweden), p. 3114, 2013.
- [20] R. Pethig, "Dielectric Properties of Biological Materials: Biophysical and Medical Applications," *IEEE Transactions on Electrical Insulation*, vol. EI-19, no. 5, pp. 453–474, 1984.
- [21] K. R. Foster and H. P. Schwan, "Dielectric properties of tissues and biological materials: a critical review.," *Critical Reviews in Biomedical Engineering*, vol. 17, no. 1, pp. 25–104, 1989.
- [22] P. Hasgall, F. Di Gennaro, C. Baumgartner, E. Neufeld, B. Lloyd, M. Gosselin, D. Payne, A. Klingeböck, and N. Kuster, "IT'IS Database for thermal and electromagnetic parameters of biological tissues," <https://itis.swiss/virtual-population/tissue-properties/overview/>, p. Version 4.0, 2018.
- [23] M. Lazebnik, M. C. Converse, J. H. Booske, and S. C. Hagness, "Ultrawideband temperature-dependent dielectric properties of animal liver tissue in the microwave frequency range," *Physics in Medicine and Biology*, vol. 51, no. 7, pp. 1941–1955, 2006.
- [24] D. A. Pollacco, L. Farina, P. S. Wismayer, L. Farrugia, and C. V. Sammut, "Characterization of the dielectric properties of biological tissues and their correlation to tissue hydration," *IEEE Transactions on Dielectrics and Electrical Insulation*, vol. 25, no. 6, pp. 2191–2197, 2018.
- [25] C. Gabriel, "Dielectric properties of biological tissue: Variation with age," *Bioelectromagnetics*, vol. 26, pp. S12–S18, 2005.
- [26] D. Miklavčič, N. Pavšelj, and F. X. Hart, "Electric Properties of Tissues," in *Wiley Encyclopedia of Biomedical Engineering*, pp. 1–12, Hoboken, NJ, USA: John Wiley & Sons, Inc., 2006.
- [27] H. Wang, Y. He, Q. Yan, F. You, F. Fu, X. Dong, X. Shi, and M. Yang, "Correlation between the dielectric properties and biological activities of human ex vivo hepatic tissue," *Physics in Medicine and Biology*, vol. 60, no. 6, pp. 2603–2617, 2015.
- [28] G. Schmid, G. Neubauer, U. M. Illievich, and F. Alesch, "Dielectric properties of porcine brain tissue in the transition from life to death at frequencies from 800 to 1900 MHz," *Bioelectromagnetics*, vol. 24, no. 6, pp. 413–422, 2003.
- [29] P. M. Meaney, A. P. Gregory, N. R. Epstein, and K. D. Paulsen, "Microwave open-ended coaxial dielectric probe: interpretation of the sensing volume re-visited," *BMC Medical*

- Physics*, vol. 14, p. 3, dec 2014.
- [30] A. La Gioia, E. Porter, I. Merunka, A. Shahzad, S. Salahuddin, M. Jones, and M. O'Halloran, "Open-Ended Coaxial Probe Technique for Dielectric Measurement of Biological Tissues: Challenges and Common Practices," *Diagnostics*, vol. 8, no. 2, p. 40, 2018.
- [31] P. Seeger and S. Wolz, *Successful biological control of cancer by combat against the causes*. Melsbach, Germany: Neuwieder Verlagsgesellschaft., 1990.
- [32] A. Peyman, S. Holden, and C. Gabriel, "Dielectric Properties of Tissues at Microwave Frequencies," in *RUM3: Final technical report MTHR Department of Health - Mobile Telecommunications and Health Research Programme*, (London, UK), 2005.
- [33] E. C. Fear, "Microwave imaging of the breast," *Technology in Cancer Research and Treatment*, vol. 4, no. 1, pp. 69–82, 2005.
- [34] R. Chandra, I. Balasingham, H. Zhou, and R. M. Narayanan, "Medical Microwave Imaging and Analysis," in *Medical Image Analysis and Informatics: Computer-Aided Diagnosis and Therapy*, pp. 451–466, Boca Raton, FL, USA: CRC Press, 2017.
- [35] E. M. Purcell, H. C. Torrey, and R. V. Pound, "Resonance Absorption by Nuclear Magnetic Moments in a Solid," *Physical Review*, vol. 69, no. 1-2, pp. 37–38, 1946.
- [36] R. Damadian, "Tumor detection by nuclear magnetic resonance," *Science*, vol. 171, no. 3976, pp. 1151–1153, 1971.
- [37] P. C. Lauterbur, "Image formation by induced local interactions: Examples employing nuclear magnetic resonance," *Nature*, vol. 242, no. 5394, pp. 190–191, 1973.
- [38] P. Mansfield and P. K. Grannell, "NMR 'diffraction' in solids?," *Journal of Physics C: Solid State Physics*, vol. 6, no. 22, pp. L422–L426, 1973.
- [39] E. M. Haacke, R. W. Brown, M. R. Thompson, and R. Venkatesan, *Magnetic Resonance Imaging: Physical Principles and Sequence Design*. Hoboken, NJ, USA: John Wiley & Sons, Inc., 1st ed., 1999.
- [40] R. W. Brown, Y. C. N. Cheng, E. M. Haacke, M. R. Thompson, and R. Venkatesan, *Magnetic Resonance Imaging: Physical Principles and Sequence Design: Second Edition*. Chichester, UK: Wiley Blackwell, 2014.
- [41] D. W. McRobbie, E. A. Moore, M. J. Graves, and M. R. Prince, *MRI From Picture to Proton*. Cambridge, UK: Cambridge University Press, 2006.
- [42] F. Bloch, "Nuclear Induction," *Physical Review*, vol. 70, pp. 460–474, 1946.
- [43] D. I. Hoult, "The principle of reciprocity in signal strength calculations? A mathematical guide," *Concepts in Magnetic Resonance*, vol. 12, no. 4, pp. 173–187, 2000.
- [44] G. Glover, C. Hayes, N. Pelc, W. Edelstein, O. Mueller, H. Hart, C. Hardy, M. O'Donnell, and W. Barber, "Comparison of linear and circular polarization for magnetic resonance imaging," *Journal of Magnetic Resonance*, vol. 64, no. 2, pp. 255–270, 1985.
- [45] Q. X. Yang, J. Wang, X. Zhang, C. M. Collins, M. B. Smith, H. Liu, X.-H. H. Zhu, J. T. Vaughan, K. Ugurbil, and W. Chen, "Analysis of wave behavior in lossy dielectric samples at high field," *Magnetic Resonance in Medicine*, vol. 47, no. 5, pp. 982–989, 2002.
- [46] T. S. Ibrahim, Y. K. Hue, and L. Tang, "Understanding and manipulating the RF fields at high field MRI," *NMR in Biomedicine*, vol. 22, no. 9, pp. 927–936, 2009.
- [47] M. V. Vaidya, C. M. Collins, D. K. Sodickson, R. Brown, G. C. Wiggins, and R. Lattanzi, "Dependence of B1- and B1+ field patterns of surface coils on the electrical properties of the sample and the MR operating frequency," *Concepts in Magnetic Resonance Part B: Magnetic Resonance Engineering*, vol. 46, no. 1, pp. 25–40, 2016.
- [48] P.-F. Van de Moortele, C. Akgun, G. Adriany, S. Moeller, J. Ritter, C. M. Collins, M. B. Smith, J. T. Vaughan, and K. Ugurbil, "B1 destructive interferences and spatial phase patterns at 7 T with a head transceiver array coil," *Magnetic Resonance in Medicine*, vol. 54, no. 6, pp. 1503–1518, 2005.
- [49] C. M. Collins, W. Liu, W. Schreiber, Q. X. Yang, and M. B. Smith, "Central brightening

- due to constructive interference with, without, and despite dielectric resonance," *Journal of Magnetic Resonance Imaging*, vol. 21, no. 2, pp. 192–196, 2005.
- [50] J. P. Marques, D. K. Sodickson, O. Ipek, C. M. Collins, and R. Gruetter, "Single acquisition electrical property mapping based on relative coil sensitivities: A proof-of-concept demonstration," *Magnetic Resonance in Medicine*, vol. 74, no. 1, pp. 185–195, 2015.
- [51] P. Farace, R. Pontalti, L. Cristoforetti, R. Antolini, and M. Scarpa, "An automated method for mapping human tissue permittivities by MRI in hyperthermia treatment planning," *Physics in Medicine and Biology*, vol. 42, no. 11, pp. 2159–2174, 1997.
- [52] M. Mazzurana, L. Sandrini, A. Vaccari, C. Malacarne, L. Cristoforetti, and R. Pontalti, "A semi-automatic method for developing an anthropomorphic numerical model of dielectric anatomy by MRI," *Physics in Medicine and Biology*, vol. 48, no. 19, pp. 3157–3170, 2003.
- [53] E. Michel, D. Hernandez, and S. Y. Lee, "Electrical conductivity and permittivity maps of brain tissues derived from water content based on T1-weighted acquisition," *Magnetic Resonance in Medicine*, vol. 77, no. 3, pp. 1094–1103, 2017.
- [54] U. Katscher, T. Voigt, C. Findeklee, P. Vernickel, K. Nehrke, and O. Dössel, "Determination of electric conductivity and local SAR via B1 mapping," *IEEE transactions on medical imaging*, vol. 28, no. 9, pp. 1365–1374, 2009.
- [55] E. M. Haacke, L. S. Petropoulos, E. W. Nilges, and D. H. Wu, "Extraction of conductivity and permittivity using magnetic resonance imaging," *Physics in Medicine and Biology*, vol. 36, no. 6, pp. 723–734, 1991.
- [56] H. Wen, "Noninvasive quantitative mapping of conductivity and dielectric distributions using RF wave propagation effects in high-field MRI," in *Proc. SPIE 5030, Medical Imaging: Physics of Medical Imaging*, (San Diego, CA, USA), p. 471, 2003.
- [57] U. Katscher and C. A. T. van den Berg, "Electric properties tomography: Biochemical, physical and technical background, evaluation and clinical applications," *NMR in Biomedicine*, vol. 30, no. 8, p. e3729, 2017.
- [58] J. Liu, Y. Wang, U. Katscher, and B. He, "Electrical Properties Tomography Based on B1 Maps in MRI: Principles, Applications, and Challenges," *IEEE Transactions on Biomedical Engineering*, vol. 64, no. 11, pp. 2515–2530, 2017.
- [59] A. L. H. M. W. van Lier, D. O. Brunner, K. P. Pruessmann, D. W. J. Klomp, P. R. Luijten, J. J. W. Lagendijk, and C. A. T. van den Berg, "B1+ Phase mapping at 7 T and its application for in vivo electrical conductivity mapping," *Magnetic Resonance in Medicine*, vol. 67, no. 2, pp. 552–561, 2012.
- [60] T. Voigt, U. Katscher, and O. Doessel, "Quantitative conductivity and permittivity imaging of the human brain using electric properties tomography," *Magnetic Resonance in Medicine*, vol. 66, no. 2, pp. 456–466, 2011.
- [61] Y. LeCun, Y. Bengio, and G. Hinton, "Deep learning," *Nature*, vol. 521, no. 7553, pp. 436–444, 2015.
- [62] I. Goodfellow, Y. Bengio, and A. Courville, *Deep Learning*. Cambridge, MA, USA: MIT Press, 2016.
- [63] M. A. Nielsen, *Neural Networks and Deep Learning*. Determination Press, 2015.
- [64] A. S. Lundervold and A. Lundervold, "An overview of deep learning in medical imaging focusing on MRI," *Zeitschrift für Medizinische Physik*, vol. 29, no. 2, pp. 102–127, 2019.
- [65] E. K. Insko and L. Bolinger, "Mapping of the Radiofrequency Field," *Journal of Magnetic Resonance, Series A*, vol. 103, no. 1, pp. 82–85, 1993.
- [66] R. Stollberger and P. Wach, "Imaging of the active B1+ field in vivo," *Magnetic Resonance in Medicine*, vol. 38, no. 2, pp. 336–336, 1997.
- [67] C. H. Cunningham, J. M. Pauly, and K. S. Nayak, "Saturated double-angle method for rapid B1+ mapping," *Magnetic Resonance in Medicine*, vol. 55, no. 6, pp. 1326–1333, 2006.

-
- [68] V. L. Yarnykh, "Actual flip-angle imaging in the pulsed steady state: A method for rapid three-dimensional mapping of the transmitted radiofrequency field," *Magnetic Resonance in Medicine*, vol. 57, no. 1, pp. 192–200, 2007.
- [69] T. Voigt, K. Nehrke, O. Doessel, and U. Katscher, "T1 corrected B1 mapping using multi-TR gradient echo sequences," *Magnetic Resonance in Medicine*, vol. 64, no. 3, pp. 725–733, 2010.
- [70] N. Choi, J. Lee, M.-O. Kim, J. Shin, and D.-H. Kim, "A modified multi-echo AFI for simultaneous B1+ magnitude and phase mapping," *Magnetic Resonance Imaging*, vol. 32, no. 4, pp. 314–320, 2014.
- [71] S. Akoka, F. Franconi, F. Seguin, and A. Le Pape, "Radiofrequency map of an NMR coil by imaging," *Magnetic Resonance Imaging*, vol. 11, no. 3, pp. 437–441, 1993.
- [72] K. Nehrke and P. Börner, "DREAM—a novel approach for robust, ultrafast, multislice B1 mapping," *Magnetic Resonance in Medicine*, vol. 68, no. 5, pp. 1517–1526, 2012.
- [73] G. R. Morrell, "A phase-sensitive method of flip angle mapping," *Magnetic Resonance in Medicine*, vol. 60, no. 4, pp. 889–894, 2008.
- [74] L. I. Sacolick, F. Wiesinger, I. Hancu, and M. W. Vogel, "B1 mapping by Bloch-Siegert shift," *Magnetic Resonance in Medicine*, vol. 63, no. 5, pp. 1315–1322, 2010.
- [75] K. V. Jordanova, D. G. Nishimura, and A. B. Kerr, "B1 estimation using adiabatic refocusing: BEAR," *Magnetic Resonance in Medicine*, vol. 72, no. 5, pp. 1302–1310, 2014.
- [76] T. Wade and B. Rutt, "Comparison of Current B1-Mapping Techniques," in *Proceeding of the 15th Annual Meeting of ISMRM*, (Berlin, Germany), p. 354, 2007.
- [77] G. R. Morrell and M. C. Schabel, "An analysis of the accuracy of magnetic resonance flip angle measurement methods," *Physics in Medicine and Biology*, vol. 55, no. 20, pp. 6157–6174, 2010.
- [78] R. Pohmann and K. Scheffler, "A theoretical and experimental comparison of different techniques for B1 mapping at very high fields," *NMR in Biomedicine*, vol. 26, no. 3, pp. 265–275, 2013.
- [79] F. Schweser, L. Huang, K.-H. Herrmann, M. Krmer, A. Deistung, and J. R. Reichenbach, "Conductivity mapping using Ultrashort Echo Time (UTE) imaging," in *Proceedings of the 21st Annual Meeting of ISMRM*, (Salt Lake City, Utah, USA), p. 4190, 2013.
- [80] S.-K. Lee, S. Bulumulla, F. Wiesinger, L. Sacolick, W. Sun, and I. Hancu, "Tissue Electrical Property Mapping From Zero Echo-Time Magnetic Resonance Imaging," *IEEE Transactions on Medical Imaging*, vol. 34, no. 2, pp. 541–550, 2015.
- [81] L. Huang, F. Schweser, K.-H. Herrmann, M. Krämer, A. Deistung, and J. R. Reichenbach, "A Monte Carlo method for overcoming the edge artifacts in MRI-based electrical conductivity mapping," in *Proceedings of the 22nd Annual Meeting of ISMRM*, (Milan, Italy), p. 3190, 2014.
- [82] D.-H. Kim, N. Choi, S. M. Ghoo, J. Shin, and C. Liu, "Simultaneous imaging of in vivo conductivity and susceptibility," *Magnetic Resonance in Medicine*, vol. 71, no. 3, pp. 1144–1150, 2014.
- [83] J. K. Seo, M.-O. Kim, J. Lee, N. Choi, E. J. Woo, H. J. Kim, O. I. Kwon, and D.-H. Kim, "Error analysis of nonconstant admittivity for MR-based electric property imaging," *IEEE Transactions on Medical Imaging*, vol. 31, no. 2, pp. 430–437, 2012.
- [84] S. Bulumulla, S. Lee, and D. Yeo, "Conductivity and permittivity imaging at 3.0 T," *Concepts in Magnetic Resonance Part B: Magnetic Resonance Engineering*, vol. 41B, no. 1, pp. 13–21, 2012.
- [85] A. Savitzky and M. J. E. Golay, "Smoothing and Differentiation of Data by Simplified Least Squares Procedures," *Analytical Chemistry*, vol. 36, no. 8, pp. 1627–1639, 1964.
- [86] S. Duan, C. Xu, G. Deng, J. Wang, F. Liu, and S. X. Xin, "Quantitative analysis of the reconstruction errors of the currently popular algorithm of magnetic resonance electrical property tomography at the interfaces of adjacent tissues," *NMR in Biomedicine*, vol. 29,
-

- no. 6, pp. 744–750, 2016.
- [87] S. Mandija, A. Sbrizzi, U. Katscher, P. R. Luijten, and C. A. T. van den Berg, “Error analysis of Helmholtz-based MR-electrical properties tomography,” *Magnetic Resonance in Medicine*, vol. 80, no. 1, pp. 90–100, 2018.
- [88] S.-K. Lee, S. Bulumulla, and I. Hancu, “Theoretical Investigation of Random Noise-Limited Signal-to-Noise Ratio in MR-Based Electrical Properties Tomography,” *IEEE Transactions on Medical Imaging*, vol. 34, no. 11, pp. 2220–2232, 2015.
- [89] A. L. H. M. W. van Lier, A. Raaijmakers, T. Voigt, J. J. W. Lagendijk, P. R. Luijten, U. Katscher, and C. A. T. van den Berg, “Electrical properties tomography in the human brain at 1.5, 3, and 7 T: A comparison study,” *Magnetic Resonance in Medicine*, vol. 71, no. 1, pp. 354–363, 2014.
- [90] T. Voigt, H. Homann, U. Katscher, and O. Doessel, “Patient-individual local SAR determination: In vivo measurements and numerical validation,” *Magnetic Resonance in Medicine*, vol. 68, no. 4, pp. 1117–1126, 2012.
- [91] F. S. Hafalir, O. F. Oran, N. Gurler, and Y. Z. Ider, “Convection-reaction equation based magnetic resonance electrical properties tomography (cr-MREPT),” *IEEE Transactions on Medical Imaging*, vol. 33, no. 3, pp. 777–793, 2014.
- [92] E. Michel, D. Hernandez, M. H. Cho, and S. Y. Lee, “Denoising of B1+ field maps for noise-robust image reconstruction in electrical properties tomography,” *Medical Physics*, vol. 41, no. 10, p. 102304, 2014.
- [93] J. Liu, X. Zhang, S. Schmitter, P.-F. van de Moortele, and B. He, “Gradient-based electrical properties tomography (gEPT): A robust method for mapping electrical properties of biological tissues in vivo using magnetic resonance imaging,” *Magnetic Resonance in Medicine*, vol. 74, no. 3, pp. 634–646, 2015.
- [94] U. Katscher, K. Djamshidi, T. Voigt, M. K. Ivancevic, A. Hiroyuki, G. Newstead, and J. Keupp, “Estimation of breast tumor conductivity using parabolic phase fitting,” in *Proceedings of the 20th Annual Meeting of ISMRM*, (Melbourne, Victoria, Australia), p. 3482, 2012.
- [95] J. Shin, J. Kim, and D.-H. Kim, “Redesign of the Laplacian kernel for improvements in conductivity imaging using MRI,” *Magnetic Resonance in Medicine*, vol. 81, no. 3, pp. 2167–2175, 2019.
- [96] J. Shin, M.-O. Kim, S. Cho, and D.-H. Kim, “Fast Spin Echo Imaging-Based Electric Property Tomography With K-Space Weighting via T2 Relaxation (rEPT),” *IEEE Transactions on Medical Imaging*, vol. 36, no. 8, pp. 1615–1625, 2017.
- [97] E. Balidemaj, A. L. H. M. W. van Lier, H. Crezee, A. J. Nederveen, L. J. A. Stalpers, and C. A. T. van den Berg, “Feasibility of Electric Property Tomography of pelvic tumors at 3T,” *Magnetic Resonance in Medicine*, vol. 73, no. 4, pp. 1505–1513, 2015.
- [98] X. Zhang, P.-F. van de Moortele, S. Schmitter, and B. He, “Complex B1 mapping and electrical properties imaging of the human brain using a 16-channel transceiver coil at 7T,” *Magnetic Resonance in Medicine*, vol. 69, no. 5, pp. 1285–1296, 2013.
- [99] J. Liu, X. Zhang, P.-F. Van de Moortele, S. Schmitter, and B. He, “Determining electrical properties based on B1 fields measured in an MR scanner using a multi-channel transmit/receive coil: a general approach,” *Physics in Medicine and Biology*, vol. 58, no. 13, pp. 4395–4408, 2013.
- [100] J. Liu, P.-F. Van De Moortele, X. Zhang, Y. Wang, and B. He, “Simultaneous Quantitative Imaging of Electrical Properties and Proton Density from B1 Maps Using MRI,” *IEEE Transactions on Medical Imaging*, 2016.
- [101] C. Stehning, T. Voigt, P. Karkowski, and U. Katscher, “Electric Properties Tomography (EPT) of the Liver in a Single Breathhold Using SSFP,” in *Proceedings of the 20th Annual Meeting of ISMRM*, (Melbourne, Victoria, Australia), p. 386, 2012.
- [102] E. Balidemaj, P. de Boer, A. L. H. M. W. van Lier, R. F. Remis, L. J. A. Stalpers, G. H.

- Westerveld, A. J. Nederveen, C. A. T. van den Berg, and J. Crezee, "In vivo electric conductivity of cervical cancer patients based on B1+ maps at 3T MRI," *Physics in Medicine and Biology*, vol. 61, no. 4, pp. 1596–1607, 2016.
- [103] N. Gurler and Y. Z. Ider, "Gradient-based electrical conductivity imaging using MR phase," *Magnetic Resonance in Medicine*, vol. 77, no. 1, pp. 137–150, 2017.
- [104] Y. Wang, P.-F. Van de Moortele, and B. He, "Automated gradient-based electrical properties tomography in the human brain using 7 Tesla MRI," *Magnetic Resonance Imaging*, vol. 63, pp. 258–266, 2019.
- [105] Y. Hua, I. Hancu, S.-K. Lee, T. D. Yeo, and J. Liu, "Evaluation of the Noise Behavior of Gradient-based vs. Helmholtz-based Reconstruction of Electrical Properties Tomography in Simulation," in *Proceedings of the 26th Annual Meeting of ISMRM*, (Paris, France), p. 5103, 2018.
- [106] C. Liu, J. Jin, L. Guo, M. Li, Y. Tesiram, H. Chen, F. Liu, X. Xin, and S. Crozier, "MR-based electrical property tomography using a modified finite difference scheme," *Physics in Medicine & Biology*, vol. 63, no. 14, p. 145013, 2018.
- [107] P. S. Fuchs, S. Mandija, P. R. S. Stijnman, W. M. Brink, C. A. T. van den Berg, and R. F. Remis, "First-Order Induced Current Density Imaging and Electrical Properties Tomography in MRI," *IEEE Transactions on Computational Imaging*, vol. 4, no. 4, pp. 624–631, 2018.
- [108] Y. Wang, P.-F. Van De Moortele, and B. He, "CONTRAST CONFORMED ELECTRICAL PROPERTIES TOMOGRAPHY (CONCEPT) BASED ON MULTI-CHANNEL TRANSMISSION AND ALTERNATING DIRECTION METHOD OF MULTIPLIERS," *IEEE Transactions on Medical Imaging*, vol. 38, no. 2, pp. 349–359, 2019.
- [109] E. Balidemaj, C. A. T. van den Berg, J. Trinks, A. L. H. M. W. Van Lier, A. J. Nederveen, L. J. A. Stalpers, H. Crezee, and R. F. Remis, "CSI-EPT: A Contrast Source Inversion Approach for Improved MRI-Based Electric Properties Tomography," *IEEE Transactions on Medical Imaging*, vol. 34, no. 9, pp. 1788–1796, 2015.
- [110] R. Schmidt and A. Webb, "A new approach for electrical properties estimation using a global integral equation and improvements using high permittivity materials," *Journal of Magnetic Resonance*, vol. 262, pp. 8–14, 2016.
- [111] A. Borsic, I. Perreard, A. Mahara, and R. J. Halter, "An inverse problems approach to MR-EPT image reconstruction," *IEEE Transactions on Medical Imaging*, vol. 35, no. 1, pp. 244–256, 2016.
- [112] K. M. Ropella and D. C. Noll, "A regularized, model-based approach to phase-based conductivity mapping using MRI," *Magnetic Resonance in Medicine*, vol. 78, no. 5, pp. 2011–2021, 2017.
- [113] A. Rahimov, A. Litman, and G. Ferrand, "MRI-based electric properties tomography with a quasi-Newton approach," *Inverse Problems*, vol. 33, no. 10, p. 105004, 2017.
- [114] R. L. Leijssen, W. M. Brink, C. A. T. van den Berg, A. G. Webb, and R. F. Remis, "3-D Contrast Source Inversion-Electrical Properties Tomography," *IEEE Transactions on Medical Imaging*, vol. 37, no. 9, pp. 2080–2089, 2018.
- [115] L. Guo, J. Jin, C. Liu, F. Liu, and S. Crozier, "An efficient integral-based method for three-dimensional MR-EPT and the calculation of the RF-Coil-Induced Bzfield," *IEEE Transactions on Biomedical Engineering*, vol. 65, no. 2, pp. 282–293, 2018.
- [116] A. Arduino, O. Bottauscio, M. Chiampì, and L. Zilberti, "Magnetic resonance-based imaging of human electric properties with phaseless contrast source inversion," *Inverse Problems*, vol. 34, no. 8, p. 084002, 2018.
- [117] M. T. Bevacqua, G. G. Bellizzi, L. Crocco, and T. Isernia, "A method for quantitative imaging of electrical properties of human tissues from only amplitude electromagnetic data," *Inverse Problems*, vol. 35, no. 2, p. 025006, 2019.
- [118] J. E. C. Serralles, R. Lattanzi, I. I. Giannakopoulos, B. Zhang, C. Ianniello, M. A. Cloos,

- A. G. Polimeridis, J. K. White, D. K. Sodickson, and L. Daniel, "Noninvasive Estimation of Electrical Properties From Magnetic Resonance Measurements via Global Maxwell Tomography and Match Regularization," *IEEE Transactions on Biomedical Engineering*, vol. 67, no. 1, pp. 3–15, 2020.
- [119] R. Leijssen, P. Fuchs, W. Brink, A. Webb, and R. Remis, "Developments in Electrical-Property Tomography Based on the Contrast-Source Inversion Method," *Journal of Imaging*, vol. 5, no. 2, p. 25, 2019.
- [120] N. Hampe, M. Herrmann, T. Amthor, C. Findeklee, M. Doneva, and U. Katscher, "Dictionary-based electric properties tomography," *Magnetic Resonance in Medicine*, vol. 81, no. 1, pp. 342–349, 2019.
- [121] S. Mandija, E. F. Meliadó, N. R. F. Huttinga, P. R. Luijten, and C. A. T. van den Berg, "Opening a new window on MR-based Electrical Properties Tomography with deep learning," *Scientific Reports*, vol. 9, no. 1, p. 8895, 2019.
- [122] N. Hampe, U. Katscher, C. A. T. van den Berg, K. K. Tha, S. Mandija, C. A. van den Berg, K. K. Tha, and S. Mandija, "Deep learning brain conductivity mapping using a patch-based 3D U-net," in *Proceedings of the 27th Annual Meeting of ISMRM*, (Montréal, QC, Canada), p. 5045, 2019.
- [123] A. Arduino, M. Chiampi, F. Pennecchi, L. Zilberti, and O. Bottauscio, "Monte Carlo Method for Uncertainty Propagation in Magnetic Resonance-Based Electric Properties Tomography," *IEEE Transactions on Magnetics*, vol. 53, no. 11, pp. 1–4, 2017.
- [124] T. Voigt, O. Väterlein, C. Stehning, U. Katscher, and J. Fiehler, "In vivo Glioma Characterization using MR Conductivity Imaging," in *Proceedings of the 19th Annual Meeting of ISMRM*, (Montréal, Québec, Canada), p. 2865, 2011.
- [125] A. L. H. M. W. van Lier, J. M. Hoogduin, D. L. Polders, V. O. Boer, J. Hendrikse, P. A. Robe, P. A. Woerdeman, J. J. Lagendijk, and P. R. Luijten, "Electrical conductivity imaging of brain tumours," in *Proceedings of the 19th Annual Meeting of ISMRM*, (Montréal, Québec, Canada), p. 4464, 2011.
- [126] M. Huhndorf, C. Stehning, A. Rohr, M. Helle, U. Katscher, and O. Jansen, "Systematic Brain Tumor Conductivity Study with Optimized EPT Sequence and Reconstruction Algorithm," in *Proceedings of the 21th Annual Meeting of ISMRM x*, (Salt Lake City, Utah, USA), p. 3626, 2013.
- [127] K. K. Tha, U. Katscher, S. Yamaguchi, C. Stehning, S. Terasaka, N. Fujima, K. Kudo, K. Kazumata, T. Yamamoto, M. Van Cauteren, and H. Shirato, "Noninvasive electrical conductivity measurement by MRI: a test of its validity and the electrical conductivity characteristics of glioma," *European Radiology*, vol. 28, no. 1, pp. 348–355, 2018.
- [128] U. Katscher, H. Abe, M. K. Ivancevic, and J. Keupp, "Investigating breast tumor malignancy with electric conductivity measurements," in *Proceedings of the 23rd Annual Meeting of ISMRM*, (Toronto, Ontario, Canada), p. 3306, 2015.
- [129] J. Shin, M. J. Kim, J. Lee, Y. Nam, M.-o. Kim, N. Choi, S.-Y. Kim, and D.-H. Kim, "Initial study on in vivo conductivity mapping of breast cancer using MRI," *Journal of Magnetic Resonance Imaging*, vol. 42, no. 2, pp. 371–378, 2015.
- [130] N. Mori, K. Tsuchiya, D. Sheth, S. Mugikura, K. Takase, U. Katscher, and H. Abe, "Diagnostic value of electric properties tomography (EPT) for differentiating benign from malignant breast lesions: comparison with standard dynamic contrast-enhanced MRI," *European Radiology*, vol. 29, no. 4, pp. 1778–1786, 2019.
- [131] E. Balidemaj, H. P. Kok, G. Schooneveldt, A. L. H. M. W. van Lier, R. F. Remis, L. J. A. Stalpers, H. Westerveld, A. J. Nederveen, C. A. T. van den Berg, and J. Crezee, "Hyperthermia treatment planning for cervical cancer patients based on electrical conductivity tissue properties acquired in vivo with EPT at 3 T MRI," *International journal of hyperthermia*, vol. 32, no. 5, pp. 558–568, 2016.
- [132] Y. Wang, Q. Shao, P.-F. van de Moortele, E. Racila, J. Liu, J. Bischof, and B. He, "Map-

- ping electrical properties heterogeneity of tumor using boundary informed electrical properties tomography (BIEPT) at 7T," *Magnetic Resonance in Medicine*, vol. 81, no. 1, pp. 393–409, 2019.
- [133] I. O. Ko, B. K. Choi, N. Katoch, J. A. Park, J. W. Kim, H. J. Kim, O. I. Kwon, and E. J. Woo, "In Vivo Conductivity Imaging of Tissue Response after Radiation Therapy," in *Proceedings of the 26th Annual Meeting of ISMRM*, (Paris, France), p. 0547, 2018.
- [134] Y. Liao, N. Lechea, A. W. Magill, W. A. Worthoff, V. Gras, and N. J. Shah, "Correlation of quantitative conductivity mapping and total tissue sodium concentration at 3T/4T," *Magnetic Resonance in Medicine*, vol. 82, no. 4, pp. 1518–1526, 2019.
- [135] S. Mandija, P. W. de Bruin, A. G. Webb, P. R. Luijten, and C. A. van den Berg, "Investigating the relation between electrical conduction and tissue composition with proton and sodium MRI," in *Proceedings of the 25th Annual Meeting of ISMRM*, (Honolulu, Hawai'i, USA), p. 3639, 2017.
- [136] Y. Shcherbakova, C. A. T. van den Berg, C. T. W. Moonen, and L. W. Bartels, "PLANET: An ellipse fitting approach for simultaneous T1 and T2 mapping using phase-cycled balanced steady-state free precession," *Magnetic Resonance in Medicine*, vol. 79, no. 2, pp. 711–722, 2018.
- [137] P. A. Bottomley and E. R. Andrew, "RF magnetic field penetration, phase shift and power dissipation in biological tissue: implications for NMR imaging," *Physics in Medicine and Biology*, vol. 23, no. 4, p. 006, 1978.
- [138] C. M. Collins, S. Li, and M. B. Smith, "SAR and B1 field distributions in a heterogeneous human head model within a birdcage coil," *Magnetic Resonance in Medicine*, vol. 40, no. 6, pp. 847–856, 1998.
- [139] U. Katscher, C. Findekle, and T. Voigt, "B1-based specific energy absorption rate determination for nonquadrature radiofrequency excitation," *Magnetic Resonance in Medicine*, vol. 68, no. 6, pp. 1911–1918, 2012.
- [140] J. Crezee, M. Bennis, S. Gavazzi, L. J. A. Stalpers, A. L. H. M. W. van Lier, and H. P. Kok, "Development of electrical properties tomography for hyperthermia treatment planning," in *First IEEE MTT-S International Microwave Bio Conference (IMBIOC)*, (Gothenburg, Sweden), pp. 1–4, 2017.
- [141] S. Mandija, P. I. Petrov, S. F. W. Neggers, and P. R. Luijten, "Noninvasive Electric Current Induction for Low-Frequency Tissue Conductivity Reconstruction: Is It Feasible With a TMS-MRI Setup?," *Tomography*, vol. 2, no. 3, pp. 203–214, 2016.
- [142] R. D. Peters and R. M. Henkelman, "Proton-resonance frequency shift MR thermometry is affected by changes in the electrical conductivity of tissue," *Magnetic Resonance in Medicine*, vol. 43, no. 1, pp. 62–71, 2000.
- [143] G. Salim, P. Baron, D. H. J. Poot, J. A. Hernandez Tamames, T. Dridzal, M. M. Paulides, S. Klein, and G. Salim, "Effect of the transceive phase on MR thermometry in aqueous mediums," in *Proceedings of the 25th Annual Meeting of ISMRM*, (Honolulu, Hawai'i, USA), p. 5422, 2017.
- [144] S. D. Robinson, K. Bredies, D. Khabipova, B. Dymerska, J. P. Marques, and F. Schweser, "An illustrated comparison of processing methods for MR phase imaging and QSM: combining array coil signals and phase unwrapping," *NMR in Biomedicine*, vol. 30, no. 4, p. e3601, 2017.
- [145] M. Weiger and K. P. Pruessmann, "MRI with Zero Echo Time," in *Encyclopedia of Magnetic Resonance*, pp. 311–322, Chichester, UK: John Wiley & Sons, Ltd, 2012.
- [146] C. Stehning, T. Voigt, and U. Katscher, "Real time conductivity mapping using balanced SSFP and phase based reconstruction," in *Proceedings of the 19th Annual Meeting of ISMRM*, (Montréal, Québec, Canada), p. 128, 2011.
- [147] Q. S. Xiang and M. N. Hoff, "Banding artifact removal for bSSFP imaging with an elliptical signal model," *Magnetic Resonance in Medicine*, vol. 71, no. 3, pp. 927–933, 2014.

- [148] M. Björk, R. R. Ingle, E. Gudmundson, P. Stoica, D. G. Nishimura, and J. K. Barral, "Parameter estimation approach to banding artifact reduction in balanced steady-state free precession," *Magnetic resonance in medicine*, vol. 72, no. 3, pp. 880–892, 2014.
- [149] N. K. Bangerter, B. A. Hargreaves, S. S. Vasanaawala, J. M. Pauly, G. E. Gold, and D. G. Nishimura, "Analysis of Multiple-Acquisition SSFP," *Magnetic Resonance in Medicine*, vol. 51, no. 5, pp. 1038–1047, 2004.
- [150] M. L. Lauzon and R. Frayne, "Analytical characterization of RF phase-cycled balanced steady-state free precession," *Concepts in Magnetic Resonance Part A*, vol. 34A, no. 3, pp. 133–143, 2009.
- [151] S. Ozdemir and Y. Z. Ider, "bSSFP phase correction and its use in magnetic resonance electrical properties tomography," *Magnetic Resonance in Medicine*, vol. 81, no. 2, pp. 934–946, 2019.
- [152] M.-O. Kim, N. Choi, J. Shin, J. Lee, and D.-H. Kim, "Phase unbanding in bSSFP for Liver conductivity imaging at 3.0T," in *Proceedings of the 21st Annual Meeting of ISMRM*, (Salt Lake City, Utah, USA), p. 4173, 2013.
- [153] S. Gavazzi, S. Mandija, C. A. T. van den Berg, Y. Shcherbakova, M. Bennis, J. J. W. Lagendijk, L. J. A. Stalpers, H. Crezee, and A. L. H. M. W. van Lier, "Sequences for transceive phase mapping: a comparison study and application to conductivity imaging," in *Proceedings of the 26th Annual Meeting of ISMRM*, (Paris, France), p. 5084, 2018.
- [154] O. Bieri and K. Scheffler, "Fundamentals of balanced steady state free precession MRI," *Journal of Magnetic Resonance Imaging*, vol. 38, no. 1, pp. 2–11, 2013.
- [155] Y. Shcherbakova, C. A. T. van den Berg, C. T. W. Moonen, and L. W. Bartels, "On the accuracy and precision of PLANET for multiparametric MRI using phase-cycled bSSFP imaging," *Magnetic Resonance in Medicine*, vol. 81, no. 3, pp. 1534–1552, 2019.
- [156] B. Hargreaves, "Bloch Equation Simulator," <http://mrsrl.stanford.edu/~brian/bloch/>.
- [157] J. P. Wansapura, S. K. Holland, R. S. Dunn, and W. S. Ball, "NMR relaxation times in the human brain at 3.0 Tesla," *Journal of Magnetic Resonance Imaging*, vol. 9, no. 4, pp. 531–538, 1999.
- [158] K. L. Miller, S. M. Smith, and P. Jezzard, "Asymmetries of the balanced SSFP profile. Part II: White matter," *Magnetic Resonance in Medicine*, vol. 63, no. 2, pp. 396–406, 2010.
- [159] E. Alonso-Ortiz, I. R. Levesque, and G. B. Pike, "MRI-based myelin water imaging: A technical review," *Magnetic Resonance in Medicine*, vol. 73, no. 1, pp. 70–81, 2015.
- [160] J. A. Rioux, I. R. Levesque, and B. K. Rutt, "Biexponential longitudinal relaxation in white matter: Characterization and impact on T1 mapping with IR-FSE and MP2RAGE," *Magnetic Resonance in Medicine*, vol. 75, no. 6, pp. 2265–2277, 2016.
- [161] M. Bouhrara and R. G. Spencer, "Rapid simultaneous high-resolution mapping of myelin water fraction and relaxation times in human brain using BMC-mcDESPOt," *NeuroImage*, vol. 147, pp. 800–811, 2017.
- [162] E. Kellner, B. Dhital, V. G. Kiselev, and M. Reiser, "Gibbs-ringing artifact removal based on local subvoxel-shifts," *Magnetic Resonance in Medicine*, vol. 76, no. 5, pp. 1574–1581, 2016.
- [163] J. R. Taylor, *An introduction to error analysis: the study of uncertainties in physical measurements*. Sausalito, CA, USA: University Science Books, 1997.
- [164] H. Gudbjartsson and S. Patz, "The Rician Distribution of Noisy MRI Data," *Magnetic Resonance in Medicine*, vol. 34, no. 6, pp. 910–914, 1995.
- [165] P. Kellman and E. R. McVeigh, "Image reconstruction in SNR units: A general method for SNR measurement," *Magnetic Resonance in Medicine*, vol. 54, no. 6, pp. 1439–1447, 2005.
- [166] U. Katscher, C. Stehning, and K. K. Tha, "The impact of CSF pulsation on reconstructed brain conductivity," in *Proceedings of the 26th Annual Meeting of ISMRM*, (Paris, France),

- p. 0546, 2018.
- [167] C. Li, J. C. Gore, and C. Davatzikos, "Multiplicative intrinsic component optimization (MICO) for MRI bias field estimation and tissue segmentation," *Magnetic Resonance Imaging*, vol. 32, no. 7, pp. 913–923, 2014.
- [168] K. Zhong, J. Leupold, D. von Elverfeldt, and O. Speck, "The molecular basis for gray and white matter contrast in phase imaging," *NeuroImage*, vol. 40, no. 4, pp. 1561–1566, 2008.
- [169] K. L. Miller, "Asymmetries of the balanced SSFP profile. Part I: Theory and observation," *Magnetic Resonance in Medicine*, vol. 63, no. 2, pp. 385–395, 2010.
- [170] U. Katscher, P. Börner, C. Leussler, and J. S. Van den Brink, "Transmit SENSE," *Magnetic Resonance in Medicine*, vol. 49, no. 1, pp. 144–150, 2003.
- [171] T. Cukur, "Accelerated Phase-Cycled SSFP Imaging With Compressed Sensing," *IEEE Transactions on Medical Imaging*, vol. 34, no. 1, pp. 107–115, 2015.
- [172] T. Wood, A. Combes, and M. Shaihan, "Elliptical Magnetization Transfer: Calculating MT Parameters from the bSSFP Signal Ellipse," in *Proceedings of the 26th Annual Meeting of ISMRM*, (Paris, France), p. 0789, 2018.
- [173] X. Zhang, S. Schmitter, P.-F. van de Moortele, J. Liu, B. He, and Bin He, "From Complex B1 Mapping to Local SAR Estimation for Human Brain MR Imaging Using Multi-Channel Transceiver Coil at 7T," *IEEE Transactions on Medical Imaging*, vol. 32, no. 6, pp. 1058–1067, 2013.
- [174] J. B. van de Kamer, N. van Wieringen, A. A. C. De Leeuw, and J. J. W. Lagendijk, "The significance of accurate dielectric tissue data for hyperthermia," *International Journal of Hyperthermia*, vol. 17, no. 2, pp. 123–142, 2001.
- [175] H. P. Kok, A. N. T. J. Kotte, and J. Crezee, "Planning, optimisation and evaluation of hyperthermia treatments," *International Journal of Hyperthermia*, vol. 33, no. 6, pp. 593–607, 2017.
- [176] G. M. Hahn, P. Kernahan, A. Martinez, D. Pounds, S. Prionas, T. Anderson, and G. Justice, "Some heat transfer problems associated with heating by ultrasound, microwave or radio frequency," *Annals of the New York Academy of Sciences*, vol. 335, pp. 327–346, 1980.
- [177] J. L. Schepps and K. R. Foster, "The UHF and microwave dielectric properties of normal and tumor tissues variation in dielectric properties with tissue water content," *Physics in Medicine and Biology*, vol. 25, no. 6, pp. 1149–1159, 1980.
- [178] J. A. Rogers, R. J. Sheppard, E. H. Grant, N. M. Bleehen, and D. J. Honess, "The dielectric properties of normal and tumour mouse tissue between 50 MHz and 10 GHz," *British Journal of Radiology*, vol. 56, no. 665, pp. 335–338, 1983.
- [179] R. J. Halter, T. Zhou, P. M. Meaney, A. Hartov, R. J. Barth, K. M. Rosenkranz, W. A. Wells, C. A. Kogel, A. Borsic, E. J. Rizzo, K. D. Paulsen, and K. D. Paulsen, "The correlation of in vivo and ex vivo tissue dielectric properties to validate electromagnetic breast imaging: Initial clinical experience," *Physiological Measurement*, vol. 30, no. 6, pp. S121–S136, 2009.
- [180] X. Zhang, S. Zhu, and B. He, "Imaging Electric Properties of Biological Tissues by RF Field Mapping in MRI," *IEEE Transactions on Medical Imaging*, vol. 29, no. 2, pp. 474–481, 2010.
- [181] H.-J. Chung, J.-M. Kim, Y.-J. Jeong, J.-H. Kim, C. Lee, and C.-H. Oh, "Electro-Magnetic Property Mapping Using Kalman Filtering with a Single Acquisition at 3.0 T and 7.0 T MRI," in *Proceedings of the 26th Annual Meeting of ISMRM*, (Paris, France), p. 5081, 2018.
- [182] D. K. Sodickson, C. M. Deniz, N. B. Eliezer, M. Cloos, L. A. Sodickson, C. M. Collins, G. C. Wiggins, and D. S. Novikov, "Generalized Local Maxwell Tomography for Mapping of Electrical Property Gradients and Tensors," in *Proceedings of the 21st Annual Meeting of ISMRM*, (Salt Lake City, Utah, USA), p. 4175, 2013.
- [183] J. E. C. Serralles, L. Daniel, J. K. White, D. K. Sodickson, R. Lattanzi, and A. G.

- Polimeridis, "Global maxwell tomography: A novel technique for electrical properties mapping based on MR measurements and volume integral equation formulations," in *IEEE International Symposium on Antennas and Propagation (APSURSI)*, (Fajardo, Puerto Rico), pp. 1395–1396, IEEE, 2016.
- [184] D. J. Park, N. K. Bangerter, A. Javed, J. Kaggie, M. M. Khalighi, and G. R. Morrell, "A statistical analysis of the Bloch-Siegert B1 mapping technique," *Physics in Medicine and Biology*, vol. 58, no. 16, pp. 5673–5691, 2013.
- [185] M. De Greef, H. P. Kok, D. Correia, P. P. Borsboom, A. Bel, and J. Crezee, "Uncertainty in hyperthermia treatment planning: The need for robust system design," *Physics in Medicine and Biology*, vol. 56, no. 11, pp. 3233–3250, 2011.
- [186] J. B. Van De Kamer, A. A. C. De Leeuw, S. N. Hornsleth, H. Kroeze, A. N. T. J. Kotte, and J. J. W. Lagendijk, "Development of a regional hyperthermia treatment planning system," *International Journal of Hyperthermia*, vol. 17, no. 3, pp. 207–220, 2001.
- [187] H. Ku, "Notes on the use of propagation of error formulas," *Journal of Research of the National Bureau of Standards, Section C: Engineering and Instrumentation*, vol. 70C, no. 4, pp. 263–273, 1966.
- [188] O. Dietrich, J. G. Raya, S. B. Reeder, M. F. Reiser, and S. O. Schoenberg, "Measurement of signal-to-noise ratios in MR images: Influence of multichannel coils, parallel imaging, and reconstruction filters," *Journal of Magnetic Resonance Imaging*, vol. 26, no. 2, pp. 375–385, 2007.
- [189] K. Nehrke, M. J. Versluis, A. G. Webb, and P. Börnert, "Volumetric B1+ mapping of the brain at 7T using DREAM," *Magnetic Resonance in Medicine*, vol. 71, no. 1, pp. 246–256, 2014.
- [190] M. M. Khalighi, L. I. Sacolick, and B. K. Rutt, "Signal to Noise Ratio Analysis of Bloch-Siegert B1+ Mapping," in *Proceedings of the 18th Annual Meeting of ISMRM*, (Stockholm, Sweden), p. 2842, 2010.
- [191] X. Wan, W. Wang, J. Liu, and T. Tong, "Estimating the sample mean and standard deviation from the sample size, median, range and/or interquartile range," *BMC Medical Research Methodology*, vol. 14, no. 1, p. 135, 2014.
- [192] W. M. Brink, P. Boernert, K. Nehrke, and A. G. Webb, "Ventricular B1+ perturbation at 7T - real effect or measurement artifact?," *NMR in Biomedicine*, vol. 27, no. 6, pp. 617–620, 2014.
- [193] A. Haase, J. Frahm, D. Matthaei, W. Hänicke, H. Bomsdorf, D. Kunz, and R. Tischler, "MR imaging using stimulated echoes (STEAM)," *Radiology*, vol. 160, no. 3, pp. 787–790, 1986.
- [194] C. Durney, "Electromagnetic dosimetry for models of humans and animals: A review of theoretical and numerical techniques," *Proceedings of the IEEE*, vol. 68, no. 1, pp. 33–40, 1980.
- [195] J. W. Hand, "Modelling the interaction of electromagnetic fields (10 MHz–10 GHz) with the human body: methods and applications," *Physics in Medicine and Biology*, vol. 53, no. 16, pp. R243–R286, 2008.
- [196] A. Christ, W. Kainz, E. G. Hahn, K. Honegger, M. Zefferer, E. Neufeld, W. Rascher, R. Janka, W. Bautz, J. Chen, B. Kiefer, P. Schmitt, H.-P. Hollenbach, J. Shen, M. Oberle, D. Szczerba, A. Kam, J. W. Guag, and N. Kuster, "The Virtual Family—development of surface-based anatomical models of two adults and two children for dosimetric simulations," *Physics in Medicine and Biology*, vol. 55, no. 2, pp. N23–N38, 2010.
- [197] H. P. Kok, P. Wust, P. R. Stauffer, F. Bardati, G. C. van Rhoon, and J. Crezee, "Current state of the art of regional hyperthermia treatment planning: a review," *Radiation Oncology*, vol. 10, no. 1, p. 196, 2015.
- [198] M. Guardiola, S. Buitrago, G. Fernández-Esparrach, J. M. O'Callaghan, J. Romeu, M. Cuatrecasas, H. Córdova, M. Á. González Ballester, and O. Camara, "Dielectric

- properties of colon polyps, cancer, and normal mucosa: Ex vivo measurements from 0.5 to 20 GHz," *Medical Physics*, vol. 45, no. 8, pp. 3768–3782, 2018.
- [199] S. Gavazzi, C. A. T. van den Berg, A. Sbrizzi, H. P. Kok, L. J. A. Stalpers, J. J. W. Lagendijk, H. Crezee, and A. L. H. M. W. van Lier, "Accuracy and precision of electrical permittivity mapping at 3T: the impact of three mapping techniques," *Magnetic Resonance in Medicine*, vol. 81, no. 6, pp. 3628–3642, 2019.
- [200] G. Schooneveldt, H. P. Kok, A. Bakker, E. D. Geijssen, C. R. N. Rasch, J. J. M. C. H. de la Rosette, M. C. C. M. Hulshof, T. M. de Reijke, and H. Crezee, "Clinical validation of a novel thermophysical bladder model designed to improve the accuracy of hyperthermia treatment planning in the pelvic region," *International Journal of Hyperthermia*, vol. 35, no. 1, pp. 383–397, 2018.
- [201] C. M. J. de Bazelaire, G. D. Duhamel, N. M. Rofsky, and D. C. Alsop, "MR Imaging Relaxation Times of Abdominal and Pelvic Tissues Measured in Vivo at 3.0 T: Preliminary Results," *Radiology*, vol. 230, no. 3, pp. 652–659, 2004.
- [202] J. A. Zavala Bojorquez, P.-M. Jodoin, S. Bricq, P. M. Walker, F. Brunotte, and A. Lalande, "Automatic classification of tissues on pelvic MRI based on relaxation times and support vector machine," *PLOS ONE*, vol. 14, no. 2, p. e0211944, 2019.
- [203] S. Gavazzi, Y. Shcherbakova, L. W. Bartels, L. J. A. Stalpers, J. J. W. Lagendijk, H. Crezee, C. A. T. van den Berg, and A. L. H. M. W. van Lier, "Transceive phase mapping using the PLANET method and its application for conductivity mapping in the brain," *Magnetic Resonance in Medicine*, vol. 83, no. 2, pp. 590–607, 2020.
- [204] P. de Boer, A. M. Spijkerboer, M. C. G. Bleeker, L. R. C. W. van Lonkhuijzen, M. A. Monraats, A. J. Nederveen, M. J. van de Vijver, G. G. Kenter, A. Bel, C. R. N. Rasch, J. Stoker, and L. J. A. Stalpers, "Prospective validation of craniocaudal tumour size on MR imaging compared to histoPathology in patients with uterine cervical cancer: The MPAC study," *Clinical and Translational Radiation Oncology*, vol. 18, pp. 9–15, 2019.
- [205] K. Lim, W. Small, L. Portelance, C. Creutzberg, I. M. Jürgenliemk-Schulz, A. Mundt, L. K. Mell, N. Mayr, A. Viswanathan, A. Jhingran, B. Erickson, J. De Los Santos, D. Gaffney, C. Yashar, S. Beriwal, A. Wolfson, A. Taylor, W. Bosch, I. El Naqa, and A. Fyles, "Consensus guidelines for delineation of clinical target volume for intensity-modulated pelvic radiotherapy for the definitive treatment of cervix cancer," *International Journal of Radiation Oncology Biology Physics*, vol. 79, no. 2, pp. 348–355, 2011.
- [206] W. Li, G. Wang, L. Fidon, S. Ourselin, M. J. Cardoso, and T. Vercauteren, "On the Compactness, Efficiency, and Representation of 3D Convolutional Networks: Brain Parcellation as a Pretext Task," in *Information Processing in Medical Imaging.*, vol. 10265 of *Lecture Notes in Computer Science*, pp. 348–360, Cham, Switzerland: Springer International Publishing, 2017.
- [207] E. Gibson, W. Li, C. Sudre, L. Fidon, D. I. Shakir, G. Wang, Z. Eaton-Rosen, R. Gray, T. Doel, Y. Hu, T. Whyntie, P. Nachev, M. Modat, D. C. Barratt, S. Ourselin, M. J. Cardoso, and T. Vercauteren, "NiftyNet: a deep-learning platform for medical imaging," *Computer Methods and Programs in Biomedicine*, vol. 158, pp. 113–122, 2018.
- [208] B. Krawczyk, "Learning from imbalanced data: open challenges and future directions," *Progress in Artificial Intelligence*, vol. 5, no. 4, pp. 221–232, 2016.
- [209] R. Leijssen, C. A. T. van den Berg, A. G. Webb, R. F. Remis, and S. Mandija, "Combining deep learning and 3D contrast source inversion in MR-based electrical properties tomography," *NMR in Biomedicine*, p. e4211, 2019.
- [210] M. F. Franckena, L. J. A. Stalpers, P. C. M. Koper, R. G. J. Wiggeraad, W. J. Hoogenraad, J. D. P. van Dijk, C. C. Wárlám-Rodenhuis, J. J. Jobsen, G. C. van Rhoon, and J. van der Zee, "Long-Term Improvement in Treatment Outcome After Radiotherapy and Hyperthermia in Locoregionally Advanced Cervix Cancer: An Update of the Dutch Deep Hyperthermia Trial," *International Journal of Radiation Oncology Biology Physics*, vol. 70,

- no. 4, pp. 1176–1182, 2008.
- [211] N. R. Datta, E. Stutz, S. Gomez, and S. Bodis, “Efficacy and Safety Evaluation of the Various Therapeutic Options in Locally Advanced Cervix Cancer: A Systematic Review and Network Meta-Analysis of Randomized Clinical Trials,” *International Journal of Radiation Oncology, Biology, Physics*, vol. 103, no. 2, pp. 411–437, 2019.
- [212] N. R. Datta, E. Puric, D. Klingbiel, S. Gomez, and S. Bodis, “Hyperthermia and Radiation Therapy in Locoregional Recurrent Breast Cancers: A Systematic Review and Meta-analysis,” *International Journal of Radiation Oncology, Biology, Physics*, vol. 94, no. 5, pp. 1073–1087, 2016.
- [213] R. Colombo, A. Salonia, Z. Leib, M. Pavone-Macaluso, and D. Engelstein, “Long-term outcomes of a randomized controlled trial comparing thermochemotherapy with mitomycin-C alone as adjuvant treatment for non-muscle-invasive bladder cancer (NMIBC),” *BJU International*, vol. 107, no. 6, pp. 912–918, 2011.
- [214] R. D. Issels, L. H. Lindner, J. Verweij, R. Wessalowski, P. Reichardt, P. Wust, P. Ghadjar, P. Hohenberger, M. Angele, C. Salat, Z. Vujaskovic, S. Daugaard, O. Mella, U. Mansmann, H. R. Dürr, T. Knösel, S. Abdel-Rahman, M. Schmidt, W. Hiddemann, K.-W. Jauch, C. Belka, and A. Gronchi, “Effect of Neoadjuvant Chemotherapy Plus Regional Hyperthermia on Long-term Outcomes Among Patients With Localized High-Risk Soft Tissue Sarcoma,” *JAMA Oncology*, vol. 4, no. 4, pp. 483–492, 2018.
- [215] S. A. Sapareto and W. C. Dewey, “Thermal dose determination in cancer therapy,” *International Journal of Radiation Oncology, Biology, Physics*, vol. 10, no. 6, pp. 787–800, 1984.
- [216] G. C. van Rhoon, T. Samaras, P. S. Yarmolenko, M. W. Dewhurst, E. Neufeld, and N. Kuster, “CEM43 C thermal dose thresholds: a potential guide for magnetic resonance radiofrequency exposure levels?,” *European Radiology*, vol. 23, pp. 2215–2227, aug 2013.
- [217] W. C. Dewey, L. E. Hopwood, S. A. Sapareto, and L. E. Gerweck, “Cellular responses to combinations of hyperthermia and radiation,” *Radiology*, vol. 123, no. 2, pp. 463–474, 1977.
- [218] W. C. Dewey, D. E. Thrall, and E. L. Gillette, “Hyperthermia and radiation—A selective thermal effect on chronically hypoxic tumor cells in vivo,” *International Journal of Radiation Oncology, Biology, Physics*, vol. 2, no. 1-2, pp. 99–103, 1977.
- [219] M. F. Franckena, D. Fatehi, M. de Bruijne, R. A. M. Canters, Y. van Norden, J. W. Mens, G. C. van Rhoon, and J. van der Zee, “Hyperthermia dose-effect relationship in 420 patients with cervical cancer treated with combined radiotherapy and hyperthermia,” *European Journal of Cancer*, vol. 45, no. 11, pp. 1969–1978, 2009.
- [220] G. Bruggmoser, S. Bauchowitz, R. Canters, H. Crezee, M. Ehmann, J. Gellermann, U. Lamprecht, N. Lomax, M. B. Messmer, O. Ott, S. Abdel-Rahman, M. Schmidt, R. Sauer, A. Thomsen, R. Wessalowski, and G. C. van Rhoon, “Guideline for the clinical application, documentation and analysis of clinical studies for regional deep hyperthermia,” *Strahlentherapie und Onkologie*, vol. 188, no. S2, pp. 198–211, 2012.
- [221] P. R. Stauffer, “Evolving technology for thermal therapy of cancer,” in *International Journal of Hyperthermia*, vol. 21, pp. 731–744, 2005.
- [222] G. Bruggmoser, S. Bauchowitz, R. A. M. Canters, H. Crezee, M. Ehmann, J. Gellermann, U. Lamprecht, N. Lomax, M. B. Messmer, O. Ott, S. Abdel-Rahman, R. Sauer, M. Schmidt, A. Thomsen, R. Wessalowski, and G. C. van Rhoon, “Quality assurance for clinical studies in regional deep hyperthermia,” *Strahlentherapie und Onkologie*, vol. 187, no. 10, pp. 605–610, 2011.
- [223] L. Winter, C. Özerdem, W. Hoffmann, D. Santoro, A. Müller, H. Waiczies, R. Seemann, A. Graessl, P. Wust, and T. Niendorf, “Design and Evaluation of a Hybrid Radiofrequency Applicator for Magnetic Resonance Imaging and RF Induced Hyperthermia: Electromagnetic Field Simulations up to 14.0 Tesla and Proof-of-Concept at 7.0 Tesla,”

- PLoS ONE*, vol. 8, no. 4, p. e61661, 2013.
- [224] M. M. Paulides, G. M. Verduijn, and N. Van Holthe, "Status quo and directions in deep head and neck hyperthermia," *Radiation Oncology*, vol. 11, no. 1, p. 21, 2016.
- [225] P. Wust, M. Seebass, J. Nadobny, P. Deuflhard, G. Mönich, and R. Felix, "Simulation studies promote technological development of radiofrequency phased array hyperthermia," *International Journal of Hyperthermia*, vol. 25, no. 7, pp. 517–528, 2009.
- [226] R. A. Canters, M. M. Paulides, M. F. Franckena, J. van Der Zee, and G. C. van Rhoon, "Implementation of treatment planning in the routine clinical procedure of regional hyperthermia treatment of cervical cancer: An overview and the Rotterdam experience," *International Journal of Hyperthermia*, vol. 28, no. 6, pp. 570–581, 2012.
- [227] R. F. Verhaart, V. Fortunati, G. M. Verduijn, A. van der Lugt, T. van Walsum, J. F. Veenland, and M. M. Paulides, "The relevance of MRI for patient modeling in head and neck hyperthermia treatment planning: A comparison of CT and CT-MRI based tissue segmentation on simulated temperature," *Medical Physics*, vol. 41, no. 12, p. 123302, 2014.
- [228] P. Wust, J. Gellermann, J. Beier, S. Wegner, W. Tilly, J. Tröger, D. Stalling, H. Oswald, H. C. Hege, P. Deuflhard, and R. Felix, "Evaluation of segmentation algorithms for generation of patient models in radiofrequency hyperthermia," *Physics in Medicine and Biology*, vol. 43, no. 11, pp. 3295–3307, 1998.
- [229] H. H. Pennes, "Analysis of tissue and arterial blood temperatures in the resting human forearm," *Journal of applied physiology*, vol. 1, no. 2, pp. 93–122, 1948.
- [230] T. Köhler, P. Maass, P. Wust, and M. Seebass, "A fast algorithm to find optimal controls of multiantenna applicators in regional hyperthermia," *Physics in Medicine and Biology*, vol. 46, no. 9, pp. 2503–2514, 2001.
- [231] F. Bardati, A. Borrani, A. Gerardino, and G. A. Lovisolo, "SAR Optimization in a Phased Array Radiofrequency Hyperthermia System," *IEEE Transactions on Biomedical Engineering*, vol. 42, no. 12, pp. 1201–1207, 1995.
- [232] J. Wiersma, R. A. van Maarseveen, and J. D. van Dijk, "A flexible optimization tool for hyperthermia treatments with RF phased array systems," *International Journal of Hyperthermia*, vol. 18, no. 2, pp. 73–85, 2002.
- [233] M. de Greef, H. P. Kok, D. Correia, A. Bel, and J. Crezee, "Optimization in hyperthermia treatment planning: The impact of tissue perfusion uncertainty," *Medical Physics*, vol. 37, no. 9, pp. 4540–4550, 2010.
- [234] P. M. van Haaren, H. P. Kok, C. A. van den Berg, P. J. Zum Vörde Sive Vörding, S. Oldenburg, L. J. A. Stalpers, M. S. Schilthuis, A. A. de Leeuw, and J. Crezee, "On verification of hyperthermia treatment planning for cervical carcinoma patients," *International Journal of Hyperthermia*, vol. 23, no. 3, pp. 303–314, 2007.
- [235] G. Sreenivasa, J. Gellermann, B. Rau, J. Nadobny, P. Schlag, P. Deuflhard, R. Felix, and P. Wust, "Clinical use of the hyperthermia treatment planning system HyperPlan to predict effectiveness and toxicity," *International Journal of Radiation Oncology Biology Physics*, vol. 55, no. 2, pp. 407–419, 2003.
- [236] M. F. Franckena, R. A. M. Canters, F. Termorshuizen, J. Van Der Zee, and G. Van Rhoon, "Clinical implementation of hyperthermia treatment planning guided steering: A cross over trial to assess its current contribution to treatment quality," *International Journal of Hyperthermia*, vol. 26, no. 2, pp. 145–157, 2010.
- [237] H. P. Kok, S. Ciampa, R. de Kroon-Oldenhof, E. J. Steggerda-Carvalho, G. van Stam, P. J. Zum Vörde Sive Vörding, L. J. A. Stalpers, E. D. Geijsen, F. Bardati, A. Bel, and J. Crezee, "Toward Online Adaptive Hyperthermia Treatment Planning: Correlation Between Measured and Simulated Specific Absorption Rate Changes Caused by Phase Steering in Patients," *International Journal of Radiation Oncology, Biology, Physics*, vol. 90, no. 2, pp. 438–445, 2014.

- [238] R. A. M. Canters, M. M. Paulides, M. F. Franckena, J. W. Mens, and G. C. Van Rhoon, "Benefit of replacing the Sigma-60 by the Sigma-Eye applicator: A Monte Carlo-based uncertainty analysis," *Strahlentherapie und Onkologie*, vol. 189, no. 1, pp. 74–80, 2013.
- [239] G. M. J. Van Leeuwen, A. N. T. J. Kotte, B. W. Raaymakers, and J. J. W. Lagendijk, "Temperature simulations in tissue with a realistic computer generated vessel network," *Physics in Medicine and Biology*, vol. 45, no. 4, pp. 1035–1049, 2000.
- [240] C. A. T. van Den Berg, J. B. van De Kamer, A. A. C. De Leeuw, C. R. L. P. N. Jeukens, B. W. Raaymakers, M. Van Vulpen, and J. J. W. Lagendijk, "Towards patient specific thermal modelling of the prostate," *Physics in Medicine and Biology*, vol. 51, no. 4, pp. 809–825, 2006.
- [241] S. Gavazzi, C. A. T. den Berg, M. H. F. Savenije, H. P. Kok, P. Boer, L. J. A. Stalpers, J. J. W. Lagendijk, H. Crezee, and A. L. H. M. W. Lier, "Deep learning-based reconstruction of in vivo pelvis conductivity with a 3D patch-based convolutional neural network trained on simulated MR data," *Magnetic Resonance in Medicine*, vol. 84, no. 5, pp. 2772–2787, 2020.
- [242] J. J. W. Lagendijk, "The influence of bloodflow in large vessels on the temperature distribution in hyperthermia," *Physics in Medicine and Biology*, vol. 27, no. 1, pp. 17–23, 1982.
- [243] J. Mooibroek and J. J. W. Lagendijk, "A Fast and Simple Algorithm for the Calculation of Convective Heat Transfer by Large Vessels in Three-Dimensional Inhomogeneous Tissues," *IEEE Transactions on Biomedical Engineering*, vol. 38, no. 5, pp. 490–501, 1991.
- [244] E. G. Moros, B. Straube, and R. J. Myerson, "Finite difference vascular model for 3-D cancer therapy with hyperthermia.," in *Advances in Bioheat and Mass Transfer 199* (R. B. Roemer, ed.), pp. 107–111, 1993.
- [245] A. N. T. J. Kotte, G. M. J. van Leeuwen, J. De Bree, J. van Der Koijk, H. Crezee, and J. J. W. Lagendijk, "A description of discrete vessel segments in thermal modelling of tissues," *Physics in Medicine and Biology*, vol. 41, no. 5, pp. 865–884, 1996.
- [246] A. N. T. J. Kotte, G. M. J. van Leeuwen, and J. J. W. Lagendijk, "Modelling the thermal impact of a discrete vessel tree," *Physics in Medicine and Biology*, vol. 44, no. 1, pp. 57–74, 1999.
- [247] B. W. Raaymakers, J. Crezee, and J. J. W. Lagendijk, "Modelling individual temperature profiles from an isolated perfused bovine tongue," *Physics in Medicine and Biology*, vol. 45, no. 3, pp. 765–780, 2000.
- [248] K. Sumser, E. Neufeld, R. F. Verhaart, V. Fortunati, G. M. Verduijn, T. Drizdal, T. van Walsum, J. F. Veenland, and M. M. Paulides, "Feasibility and relevance of discrete vasculature modeling in routine hyperthermia treatment planning," *International Journal of Hyperthermia*, vol. 36, no. 1, pp. 800–810, 2019.
- [249] G. Schooneveldt, H. P. Kok, E. Balidemaj, E. D. Geijsen, F. Van Ommen, J. Sijbrands, A. Bakker, J. J. M. C. H. De La Rosette, M. C. C. M. Hulshof, T. M. De Reijke, and J. Crezee, "Improving hyperthermia treatment planning for the pelvis by accurate fluid modeling," *Medical Physics*, vol. 43, no. 10, pp. 5442–5452, 2016.
- [250] G. Schooneveldt, H. Dobšiček Trefná, M. Persson, T. M. de Reijke, K. Blomgren, H. P. Kok, and H. Crezee, "Hyperthermia Treatment Planning Including Convective Flow in Cerebrospinal Fluid for Brain Tumour Hyperthermia Treatment Using a Novel Dedicated Paediatric Brain Applicator," *Cancers*, vol. 11, no. 8, p. 1183, 2019.
- [251] R. A. M. Canters, M. F. Franckena, J. van Der Zee, and G. C. van Rhoon, "Complaint-adaptive power density optimization as a tool for HTP-guided steering in deep hyperthermia treatment of pelvic tumors," *Physics in Medicine and Biology*, vol. 53, no. 23, pp. 6799–6820, 2008.
- [252] G. G. Bellizzi, T. Drizdal, G. C. van Rhoon, L. Crocco, T. Isernia, and M. M. Paulides, "The potential of constrained SAR focusing for hyperthermia treatment planning: Anal-

- ysis for the head & neck region," *Physics in Medicine and Biology*, vol. 64, no. 1, p. 015013, 2019.
- [253] H. P. Kok, P. M. A. van Haaren, J. B. van De Kamer, J. Wiersma, J. D. P. van Dijk, and J. Crezee, "High-resolution temperature-based optimization for hyperthermia treatment planning," *Physics in Medicine and Biology*, vol. 50, no. 13, pp. 3127–3141, 2005.
- [254] K.-S. Cheng, V. Stakhursky, O. I. Craciunescu, P. Stauffer, M. Dewhirst, and S. K. Das, "Fast temperature optimization of multi-source hyperthermia applicators with reduced-order modeling of 'virtual sources'," *Physics in Medicine and Biology*, vol. 53, no. 6, pp. 1619–1635, 2008.
- [255] S. K. Das, S. T. Clegg, and T. V. Samulski, "Computational techniques for fast hyperthermia temperature optimization," *Medical Physics*, vol. 26, no. 2, pp. 319–328, 1999.
- [256] H. P. Kok, C. A. T. Van Den Berg, A. Bel, and J. Crezee, "Fast thermal simulations and temperature optimization for hyperthermia treatment planning, including realistic 3D vessel networks," *Medical Physics*, vol. 40, no. 10, pp. 1–15, 2013.
- [257] H. P. Kok, J. Crezee, N. A. P. Franken, L. J. A. Stalpers, G. W. Barendsen, and A. Bel, "Quantifying the combined effect of radiation therapy and hyperthermia in terms of equivalent dose distributions," *International Journal of Radiation Oncology, Biology, Physics*, vol. 88, no. 3, pp. 739–745, 2014.
- [258] F. Pajonk, A. van Ophoven, and W. H. McBride, "Hyperthermia-induced proteasome inhibition and loss of androgen receptor expression in human prostate cancer cells," *Cancer Research*, vol. 65, no. 11, pp. 4836–4843, 2005.
- [259] N. A. P. Franken, A. L. Oei, H. P. Kok, H. M. Rodermond, P. Sminia, J. Crezee, L. J. A. Stalpers, and G. W. Barendsen, "Cell survival and radiosensitisation: Modulation of the linear and quadratic parameters of the LQ model," *International Journal of Oncology*, vol. 42, no. 5, pp. 1501–1515, 2013.
- [260] R. J. Myerson, J. L. Roti Roti, E. G. Moros, W. L. Straube, and M. Xu, "Modelling heat-induced radiosensitization: Clinical implications," *International Journal of Hyperthermia*, vol. 20, no. 2, pp. 201–212, 2004.
- [261] C. M. van Leeuwen, A. L. Oei, R. ten Cate, N. A. P. Franken, A. Bel, L. J. A. Stalpers, J. Crezee, and H. P. Kok, "Measurement and analysis of the impact of time-interval, temperature and radiation dose on tumour cell survival and its application in thermoradiotherapy plan evaluation," *International Journal of Hyperthermia*, vol. 34, no. 1, pp. 30–38, 2018.
- [262] N. R. Datta and S. Bodis, "Hyperthermia with radiotherapy reduces tumour alpha/beta: Insights from trials of thermoradiotherapy vs radiotherapy alone," *Radiotherapy and Oncology*, vol. 138, pp. 1–8, 2019.
- [263] J. Overgaard, "Simultaneous and sequential hyperthermia and radiation treatment of an experimental tumor and its surrounding normal tissue in vivo," *International Journal of Radiation Oncology, Biology, Physics*, vol. 6, no. 11, pp. 1507–1517, 1980.
- [264] H. Crezee, C. M. van Leeuwen, A. L. Oei, L. J. A. Stalpers, A. Bel, N. A. P. Franken, and H. P. Kok, "Thermoradiotherapy planning: Integration in routine clinical practice," *International Journal of Hyperthermia*, vol. 32, no. 1, pp. 41–49, 2016.
- [265] J. Crezee, C. M. van Leeuwen, A. L. Oei, L. E. van Heerden, A. Bel, L. J. A. Stalpers, P. Ghadjar, N. A. P. Franken, and H. P. Kok, "Biological modelling of the radiation dose escalation effect of regional hyperthermia in cervical cancer," *Radiation Oncology*, vol. 11, no. 1, pp. 1–9, 2016.
- [266] H. P. Kok, I. van Dijk, K. Crama, N. A. P. Franken, C. R. N. Rasch, J. Merks, J. Crezee, B. Balgobind, and A. Bel, "Re-irradiation plus hyperthermia for recurrent pediatric sarcoma; a simulation study to investigate feasibility," *International Journal of Oncology*, vol. 54, no. 1, pp. 209–218, 2018.

- [267] H. Eggers, B. Brendel, A. Duijndam, and G. Herigault, "Dual-echo Dixon imaging with flexible choice of echo times," *Magnetic Resonance in Medicine*, vol. 65, no. 1, pp. 96–107, 2011.
- [268] B. Denis De Senneville, C. Zachiu, M. Ries, and C. T. W. Moonen, "Evolution: An edge-based variational method for non-rigid multi-modal image registration," *Physics in Medicine and Biology*, vol. 61, no. 20, pp. 7377–7396, 2016.
- [269] C. Zachiu, B. D. De Senneville, C. T. W. Moonen, B. W. Raaymakers, and M. Ries, "Anatomically plausible models and quality assurance criteria for online mono- and multi-modal medical image registration," *Physics in Medicine and Biology*, vol. 63, no. 15, p. 155016, 2018.
- [270] C. Rossmann and D. Haemmerich, "Review of Temperature Dependence of Thermal Properties, Dielectric Properties, and Perfusion of Biological Tissues at Hyperthermic and Ablation Temperatures," *Critical Reviews in Biomedical Engineering*, vol. 42, no. 6, pp. 467–492, 2014.
- [271] K.-S. Cheng, Y. Yuan, Z. Li, P. R. Stauffer, P. MacCarini, W. T. Joines, M. W. Dewhurst, and S. K. Das, "The performance of a reduced-order adaptive controller when used in multi-antenna hyperthermia treatments with nonlinear temperature-dependent perfusion," *Physics in Medicine and Biology*, vol. 54, no. 7, pp. 1979–1995, 2009.
- [272] Y. Yuan, K.-S. Cheng, O. I. Craciunescu, P. R. Stauffer, P. F. MacCarini, K. Arunachalam, Z. Vujaskovic, M. W. Dewhurst, and S. K. Das, "Utility of treatment planning for thermochemotherapy treatment of nonmuscle invasive bladder carcinoma," *Medical Physics*, vol. 39, no. 3, pp. 1170–1181, 2012.
- [273] B. J. James and D. M. Sullivan, "Direct Use of CT Scans for Hyperthermia Treatment Planning," *IEEE Transactions on Biomedical Engineering*, vol. 39, no. 8, pp. 845–851, 1992.
- [274] R. Zweije, H. P. Kok, A. Bakker, A. Bel, and J. Crezee, "Technical and Clinical Evaluation of the ALBA-4D 70MHz Loco-Regional Hyperthermia System," in *48th European Microwave Conference*, (Madrid, Spain), pp. 328–331, 2018.
- [275] J. P. Berenger, "A perfectly matched layer for the absorption of electromagnetic waves," *Journal of Computational Physics*, vol. 114, no. 2, pp. 185–200, 1994.
- [276] J. Crezee and J. J. W. Lagendijk, "Temperature uniformity during hyperthermia: the impact of large vessels," *Physics in medicine and biology*, vol. 37, no. 6, pp. 1321–1337, 1992.
- [277] C. M. van Leeuwen, J. Crezee, A. L. Oei, N. A. P. Franken, L. J. A. Stalpers, A. Bel, and H. P. Kok, "3D radiobiological evaluation of combined radiotherapy and hyperthermia treatments," *International Journal of Hyperthermia*, vol. 33, no. 2, pp. 160–169, 2017.
- [278] C. M. van Leeuwen, J. Crezee, A. L. Oei, N. A. P. Franken, L. J. A. Stalpers, A. Bel, and H. P. Kok, "The effect of time interval between radiotherapy and hyperthermia on planned equivalent radiation dose," *International Journal of Hyperthermia*, vol. 34, no. 7, pp. 901–909, 2018.
- [279] T. Leiner, J. Habets, B. Versluis, L. Geerts, E. Alberts, N. Blanken, J. Hendrikse, E. J. Vonken, and H. Eggers, "Subtractionless first-pass single contrast medium dose peripheral MR angiography using two-point Dixon fat suppression," *European Radiology*, vol. 23, no. 8, pp. 2228–2235, 2013.
- [280] G. M. J. van Leeuwen, A. N. T. J. Kotte, and J. J. W. Lagendijk, "A flexible algorithm for construction of 3-D vessel networks for use in thermal modeling," *IEEE Transactions on Biomedical Engineering*, vol. 45, no. 5, pp. 596–604, 1998.
- [281] C. W. Song, "Effect of local hyperthermia on blood flow and microenvironment: A review," *Cancer Research*, vol. 44, pp. 4721s–4730s, 1984.
- [282] F. M. Waterman, R. E. Nerlinger, D. J. Moylan, and D. B. Leeper, "Response of human tumor blood flow to local hyperthermia," *International Journal of Radiation Oncology, Biology, Physics*, vol. 13, no. 1, pp. 75–82, 1987.

-
- [283] H. P. Kok, G. Schooneveldt, A. Bakker, R. de Kroon-Oldenhof, L. Korshuize-van Straten, C. E. de Jong, E. Steggerda-Carvalho, E. D. Geijssen, L. J. A. Stalpers, and J. Crezee, "Predictive value of simulated SAR and temperature for changes in measured temperature after phase-amplitude steering during locoregional hyperthermia treatments," *International Journal of Hyperthermia*, vol. 35, no. 1, pp. 330–339, 2018.
- [284] J. van der Zee, D. González González, G. C. van Rhoon, J. D. van Dijk, W. L. van Putten, and A. A. Hart, "Comparison of radiotherapy alone with radiotherapy plus hyperthermia in locally advanced pelvic tumours: a prospective, randomised, multicentre trial. Dutch Deep Hyperthermia Group.," *Lancet*, vol. 355, no. 9210, pp. 1119–1125, 2000.
- [285] H. P. Kok, L. Korshuize-van Straten, A. Bakker, R. de Kroon-Oldenhof, G. H. Westerveld, E. Versteijne, L. J. A. Stalpers, and J. Crezee, "Feasibility of on-line temperature-based hyperthermia treatment planning to improve tumour temperatures during locoregional hyperthermia," *International Journal of Hyperthermia*, vol. 34, no. 7, pp. 1082–1091, 2018.
- [286] V. L. Stakhursky, O. Arabe, K.-S. Cheng, J. MacFall, P. Maccarini, O. Craciunescu, M. Dewhirst, P. Stauffer, and S. K. Das, "Real-time MRI-guided hyperthermia treatment using a fast adaptive algorithm," *Physics in Medicine and Biology*, vol. 54, no. 7, pp. 2131–2145, 2009.
- [287] N. R. Datta, H. P. Kok, H. Crezee, U. S. GaipI, and S. Bodis, "Integrating Loco-Regional Hyperthermia Into the Current Oncology Practice: SWOT and TOWS Analyses," *Frontiers in Oncology*, vol. 10, p. 819, 2020.
- [288] L. Winter, E. Oberacker, K. Paul, Y. Ji, C. Oezerdem, P. Ghadjar, A. Thieme, V. Budach, P. Wust, and T. Niendorf, "Magnetic resonance thermometry: Methodology, pitfalls and practical solutions," *International Journal of Hyperthermia*, vol. 32, no. 1, pp. 63–75, 2016.
- [289] S. Aja-Fernández and G. Vegas-Sánchez-Ferrero, *Statistical Analysis of Noise in MRI*. Cham, Switzerland: Springer International Publishing, 2016.
- [290] K. J. Layton, S. Kroboth, F. Jia, S. Littin, H. Yu, J. Leupold, J.-F. Nielsen, T. Stöcker, and M. Zaitsev, "Pulseseq: A rapid and hardware-independent pulse sequence prototyping framework," *Magnetic Resonance in Medicine*, vol. 77, no. 4, pp. 1544–1552, 2017.
- [291] T. Stöcker, K. Vahedipour, D. Pflugfelder, and N. J. Shah, "High-performance computing MRI simulations," *Magnetic Resonance in Medicine*, vol. 64, no. 1, pp. 186–193, 2010.
- [292] G. Amouzandeh, F. Mentink-Vigier, S. Helsper, F. A. Bagdasarian, J. T. Rosenberg, and S. C. Grant, "Magnetic resonance electrical property mapping at 21.1 T: a study of conductivity and permittivity in phantoms, ex vivo tissue and in vivo ischemia," *Physics in Medicine & Biology*, vol. 65, no. 5, p. 055007, 2020.
- [293] A. Lesch, M. Schlöegl, M. Holler, K. Bredies, and R. Stollberger, "Ultrafast 3D Bloch–Siegert B-mapping using variational modeling," *Magnetic Resonance in Medicine*, vol. 81, no. 2, pp. 881–892, 2019.
- [294] K. P. Pruessmann, M. Weiger, M. B. Scheidegger, and P. Boesiger, "SENSE: Sensitivity encoding for fast MRI," *Magnetic Resonance in Medicine*, vol. 42, no. 5, pp. 952–962, 1999.
- [295] M. A. Griswold, P. M. Jakob, R. M. Heidemann, M. Nittka, V. Jellus, J. Wang, B. Kiefer, and A. Haase, "Generalized autocalibrating partially parallel acquisitions (GRAPPA)," *Magnetic Resonance in Medicine*, vol. 47, no. 6, pp. 1202–1210, 2002.
- [296] P. Ehses, D. Brenner, R. Stirnberg, E. D. Pracht, and T. Stöcker, "Whole-brain B1-mapping using three-dimensional DREAM," *Magnetic Resonance in Medicine*, vol. 82, no. 3, pp. 924–934, 2019.
- [297] Y. Gal, *Uncertainty in Deep Learning Yarin*. PhD thesis, University of Cambridge, 2016.
- [298] A. Kendall and Y. Gal, "What Uncertainties Do We Need in Bayesian Deep Learning for Computer Vision?," in *Proceedings of the 31st International Conference on Neural Information Processing Systems*, (Long Beach, CA, USA), pp. 5580–5590, 2017.
- [299] Y. Gal and Z. Ghahramani, "Dropout as a Bayesian Approximation : Representing Model Uncertainty in Deep Learning," in *Proceedings of the 33rd International Conference*
-

- on *Machine Learning*, vol. 48, (New York, NY, USA), pp. 1050–1059, 2016.
- [300] B. Lakshminarayanan, A. Pritzel, and C. Blundell, “Simple and Scalable Predictive Uncertainty Estimation using Deep Ensembles,” in *Proceedings of the 31st Conference on Neural Information Processing Systems*, (Long Beach, CA, USA), 2017.
- [301] Y. Ovadia, Z. Nado, and J. V. Dillon, “Can You Trust Your Model’s Uncertainty? Evaluating Predictive Uncertainty Under Dataset Shift,” in *Proceedings of the 33rd Conference on Neural Information Processing Systems*, (Vancouver, Canada), 2019.
- [302] A. Hauptmann, F. Lucka, M. Betcke, N. Huynh, J. Adler, B. Cox, P. Beard, S. Ourselin, and S. Arridge, “Model-Based Learning for Accelerated, Limited-View 3-D Photoacoustic Tomography,” *IEEE Transactions on Medical Imaging*, vol. 37, no. 6, pp. 1382–1393, 2018.
- [303] J. Adler and O. Öktem, “Solving ill-posed inverse problems using iterative deep neural networks,” *Inverse Problems*, vol. 33, no. 12, 2017.
- [304] I. V. Ribeiro, N. van Holthe, G. C. van Rhooon, and M. M. Paulides, “Impact of segmentation detail in hyperthermia treatment planning: comparison between detailed and clinical tissue segmentation,” in *Proceedings of the 1st World Conference on Biomedical Applications of Electromagnetic Fields (EMF-Med)*, (Split, Croatia), pp. 1–2, IEEE, 2018.
- [305] E. A. Rashed, Y. Diao, and A. Hirata, “Learning-based estimation of dielectric properties and tissue density in head models for personalized radio-frequency dosimetry,” *Physics in Medicine & Biology*, vol. 65, no. 6, p. 065001, 2020.
- [306] E. F. Meliàdò, A. J. E. Raaijmakers, A. Sbrizzi, B. R. Steensma, M. Maspero, M. H. F. Savenije, P. R. Luijten, and C. A. T. van den Berg, “A deep learning method for image-based subject-specific local SAR assessment,” *Magnetic Resonance in Medicine*, vol. 83, no. 2, pp. 695–711, 2020.

Summary

This thesis focused on measuring the electrical properties (EPs, permittivity and conductivity) of body tissues. The electrical properties of tissues regulate the distribution and the effects of electromagnetic (EM) fields in the human body. Knowledge of the EPs permits assessing the safety of human exposure to EM fields as generated by telecommunication and medical devices (e.g. mobile phones and magnetic resonance systems). It also allows reliable planning of medical treatments using EM fields. Examples of these treatments are radiofrequency (RF) hyperthermia for cancer therapy and EM stimulation for neurological disorders. The EPs are intrinsic tissue characteristics, and their values often vary with pathogenic processes or in response to a therapeutic intervention. Thus, they could be valuable to detect or discriminate a pathological condition or monitor treatment effects.

Currently, knowledge of the EPs relies on dielectric probe measurements of excised animal and human tissue. Nevertheless, the EPs of living tissue differ from the EPs of excised tissue specimens. In vivo EP measurements are crucial for the abovementioned scopes, but cannot be obtained with dielectric probes, due to practical and ethical reasons. Therefore, a more viable and non-invasive measurement technique is desired. “Electrical Properties Tomography” (EPT) uses magnetic resonance imaging (MRI) to measure the electrical properties within the human body and is the subject of this thesis.

Chapter 1 introduced the EPT technique and presented a compact overview of the state-of-art of EPT research. In EPT, dedicated algorithms reconstruct patient-specific permittivity and conductivity maps from measurements of the B_1 field, i.e. the time-varying magnetic field used in MRI to generate and detect the MR signal. In practice, EPT requires the measurement of both amplitude and phase distributions of B_1 , followed by reconstruction of the EPs. However, getting accurate and precise EPT maps within acceptable scan and reconstruction times is not a trivial task, as these characteristics depend on the implementation and settings of acquisition and reconstruction methods. This thesis investigated the accuracy and precision of EPT maps derived from different B_1 measurement techniques and a new EPT reconstruction approach. It also delved into hyperthermia treatment planning, as an example of clinical application benefiting from EPT.

Chapters 2 and 3 quantified for the first time the impact of B_1 acquisition on EP maps reconstructed with a conventional EPT algorithm (based on the Helmholtz equation). Chapter 2 revolved around B_1 phase mapping methods and their impact on conductivity reconstruction. Chapter 3 dealt with the influence of B_1 amplitude mapping methods on permittivity reconstruction. Both chapters used MRI simulations to predict the accuracy and precision of B_1 mapping methods, and MRI measurements on phantoms and volunteers at a clinical 3T MRI scanner to validate the simulated predictions. Accuracy and precision were associated with systematic errors and noise propagation in the B_1 acquisition, respectively.

Both studies showed that systematic errors in the acquired B_1 maps could considerably affect the accuracy of conductivity and permittivity maps. These errors also varied per measurement technique. Thus, it can be deduced that researchers should start taking the severity of acquisition-related errors into account to guarantee accurate EPT reconstructions. In terms of precision, both conductivity and permittivity EPT maps were sensitive to noise in the underlying B_1 map, no matter which technique was used for acquisition. Nevertheless, noise propagation was more severe during permittivity reconstruction. At 3T, for example, no meaningful permittivity information could be retrieved because of extreme noise contamination. More precise B_1 amplitude maps would be necessary, but commonly available B_1 mapping techniques cannot achieve the needed precision at clinical MRI field strengths and within clinically feasible scan times (e.g. 5 min), as revealed by Chapter 3. This implies that permittivity reconstruction with a conventional EPT algorithm is not feasible in clinical scenarios. Therefore, future research should focus on different classes of EPT reconstruction approaches to permit permittivity mapping with available B_1 acquisition techniques, clinical MRI systems and within acceptable times.

Despite differences in accuracy, precision and time efficiency among the examined B_1 phase and amplitude mapping methods, none of the techniques performed significantly better than the others for EPT. Hence, both Chapters 2 and 3 provided indications to select or set B_1 mapping techniques depending on the priority requirements (e.g. accuracy) for conductivity and permittivity mapping. These requirements generally depend on the intended final use of EPT maps (e.g. for diagnosis or treatment planning purposes), and on other factors, such as desired resolution and available scan time. Finally, Chapter 2 demonstrated the feasibility of B_1 phase mapping — and conductivity mapping — in the brain with a novel technique, called PLANET. Beyond B_1 phase, PLANET simultaneously reconstructs the T_1 , T_2 and B_0 maps within clinically acceptable scan times. Thus, the PLANET method is appealing for clinical applications based on quantitative MRI parameters.

Chapter 4 presented a new EPT reconstruction approach based on deep learning (DL). In this approach, a convolutional neural network (CNN) — a particular class of DL algorithms — learns the relevant features for EPT reconstruction from a multitude of training data consisting of paired B_1 inputs – EP outputs. As training data, B_1 fields of 210 dielectric pelvic models with realistic EP values were simulated. These pelvic models were based on segmentation of CT scans of 42 cervical cancer patients. An open-source 3D CNN architecture was trained (and tested) with these B_1 fields to reconstruct the conductivity in the pelvis at 3T. The network was further tested with MRI data of three subjects (one volunteer, two cervical cancer patients). Both in silico and in vivo maps showed that pelvis conductivity mapping with this DL-EPT method is feasible. In detail, the trained network could reconstruct in ~ 10 seconds a 3D pelvis conductivity map (of $550 \times 360 \times 130 \text{ mm}^3$) with sharp tissue interfaces, robust to experimental noise levels and relatively sensitive to tissue conductivity variations. These characteristics determined a remarkable improvement over pelvis conductivity maps reconstructed with the conventional EPT algorithm, which showed under-/over-shooting errors at tissue boundaries and higher sensitivity to noise. Nevertheless, using a DL approach for EPT reconstruction brought up new challenges. For example, questions arise on the generalization capability of DL, since the quality and reliability of the reconstructed maps heavily depends on the quality and characteristics of training data. Other issues include, for example, dealing with imbalanced datasets (e.g. with/without pathological tissues) and estimating the confidence of the generated results, as discussed in Chapter 6. These challenges still need to be solved to guarantee accurate and trustworthy reconstructions, and therefore the safe clinical applicability of DL-EPT.

Chapter 5 gravitated around hyperthermia and its treatment planning workflow. In hyperthermia, the tumour tissue is heated up to 39–43°C for ~1 hour to enhance the effect of radiotherapy and chemotherapy. External devices are used to produce localized heating for deep-seated tumours, such as pelvic tumours. These devices comprise multiple RF antennas surrounding the patient and, therefore, a temperature increase in healthy tissue is unavoidable. Generating focused heating in the tumour while minimizing the incidence of hot spots in normal tissue is clinically challenging and requires setting optimization of each RF antenna. To this end, hyperthermia treatment planning (HTP) predicts the temperature distribution in the patient and optimal settings for effective hyperthermia delivery.

Chapter 5 first reviewed the routine HTP practice and the latest research progress in the field. Then, it illustrated an advanced patient-specific HTP workflow on a cervical cancer patient who underwent radiotherapy and hyperthermia. This advanced workflow combined several research elements and integrated them with the routine HTP infrastructure to improve the reliability of hyperthermia treatment plans. Here follows a brief list of these advanced elements. The patient-specific tissue conductivity was reconstructed with the DL-EPT developed in Chapter 4, rather than relying on average conductivity values derived from literature. The heat convection in body fluids (e.g. urine in the bladder) was also accounted for, instead of being neglected. Moreover, blood vessels (diameter $\gtrsim 3$ mm) were segmented from the patient's CT and MR scans and included in the temperature computation, unlike standard treatment plans where the thermal impact of the vasculature is ignored. All these aspects ensured a more accurate prediction of the temperature within the patient. Finally, a radiobiological model predicted the effect of the combined radiotherapy plus hyperthermia treatment. This effect, expressed in equivalent radiation dose, is linked to tumour control probability.

Chapter 6 discussed how these contributions add to the general knowledge on EPT and HTP, and delineated future perspectives for research in these two fields. In conclusion, this thesis implemented technical frameworks on which future research may further build to study the acquisition and reconstruction aspects contributing to the accuracy, precision and clinical applicability of EPT maps. This work also paved the way for more reliable, clinically feasible and personalised hyperthermia treatment planning.

Samenvatting

Dit proefschrift focust op het meten van de elektrische eigenschappen (EP_s , i.e. permittiviteit en conductiviteit) van de weefsels in het menselijk lichaam. Deze elektrische eigenschappen zijn weefselspecifiek en bepalen het effect van elektromagnetische (EM) velden op het lichaam. Aan de hand van deze EP_s kan de veiligheid van het gebruik van EM velden, die bijvoorbeeld gegenereerd worden door telecommunicatie (bv. mobiele telefoon) en medische apparaten (bv. MRI scanner), bepaald worden. Verder zijn deze EP_s onmisbaar voor het maken van een betrouwbare behandelplannen voor medische behandelingen gebaseerd op EM velden, zoals radiofrequentie (RF) hyperthermie voor kanker behandelingen en EM stimulatie voor neurologische aandoeningen. Tot slot zijn de EP_s niet constant, maar kunnen veranderen door ziekte of als gevolg van therapie. Hierdoor zouden de EP_s ook gebruikt kunnen worden voor de detectie van pathologieën en het monitoren van het effect van de behandeling.

De huidige kennis van EP_s is gebaseerd op metingen met een diëlektrische probe op uitgenomen dierlijk en menselijk weefsel. Deze eigenschappen verschillen echter significant voor levend weefsel. Daarom is het van cruciaal belang om in vivo EP metingen te kunnen doen. Aangezien metingen met een diëlektrische probe invasief zijn, kunnen deze niet gebruikt worden en is een alternatieve non-invasieve methode nodig. "Electrical Properties Tomography" (EPT) is een non-invasieve methode gebaseerd op MRI waarmee de elektrische eigenschappen in het menselijk lichaam gemeten kunnen worden. Deze methode is het onderwerp van dit proefschrift.

In hoofdstuk 1 wordt de EPT methode geïntroduceerd en een kort overzicht gegeven van de meest recente ontwikkelingen op het gebied van EPT. EPT is gebaseerd op het zogenaamde B_1 veld, dit is een magnetisch veld dat gebruikt wordt voor het genereren en detecteren van het signaal voor MRI beelden. Uit de magnitude en fase van dit B_1 veld kunnen patiënt-specifieke permittiviteit en conductiviteit beelden gereconstrueerd worden. Om accurate en precieze EP beelden te krijgen in een acceptabele scan- en reconstructietijd is niet triviaal. Daarom worden in dit proefschrift de effecten van verschillende technieken om B_1 te meten en van een nieuwe reconstructie methode op de nauwkeurigheid en precisie van EP beelden onderzocht. Tot slot worden in dit proefschrift de behandelplannen voor hyperthermie beschreven. Deze zijn een voorbeeld van de klinische toepassing van EPT.

In hoofdstuk 2 en 3 wordt voor het eerst het effect van verschillende metingsmethoden van B_1 op de nauwkeurigheid en precisie van EP beelden (gereconstrueerd met de conventionele Helmholtz methode) gekwantificeerd. De focus van hoofdstuk 2 ligt op de metingsmethoden van de fase van B_1 en het effect hiervan op de conductiviteit beelden die hierop gebaseerd zijn. Analoot hieraan, wordt het effect van methoden om de magnitude van B_1 te meten op de permittiviteit beelden onderzocht in hoofdstuk 3. In beide hoofdstukken worden MRI simulaties gebruikt om de nauwkeurigheid en precisie van de metingsmethoden van B_1 te voorspellen. MRI metingen op fantomen en vrijwilligers zijn gedaan met een klinische 3T scanner om de

voorspellingen te valideren. De nauwkeurigheid en precisie hangen samen met systematische fouten en ruispropagatie in de B_1 metingen, respectievelijk. Beide hoofdstukken laten zien dat systematische fouten in B_1 metingen een significant effect hebben op de nauwkeurigheid van EP beelden. Deze fouten varieerden ook bij verschillende metingsmethoden. Dus, is het duidelijk dat onderzoekers de fouten tijdens de metingprocedure serieus moeten nemen om een accurate EPT reconstructie te garanderen.

De reconstructie van de EP beelden is gevoelig voor de ruis in de gemeten B_1 , onafhankelijk van de gebruikte metingsmethode. Het grootste effect van de ruis was zichtbaar in de permittiviteit beelden door de ruispropagatie in de reconstructie. Bij 3T was het niet mogelijk om betrouwbare permittiviteit beelden te genereren door deze ruispropagatie. Preciezere B_1 beelden zijn nodig, maar de beschikbare technieken kunnen de benodigde precisie niet bereiken op een klinische MRI scanner binnen de beoogde scan tijd (bv. 5 min), zoals beschreven in hoofdstuk 3. Dit impliceert dat het niet mogelijk is om permittiviteit beelden met conventionele methoden te reconstrueren in een klinische setting. De focus van toekomstig onderzoek zou daarom moeten liggen in nieuwe reconstructie technieken om permittiviteit beelden te genereren met de beschikbare B_1 -meetmethoden, met een klinische MRI scanner en in een acceptabele scan tijd.

Ondanks de verschillen in nauwkeurigheid, precisie en tijd efficiëntie van de onderzochte methoden om de fase en magnitude van B_1 te meten, is er geen techniek die het beste is voor EPT. De resultaten uit hoofdstuk 2 en 3 kunnen wel gebruikt worden om een B_1 -meetmethode te kiezen die aansluit bij de specifieke behoeftes (bv. nauwkeurigheid) voor de conductiviteit en/of permittiviteit beelden. Deze behoeftes hangen over het algemeen af van het doel van de EP beelden (bv. diagnose of het maken van een behandelplan) en ander factoren, zoals gewenste resolutie en beschikbare scan tijd. Tot slot, wordt in hoofdstuk 2 gedemonstreerd dat het mogelijk is om B_1 fase beelden — en conductiviteit beelden — te maken van het brein binnen klinisch acceptabele scan tijden met een nieuwe methode genaamd planet. Het voordeel van planet is dat op basis van deze methode niet alleen de B_1 fase maar ook T_1 , T_2 en B_0 beelden gereconstrueerd kunnen worden. Planet is dus een interessante methode voor klinische toepassingen gebaseerd op kwantitatieve MRI parameters.

In hoofdstuk 4 wordt een nieuwe EPT reconstructie methode gebaseerd op deep learning (DL) beschreven. Bij deze aanpak leert een convolutioneel neuraal netwerk (CNN), een DL algoritme, de relevante karakteristieken van een EPT reconstructie door middel van een training set die bestaat uit gepaarde B_1 en EP beelden. De training data bestond uit de gesimuleerde B_1 velden van 210 pelvis modellen met realistische EP waarden. Deze pelvis modellen zijn gebaseerd op gesegmenteerde CT scans van 42 patiënten met cervix kanker. Een open-source 3D CNN is getraind (en getest) op deze B_1 velden met als doel om de conductiviteit in de pelvis te reconstrueren bij 3T. Het netwerk is verder getest met MRI data van drie personen (één vrijwilliger en twee patiënten met cervix kanker). Zowel in silico en in vivo resultaten lieten zien dat het mogelijk is om conductiviteit beelden te reconstrueren met deze DL methode. Het getrainde netwerk kon 3D conductiviteit beelden ($500 \times 360 \times 130 \text{ mm}^3$) met scherpe weefselovergangen reconstrueren in ongeveer 10 seconden. Deze reconstructies waren robuust tegen verandering in het ruis niveau van de experimenten en relatief gevoelig voor veranderingen in de conductiviteit van de verschillende weefsels. De DL methode is een grote stap vooruit ten opzichte van conventionele EPT reconstructie, die de conductiviteit onder/overschat bij weefselovergangen en gevoeliger is voor ruis. Ondanks de veelbelovende resultaten, zitten er wel een paar haken en ogen aan de DL reconstructie. De generalisatie van de CNN, bijvoorbeeld. De kwaliteit en betrouwbaarheid van de reconstructie hangt sterk

af van de kwaliteit en karakteristieken van de training data. Andere potentiële problemen zijn ongebalanceerde training data sets (bv. met/zonder pathologie) en het inschatten van de betrouwbaarheid van de resultaten, zoals bediscussieerd in hoofdstuk 6. Deze problemen moeten opgelost worden om nauwkeurige en betrouwbare DL reconstructies te kunnen garanderen die voor klinische toepassingen gebruikt kunnen worden.

De focus van hoofdstuk 5 ligt op hyperthermie behandelingen en het maken van behandelplannen hiervoor. Bij hyperthermie wordt het tumor weefsel opgewarmd tot 39–43°C voor ongeveer een uur om het effect van radiotherapie en chemotherapie te versterken. Een extern apparaat wordt gebruikt voor lokale opwarming van diepgelegen tumoren, zoals pelvis tumoren. Dit apparaat bestaat uit meerder RF antennes rondom de patiënt, waardoor het onvermijdelijk is dat de temperatuur ook zal toenemen in het gezonde weefsel. Het is uitdagend om de tumor op te warmen en tegelijkertijd het ontstaan van hotspots in gezond weefsel te voorkomen. Om dit zo goed mogelijk te doen, wordt de temperatuur verdeling in de patiënt voorspeld bij het maken van een hyperthermie behandelplan (HTP) en worden de optimale instellingen voor alle individuele RF antennes berekend. Hoofdstuk 5 begint met een beschrijving van conventionele hyperthermie behandelingen en de laatste nieuwe ontwikkelingen op dit gebied. Vervolgens wordt een beeld geschetst van een geavanceerde, patiënt-specifieke HTP behandelplan workflow voor een patiënt met cervix kanker die radiotherapie en hyperthermie heeft ondergaan. Deze geavanceerde workflow combineert meerdere experimentele elementen die geïntegreerd zijn met de routine hyperthermie behandeling infrastructuur om de hyperthermie behandelplannen te verbeteren. Hier volgt een lijstje met de geavanceerde elementen. De patiënt-specifieke conductiviteit is gereconstrueerd met de DL-EPT reconstructie beschreven in hoofdstuk 4 in plaats van het gebruik van een gemiddelde conductiviteit waarde uit de literatuur. De convectie van warmte (bv. urine in de blaas) is meegenomen, in plaats van deze te negeren. In plaats van het negeren van de thermische impact van bloedvaten, zoals standaard gedaan wordt, zijn de bloedvaten (diameter ≥ 3 mm) gesegmenteerd op CT en MRI beelden en meegenomen in de temperatuur berekening. Al deze aspecten zorgen voor een nauwkeurigere temperatuur voorspelling in de patiënt. Tot slot is een radiobiologisch model gebruikt om het gecombineerde effect van radiotherapie plus hyperthermie te voorspellen. Dit effect, uitgedrukt in equivalente stralingsdosis, is gelinkt aan de kans op een positieve behandelingsuitkomst.

In hoofdstuk 6 wordt de bijdrage van dit werk aan de onderzoeksvelden EPT en hyperthermie bediscussieerd en worden aanbevelingen gedaan voor toekomstige perspectieven in beide onderzoeksvelden. In conclusie, in dit proefschrift wordt de implementatie van technische raamwerken gepresenteerd die kunnen dienen als fundament voor toekomstig onderzoek naar acquisitie en reconstructie aspecten die bijdragen aan de nauwkeurigheid, precisie en klinische implementatie van EPT. Dit werk opent ook de deur voor het maken van betrouwbaardere, klinisch haalbare en gepersonaliseerde hyperthermie behandelplannen.

Publications

Peer reviewed journal articles

S. Gavazzi, A.L.H.M.W. van Lier, C. Zachiu, E. Jansen, L.J.A. Stalpers, J.J.W. Lagendijk, H. Crezee, H.P. Kok, "Advanced patient-specific hyperthermia treatment planning" *International Journal of Hyperthermia*, vol. 37, no. 1, pp. 992–1007, 2020. doi:10.1080/02656736.2020.1806361

S. Gavazzi, C.A.T. van den Berg, M.H.F. Savenije, H.P. Kok, P. de Boer, L.J.A. Stalpers, J.J.W. Lagendijk, H. Crezee, A.L.H.M.W. van Lier, "Deep learning-based reconstruction of in vivo pelvis conductivity with a 3D patch-based convolutional neural network trained on simulated MR data," *Magnetic Resonance in Medicine*, vol. 84, no. 5, pp. 2772–2787, 2020. doi:10.1002/MRM.28285

S. Gavazzi, Y. Shcherbakova, L.W. Bartels, L.J.A. Stalpers, J.J.W. Lagendijk, H. Crezee, C.A.T. van den Berg, A.L.H.M.W. van Lier, "Transceive phase mapping using the PLANET method and its application for conductivity mapping in the brain," *Magnetic Resonance in Medicine*, vol. 83, no. 2, pp. 590–607, 2020. doi:10.1002/MRM.27958

S. Gavazzi, C.A.T. van den Berg, A. Sbrizzi, H.P. Kok, L.J.A. Stalpers, J.J.W. Lagendijk, H. Crezee, A.L.H.M.W. van Lier, "Accuracy and precision of electrical permittivity mapping at 3T: the impact of three B_1^+ mapping techniques," *Magnetic Resonance in Medicine*, vol. 81, no. 6, pp. 3628–3642, 2019. doi:10.1002/MRM.27675

S. Gavazzi, P. Limone, G. De Rosa, F. Molinari, G. Vecchi, "Comparison of microwave dielectric properties of human normal, benign and malignant thyroid tissues obtained from surgeries: a preliminary study," *Biomedical Physics & Engineering Express*, vol. 4, p. 047003, 2018. doi:10.1088/2057-1976/AA9F77

Conference proceedings

S. Gavazzi, C.A.T. van den Berg, M.H.F. Savenije, H.P. Kok, P. de Boer, L.J.A. Stalpers, J.J.W. Lagendijk, H. Crezee, A.L.H.M.W. van Lier, "In vivo pelvis conductivity mapping with a 3D patch-based convolutional neural network trained on in silico MR data," in *Proceedings of the 28th Annual Meeting of ISMRM*, p. 3185, 2020 [Digital Poster]

Y. Shcherbakova, C.A.T. van den Berg, **S. Gavazzi**, C.T.W. Moonen, L.W. Bartels, "Detecting the presence of fat using PLANET-based parameter mapping," in *Proceedings of the 27th Annual Meeting of ISMRM*, p. 4015, Montréal, Canada, 2019 [Digital Poster]

S. Gavazzi, S. Mandija, C.A.T. van den Berg, Y. Shcherbakova, M. Bennis, J.J.W. Lagendijk, L.J.A. Stalpers, H. Crezee, A.L.H.M.W. van Lier, "Sequences for transceive phase mapping: a comparison study and application to conductivity imaging," in *Proceedings of the 26th Annual Meeting of ISMRM*, p. 5084, Paris, France, 2018 [Digital Poster]

S. Gavazzi, C.A.T. van den Berg, A. Sbrizzi, M. Bennis, L.J.A. Stalpers, J.J.W. Lagendijk, H. Crezee, A.L.H.M.W. van Lier, "Electrical permittivity imaging at 3T: a precision and accuracy study of three B_1^+ mapping techniques," in *Proceedings of the 26th Annual Meeting of ISMRM*, p. 544, Paris, France, 2018 [Power Pitch]

S. Gavazzi, S. Mandija, C.A.T. van den Berg, Y. Shcherbakova, M. Bennis, J.J.W. Lagendijk, L.J.A. Stalpers, H. Crezee, A.L.H.M.W. van Lier, "Fast clinically feasible MR sequences to map electrical tissue conductivity for improved accuracy in hyperthermia treatment planning (HTP)," in *Strahlentherapie und Onkologie*, vol. 194, pp. 491–492, 2018 [Best Poster "Flash" Presentation at the 32nd Annual Meeting of ESHO, Berlin, Germany, 2018]

H. Crezee, M. Bennis, **S. Gavazzi**, A.L.H.M.W. van Lier, H.P. Kok, "Development of Electrical Properties Tomography for Hyperthermia Treatment Planning," in *First IEEE MTT-S International Microwave Bio Conference (IMBIOC)*, pp. 1–4, Göteborg, Sweden, 2017

Invited Talk

"MR sequences for Electrical Properties Tomography" for the Symposium *The role of MRI in hyperthermia*, Amsterdam UMC (AMC Location), The Netherlands (3rd July 2018)

Awards

Magna Cum Laude Award (Top 15%), ISMRM, Paris, France, 2018

S. Gavazzi *et al.*, "Electrical permittivity imaging at 3T: a precision and accuracy study of three B_1^+ mapping techniques" in *Proceedings of the 26th Annual Meeting of ISMRM*, 2018, p. 544

Best Poster Presentation (1st prize), ISMRM Electro-Magnetic Tissue Properties Group, ISMRM, Paris, France, 2018

S. Gavazzi *et al.*, "Sequences for transceive phase mapping: a comparison study and application to conductivity imaging" in *Proceedings of the 26th Annual Meeting of ISMRM*, 2018, p. 5084

Top Downloaded Article 2018-2019 (Top 10%) in *Magnetic Resonance in Medicine*

S. Gavazzi *et al.*, "Accuracy and precision of electrical permittivity mapping at 3T: the impact of three B_1^+ mapping techniques," *Magnetic Resonance in Medicine*, vol. 81, pp. 3628–3642, 2019

Acknowledgments

No one who achieves success does so without acknowledging the help of others. The wise and confident acknowledge this help with gratitude.

— Alfred North Whitehead

A little wiser and more confident than 4.5 years ago when I started this journey, I would like to express my gratitude to many people who kindly transferred their knowledge to me and supported me during this intense PhD experience.

Dear **Astrid**, I am sincerely grateful for your scientific and personal guidance in these years as my weekly supervisor. Throughout our collaboration, I have appreciated your transparent communication, your critical eye on my methods or results, and your diligent respect for rules and protocols. I also remember with pleasure some MR scan sessions together: it is amazing how we could spot different things looking at the same image! Admittedly, our different thinking processes led to quite some interesting brainstormings and discussions. You taught me several lessons – "Never assume" (when dealing with people) and "it's research, don't take it personally" (for failed experiments or paper rejections) to mention a few – and allowed me to attend conferences, workshops and courses whenever possible. Thanks! I believe that juggling with supervisory and clinical duties was not always straightforward, but I hope this experience has been as enriching for you as it has been for me.

Almost at the end of my 1st year, I felt the need to get some more research inputs... and found *un vulcano di idee* instead! **Nico**, your scientific inputs and your ability to connect people have given interesting twists to my original research ideas. You run on enthusiasm, with which you managed to lighten up my mood when research outputs seemed too negative to me. I am happy you stepped in the EPT meetings, and that you have now become my promotor too. Thanks to my other promotor, **Jan**, for welcoming me in your department, where I probably learned more than I can acknowledge! Thank you also for your encouragement at every article submission and during this career transition period of my life, as well as for some important "pings".

I would also like to thank the hyperthermia team in Amsterdam for their cooperation, starting from my 2nd copromotor. **Hans**, your diplomacy, your enormous knowledge on the ins & outs of hyperthermia and your prompt reaction to emails truly impressed me during our collaboration! Thanks for sharing various helpful observations, for elucidating HT concepts during our intensive February sessions and for notifying the group on latest relevant publications. **Petra**, I am indebted to you for your practical efforts in making Chapter 5 possible: the hyperthermia simulations there have your signature. I learned an overwhelming amount of HTP information in a couple of months thanks to our scientific correspondence, by

email and in Word comments ;-)! **Lukas**, I will hardly forget your funny Disney comments on my PLANET article and your Pixar storytelling recommendations. Thanks for sharing your medical perspective and many other anecdotes in meetings, always with a friendly smile! **Mick**, thank you for our pleasant collaboration during the first year.

Ik wil ook hartelijk bedanken alle leden van de beoordelingscommissie, **prof. dr. Dennis Klomp**, **prof. dr. Chrit Moonen**, **prof. dr. Rolf Boelens**, **prof. dr. Gerard van Rhooen** en **prof. dr. Ton van Leeuwen**, voor het beoordelen van dit proefschrift en jullie aanwezigheid bij de promotieplechtigheid.

Side by side during our PhDs, side by side during our promotions! **Robin**, thank you for being there, in and out of work, to help with scripts or MR scans or IKEA furniture, discuss whatever idea or problem (mostly in our famous daily tea breaks), celebrate small victories (often with a good Belgian beer), share frustration moments (occasionally cheered up by your cookies or *hemelse modder*) and enjoy various fun adventures. You're *buono come il pane*, as we say in Italy, and I am thankful for our friendship.

Caro **Ciucione**, eravamo una "squadra fortissimi" all'università... e lo siamo tuttora, seppur in maniera diversa. Non a caso ti ho scelto come mio *paranimf*! Oltre che per la bella amicizia che ci lega, ti ringrazio per il supporto che mi hai trasmesso e per ricordarmi spesso che c'è un mondo di opportunità e cose nuove là fuori! Sei er mejjo!

Many colleagues deserve a "thank you" for giving me a precious hand during my research efforts. **Stefano**, colleague, housemate and even officemate for a little while! Thank you for fruitful EPT discussions, assistance in building phantoms and useful tips, e.g. on how to combine doing research and writing papers or how to cook a chicken in the MR scanner. **Alessandro**, your help in troubleshooting my B_1^+ sequence simulations and your critical appraisal of my pitch in the B_1^+ article were invaluable. I must admit that your straight and critical feedback struck me so much that I have later found myself thinking "how would Alessandro say/present this? Does this sound honest and critical enough?" when writing the following articles. **Yulia**, thank you! Not only for being readily available to answer my PLANET-related questions or double-check simulations, but also for many pleasant lunches together and your encouragement along the way. **Mark**, I am glad we surmounted the *hobbels* between our different backgrounds to kick off the DL-EPT project. Your practical explanations, at times "seasoned" with lots of anecdotes, got me started with DL & NiftyNet. Thanks also to **Peter** for validating the tumour delineations of patients' MR scans and retrieving necessary clinical information for the DL-EPT study. **Cornel**, thank you for registering the vessel delineations from MRI to CT of Chapter 5 – and for a very good advice! **Wilbert & Clemens**, thanks to you I no longer fear the "Haacke book" [39]! And I extend my gratitude to **Janot**, for your assistance with setting up Sim4Life simulations; **Peter S.**, for welcoming my random consultation requests on EM fields and CSI-EPT; **Maarten**, for kindly brainstorming with me over my deep learning doubts (and I had/have many!); **Stefan**, for facilitating the compilation of this thesis with your Word2Latex script, and for your sense of humour – please keep spreading it around; **Tim & Tom**, for your support with porting issues related to DREAM and BS sequences and for organising the useful MR scientific meetings. Ah, Tom: kudos to you for convincing me to subscribe to the gym ("MRI don't lie") and for initiating Machiavelli nights in LN – but a bit less thank you for garlic smell at 8 am!

Een bijzonder woord van dank wil ik richten aan mijn kamergenoten in Q.0S.437, zowel de oude als de nieuwe garde. Lieve **Hans**, "mijn Nederlandse papa", jouw geduld en brede kennis

van uitdrukkingen en gezegden¹ zijn verbazingwekkend! Ik bewaar mooie herinneringen aan onze dagelijkse theepauzes, angekondigd door jouw "thee bel" en gevolgd door onze Nederlandse lessen! Dank aan **Joris**, voor je hulp met coding issues in Linux, aan **Sophie**, voor jouw precieze tips over praktische zaken rond de PhD, en aan de huidige kamernestor, **Dennis**, voor jouw omnibare subtiele ironie. **Filipa**, thanks for completing the duo [or trio? sorry **Robin** ;-)] of "buitenlanders" in the room for a little while. En dan is er de pouleleider, masker ingenieur, lolbroek van de kamer, en mijn persoonlijke bash scripting expert voor het verwerken van tekeningen, **Mick**. Wij hebben nog een appeltje te schillen... Computer piepjes, geeuwen, zegt dit je iets ;-)? **Daan**, mijn super georganiseerde *bureau buurman*. Dank je voor je vele nuttige adviezen. Ik waardeer het ook dat je mij een hart onder de riem gestoken hebt als ik me moedeloos voelde. Ik kijk er naar uit om je de GoT muziek in de Sint-Joriskerk te horen spelen! **Steven**, gelukkig heb je de kunst naar onze kamer gebracht, met je kleurrijke posters. Ook dank voor jouw playlist met Nederlandse cultmuziek: echt belangrijk voor mijn inburgeringsproces... Bedankt ook aan **Jorine** voor het plannen van sociale kamersactiviteiten, met behulp van Steven en Thomas. Wanneer doen we het fietsdiner? Dank **Thomas**, voor je vriendelijke toezicht bij het intekenen van bloedvaten voor Hoofdstuk 5. Dank aan **Prescilla**, **Stefan**, **Victor**, **Sanam**, en **Cathalijne** voor leuke gesprekken. Ik wil hier ook **Saranto** vermelden, voor haar vriendelijke geduld met mij en mijn chaotische bureau! *Grazie ancora, ragazzi!* Ik heb heel veel genoten van de sfeer, de gezelligheid, behulpzaamheid en recreatieve momenten (inclusief de taarten en de vrijdagen!) die we samen hebben gecreërd!

And I cannot forget my other officemates, Stefano, Flavio & Niek, during my 4-month "sejour at Q2 Italian office". It is in that room and in those months that DL-EPT started! **Flavio**, sei la pazienza fatta a persona ed è sempre un piacere ritrovarci per una chiacchierata. Ti ringrazio per le tue generose consulenze ingegneristiche e la tua gentilezza. **Niek**, your funny "Hey Siri!" still echoes in the back of my mind. Thank you guys for your friendly company!

Many thanks to the other colleagues of Radiotherapy and 7 T groups for keeping a relaxed and pleasant workplace: **Matteo**, **Simon**, **Gert**, **Marielle**, **Bjorn**, **Oscar**, **Arjan**, **Maureen**, **Ellis**, **Anna D**, **Maxence**, **Charis**, **Markus**, **Pim**, **Federico**, **Bart**, **Christopher**, **Mike vR**, **Mike E**, **Carel**, **Deji**, **Tuan**, **Teun**, **Tristan**, **Ingmar**, **Dmitri** and many more. I am glad to have gotten to know you during breaks, *uitjes*, meetings or conferences. Thanks everybody for nice chit chats or scientific discussions. Also thanks to the ICT guys, **Alexis**, **Dawit**, **Mark**, **Rob**, **Erwin** and **Marcel**, and the secretaries, **Leonie**, **Judith**, **Therèse** and **Yvette**, for their availability whenever needed. And **Reneé**, for the prompt help with myPhD platform.

If I embarked in this PhD project continuing my journey in the characterization of dielectric properties is also thanks to **Prof. Giuseppe Vecchi**. Prof. Vecchi, you have been an inspiring advisor while I was moving my first steps in the research world, and your benevolent advice and messages of encouragement these years have always been very much appreciated. Grazie!

I am also thankful to a bunch of friends who made my PhD journey lighter outside office hours. **Alessia**, in the last couple of years we have shared joys and pains of PhD life and of gym trainings... and lately some good victories at *burraco* too! Il team #speriamochemidottorocè l'ha fatta, finalmente! Thanks for offering your genuine opinion and help in many occasions or simply listening when I just needed to vent. Much appreciated! **Jorgos**, thanks for your straight (and at times brutal) honesty, for your loud music (because I learn interesting stuff there) and for proofreading some of the chapters in this thesis. **Stefano**, thanks for your

1. en je creativiteit ook! Wie zal ooit *Geachte Hans*, heb je de ganse, ranzige gehakte gans gegeten? vergeten?

hospitality when I first arrived in Utrecht and for keeping in contact afterwards! Curious that we ended up sharing the living room more often now. **Paolo**, I am glad you discovered your baking skills. Your cakes were a real delight during writing sessions of this thesis! And thanks to Mr. Jingles, for being my little distraction during the lockdown nights spent on this thesis...

Gaurav, my dear housemate, your positive energy and kindness are admirable. It is good to know that I can count on you for thoughtful tips on people management and clear/effective communication, and for good laughs, good jazz during dinner and a hot cup of chai! Rest assured that I always appreciate your advice, which you share as generously as you dispense the 5 Ks in your meals. Grazie!

Huge thanks also to my former housemates (and their regular guests) in LN for sharing part of the PhD experience together: **Aisha, Jojo, Matteo & Tessa, Carlo, Maxence, Tom & Mirthe** (& Fabrizio, what a discovery!), **Casper, Lisa, Anna & Micha, Elena, Stefano, Hester, Alex & Magda, Saskia & Jurica, Anne**. Those dinners, parties, Machiavelli nights, Stranger Things nights, sailing and Irish holidays with you were fantastic!!! Grazie **Carlo**, per aver colmato un po' il gap tra la cultura romana e quella nord-italica, ma anche per i ripassi di olandese insieme e per aver immortalato le mie naturali espressioni buffe in varie occasioni; **Matteo**, grazie per le innumerevoli chiacchierate sulle scale tra i piani S e Q2, i gentili consigli e le cene pantagrueliche dentro e fuori LN.

Grazie alla comitiva italiana a Utrecht, in particolare a **Erika** (mancata coinquilina, ma futura sommelier di fiducia?), **Chiara & Enrico**, e **Ambra**, per le piacevoli serate e mangiate insieme.

Grazie a **Matte**, Matteugo, perché questa copertina è semplicemente fighissima!!!

Un ringraziamento speciale agli amici di lunga data, quelli che ormai vedi una volta l'anno se va bene, ma sono sempre pronti ad accoglierti a braccia aperte. **Ante**, chissà se riuscirai a trascinarci a Monaco con te. Devo dire che la tenacia non ti manca. Grazie per l'affetto e la tua generosa ospitalità (e qui grazie anche a **Dani**!). Team **Bulgheresi**, urge una nuova vacanza insieme! Ringrazio **La Morra, Ricuz, Lory, Ricky & Pess**, perché con voi un motivo per festeggiare lo si trova sempre. Ed è sempre memorabile. Grazie anche alla mia **Gelinda**, per l'amicizia ultraventennale e per molti aperitivi insieme, a **Nico** e alla piccola **Ilenia**, per il suo dolcissimo sorriso, che spero la accompagnerà durante la scoperta del mondo.

Con o senza i 1000 km di distanza a separarci, la tua è stata una presenza costante durante questa esperienza. **Pess**, grazie per le coccole e la premura che mi riservi. Il mio augurio per noi è di vivercela così, *come il fegato con la milza!*

Infine, un grazie di cuore alla mia famiglia per la gioia che sapete regalarmi ad ogni rientro a casa, per la fiducia che riponete in me e per la vostra cura nonostante la distanza. **Alessio**, i tuoi generosi sforzi di produzione di salame, génépy & quant'altra delizia (che poi prontamente finiscono in valigia, direzione Olanda) sono sempre molto apprezzati. **Oscar**, come rompi le scatole tu, nessuno mai [guai a te se smetti ;-)!]. Grazie perché, tra un battibecco e una risata, io so di poter contare su di te. **Mamma**, grazie per essere semplicemente *così come sei*. *Quanta vita mi hai passato, e non la chiedi indietro mai...*

Soraya

About the author

Soraya Gavazzi was born on 15th December 1990 in Aosta (Aosta Valley region), Italy. She spent a happy childhood in Pontey, a small village, and attended the primary school there. Afterwards, she attended the high-school "Liceo Scientifico Maria Ida Viglino" in Saint-Vincent. She received her diploma in 2009 and then moved to Turin to study Biomedical Engineering at Politecnico di Torino. During her Master education, she got particularly enthusiastic about both bioelectronics and biomedical applications of electromagnetic fields. Pursuing her interest in this second field, she performed a 1-year research project on the characterization of ex vivo electrical properties of human thyroid tissues. She obtained a *cum laude* M.Sc. degree in March 2015.

Besides studying and enjoying a lively student life, Soraya worked as waitress and barmaid in several restaurants and bars in Aosta Valley. Begun as summer job during high school, this activity turned into a regular part-time job in parallel to her university studies. In December 2015, she started working as PhD candidate at the Radiotherapy Department of University Medical Center Utrecht, The Netherlands, specializing in quantitative MRI. During her PhD education, she had the opportunity to measure the electrical properties of human body tissues — this time in vivo. She also discovered the wonders of MRI, the ins & outs of treatment planning for hyperthermia cancer therapy, the pleasure of presenting, and learned many valuable lessons.

